

Table of Contents

List of Figures	v
1 Introduction	1
1.1 Outline of Thesis	3
1.2 Evidence for Dark Matter	4
1.2.1 Galactic Rotation Curves	5
1.2.2 BBN	7
1.2.3 CMB	8
1.2.4 BAO	11
1.2.5 Gravitational Lensing	13
1.3 Dark Matter Candidates	14
1.3.1 AXIONS	15
1.3.2 WIMPs	17
1.4 WIMP Dark Matter Searches	19
1.4.1 Direct Detection	21
1.4.2 WIMP Detection Experiments	26
List of Abbreviations	1
2 The LUX Detector	28
2.1 Introduction	28
2.2 The LUX TPC	29
2.2.1 Target Xenon	31
2.2.2 Background Rejection	32
2.2.3 The Drift Field inside the LUX TPC	35
2.3 Light and Charge Signals in Liquid Xenon	37
2.3.1 Electronic Recoils (ER)	38
2.3.2 Nuclear Recoils (NR)	40
2.3.3 Energy and Position Reconstruction	41
2.4 Identifying S1, S2	42
2.5 LUX Science Result (WIMP limit)	46

3	Spacial Dependent Correction of the S1 and S2 Signals	53
3.1	^{83m}Kr Calibration	55
3.2	^{83m}Kr Mixing in Liquid Xenon	59
3.3	S2 Electron Lifetime and x,y Correction	59
3.4	S1 Spacial Dependant Correction	63
3.5	Application to x,y,z Corrections in Data Processing	69
4	Calibrating the Combined Energy Scale	73
4.1	Anti-Correlation Space	76
4.2	Refitting in Combined Energy Space	77
4.3	Finding Errors with MCMC	83
4.4	Combined Energy Space	84
4.5	Light Collection and Electron extraction	86
4.6	Tritium Beta Spectrum	88
5	Event Level Fluctuations	94
5.1	Modeling Intrinsic Detector Resolution	94
5.2	Measuring Recombination Fluctuations with Mono-Energetic Sources	98
5.3	Measuring Recombination Fluctuations in Desecrate Energy Bins . .	102
5.3.1	Measuring the Fano Factor in Bins of Energy	108
5.3.2	Application to ^{83}Kr	110
5.3.3	Application to Simulated Tritium Data (any continuous spectrum)	113
5.3.4	Centriod Subtraction	116
5.4	Extracting Recombination Fluctuations from Tritium Calibration Data	120
5.4.1	Extracting Recombination fraction From Tritium Data	124
5.4.2	Modeling the ER Band	124
5.4.3	Measuring Alpha From the Tritium Data	127
5.5	Extracting Recombination Fluctuations from ^{137}Cs Calibration	129
5.6	Recombination Fluctuations, The Bigger Picture	131
5.6.1	Encounter Recombination Probability	133
5.6.2	Clusters of Encounter Recombination	141
5.7	Conclusion	149
6	Ionization and Scintillation Yield from Tritium Calibration	151
6.1	Correcting for Spectral Shape for Finite Resolution	152
6.1.1	Calculating the Observed Energy	153
6.1.2	Smearing a Toy Spectrum	155
6.2	Light Yield, Charge Yield and Comparison to NEST Modeling	157
6.2.1	Tritium S1 and S2 vs. NEST	158
6.2.2	Tritium Energy Spectrum	161
6.2.3	Results for Light Yield, Charge Yield and Recombination . . .	165
6.3	Measuring Light Yield, Charge Yield and Recombination, Corrected for Spectral Shape	168
6.3.1	Tritium S1 and S2 Correction	168

6.4	Ionization and Scintillation Yield After Correction	172
6.5	Comparison of Light Yield Measured With Tritium to Other Measurements With Compton Scatters	177
6.5.1	The Standard Candle: Light Yield from ^{83m}Kr	177
6.5.2	Comparing Tritium Scintillation Yield with Compton Scatters	179
6.6	Summery	182
7	Tritiated-Methane Calibration Source and the ER Band	184
7.1	The need for an Internal Calibration Source	184
7.2	Tritiated-Methane as a Calibration Source	186
7.3	Removal of CH_4 from LUX	188
7.4	Light Yield Quenching from CH_4 in LUX	190
7.4.1	Tritiated Methane injection into the LUX detector	192
7.4.2	Mixing of Tritiated Methane in Liquid Xenon	193
7.4.3	Definition of Electronic Recoil Band. ER and NR Discrimination	195
7.5	ER Band Gaussianity	199
7.6	S1 Threshold For Golden Events, Using Tritium	200
7.7	Conclusion	202
	Bibliography	204

List of Figures

1.1	Kepler explains the elliptical orbit of Mars, held fixed by a resident angel guiding its orbit.	2
1.2	Λ CDM parameters depicted on a unicorn by the LUX detector. The magic component which comprise the horn has yet to be directly detected, however it provides the backbone for the model. Note, the parameters in the diagram may not be representative of the specific universe in which this thesis is published.	3
1.3	Measured rotational velocities vs. radius in the Milky Way galaxy. The velocity distribution is consistent with a halo of mass surrounding the galaxy well beyond the observed luminous disk [1].	6
1.4	Maru the cat explains the cosmic microwave background. Consider that Maru is a photon and the box size represents local energy densities of the universe. The scale of the the box size is inversely proportional to the local energy density and temperature. At the time of last scatter all boxes containing Marus cease to exist, to the horror of the cats! The Marus are now left to propagate freely through the universe, with their configurations unchanged (the cats are too lazy to move and are content napping for 13.7 billion years). Figures a-d show Maru the cat contained within increasing box sizes corresponding to decreasing energy densities.	10
1.5	Improvement of resolution from COBE, first to discover anisotropies in the CMB, to WMAP and Planck which have set stringent limits on cosmological parameters by mapping variations in temperature of 1 part in 100,000. Image credit: NASA/JPL-Caltech/ESA.	11
1.6	BAO peak obtained from BOSS [2]	12
1.7	The concentration of mass in the bullet-cluster as observed from X-rays, emitted by baryonic matter, in pink and the concentration of mass from gravitational lensing in blue. [Composite image credit: X-ray: NASA/CXC/CfA/M.Markevitch et al.; Optical: NASA/STScI; Magellan/U.Arizona/D.Clowe et al.; Lensing Map: NASA/STScI; ESO WFI; Magellan/U.Arizona/D.Clowe et al.]	14

1.8	Illustration of the CP problem and the axion solution. “Analogy for the CP problem and the axion solution. In a room (the Standard Model), there is a table (QCD) sitting on an uneven floor (CP). A billiard ball (nEDM) placed on top of the table is expected to rapidly move across the uneven surface. However, the billiard ball is observed to stand still and the horizontal angle of the table is measured to be $\theta < 10^{-11}$. The solution to this puzzling observation is the existence a new degree of freedom (manifested in the axion) that levels the table (drives $\theta = 0$)”, [Carlos’ Thesis]	17
1.9	Methods for detecting WIMPs from interactions of q, standard model particles, and dark matter particles χ . WIMPs can be detected through the annihilation of dark matter particles into standard model particles, $\chi\chi \rightarrow qq$. WIMPs can be produced by colliding standard model particles, $qq \rightarrow \chi\chi$. Or one can look for the scatter of a dark matter particle off a standard model particle, $\chi q \rightarrow \chi q$	20
1.10	Dark matter density vs. distance from the galactic center, calculated from galactic rotation curves of the Milky Way galaxy. The Earth is located at 8.3 kpc. Figure from [1].	22
1.11	Plot of WIMP event rate per kg/day/keV vs. Nuclear recoil energy (keV) for several target nuclei, using parameters from [3]. At low detection threshold xenon is the most attractive target nuclei. The drop off in the xenon spectral shape is due to decoherence described by the Helm factor [4].	25
2.1	Photo of the outer vessel of the LUX detector from inside the water tank.	29
2.2	Illustration of the LUX detector’s internals. The detector contains two arrays of PMTs on the top and bottom housing 61 PMTs each. Teflon panels on the edges of the active region are used to reflect scintillation signals. The vertical distance between the two PMT arrays is 60 cm, and the diameter to the outer edge of the teflon panels is 50 cm.	30
2.3	Simulation of expected gamma background events inside the LUX detector, using the single scatter cut requirement[5]. There is an additional factor of 1000 background rejection within the fiducial volume where the WIMP search is conducted (inside the black dashed lines) .	33
2.4	The ER type and NR type bands from a) AmBe and ^{252}Cf (Red) and b) tritium calibration (Blue). The band means are solid lines and the 10-90% CL are shown as dashed lines. The ER to NR discrimination by using the charge to light ratio was measured to 99.6 ± 0.1 % at 50% NR acceptance.	35

2.5	Field grids in the LUX detector during the 2013 science run. T,A,G,C,B are biassed to -1,+3.5,-1.5,-10,-2 (all in kV), respectively. The PMTs are biased to -1.2 kV on average. The figure on the right shows the electric field model in the drift region between the cathode and gate for drift distance z vs. detector radius r. On average the drift field is 170 V/cm with variation from 140 V/cm to 200 V/cm from cathode to gate. Electric field model from [6].	36
2.6	An electronic recoil (ER) event in xenon. The energy deposited is converted primarily to ionization and roughly one tenth for excitation. Only several percent is lost to heat. Xenon excitons and recombining electron ion pairs for xenon dimers which de-excite producing very ultra violet (VUV) scintillation light at 175nm producing the primary scintillation signal (S1). Electrons that do not recombine are drifted by an electric field into the gas phase where they are accelerated producing the secondary scintillation (S2) signal.	39
2.7	A nuclear recoil (NR) event in xenon. The energy deposited goes mainly towards heat (phonons), the remaining energy is split evenly between ionization and excitation. Xenon excitons and recombining electron ion pairs for xenon dimers which de-excite producing very ultra violet (VUV) scintillation light at 175nm producing the primary scintillation signal (S1). Electrons that do not recombine are drifted by an electric field into the gas phase where they are accelerated producing the secondary scintillation (S2) signal.	40
2.8	Event diagram.	42
2.9	2keV ER event as seen by each PMT channel of the LUX detector. The S1 signal summed across all channels is overlaid on the top left, and the S2 signal summed across all channels is overlaid on the top right.	43
2.10	Density plot of prompt fraction vs. Pulse Area. Top: ^{83m}Kr data set. Bottom: Tritium data set. Populations of single electrons, single photons and the S1 S2 pairs associated with γ , β and α are highlighted as rectangles.	45
2.11	All single scatter events seen in the active region of the LUX detector over the course of the first science run passing all cuts listed in table 2.3 excluding the fiducial cut. The dashed cyan box indicates the fiducial volume.	47
2.12	The remaining events passing the quality cuts listed in table 2.3. The charge to light ratio (S2/S1) is plotted vs. S1 (proportional to energy) to show the separation of ER and NR type events. The 10-90% CF limits of the ER and NR band are plotted as the dashed blue and red curves, respectively. The band means are solid. S2 _b stands for the S2 signal on the bottom PMT array.	49

2.13 LUX detector is consistent with a P value of 0.35 of the background only hypothesis. The 90% upper C.L. cross section for various spin independent masses are shown in figure 2.13 in blue. Also shows are limits from Xenon100 (red), CDMS II (green), ZEPLIN III (magenta), and one sigma signal claimed for DAMA/LIBRA (shaded grey), CDMS II Silicone (shaded green), CRESST II (shaded yellow).	51
3.1 A simplified decay diagram of ^{83}Rb and $^{83\text{m}}\text{Kr}$, from [7].	55
3.2 The S1 and S2 of two $^{83\text{m}}\text{Krevents}$. Top Figures (a): Show a $^{83\text{m}}\text{Krevent}$ in which the two x-rays have overlapped within 60 ns, the S2 arrives about 93 μs later. Bottom Figures (b): Show a $^{83\text{m}}\text{Kr}$ event in which the two x-rays have overlapped within 220 ns, the S2 arrives about 205 μs later. The LUX pulse finder classifies events within a 1 μs window as a single S1. The S2 pulses are insensitive to the timing separation of the dual decay as electron diffusion smears the pulses two together as the electrons drift. The PMT hit map for these events are shown below in figure 3.3.	57
3.3 The S1 and S2 of two $^{83\text{m}}\text{Krevents}$. Top Figures (a): Show a $^{83\text{m}}\text{Krevent}$ in which the two x-rays have overlapped within 60 ns. Bottom Figures (b): Show a $^{83\text{m}}\text{Kr}$ event in which the two x-rays have overlapped within 220 ns. The black, open circle represents the location of the event. The S1 hit pattern is diffuse with more light collected on the bottom arrays due to total internal reflection at the liquid surface. The S2 is localized in the top PMT arrays in x,y at the location where the electrons are extracted, and diffuse on the bottom due to scattering. The sumed waveforms for these events are shown above in figure 3.2.	58
3.4 Distribution of $^{83\text{m}}\text{Krevents}$ 10 minutes after the injection. The source mixes uniformly throughout the liquid xenon illuminating all regions of the active volume. The solid black lines represent the fiducial volume used for the WIMP search.	60
3.5 Left: Fits to the mean of S_{2b} of the $^{83\text{m}}\text{Kr}$ data in several z slices. Right, the exponential fit to the means of S_{2b} vs. drift time used to extract electron lifetime τ . The electron lifetime is found to be $\tau = 753.1 \pm 3.2 \mu\text{s}$. The exponential fit to the means deviates near the top and bottom of the active region since the charge yield from the $^{83\text{m}}\text{Kr}$ decay is sensitive to the varying electric field. The data shown was taken data on May 10, 2013 (lux10_20130510_T1250) and contains 700,000 $^{83\text{m}}\text{Kr}$ events.	61
3.6 Left: Response of S_{2b} vs. x,y normalized to the response at the center ($x=y=0$). The region of larger response around $x=0$, $y=-25$ is likely from an enhanced extraction field between the anode and gate wires. Right: Response of S_{2b} vs. x,y after correcting the data using $\mathcal{N}\mathcal{F}_{S_{2b}}$.	62

3.7	Improvement of resolution in S2 _b after applying the z and x,y,z correction. Black: The uncorrected data. Red: The data with only z dependent correction, the electron lifetime correction. Blue: The data with full x,y,z dependent correction. The data shown was taken data on May 10, 2013 (lux10_20130510_T1250) and contains 700,000 ^{83m} Kr events.	63
3.8	S1 x,y,z response normalized to the center of the detector. The interpolated map represents the inverse of the normalization factor $\mathcal{N}\mathcal{F}$.	65
3.9	S1 x,y,z response normalized to the center of each z slice. There are greater variations near the very top and bottom 4 z slices as the solid angle for light hitting the PMT arrays increases. For the central slices the x,y response is uniform due to increased scattering off the teflon panels.	66
3.10	S1 x,y,z response normalized to the center of the detector after the data has been corrected and normalized to the detector center. The remaining variations in the fiducial volume ($r < 18\text{cm}$) is less than 1%. Near the top and bottom edges the deviation increases to as much as 3% due to the interpolation of the correction becoming poorly constrained.	68
3.11	Improvement of resolution in S1 after applying the z and x,y,z correction. Black: The uncorrected data. Red: The data with only z dependent correction. Blue: The data with full x,y,z dependent correction. The data shown was taken data on May 10, 2013 (lux10_20130510_T1250) and contains 700,000 ^{83m} Kr events.	69
3.12	Electron lifetime measured using ^{83m} Kr calibrations during the LUX science run in 2013. The blue dashed lines show the boundaries of the WIMP search from April 21 to Aug 8, 2013. The red dashed lines indicate circulation loss events.	70
3.13	Measured response of to light from ^{83m} Kr calibrations at the center of the LUX detector during of the LUX science run in 2013. The blue dashed lines show the boundaries of the WIMP search from April 21 to Aug 8, 2013. The red dashed lines indicate circulation loss events.	71
4.1	LUX data in anti correlation space (S1 vs. S2), the black lines indicate the initial cuts by eye used to isolate populations of constant energy. In both figures diagonals represent lines of constant energy with a slope depending on the local recombination probability. The centroids found by an unbind maximum likelihood analysis are shows as a black X, for sources show in table 4.1.	77

4.2	Doke plot showing the best fit for the energy calibration parameters g1 and g2 using S1 and S2 means extracted from anti-correlation space. The first three blue points, from the left, are from ^{83}Kr calibrations at 50, 100 and 170 V/cm respectively. The open circle was from the K-shell xenon X-ray and was not used for the fit as it's absolute energy and origin from the skin of the detector is uncertain.	78
4.3	Doke plot showing the best fit for the energy calibration parameters g1 and g2 using S1 and S2 extracted from a combined energy space. The first three blue points, from the left, are from ^{83}Kr calibrations at 50, 100 and 170 V/cm respectively. The open circle was from the K-shell xenon X-ray and was not used for the fit as it's absolute energy and origin from the skin of the detector is uncertain.	79
4.4	S1 fits to sources at nominal field of 170 [V/cm] unless otherwise noted. Source and energy in keV from top left to bottom right: a) ^{131}Xe : 163, b) ^{127}Xe : 207, c) ^{127}Xe & $^{129\text{m}}\text{Xe}$: 236.8, d) ^{127}Xe : 410, e) ^{214}Bi : 609, f) ^{137}Cs : 661.6, g) $^{83\text{m}}\text{Kr}$: 41.5 - at 50 [V/cm], h) $^{83\text{m}}\text{Kr}$ 41.5 - at 100 [V/cm], i) $^{83\text{m}}\text{Kr}$ 41.5	80
4.5	S2 fits to sources at nominal field of 170 [V/cm] unless otherwise noted. Source and energy in keV from top left to bottom right: a) ^{131}Xe : 163, b) ^{127}Xe : 207, c) ^{127}Xe & $^{129\text{m}}\text{Xe}$: 236.8, d) ^{127}Xe : 410, e) ^{214}Bi : 609, f) ^{137}Cs : 661.6, g) $^{83\text{m}}\text{Kr}$: 41.5 - at 50 [V/cm], h) $^{83\text{m}}\text{Kr}$ 41.5 - at 100 [V/cm], i) $^{83\text{m}}\text{Kr}$ 41.5	81
4.6	Doke plot of the data showing the light yield vs. charge yield. Only solid circles are used for the fit, the open circle is the Xe K shell X-ray from the detector edge.	82
4.7	MCMC for the linear fit to the Doke plot. There is a strong negative correlation between the slope m and intercept b which results from the degeneracy between gains g1 and g2.	84
4.8	Combined energy scale. a) The xenon activation lines from early in the run. b) ^{137}Cs calibration data. c) All calibration data including the $^{83\text{m}}\text{Kr}$ calibration. d) Xenon X-ray.	85
4.9	Single electron distribution as seen by the bottom PMT array fitted with a skew Gaussian model to account for the underling Poisson statistics of observing between 9 and 10 photo electrons (PE) for each electron leaving the liquid and entering to the gas phase at a higher field causing electro-luminescence. The μ of the fit represents the true mean of the skew Gaussian distribution.	88
4.10	The tritium energy spectrum reconstructed from the data (black). Along with LUX SIM (blue), and the true tritium beta spectrum (blue) and a tritium spectrum smeared with detector resolution (green).	90
4.11	Threshold calculated from difference of simulated Tritium S1, S2 and energy spectra at 170 V/cm. a) S1 b) S2 _b , c) Combined Energy . . .	92
4.12	Threshold calculated from difference of simulated Tritium S1, S2 and energy spectra at 100 V/cm. a) S1 b) S2 _b , c) Combined Energy . . .	93

5.1	Populations of calibration sources in discrimination space $\log\left(\frac{n_e}{n_\gamma}\right)$ vs. combined energy [keV _{ee}]. The ovals represent the combination of σR , $\sigma n_{\gamma_{\text{Det}}}$, $\sigma n_{e_{\text{Det}}}$ in black, white, red respectively.	103
5.2	Measured values of σR , $\sigma n_{\gamma_{\text{Det}}}$, $\sigma n_{e_{\text{Det}}}$ vs. Energy on the left and vs. Quanta on the right. Measured using sources listed in Table 4.1.	103
5.3	Top: Illustration of statistical variance, recombination fluctuations are set to 0. The spread in number of photons moves vertically and the spread in number of electrons moves horizontally. In black, a line of constant energy along the mean of combined energy with a width ΔE . Bottom left: Dominated by recombination fluctuations which move 45° to statistical variances. Bottom Right: Typical values for recombination and S1, S2 Stat for Kr ⁸³	106
5.4	Illustration of statistical variance for the tritium beta spectrum, recombination fluctuations are set to 0. This plot is analogous to Figure 5.3 which illustrates the case for the mono energetic ^{83m} Kr decay. Recombination fluctuation move along lines of constant energy, S1 statistical fluctuation move vertically and S2 statistical fluctuations move horizontally.	115
5.5	Light yield (left) and Charge yield (right) of a simulated tritium spectrum, with the fit to the centroid show in black. The variance in number of photon and electrons per energy bin is used to extract recombination fluctuations.	116
5.6	Simulated tritium spectrum with the detector resolution of the LUX detector, $\sigma_{S1_{\text{Det}}}$ and $\sigma_{S2_{\text{Det}}}$, and an arbitrary recombination fluctuation σR (magenta). After centroid subtraction we apply the methodology described in the previous section to extract σR (black and blue) through the light and charge channel using our knowledge of detector resolution per each energy bin χ_{Det} (green), $S1_{\text{Det}}$ (red) and $S2_{\text{Det}}$ (yellow). The plots show cases for various bin widths in [KeV]: a) $\Delta E = 0.1$ b) $\Delta E = 0.25$ c) $\Delta E = 0.5$ d) $\Delta E = 1$	119
5.7	a: Density plot of number of photons vs. energy in keV using the tritium calibration data at 170 V/cm. b: Number of electrons vs. energy in keV using the tritium calibration data at 170 V/cm. c: Number of photons vs. energy in keV using the tritium calibration data at 100 V/cm. d: Number of electrons vs. energy in keV using the tritium calibration data at 100 V/cm. The data has been corrected for spectral shape. The black line indicates the quadratic fit to the centroid of the population.	122

- 5.8 The figures on the left in 5.8 (a: 170 V/cm, c: 100 V/cm) show the extracted recombination fluctuation σ_R from the light (black) and charge (red) channel denoted with subscript γ and e respectively, note they are identical. Also shown are the fluctuations in light collection $\chi_{\gamma_{\text{Det}}}^2$ (blue), charge collection $\chi_{e_{\text{Det}}}^2$ (cyan), and their manifestation as detector resolution in a combined energy bin as χ_{Det} (magenta). The figures on the right in 5.8 (b: 170 V/cm, d: 100 V/cm) show the mean and one sigma standard deviation of the measured number of photons (blue) and electrons (red). Also shown is the total quanta (in black) which is the sum of photons and electrons and the expected number of ions (magenta) and excitons (cyan) using $\alpha = 0.20$ 123
- 5.9 Recombination Fraction at 170 V/cm (black) and 100 V/cm (blue). The shaded regions represent the one sigma of the observed fluctuations in recombination fractions σ_r . The dashed line at 1.0 keV_{ee} represents the 50% detection threshold. 125
- 5.10 The result of the ER band's mean population and its corresponding 1 sigma fluctuation for the case of 100 V/cm (blue) and 170 V/cm (black). We find an overlap below 4 keV_{ee} where the additional strength of the drift field is higher improving threshold of discrimination. Above 4 keV_{ee} the bands separate as the higher drift field increased the charge extraction leading to better discrimination. . . . 127
- 5.11 Determining the best α using the tritium calibration data, with $\alpha = 0.3$ (blue), 0.2(black), 0.15(magenta) and 0.06(red). Left: The y axis is the ratio of the measured standard deviation of recombination to that of a binomial process and is plotted vs. the expected binomial standard deviation on the x axis. The best α is one for which the observed standard deviation converges with that of a binomial process as the binomial variance tends to 1. Right, the same y axis as on the left but plotted vs. the number of ions available for recombination. As the number of ions approaches one the standard deviation of recombination should become that of a binomial process. A single ion will either recombine or not with probability r . The best intercept converging to a purely binomial process (black star) is with $\alpha = 0.20$. Falling below the value of one on the y axis implies that recombining electron-ion pairs have a variance better than binomial, which is unphysical if it is a random process. Note, the fits use only data above 90% threshold at 1.3 keV, starting from the third data point from the left. The higher end cut off at 3 keV corresponds to the end of the fitted lines. 129
- 5.12 Left: The mean and one sigma standard deviation of the measured number of photons (blue) and electrons (red). Also shown is the total quanta (in black) which is the sum of photons and electrons and the expected number of ions (magenta) and excitons (cyan) using $\alpha = 0.20$. Right: The recombination probability r (solid black) and the one sigma fluctuation σ_r (shaded). 130

5.13 Recombination fluctuations measurements are labeled on the plot and include data from tritium at 170 V/cm, tritium at 100 V/cm, ^{137}Cs calibration, the line sources used for the energy scale calibration listed in table 4.1 and a ^{57}Co calibration at a variety of electric fields ranging from 60 to 5000 V/cm from [8]. Left: the observed recombination fluctuation σ_R measurements vs. the standard deviation expected from a purely binomial process, equation 5.32. The red curves represent power law fits to the data.	132
5.14 Illustration of recombination for the case of a single ion, blue box highlighted in black at the center. The total recombination probability for one ion is the combination of the dominant self recombination probability (r_s) plus the sum of the encounter recombination probabilities (r_e) from the remaining N-1 electrons. This process is repeated for N number of ion electron pairs leading to a binomial variance given in equation 5.35.	135
5.15 Encounter recombination probability r_e extracted from the tritium and ^{137}Cs calibration data at 170 V/cm, derived from equation 5.39. Left plotted vs. energy in keV. Right: plotted vs. the number of ions. The solid red line represents the overall average of r_e from the calibration data is $r_e = 0.0042$	138
5.16 The red crosses indicate the total recombination probability r for the calibration sources labeled on the plot. The black x-s indicate the encounter recombination probability r_e . The blue points indicate the tritium data at 100 V/cm. The data includes tritium at 170 V/cm (black), tritium at 100 V/cm (blue), ^{137}Cs and data from Dahl for ^{57}Co ranging from 60 to 5000 V/cm [8].	139
5.17 Fit to the observed ER recombinations modeled with binomial fluctuations where the recombination probability includes an encounter recombination component. Case one (red) is with assuming a constant $r_e = 0.0042$, extracted from the tritium and ^{137}Cs data. Case two (green) is using $r_e = 0.0011 + 0.006r$. Case two is in significantly better agreement with the field dependent data from Dahl, as it accounts for field effects [8]. The fit for case two (green) deviates less than 30% from the data.	140
5.18 Illustration of recombination for the case of a single ion occurring in N_C clusters with number of encounters N_e . The total recombination probability for all clusters is equal to the average of each individual cluster. In each cluster the recombination probability is equal to the number of interaction N_e times the encounter recombination probability r_e . The process is repeated for N_C clusters, resulting in an additional factor N_i in the observed variance while maintaining the correct average recombination probability r	143

5.19 The data shown are labeled on the plot and include calibration data of tritium data at 170 V/cm, tritium at 100 V/cm (blue), ^{137}Cs at 170 V/cm, and data over a range of fields using ^{57}Co from Dahl. [8]. a) The encounter recombination probability r_ϵ plotted vs. energy. b) The number of encounters per cluster N_ϵ vs. energy. c) The number of clusters N_C vs. energy.	145
5.20 The measured recombination fluctuations from calibration data vs. energy. The red line indicates the expected recombination fluctuation of the clustering model given in equation 5.46, assuming a cluster size of $N_\epsilon = 50$. $N_\epsilon = 50$ corresponds to an average encounter recombination probability of $r_\epsilon = 0.01$. The deviation of the fit from the data is less than 30%. The $^{83\text{m}}\text{Kr}$ data point is the result of two decays and is expected to fall below the curve by 40% considering the sum of the individual variances.	147
6.1 Smearing of a linear spectrum using equation 6.1 for an arbitrary energy scale E. The counts in each shaded bin are redistributed into normalized Gaussians (blue) with the resolution σ_E growing like \sqrt{E} . The spectrum smeared with detector resolution is the sum of Gaussians shown in red.	153
6.2 Top Left: A linearly decaying spectrum, in blue. The black curve represents the sum of the Gaussians assuming a constant resolution. Top Right: A linearly decaying spectrum, in blue. The black curve represents the sum of the Gaussians with a $\sigma = \sqrt{E}$ dependent resolution. Bottom: The observed mean, with finite resolution, compared to the real mean with infinite resolution. The black points are for the case with linear resolution and the red points represent the case with $\sigma = \sqrt{E}$ dependent resolution.	157
6.3 a): In Black S1 tritium S1 spectrum extracted from the data. In blue, The NEST light yield curve. In red, the NEST light yield curve with recombination fluctuations. Dashed magenta is NEST light yield with smearing from equations 6.7. b): The ratio of the real S1 mean to the S1 observed mean vs. the observed mean after smearing. Note, the S1 threshold at about 3 PE in S1. c): In Black S2 tritium spectrum extracted from the data. In blue, The NEST light yield curve. In red, the NEST light yield curve with recombination fluctuations. Dashed magenta is NEST light yield with smearing from equations 6.8. d): The ratio of the real S2 mean to the S2 observed mean vs. the observed mean after smearing.	161
6.4 The tritium energy spectrum reconstructed from the data (black). Along with LUX SIM (red), the true tritium beta spectrum (dashed blue) and a tritium spectrum smeared with detector resolution of equation 6.11 (green).	163

- 6.5 Left, mapping from real Monte Carlo energy to observed energy plotted vs the observed energy after applying a finite resolution using LUXSIM. Right, comparing the correction determined from the Monte Carlo (Red) to the detector smearing model (black) given in equation 6.11. The dashed lines represent the uncertainty in the measured values. The agreement is within errors from 1 to 18 keV_{ee}. The Energy threshold is 50% at 1.0 keV_{ee}. 164
- 6.6 Top: Extracted recombination fluctuation from the tritium data from fluctuations in photons and electrons (Black and Red respectively). Bottom right: mean number of quanta in photons, electrons, ions, excitons vs. energy keV for the tritium calibrations. Bottom left: Recombination fraction and the one sigma (shaded) vs. energy keV. . 166
- 6.7 Light yield and charge yield from tritium data without spectral shape correction at 170 V/cm in black. The shaded region represents the one sigma systematic uncertainty on g1 and g2. The NEST yield prediction and its corresponding 1 sigma is shaded in blue. NEST interpolation is shown in magenta to energies where the model is not vetted. Note that the statistical errors are about the size of the data points and the dominant uncertainty illustrated by the shaded region is 100% correlated bin-to-bin. A one sigma shift up in light yield corresponds to a one sigma shift down in charge yield and visa versa. 167
- 6.8 a): In Black S1 tritium S1 spectrum extracted from the data. In red, the S1 spectrum based upon the LY and QY measured from the tritium data after applying recombination fluctuations. In dashed blue, the expected S1 spectrum after applying finite detector resolutions of equation 6.7. b): The ratio of the real mean to the observed mean vs. the observed mean after smearing the tritium photon spectrum with detector resolution. Note the S1 threshold at about 3 PE in S1. c): In black, tritium S2 spectrum from the data. In red, the S2 spectrum based upon the LY and QY measured from the tritium data after applying recombination fluctuations. In dashed blue, the expected S2 spectrum after applying finite detector resolutions of equation 6.8. d): The ratio of the real mean to the observed mean vs. the observed mean after smearing the tritium electron spectrum from NEST with detector resolution. Note the S2 threshold at about 400 PE in S2. . 170
- 6.9 Means of the light yield and charge yield from tritium data corrected for spectral shape along with the 1 sigma statistical errors. 172
- 6.10 Light yield and charge yield from tritium data corrected for spectral shape along with the 1 sigma systematic constraint on g1 and g2. The blue and magenta curve are NEST extrapolation and interpolation, respectively. 174
- 6.11 In black, the light yield and charge yield from tritium data corrected for spectral shape. In red, the light yield and charge yield from tritium data uncorrected for spectral. The shaded region represent the one sigma systematic error from the constraint on g1 and g2 shaded. . . 176

6.12 Left: The light yields of the 9.4 and 32.1 keV decay of ^{83m}Kr plotted vs. timing separation, for events separated by more than 1200 ns. The point at 600 ns is calculated assuming the 32.1 keV yield remains flat to 200 ns as observed in [9] and [10]. Right: the histogram of ^{83m}Kr events vs timing separation finding a best fit to the half life of 159.7 ± 7.5 consistent with the measured value of 154 ns [11] [12].	178
6.13 Left: S1 ^{83m}Kr peaks at zero field. Right: shows the histogram of the separated 32.1 and 9.4 keV decays plotted above vs. time. The half life fit to the population is in good agreement with the measured half-life of 154 ns [11] [12].	179
6.14 LY relative to the light yield of the 32.1 keV decay of ^{83m}Kr at zero field. The black and blue bands represent the results from tritium at 170 and 100 V/cm respectively. The shaded region represents the systematic error due to the one sigma constraints on g1 and g2. Magenta points are Compton scattering measurements from [13]. The grey and red represent zero field and 450 V/cm Compton Scattering measurements from [10].	181
7.1 True tritium beta spectrum from [14].	187
7.2 Removal of natural methane observed by the integrated xenon sampling system prior to the tritiated-methane injections. The red points indicate measurements at the getter outlet, we find a 97% one pass removal efficiency at a flow rate of 25 SLPM. The blue curve shows the improved upper limit on the effect of outgassing from the plastics. The black dashed lines shows the exponential fit to the natural methane removal from the xenon with a time constant of 5.9 ± 0.07 hours. 5×10^{-3} ppb (g/g) is the limit of detection for methane.	189
7.3 In black, the response to scintillation from ^{83m}Kr at the center of the detector normalized to the first data point before the natural methane (CH_4) injection. The dashed magenta lines represent the time window from the beginning of the natural methane injection to the time the background of 5 ppt is reached. The blue points represent that methane concentration in the gas returning from the bulk liquid of the detector. The concentration in the liquid xenon is roughly 1/6 of the concentration measured in the gas phase due to solubility.	191
7.4 The rate of single scatter events with S1 below 100 PE in the fiducial volume. 100 PE in S1 is about 18.6 keV _{ee} , the endpoint to the tritium beta spectrum. The magenta and red curves are fits to the first and second tritium injection's removal rate. Note, the removal of tritiated-methane is consistent with the natural methane removal rate measured independently.	193

7.5	The distribution of tritium events vs. detector radius squared. The solid black line represents the fiducial volume. Right: The distribution of tritium events vs. XY in the region between the gate and the cathode. The solid black line represents the fiducial volume and the black circles represent the locations of PMTs (photo multiplier tubes).	194
7.6	Charge to light ratio $\log_{10}(S2_b/S1)$ plotted vs. S1, the energy contours are also shown. Top, the tritium data uncorrected for spectral shape. Bottom, with the spectral shape correction discussed in chapter 6. The calibration consists of over 112,000 tritium beta decays between 1 and 50 PE in S1 ($1 - 10 \text{ keV}_{ee}$), in the fiducial volume of the detector. The black circles represent the ER band mean and 10% to 90% bounds, $\pm 1.28\sigma$. The red solid line is the NR band mean determined using a DD neutron generator calibration. The dashed red lines indicate the 10% to 90% bounds of the NR band.	196
7.7	Discrimination vs. S1 using over 112,000 tritium beta decays between 1 and 50 PE in S1 ($1 - 10 \text{ keV}_{ee}$), using tritium data at 170 V/cm. Top, the tritium data uncorrected for spectral shape. Bottom, with the spectral shape correction discussed in chapter 6. The dashed horizontal lines indicate the mean leakage fraction from 1 to 50 PE.	198
7.8	ER band Gaussianity from 0-50 PE with the centroid of the ER band subtracted off, using tritium data at 170 V/cm. Top, the tritium data uncorrected for spectral shape. Bottom, with the spectral shape correction discussed in chapter 6. The dashed vertical red line indicates the mean of the NR band from 1 to 50 PE.	200
7.9	The S1 detection efficiency measured from tritium data at 170 V/cm (black square) and 100 V/cm (blue circle) is plotted along with the best fit to an error function to the higher statistics 170 V/cm data. The red triangles are detection efficiency determined from LED pulsing.	201

Chapter 1: Introduction

A few centuries ago one of the greatest strides in astronomy was made by Kepler working off Tyco Brahe's data in understanding planetary orbits. Kepler discovered that planets move along elliptical orbits with the sun at one of the foci and thus developed the laws of planetary motion, along with the fact that it's useful to share data. In 1609 the concept was revolutionary yet it raised a more interesting question, why do planets move in elliptical orbits? Kepler explanation was that each planet was guided in its elliptical orbit by a resident angel, illustrated in figure 1.1.

Two hundred and fifty years later, another significant discovery was made on the nature of light by James Maxwell. Apparently, the light from mars shining into Tyco Brahe's eye (unaided by a telescope) had propagated through space as an electro magnetic wave. The propagation of light through a vacuum would require electric fields without the presence of charge, thus it was proposed that the universe is filled with aether through which electromagnetic waves could propagate.

Fast forward to the era of the standard model, and precision cosmology . The standard model provides as a nearly perfect framework to understand the interactions of particles we know of. Precision cosmological measurements are now constraining parameters deemed impossible several decades ago (Plank is a huge

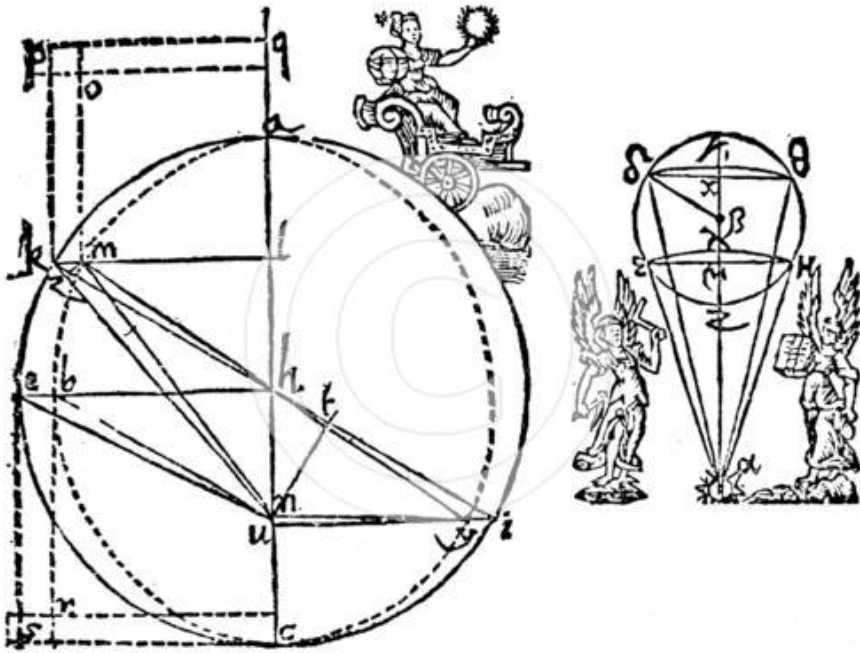


Figure 1.1: Kepler explains the elliptical orbit of Mars, held fixed by a resident angel guiding its orbit.

step up from Tyco’s eye ball). These measurements have provided the basis for the concordance cosmological model (Λ CDM). Apart from knowing that planets move in elliptical orbits we also know that the universe is primarily composed of dark energy (69.2%) and dark matter (25.8%). Ordinary particles described by the standard model which compose our current understanding of ‘everything’ only constitute 4.82% of the universe. See figure 1.2 for a diagram of the concordance cosmological model.



Figure 1.2: Λ CDM parameters depicted on a unicorn by the LUX detector. The magic component which comprise the horn has yet to be directly detected, however it provides the backbone for the model. Note, the parameters in the diagram may not be representative of the specific universe in which this thesis is published.

1.1 Outline of Thesis

In this section we review current cosmological evidence for the existence of dark matter, and give an overview of dark matter candidates along with the WIMP model. We also review if WIMPs exist and how they could be detected and the scattering off a nuclei would look.

In Chap. 2, We overview the LUX detector, a liquid xenon time projection

chamber (TPC), and how it searches for WIMPs. We conclude the chapter with the most recent LUX science results which holds the worlds leading limit for spin independent WIMP nucleon scattering cross section.

In Chap. 3, the position dependent corrections of energy deposition in the LUX detector are discussed.

In Chap. 4, the absolute energy scale calibration of the LUX detector is discussed.

Chapter 5 ... (more to come) provides the conclusion to the thesis.

1.2 Evidence for Dark Matter

Astronomical observations hinting at the existence of dark matter were first observed in 1932 by Oort [15] and more precisely in 1937 by Zwicky [16]. Both noted discrepancies in galactic mass measurements when comparing the luminous mass to the required to support galactic rotational velocities measured by red shifts. Oort had noted up to a factor of ten more mass than luminous mass in the Sombrero Galaxy and Zwicky found a factor of 500 for the Coma cluster. Both the observations were far to large to be accounted for by light absorption, indicating the existence of dark matter to account for the missing mass. Since then more evidence for the existence of dark matter has been compiled, including big bang nucleosynthesis (BBN), anisotropies in the cosmic microwave background (CMB), baryonic acoustic oscillations (BAO), formation of large structures, galactic ration curves, and gravitational lensing. All independent techniques leading to a unified conclusion for the existence

of non baryonic and non luminous matter. Individually some pieces of evidence, such as galactic rotation curves, can be explained by modifications to general relativity (GR), but not all simultaneously. The existence of non relativistic, dark matter particles are required in order to unify the current observations. This dark matter does not couple to the electromagnetic force and is thus able to avoid our standard detection techniques, making its presence felt on large scales via gravity. In the last thirty years significant progress has been made in the direct detection of such a particle, the forefront of which will be presented in this thesis.

1.2.1 Galactic Rotation Curves

There are two common methods for measuring the mass of a galaxy or cluster of galaxies. First, one can use the total luminosity and the known distance to the galaxy to determine the luminous mass, that is the mass corresponding to the visible light. Second, the rotational velocities of stars orbiting the galactic center can be mapped and used to determine the mass distribution as a function of galactic radius. Rotational velocities of stars around galactic centers at large distances can be measured with Doppler shift, with more recent measurement relying on the 21 cm H₁ line from hydrogen as the standard candle. The rotational velocities of objects orbiting galaxies are highly non relativistic moving at speeds on the order 100 km/s. At the outer edges of the luminous galactic centers, typically past 5 kpc the velocity distribution is expected to fall off as redacted by Newtonian mechanics $\sim 1/r$. Yet observations from as early as 1932 indicate that velocity distributions tend to remain

constant with radius suggesting that the objects are not rotating around the central luminous mass, rather they are rotating inside a solid body of dark matter [15] [16] [17] [1]. The velocity distributions measured for the Milky Way galaxy are show in 1.3.

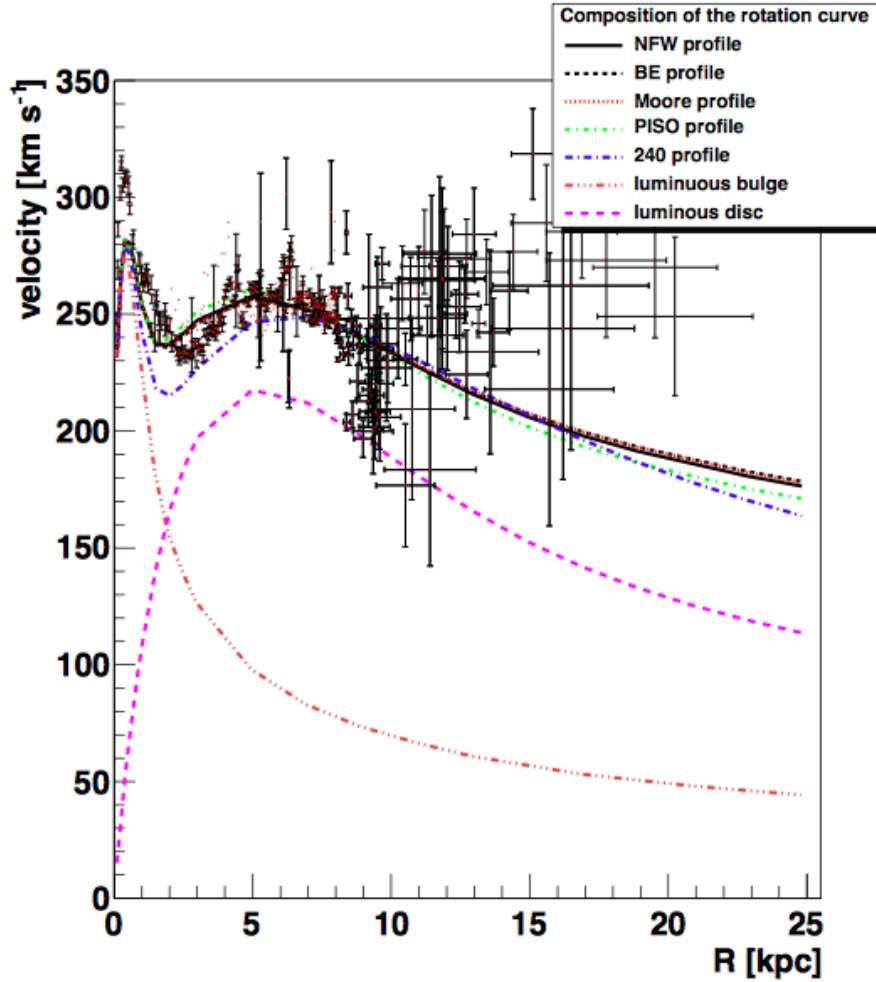


Figure 1.3: Measured rotational velocities vs. radius in the Milky Way galaxy. The velocity distribution is consistent with a halo of mass surrounding the galaxy well beyond the observed luminous disk [1].

1.2.2 BBN

Big band nucleosynthesis (BBN) accounts for the relative abundances of light elements in the universe today, including H, D, He³, He⁴ and Li⁷ [18]. BBN took place in a relatively short time window several seconds after the big bang when the universe cooled below 10¹¹K (10 MeV) and seized as the temperature cooled below 10⁹K (100 keV). Under the temperature conditions of BBN it was energetically favorable for free protons and neutrons to undergo nuclear fusion and is the only mechanism to produce light elements we see today. The heavier elements were later fused together in stars and ejected upon the star's death into the cosmos. Nuclear cross sections of protons, neutrons and light elements have been measured to high person and can be combined with the expansion rate of the universe to precisely predict the relic abundances of baryonic matter. Observations constrain the abundances of the light elements to be H~ 75%, D~ 25%, He⁴ ~ 0.01%, Li⁷ ~ 10⁻¹⁰ %. The ratio of D/H has been used to constrain the relic density of baryonic matter to be $\Omega_b h^2 = 0.02202 \pm 0.00046$ [19].

$$\Omega_b h^2 = \frac{p_b}{p_c} \quad (1.1)$$

Where h is the Hubble constant H dividend by 100 ($H_0/100$), p_b is the baryonic density and p_c is the critical density required for a flat universe (verified by the CMB). We can write the ith density component as:

$$\Omega_i \equiv \frac{p_b}{p_c} = \frac{8\pi G \rho_i}{3H^2} \quad (1.2)$$

Where G is the gravitational constant, H is the Hubble constant (found in table 1.1). The baryon density measured using BBN is constrained to within 1% and in agreement with the latest constraints from Plank's CMB data, $\Omega_b h^2 = 0.02205 \pm 0.00028$ [20].

1.2.3 CMB

The early universe consisted of a plasma making the universe opaque to photons as they scattered off free electrons. As the temperature fell below the binding energy of hydrogen 13.6 eV, electrons neutral atoms allowing photons to decouple from the plasma making the universe became transparent. The mean temperature of decoupling was actually at 0.25 eV (\sim 4000 K) as photons still scatter frequently near the binding energy of hydrogen [18]. The cosmic microwave background (CMB) emanated from this time after making a final scatter photons decoupled from electrons effectively attaining a mean free path on the scale of the universe. The photons from the CMB observed today at the red shift temperature of 2.72548 ± 0.00057 K [21] have not interacted from the time of last scatter 379,000 years after the big bang. The CMB has encoded within it a wealth of information about the universe as it was at the time of decoupling. The concept of the information encoding is illustrated in figure using Maru the cat in various boxes. Consider that Maru is a photon and the box size represents local energy densities of the universe. The smaller boxes represent areas of higher energy density and temperature. At the time of last scatter all boxes containing Marus cease to exist, to the horror of of

the cats. The cats now begging to propagate freely through the universe with their configuration unchanged (the cats are too lazy to move and are content napping while propagating though space). It should be noted, that as the universe expands so will the cats. When the Marus finally reach our telescopes, 13 billion years latter, the shape and squeezing of each Maru informs us of the box size (temperature) from which each Maru has emanated. Using this information from multiple Marus the distribution of box sizes at the time of last scatter can be mapped, reveling areas of slightly larger boxes and areas of slightly smaller boxes. This is roughly the idea behind measuring anisotropies in the cosmic microwave background using microwave telescopes.

.Ever more increasing measurements from COBE, WMAP and Planck have been able to probe slight temperature variations to 1 part in 100,000 as seen in figure 1.5. Table 1.1 shows the constraints on cosmological parameters set by Planck. The results are in good agreement with baryonic density derived from BBN and predict a dark matter component of 25.8%.

Parameter	Value	Definition
$\Omega_b h^2$	0.2214 ± 0.00024	Baryon energy density
$\Omega_c h^2$	0.1187 ± 0.0017	Cold dark matter energy density
$\Omega_m h^2$	0.1423 ± 0.0029 *	Total matter energy density
Ω_Λ	0.692 ± 0.010	Dark energy density
Ω_K	-0.0005 ± 0.0065 (95%)	Curvature
Σ_{m_ν}	< 0.230	Sum of neutrino masses [eV]
H_0	67.77 ± 0.77	Hubble Constant [$\text{km s}^{-1} \text{Mpc}^{-1}$]

Table 1.1: Cosmological parameters from Planck+WP+highL+BAO [20]. * Only Planck.

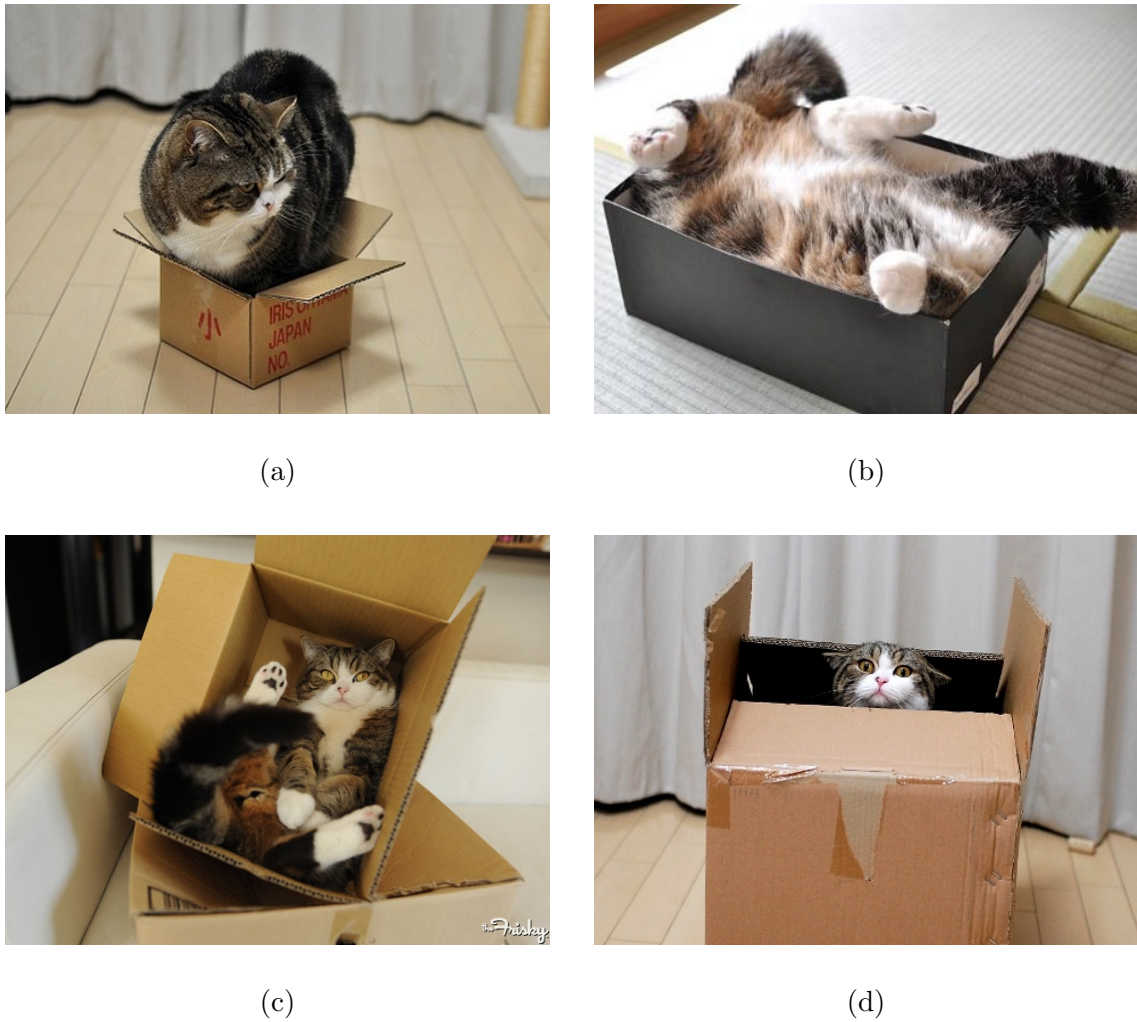


Figure 1.4: Maru the cat explains the cosmic microwave background. Consider that Maru is a photon and the box size represents local energy densities of the universe. The scale of the the box size is inversely proportional to the local energy density and temperature. At the time of last scatter all boxes containing Marus cease to exist, to the horror of the cats! The Marus are now left to propagate freely through the universe, with their configurations unchanged (the cats are too lazy to move and are content napping for 13.7 billion years). Figures a-d show Maru the cat contained within increasing box sizes corresponding to decreasing energy densities.

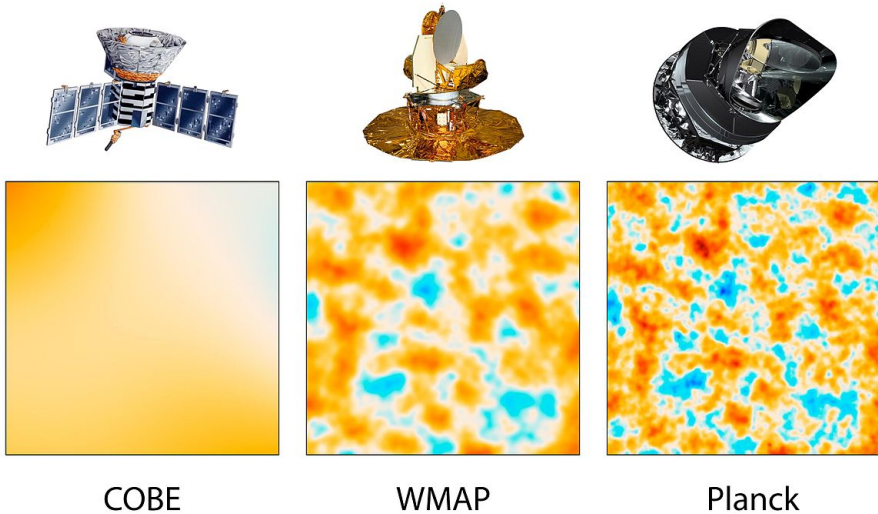


Figure 1.5: Improvement of resolution from COBE, first to discover anisotropies in the CMB, to WMAP and Planck which have set stringent limits on cosmological parameters by mapping variations in temperature of 1 part in 100,000. Image credit: NASA/JPL-Caltech/ESA.

1.2.4 BAO

The universe 379,000 years after the big bang was uniformly distributed, with only small variations observed in the CMB temperature of 1/100,000 [22]. Before decoupling took place gravity pulled baryons and dark matter into high density regions resulting in an opposing outward force from photon pressure. The outward force from the photon pressure was only felt by the baryons whereas the dark matter component would not couple to photons. The competing attractive and repulsive forces gave rise to baryonic acoustic oscillations (BAO) with density regions propagating as spherical sound waves do. The amplitudes of the waves are separated by a characteristic radius called the sound horizon r , which is sensitive to

the initial dark matter and baryon densities [23]. Anisotropies in the CMB power spectrum probe these oscillations as discussed previously in 1.2.3. At the time of decoupling the photon pressure ceased providing the opposing force allowing the gravitational restoring force to dampen the oscillations. If the picture since the time of the CMB is propagated forward in time we expect that areas of the CMB that were denser would cluster, thus statistically the universe is expected to have large scale structures on the order of the sound horizon r . Measurements of BAO by the Sloan Digital Sky Survey [24] and BOSS [2] are consistent with the sound horizon expected from anisotropies in the CMB, with a preferred scale of $100\text{hh}^{-1}\text{ Mpc}$ (~ 150 Mpc) between large scale structures. Figure fig:BOSS shows the result from BOSS using Lyman- α absorption in quasar emission spectrum due to the presence of neutral hydrogen in the intergalactic medium [2].

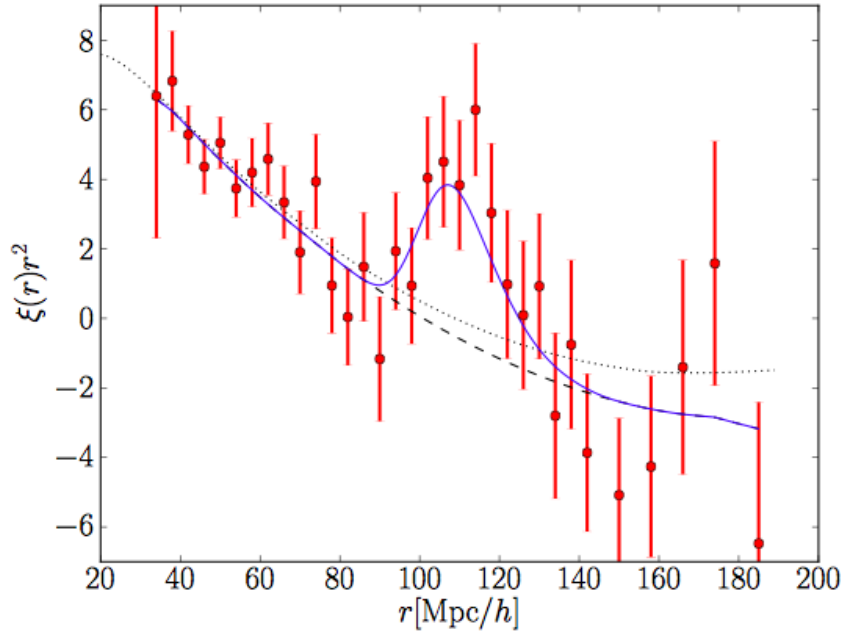


Figure 1.6: BAO peak obtained from BOSS [2]

1.2.5 Gravitational Lensing

Gravitational lensing can be used to map the focal points of gravitational mass in a galaxy or cluster. The idea is to look for repeating structures around a large central mass which have been bent around regions of large mass. These repeating structures are caused by light trajectories bending before reaching earth creating an optical illusion, appearing as if the light had emanated from multiple sources along a straight lines of sight. Observations of the Bullet cluster strongly support the existence of dark-matter. The Bullet cluster is made up of two galaxy clusters which have recently collided and passed through each other. The collision has caused the ordinary, baryonic matter to heat and emit X-rays that are observed and used to map the luminous mass distribution [25]. However, the observed concentration of mass is not consistent with the center of mass observed using gravitational lensing via GR [26]. The way light bends around the bullet-cluster would indicate the presence of a dark-matter shell which, unlike the ordinary matter, has passed through at a faster rate due to the lack of interactions. Figure 1.7 shows the concentration of mass in the bullet-cluster as observed from X-rays, emitted by baryonic matter, in pink and the concentration of mass from gravitational lensing in blue. The X-ray mapping from Chandra when compared with gravitational lensing studies of the Bullet cluster clearly demonstrate a decoupling of the dark matter center of mass from the baryonic center of mass induced by the cluster's recent collision.

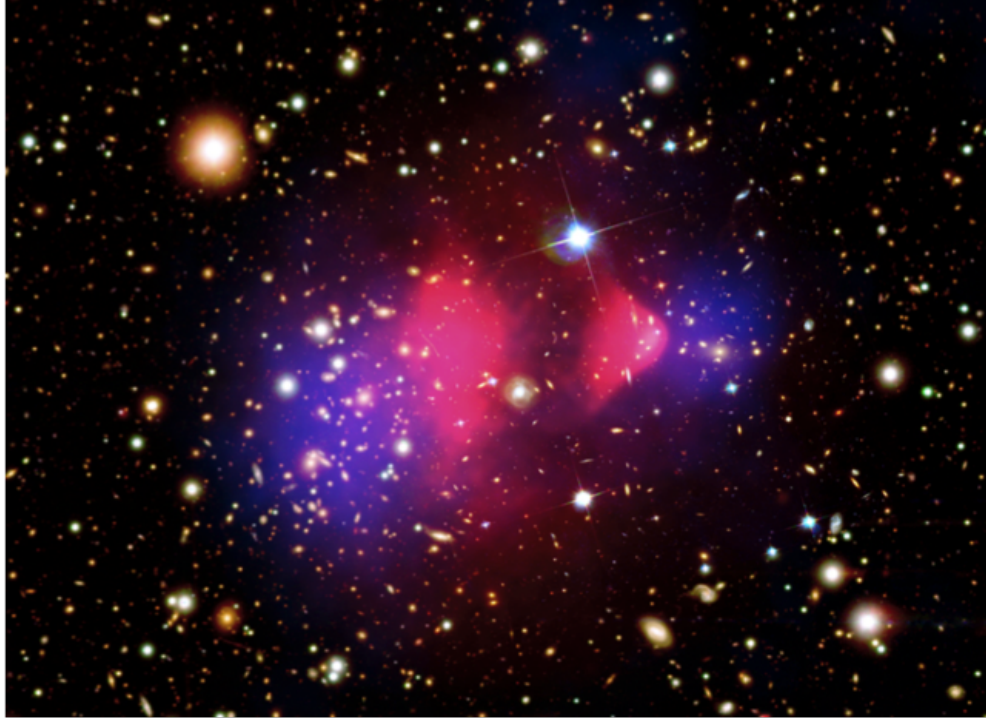


Figure 1.7: The concentration of mass in the bullet-cluster as observed from X-rays, emitted by baryonic matter, in pink and the concentration of mass from gravitational lensing in blue. [Composite image credit: X-ray: NASA/CXC/CfA/M.Markevitch et al.; Optical: NASA/STScI; Magellan/U.Arizona/D.Clowe et al.; Lensing Map: NASA/STScI; ESO WFI; Magellan/U.Arizona/D.Clowe et al.]

1.3 Dark Matter Candidates

The evidence for the existence of missing mass outlined in the previous section forces us to examine solutions to account for those cosmological phenomena. It is natural to at first try and solve the anomaly by using our understanding of standard model particles. The first candidate considered for dark matter is the existence of Massive Compact Halo Objects (MACHOs). However, the MACHO theory requires that

the extra mass be baryonic which is refuted by the precision measurements (BBN, CMB) that limit Baryonic mass to only 2.2% while the overall matter energy density required is 31.75% [27] [20] (see table 1.1). A non baryonic candidate drawn from the standard model are neutrinos, which are known to carry mass due to oscillations and only interact weakly [28]. However, large scale structure formation require that the universe have a ‘cold’ (non relativistic) dark matter component in order to become gravitationally bound to galaxies. With current constraints on the neutrinos masses to less than 0.23 eV [20], neutrinos are highly relativistic and would fail to reproduce structuring of the universe observed today [29].

1.3.1 AXIONS

“I named them after a laundry detergent, since they clean up a problem with an axial current”

Frank Wilczek

Axions were introduced to solve the strong CP problem. The Lagrangian allowed by gauge symmetry includes a term

$$\mathcal{L} = \Theta \frac{g_s^2}{32\pi^2} G_{\mu\nu}^a \tilde{G}^{\mu\nu a} \quad (1.3)$$

where g is the gluon QCD coupling constant, $G_{\mu\nu}^a$ the gluon field strength and Θ is a constant [30]. The Lagrangian breaks gauge symmetry which allows for CP violating and is expected to contribute to the electric dipole moment (NEDM). Measurements of the NEDM have been constrained to be much smaller than expected with CP violation. NEDM is constrained to be less than 2.9×10^{-26} e cm (90% CL) [31], resulting in Θ of less than 0.7×10^{-11} .

An elegant solution for the lack of observe red electric dipole moment was introduced by Pecci and Quinn. The proposed idea is to promote Θ to a dynamical field value through a new symmetry (PQ symmetry) which is spontaneously broken naturally leading to $\Theta = 0$ by minimizing the potential [32] [33]. Such a solution to the strong CP problem leads to the existence of a light pseudo scalar particle, the Axion. The axion would be a light particle which could couple to the electromagnetic field, in the presence of a strong electromagnetic field, $a \leftrightarrow \gamma\gamma$ [34].

Searches for axions involve looking for the rare electromagnetic interactions that convert axions into microwaves in resonating cavities with large magnetic fields here on earth. ADMX has been sensitive to mass scales of $3.3 \mu\text{eV}$ to $3.59 \mu\text{eV}$ with planned upgrades to explore more parameter space [35]. Coupling of photons to axions could also occur in the strong electromagnetic fields of our own sun. The CAST experiment searches for axions produced in the interior of the sun from thermal photons, with keV energies, which then arrive to the detector where they are converted back into X-rays within a large dipole magnet [34]. The axion solves the strong CP problem and is a potential dark matter candidate, there is still vast parameter space to explore with potential axion massed ranging from μeV to eV scales. Instruments are being upgraded to explore these regions and will require patience, since each potential axion mass requires tuning the cavity to a specific resonance and waiting.

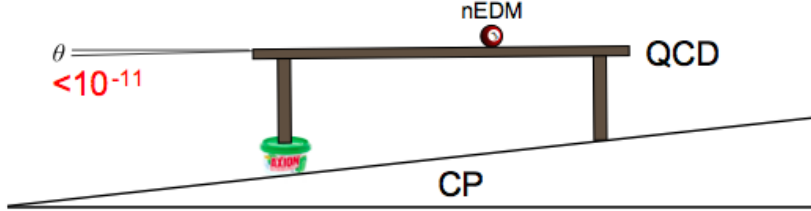


Figure 1.8: Illustration of the CP problem and the axion solution. “Analogy for the CP problem and the axion solution. In a room (the Standard Model), there is a table (QCD) sitting on an uneven floor (CP). A billiard ball (nEDM) placed on top of the table is expected to rapidly move across the uneven surface. However, the billiard ball is observed to stand still and the horizontal angle of the table is measured to be $\theta < 10^{-11}$. The solution to this puzzling observation is the existence a new degree of freedom (manifested in the axion) that levels the table (drives $\theta = 0$)”, [Carlos’ Thesis]

1.3.2 WIMPs

A leading candidate to explain the dark matter is weakly interacting massive particle (WIMP), as the name implies is a massive that only couples via the weak interaction and also gravity. The WIMP is theorized to have a mass and cross section on the order of the weak interaction. In the early universe the number density of WIMPs

and photons would have been roughly equation as there was sufficient thermal energy to keep the creation and annihilation in equilibrium.



χ represents WIMPs and q are standard model particles. The reaction can go back and forth in equilibrium as long as the thermal temperature of the universe is greater than WIMP mass $T > m_\chi$.

As the universe expanded and cooled production of WIMPs from standard model particles cease as the temperature of the universe dropped below the WIMP mass, leaving only WIMP annihilation into standard model particles. The annihilation process of WIMPs would have continued leaving only a small number density at the tail of an exponentially falling Boltzmann distribution today. However, if the universe's expansion is fast compared to the WIMP cross section then the WIMPs would have avoided finding each other and their number density could 'freeze out'. Thus, if the acceleration of the universe H is greater than the number density of WIMPs times the cross section.

$$H > \Gamma_A \equiv n_\chi \langle \sigma_A \nu \rangle \quad (1.5)$$

H is the Hubble constant , n_χ is the number density of WIMPs and $\langle \sigma_A \nu \rangle$ is the thermally averaged annihilation cross-section. The annihilation process can be described by the Boltzmann equation

$$\frac{dn}{dt} = -3Hn_\chi - \langle \sigma_A \nu \rangle (n_\chi^2 - n_{\chi_{eq}}^2) \quad (1.6)$$

Where the first term represents the dilutions of WIMP number density with three

degrees of freedom. n_χ^2 is from the annihilation process, $\chi\chi \rightarrow qq$ and $n_{\chi_{eq}}^2$ is from the reverse process $qq \rightarrow \chi\chi$. Equation 1.6 does not have an analytic solution but has been solved numerically[36] , estimating the relic density within 10% to be:

$$\Omega_\chi h^2 = \frac{3 \times 10^{-27} \text{cm}^3 \text{s}^{-1}}{\langle \sigma_A \nu \rangle} \sim \frac{10^{-10} \text{GeV}^{-2}}{\langle \sigma_A \nu \rangle} \quad (1.7)$$

Using a typical weak scale cross-section in equation 1.7,

$$\langle \sigma_A \nu \rangle \sim \frac{\alpha^2}{m_{weak}^2} \sim 10^{-9} \text{GeV}^{-2} \quad (1.8)$$

We find that the relic WIMP density reduces to $\Omega_\chi h^2 = 0.1$ for a particle with a weak scale interaction, referred to as the WIMP miracle. In good agreement with the expected cold dark matter component of the universe $\Omega_c h^2 = 0.12029$ [20]

1.4 WIMP Dark Matter Searches

There are three methods for detecting WIMPs other than looking for its gravitational effects. First, we can look for the annihilation of dark matter particles into standard model particles using space telescope based experiments. Second, we could try to produce dark matter particles by colliding standard model particles in accelerators and look for a signature of missing energy. Or we can search for rare collisions of dark matter particles with ordinary matter. The first two options would constitute indirect observations as only a standard model particle or missing energy is detected to infer the existence of dark matter, this introduces significant systematics and potential fake signals. The third option is rather attractive as it involves directly observing a collision with a dark matter particle though it too come along

with significant challenges, mainly it requires a near zero background environment in order to observe the additional flux.

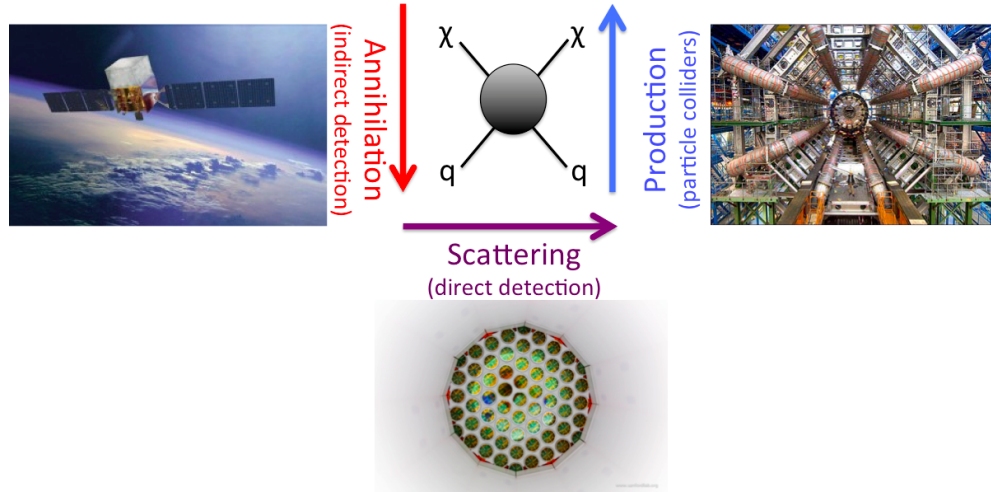


Figure 1.9: Methods for detecting WIMPs from interactions of q , standard model particles, and dark matter particles χ . WIMPs can be detected through the annihilation of dark matter particles into standard model particles, $\chi\chi \rightarrow qq$. WIMPs can be produced by colliding standard model particles, $qq \rightarrow \chi\chi$. Or one can look for the scatter of a dark matter particle off a standard model particle, $\chi q \rightarrow \chi q$.

1.4.1 Direct Detection

WIMPS could have masses in the GeV to TeV range and would comprise a quarter of the total mass of the universe. The local density of WIMPs around the earth, at 8 kpc from the galactic center, is about 0.3 GeV/cm³, estimated from the galactic rotation curve of the Milky-Way with the assumption of a halo like distribution (figure 1.10 and [1]). Assuming that the WIMP mass is on the order of the weak scale, 100GeV, there are roughly three proton masses worth of WIMPs per liter of space. The velocity of WIMPs near the Earth is about the orbital velocity of objects about the galactic center 240km/s at 8.3 kpc, shown in figure 1.3. WIMPs being highly non-relativistic would scatter coherently off of target nuclei with a cross-section corresponding to $\sim A^2$.

WIMP scattering off of target nuclei can be expressed as a classical inelastic collision. The most common energy deposit can be expressed as

$$E_{\max} = r \cdot E_0 = \frac{r}{2} M_\chi v^2 \quad (1.9)$$

Where E_{\max} is the most frequent energy deposit, M_χ is the WIMP mass and v is the WIMP velocity. The kinematic factor r for isotropic scattering off a target mass M_T in the laboratory frame is given by (using 1/2 as the average of 1-cosθ.):

$$r = \frac{4M_\chi M_T}{(M_\chi + M_T)^2} \quad (1.10)$$

Assuming classic billiard ball scattering we calculate expected energy deposits for various WIMPs with weak scale masses of 1 to 1000 GeV/c². Using xenon as the

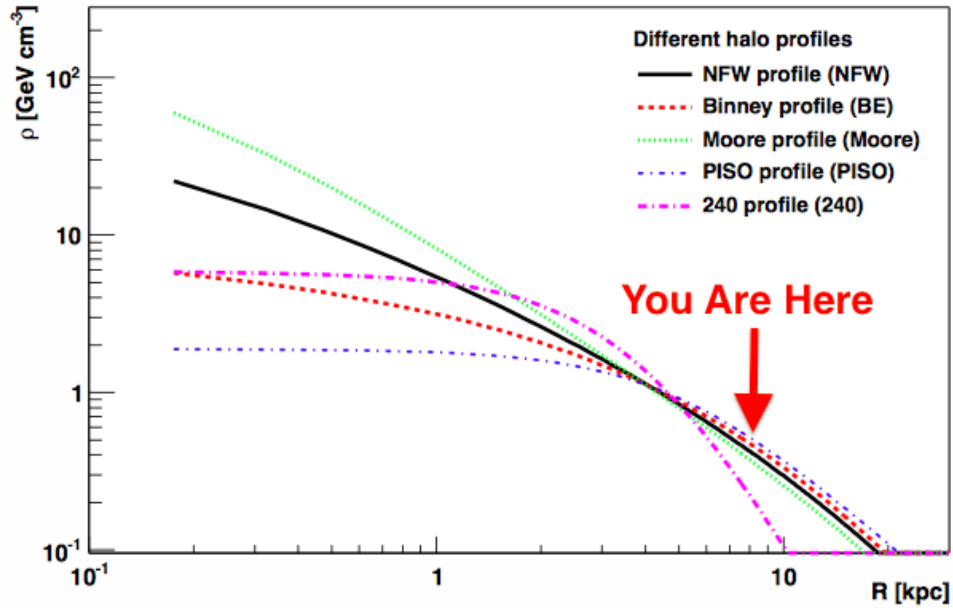


Figure 1.10: Dark matter density vs. distance from the galactic center, calculated from galactic rotation curves of the Milky Way galaxy. The Earth is located at 8.3 kpc. Figure from [1].

target mass ($M_{Xe} = 122 \text{ GeV}/c^2$), and a WIMP velocity of 240 km/s ($8 \times 10^{-4} c$).

$M_\chi [\text{GeV}/c^2]$	r	$E_{\max} [\text{keV}]$
1	0.032	0.01
10	0.28	0.90
100	0.99	31.7
10000	0.40	124

Table 1.2: The kinematic factor r and most common energy deposit E_{\max} for a WIMP of mass M_χ scattering off a xenon nucleus.

To calculate the WIMP-target scattering event rate we follow the derivation given by Lewin and Smith [3]. The differential rate of the WIMP nuclear recoils will be an exponentially decaying spectrum.

$$\frac{dR}{dE_R} = \frac{R_0}{E_0 r} e^{-E_R/E_0 r} \quad (1.11)$$

E_R is the recoil energy, E_0 is the most probable WIMP kinetic energy, r is the kinematic factor, R is the event rate per unit mass and R_0 is the total rate. The event rate dR scattering off a target size A can be written as

$$dR = \frac{N_0}{A} \sigma \nu dn \quad (1.12)$$

Where N_0 is Avagadro's number, A is the atomic mass, σ is the cross-section, ν is the WIMP velocity and dn is the differential number density of WIMPs given by:

$$dn = \frac{n_o}{k} \mathcal{F}(\nu, \nu_E) d^3\nu \quad (1.13)$$

Where $k = (\pi \nu_0^2)^{3/2}$ as $\nu_{esc} \rightarrow \infty$, an approximation good to within 0.5% for the Milky Way. n_o is the particle number density ($n_o = p_\chi/m_\chi$). The WIMP velocity distribution $\mathcal{F}(\nu, \nu_E)$ is assumed to be ideal gas described by a Maxwellian distribution:

$$\mathcal{F}(\nu, \nu_E) = e^{-(\nu + \nu_E)^2/\nu_0^2} \quad (1.14)$$

Where ν is the WIMP velocity, ν_E is the earth velocity, ν_0 is the average velocity (about 230 km/s). We now rewrite equation 1.11 in terms of an integral over all possible velocities rather than energy and plug in the result for dR (1.12) and dn (1.13) leading to :

$$\frac{dR}{dE_R} = \frac{R_0}{E_0 r k} \frac{1}{2\pi\nu_0^2} \int_{\nu_{min}}^{\nu_{max}} \frac{1}{\nu} \mathcal{F}(\nu, \nu_E) d^3\nu \quad (1.15)$$

R_0 absorbs the constants $R_0 = \frac{2}{\pi^{1/2}} \frac{N}{A} \frac{\rho_\chi}{M_\chi} \sigma_T \nu_o$.

Having solved for the differential rate we now calculate the spin independent cross section for WIMPs scattering off nucleons of an atom (σ_T). We write the cross section as a sum off scattering off protons and neutrons in the nucleus. We use the fact that nucleon coupling for protons and neutrons is approximately equal [37].

$$\sigma_T = \frac{4\mu^2 A}{\pi} [Z \cdot f_p + (A - Z)f_n] \approx \frac{4\mu^2 A^2}{\pi} \sigma_n \quad (1.16)$$

Where μ is the reduced mass of the WIMP nucleon system given by:

$$\mu = \frac{M_\chi M_n}{M_\chi + M_n} \quad (1.17)$$

Finally we must add the specific nuclear form factor for the specific target atom to account for decoherence, described by the Helm factor [4] $F(q)$. The cross section for spin independent scattering off the target nucleus can be written as a product of the idealized cross section and Helm factor:

$$\sigma_T(q) = \sigma_T F^2(q) = \frac{4A^2}{\pi} \left(\frac{M_\chi M_n}{M_\chi + M_n} \right)^2 \sigma_n F^2(q) \quad (1.18)$$

The spin-independent cross section for WIMPs is found to be proportional to the atomic number squared (A^2). The event rate per nuclear recoil energy is plotted for several potential WIMP search target nuclei in figure 1.11.

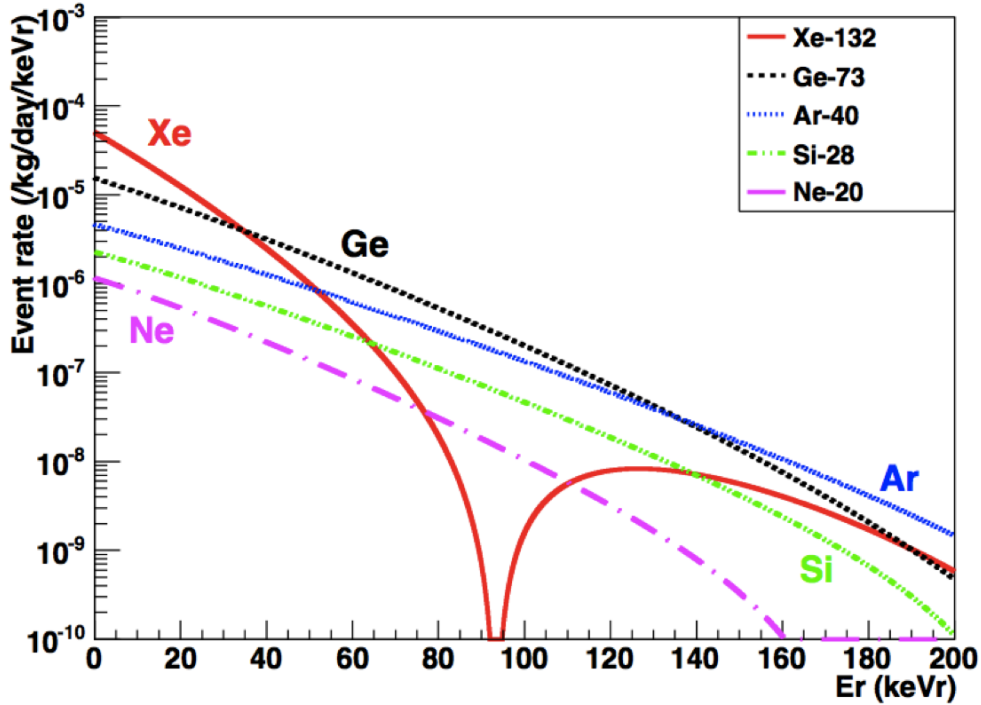


Figure 1.11: Plot of WIMP event rate per kg/day/keV vs. Nuclear recoil energy (keV) for several target nuclei, using parameters from [3]. At low detection threshold xenon is the most attractive target nuclei. The drop off in the xenon spectral shape is due to decoherence described by the Helm factor [4].

Xenon being a relatively heavy element, $A=131$, makes it an ideal candidate for a WIMP dark-matter search at low energy thresholds. Xenon detectors today have achieved thresholds as low as 3 keV_{nr} [38]. Other common detection mediums are germanium, which is rather expensive on the ton scale, and argon which is inexpensive but contains a troublesome radioactive isotope ^{39}Ar . To probe dark matter cross sections the next generation experiments must be bigger and contain less radioactive background contamination. With current limits on the WIMP cross section a ton scale xenon experiment may only detect a handful of events per year.

1.4.2 WIMP Detection Experiments

Several experiments are currently conducting WIMP dark matter searches using several target nuclei. We have found that the interaction rate for WIMPs with target nuclei is expected to be rare. In the event that a WIMP does strike a target in the detector it will primarily interact with the nucleus, deposit energy, and traverse throughout the detector without a second interaction. Neutrons could also interact with atomic nuclei and fake a WIMP signal, however after the initial energy deposit they are likely to interact again. Thus, neutrons can be rejected by cutting multiple scatters in detectors on the scale of the neutron mean free path at an energy required to fake a WIMP signal (order 10 cm). The most common source of backgrounds are electromagnetic in nature, gammas and betas from the rock surrounding the experiment, detector components, and internal to the xenon. Just like for the case of neutrons the likelihood of a single scatter within the detector is highly unlikely. Naked beta decays are the most troublesome, appearing as a single energy deposit in the detector medium. Fortunately, electronic recoil events can be discriminated from WIMP like nuclear recoil events by more than 1/100 using the ratio of charge to light or charge to phonons produced in the interaction. Xenon based experiments currently having the best limits on WIMP nucleon cross sections [38].

- Xenon experiments: LUX [38], Xenon100 [39] , PandaX [40], XMass [41].
- Argon experiments: Dark Side [42], MiniClean [43].
- Germanium experiments: CDMS [44], CoGeNT [45].

- Bubble chamber using fluorine: PICASSO [46] (^{19}F), COUPP [47] (CF_3I).

,

Chapter 2: The LUX Detector

2.1 Introduction

The LUX experiment is located 4850 ft underground (4300 m w.e.) at the Sanford Underground Research Facility in Lead, South Dakota. After running for 85.3 live days in 2013, LUX has set the most sensitive limit for a spin-independent WIMP scattering cross section [38] and is expected to achieve five times the sensitivity after a 300 day run ending in 2015.

Nobel elements are promising candidates for WIMP detection. They are easy to purify and are transparent to their own scintillation light. Xenon is especially favorable due to its large atomic mass (131.3 amu) and high liquid phase density (~ 2.9 kg/l) which provides both an excellent target for coherent WIMP scattering while simultaneously providing excellent stopping power from external radioactivity. Xenon is also free of any long lived isotopes which contribute backgrounds for the WIMP search. There are well established techniques to remove and monitor the residual, troublesome radio isotopes of ^{39}Ar and ^{85}Kr found in the atmosphere from which the xenon is distilled [48] [49] [50] [51].

WIMPs, being electrically neutral, primarily interact with the xenon target nuclei producing nuclear recoil (NR) events whereas typical backgrounds in the

detector, gammas and betas, interact with the atomic electrons producing electronic recoils (ER). In liquid xenon ER events can be further discriminated from NR events a factor of 100 or more by measuring the charge to light ratio of the interaction, as explained in section 2.2.2.

2.2 The LUX TPC



Figure 2.1: Photo of the outer vessel of the LUX detector from inside the water tank.

Figures 2.1 shows the LUX detector held in place by a stainless steel frame and the water tank that surrounds it. The water tank provides shielding from gammas and neutrons emanating from the surrounding rock, the water tank PMTs used as an active veto are also pictured along the sides of the water tank. Figure 2.2 show a cross sector of the LUX detector's inner and outer vessel. The LUX detector is a two phase xenon time projection chamber (TPC) [38]. The detector contains two PMT

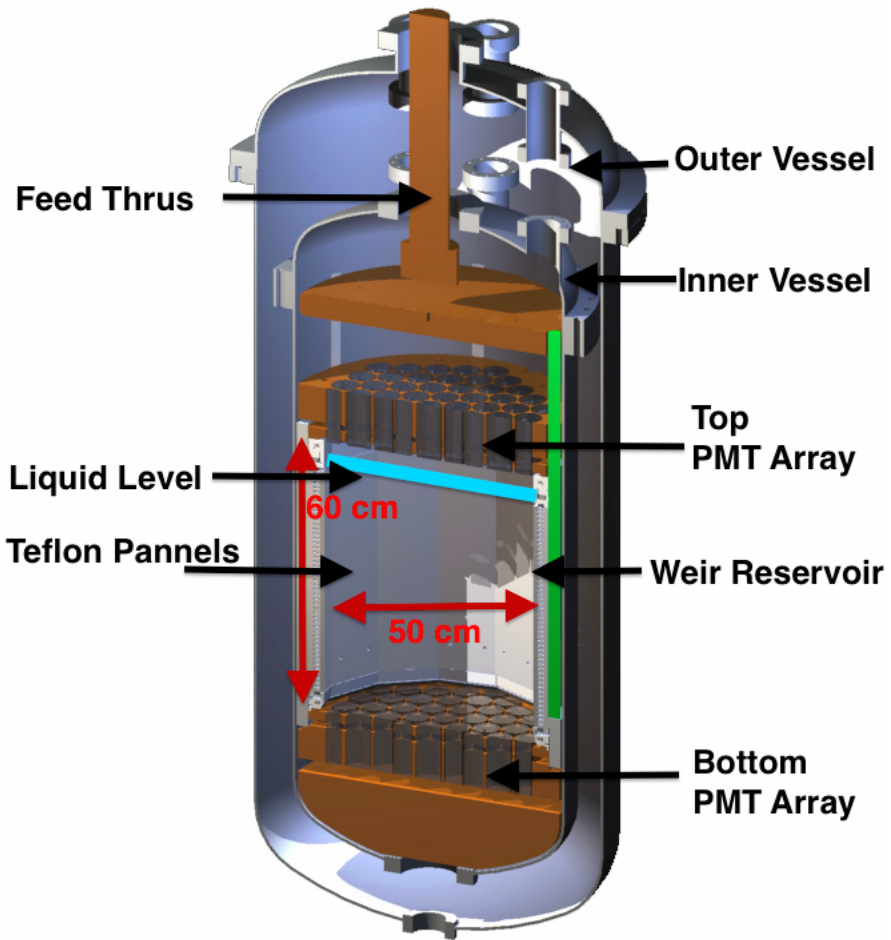


Figure 2.2: Illustration of the LUX detector’s internals. The detector contains two arrays of PMTs on the top and bottom housing 61 PMTs each. Teflon panels on the edges of the active region are used to reflect scintillation signals. The vertical distance between the two PMT arrays is 60 cm, and the diameter to the outer edge of the teflon panels is 50 cm.

arrays on the top and bottom with 61 PMTs each for a total of 122 PMTs, with quantum efficiencies ranging from 30-40%. The active region consists of a 49 cm length between the cathode and gate grid with a 47 cm diameter of the dodecagonal geometry. The drift field between the cathode and gate is 170 V/cm resulting in

an electron drift velocity of 1.51 mm/ μ s. The liquid level terminates 5-6mm above the gate grid. The liquid level is precisely maintained by a weir reservoir into which xenon between the anode and gate spills into. The anode grid is 1.0 cm above the gate grid and creates an extraction field of 6 [kV/cm] where electrons are removed from the liquid and accelerated causing electroluminescence in the gas phase. LUX contains a gross mass of 370 kg of xenon of which 250 kg are in the active region.

2.2.1 Target Xenon

The target xenon is commercially available natural xenon with standard isotopic abundances (table 2.1), initially distilled to \sim 1 part per million (ppm) residual air contamination (N₂, O₂, Ar). The commercially available xenon also contained \sim 100 parts per billion (ppb) of krypton which is far greater than the background allowance of 5 parts per trillion (ppt). Krypton contains trace amounts of a beta emitter ⁸⁵Kr and is a troublesome internal background dissolved uniformly directly in the detection medium (xenon). The unwanted krypton was removed from the bulk xenon using a gas chromatography technique [50], with the removal independently verified before the science run with a xenon gas analysis technique developed for EXO-200 and LUX [49]. The xenon purity was monitored daily throughout the 2013 science run by an in situ gas analysis system that will be described in detail in section [Sampling]. Just one standard liter of air contains enough krypton to raise the concentration in the LUX xenon above the background goals. Daily krypton monitoring ensured that the krypton content in the xenon remained constant at 4

parts per trillion over the 2013 science run[5].

Electronegative impurities such as N₂, O₂ and H₂O attenuate electrons drifting through the xenon and must be removed in order to properly reconstruct events originating deep in the detector. These impurities continuously emanate from detector components degrading the free electron attenuation length. The accumulation of electronegative impurities is countered by circulating the xenon at 26.5 SLPM through a heated zirconium getter. The gross mass of 370 kg has a turn over time of 1.65 days. The monitoring of several impurities using the in situ ahas analysis system is described in detail in section [Sampling]. Throughout the 2013 science the electron attenuation length was measured to be 75 cm to 150 cm, corresponding to 70% to 50% charge loss for events originating from the bottom of the active region.

Isotope	Natural Abundance (%)
¹²⁴ Xe	0.09
¹²⁶ Xe	0.09
¹²⁸ Xe	1.92
¹²⁹ Xe	26.44
¹³⁰ Xe	4.08
¹³¹ Xe	21.18
¹³² Xe	26.86
¹³⁴ Xe	10.44
¹³⁶ Xe	8.87

Table 2.1: Xenon isotopic abundances, from [52]

2.2.2 Background Rejection

Xenon has a density of ~ 2.9 g/cm giving it excellent stopping power for shielding against external radioactivity. External radioactivity with energies in the WIMP

search region of interest (below 50 keV) only penetrate millimeters in xenon, being completely absorbed in the outer edges of the detector. Gammas in the MeV range have mean free paths on the order of 3 cm and are likely to be cut by the single scattering requirement . The most troublesome of the gamma backgrounds are from PMT materials containing trace amounts of uranium and thorium located inside the TPC. Figure figure 2.3 shows a simulation of expected gamma background events inside the LUX detector, using the single scatter cut requirement. By cutting out the edge events we can gain at least an additional factor of 1000 background rejection within the fiducial volume (inside the black dashed lines) [5].

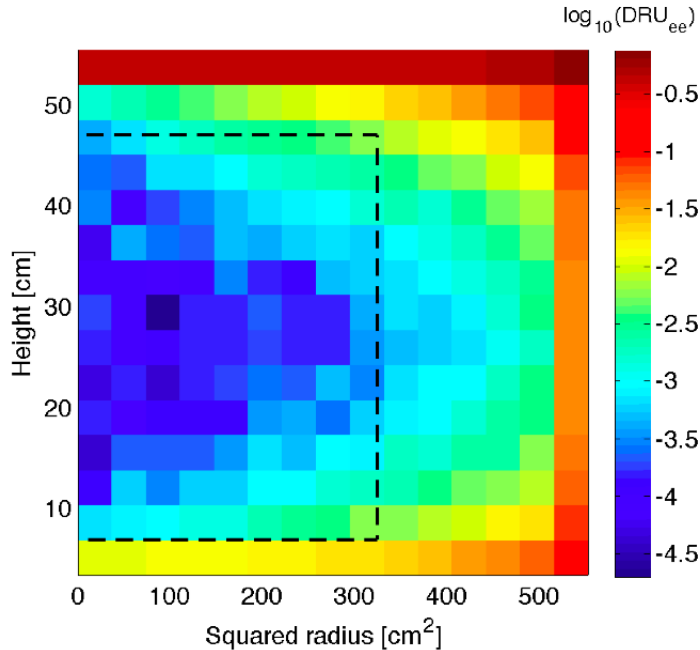


Figure 2.3: Simulation of expected gamma background events inside the LUX detector, using the single scatter cut requirement[5]. There is an additional factor of 1000 background rejection within the fiducial volume where the WIMP search is conducted (inside the black dashed lines) .

Another means for discriminating background events is through measuring the charge to light ratio of each event. WIMPs will produce nuclear recoils whereas gammas and betas interact primarily with atomic electrons, resulting in different charge to light ratios of a given energy deposit. Using AmBe and ^{252}Cf neutron sources along with a tritium calibration source the NR to ER discrimination factor was measured to be 99.6 ± 1 % at 50% NR acceptance. Meaning that only one in 250 of the residual gamma and beta background events is expected to fake a WIMP signal when cutting out half of the potential nuclear recoil candidates. The ER type and NR type bands are shown in figure 2.4 with the band means as solid lines (Blue and Red, respectively) and the 10-90% CL as dashed lines. The internal tritium calibration source will be discussed in further details in section (Tritium Section).

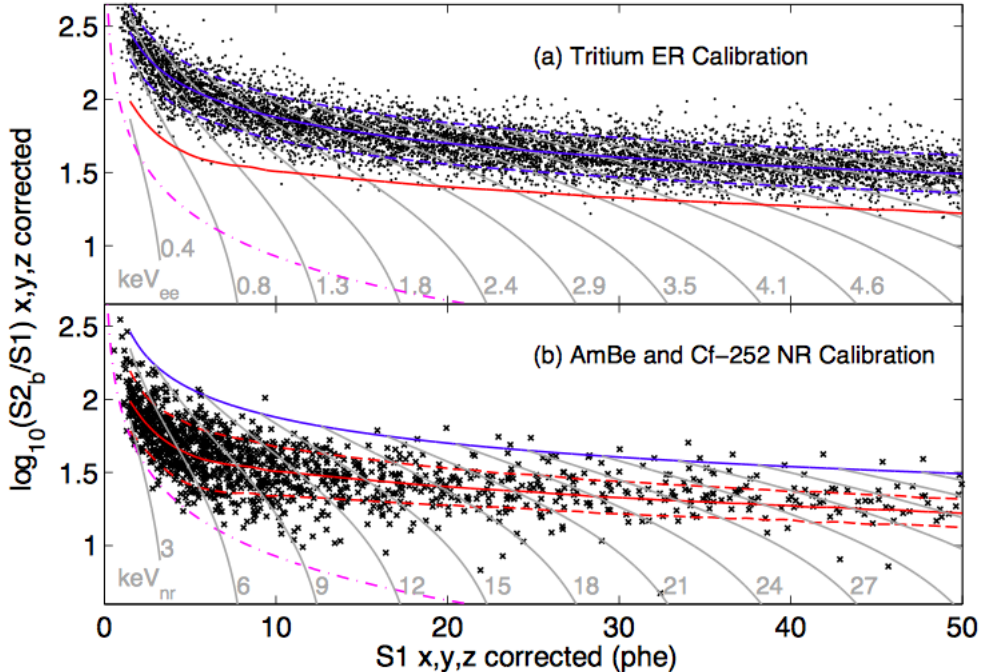


Figure 2.4: The ER type and NR type bands from a) AmBe and ^{252}Cf (Red) and b) tritium calibration (Blue). The band means are solid lines and the 10-90% CL are shown as dashed lines. The ER to NR discrimination by using the charge to light ratio was measured to $99.6 \pm 0.1\%$ at 50% NR acceptance.

2.2.3 The Drift Field inside the LUX TPC

The LUX TPC contains five wire grids used to control the electric fields inside the detector. The grids and their spacings are shown in figure 2.5, labeled from top to bottom as Top (T), Anode (A), Gate (G), Cathode (C), Bottom (B). The grids T,A,G,C,B are biassed at -1,+3.5,-1.5,-10,-2 (all in kV), respectively. The PMTs are biased to -1.2 kV on average. The field created in the active region between the cathode and gate is also shown in figure 2.5. On average the drift field is 170 V/cm with variation from 140 V/cm to 200 V/cm from cathode to gate. The extraction

region between the anode and gate has a 6 kV/cm field. This extraction field is used to create the secondary scintillation (S2) signal via electroluminescence as the electrons are extracted and accelerated. The top and bottom grids serve to shield the PMTs from the anode and cathode biases.

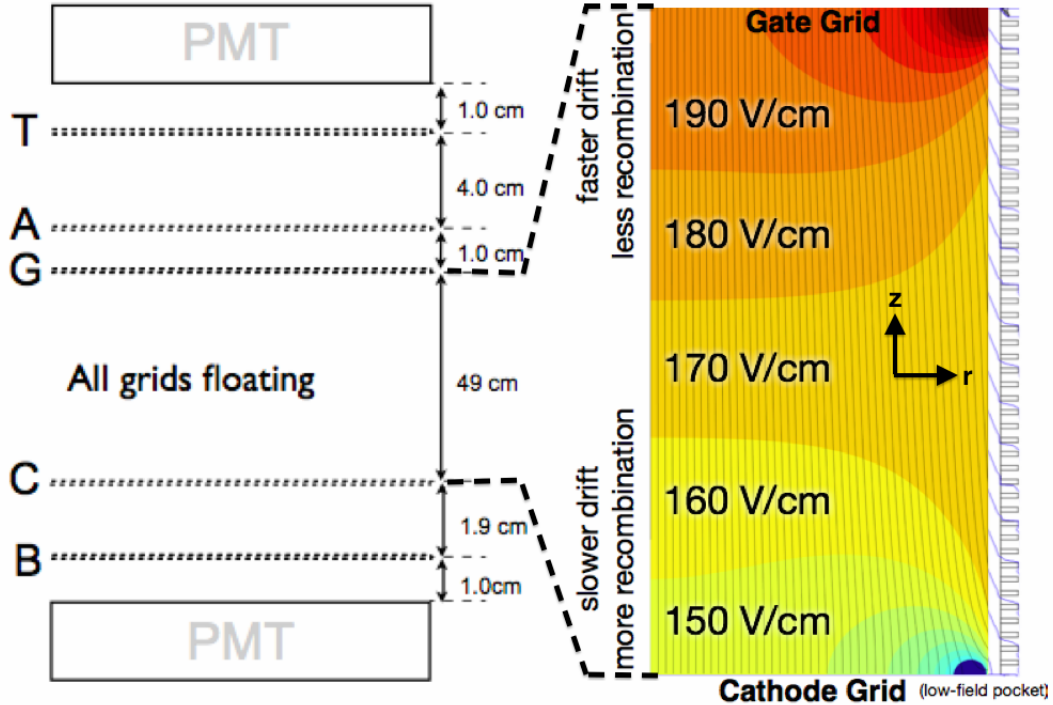


Figure 2.5: Field grids in the LUX detector during the 2013 science run. T,A,G,C,B are biassed to -1,+3.5,-1.5,-10,-2 (all in kV), respectively. The PMTs are biassed to -1.2 kV on average. The figure on the right shows the electric field model in the drift region between the cathode and gate for drift distance z vs. detector radius r . On average the drift field is 170 V/cm with variation from 140 V/cm to 200 V/cm from cathode to gate. Electric field model from [6].

2.3 Light and Charge Signals in Liquid Xenon

When energy is deposited in the active region of the xenon TPC it is converted to ionization, excitation and heat.

$$\begin{aligned} E &= W(n_i + n_{ex}) + \text{Heat} \\ E &= W(n_\gamma + n_e) + \text{Heat} \end{aligned} \quad (2.1)$$

where E is the energy of the deposition in keV, n_q is number of quanta (photons + electrons), n_i , n_{ex} , n_γ and n_e are the number of ions, excitons, photons and electrons respectively. The work function (W) for xenon has been measured to be 13.7 ± 0.2 [eV/quanta] [8]. The number of photons observed for a given energy deposit arise from the excitons that de-excite and from ions which recombine with freed electrons. The number of electrons corresponding to a given energy deposit is equal to the number of ions that did not recombine with a freed electron.

$$\begin{aligned} n_\gamma &= n_{ex} + n_i r = n_i(r + \alpha) \\ n_e &= n_i(1 - r) \end{aligned} \quad (2.2)$$

Where r represents the electron-ion recombination probability and α represents the ratio n_{ex}/n_{ion} . The model given in equation 2.2 states that for each additional photon produced from recombination a corresponding electron is lost, and visa versa. The value of α for an ER event is approximately 0.06 and is expected to be independent

of energy [53] [54] [8]. For nuclear recoils α is approximately 1 [8]. The light and charge production in liquid xenon will be discussed in further detail below. Some useful properties of xenon are listed in table listed in table 2.2.

Parameter	Value	Ref.
Scintillation wavelength	174-178 nm	[55]
W (work function)	13.7 ± 0.2 [eV/quanta]	[8]
Xe ₂ [*] singlet lifetime	3.1 ± 0.7 ns	[56] [57] [58]
Xe ₂ [*] triplet lifetime	24 ± 1 ns	[56] [57] [58]
Recombination time	7.5 ns **	[59] [58]
Liquid density at boiling point	2.95 g/l	[60]

Table 2.2: Properties of xenon. ** The expected recombination time in the LUX detector. Recombination time ranges from 0 to 46 ns depending on electric field, energy deposit, and interaction type [58] [59].

2.3.1 Electronic Recoils (ER)

For an electronic recoil event the energy lost to heat is only about 5% [61] thus, equation 2.1 is valid for use with electronic recoils, we simply drop the small loss to heat. A schematic of an ER event is shown in figures 2.6 which we will overview. When an incoming beta or gamma interacts with the electron of the xenon atom the energy deposited is converted primarily to ionization, with roughly 6% excitation and $\sim 5\%$ is lost to heat [54] [61]. Excitons arise from ionized xenon atoms that bond together forming diatomic molecules (Xe₂^{*}). Xenon excitons will de-excite with characteristic time constants of 2.2 and 27 ns for the singlet and triplet state, respectively, producing ~ 175 nm scintillation light. Ion-electron pairs produced via ionization can also recombine, with probability r , producing additional excitons resulting in the production of additional ~ 175 nm scintillation light. The characteristic

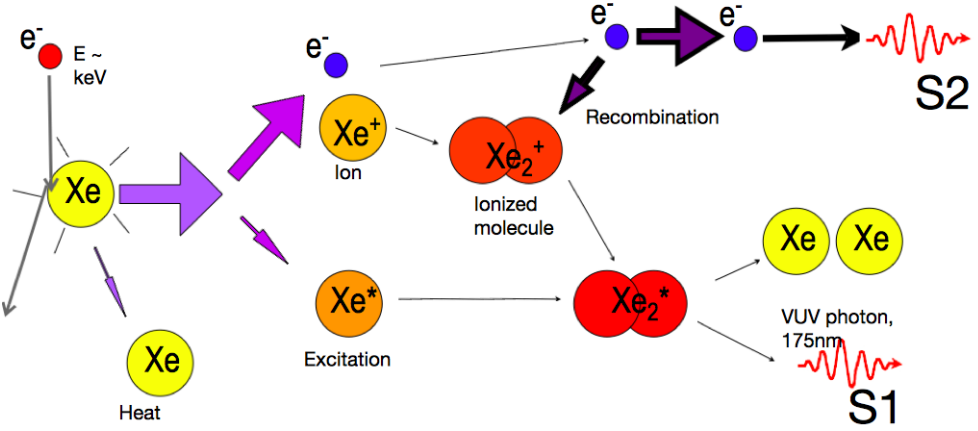


Figure 2.6: An electronic recoil (ER) event in xenon. The energy deposited is converted primarily to ionization and roughly one tenth for excitation. Only several percent is lost to heat. Xenon excitons and recombining electron ion pairs for xenon dimers which de-excite producing very ultra violet (VUV) scintillation light at 175nm producing the primary scintillation signal (S1). Electrons that do not recombine are drifted by an electric field into the gas phase where they are accelerated producing the secondary scintillation (S2) signal.

recombination time constant is 45 ns [57]. Each initial exciton or recombining ion produces one scintillation photon, as written in equation 2.2. The two paths for photon production overlap in time and sum to produce the primary scintillation signal (S1). The S1 signal is collected by the PMT arrays within 500 ns. Electrons that escape recombination , with probability $1-r$, begin to drift upwards under the influence of the electric field between the cathode and gate (shown in 2.5). The electrons eventually reach the liquid-gas interface where they are extracted into the gas. As they accelerate, the extracted electrons produce a larger secondary scintillation signal (S2) that is proportional the the number of electrons extracted. The drift times for the electrons in the 49 cm long active region range from 1 to 324 μ s with an average drift velocity of 1.51 mm/ μ s. Thus, the S2 signal is well separated from the S1.

2.3.2 Nuclear Recoils (NR)

For nuclear recoils the energy lost to heat is more than half the total energy deposition [61]. This energy is lost through elastic collisions with other xenon atoms that fall below the ionization threshold. The energy lost to heat is characterized by an energy dependent Lindhard factor (\mathcal{L}) [62], written as:

$$E = \mathcal{L}^{-1} W(n_\gamma + n_e) \quad (2.3)$$

A schematic of a NR event is shown in figure 2.7. The signal production follows the same process as described above for an ER event but with greater amount of energy going towards heat and exciton production.

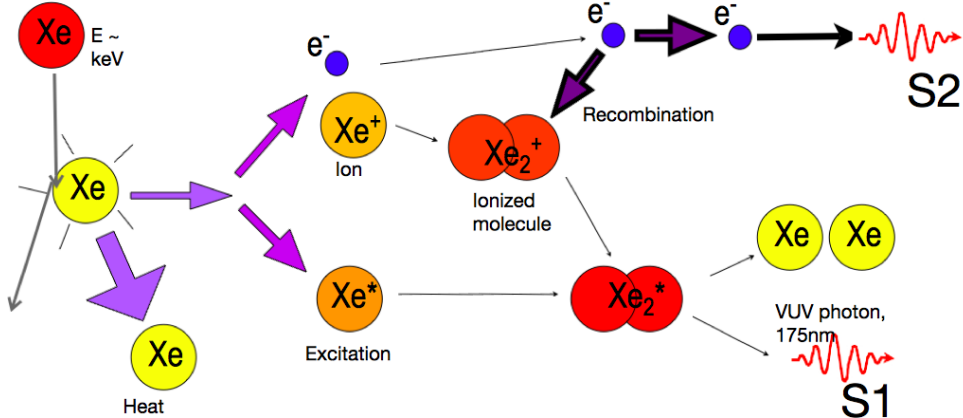


Figure 2.7: A nuclear recoil (NR) event in xenon. The energy deposited goes mainly towards heat (phonons), the remaining energy is split evenly between ionization and excitation. Xenon excitons and recombining electron ion pairs for xenon dimers which de-excite producing very ultra violet (VUV) scintillation light at 175nm producing the primary scintillation signal (S1). Electrons that do not recombine are drifted by an electric field into the gas phase where they are accelerated producing the secondary scintillation (S2) signal.

The additional energy lost to heat leaves less energy available for excitation and

ionization for an NR event. Further, NR events produce roughly equal amounts of ionization and excitation whereas ER events produce mostly ionization [61] [8]. Relative to an ER event, a NR event will have less electron ion pairs leading to a reduction of the S2 signal and enhancement of the S1. Thus, the ratio of S2 to S1 for a NR event is quenched compared to an ER event with an equivalent energy deposition. The quenching of the charge to light ratio is what leads to additional discrimination between nuclear and electronic recoil demonstrated in figure 2.4.

2.3.3 Energy and Position Reconstruction

In order to reconstruct the true energy of an event we will need to know its nature, ER or NR. For ER events we work in units of electronic equivalent energy, (keV_{ee}), using equation 2.1 neglecting the small heat loss. ER calibrations will be discussed in greater detail in section [ER calibration]. For NR events the energy is reconstructed in terms of nuclear recoil equivalent energy (keV_{nr}), using equation 2.3 with the Lindhard factor measured from calibration data given in [63] [64]. An illustration of an energy deposition in the LUX detector is shown in figure 2.8. The time difference between the S1 and S2 pulse defines the drift time, the drift time gives the measure of the z coordinate (depth). The hit pattern of the S2 signal on the top PMT array measures the x,y coordinates of the event. From the S1 and S2 signals the full x,y,z position and energy deposit of the event can be reconstructed.

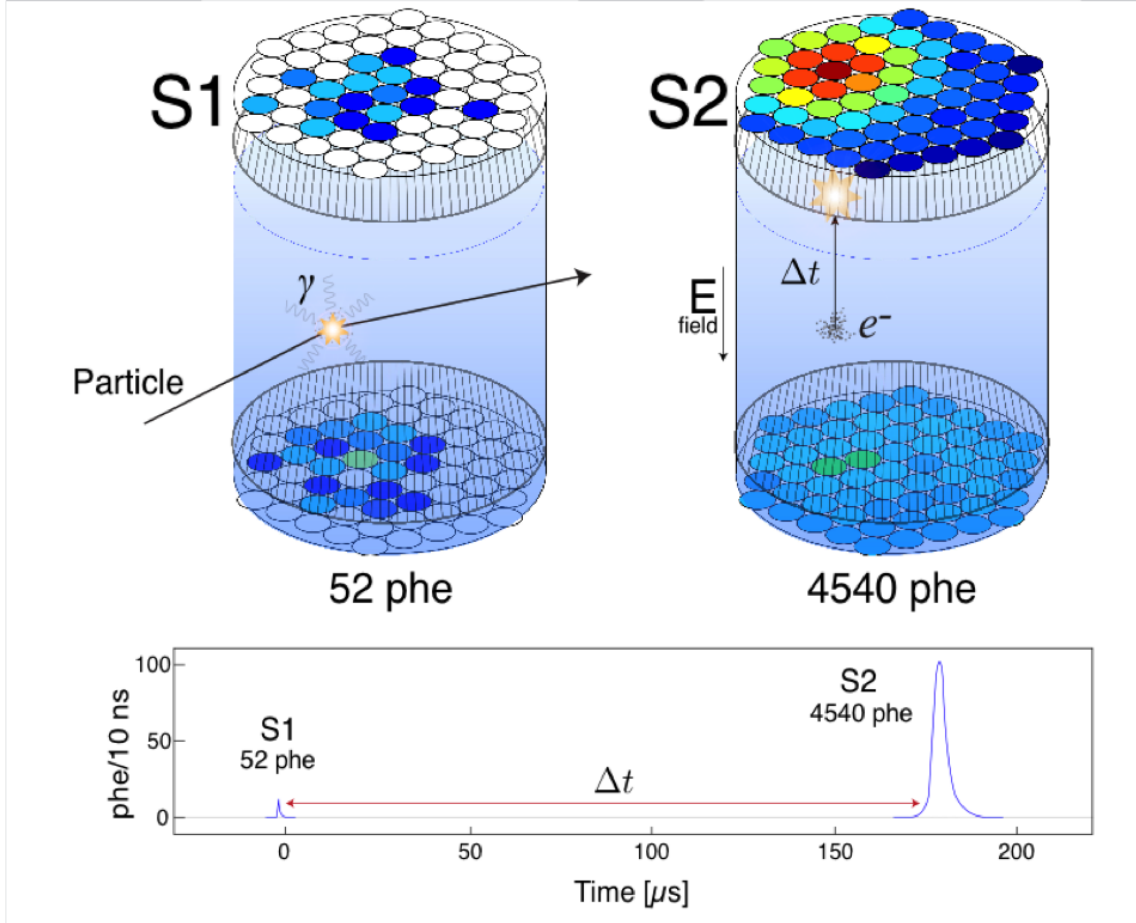


Figure 2.8: Event diagram.

2.4 Identifying S1, S2

The primary and secondary scintillation signals can be identified by their unique properties. The S1 signal has a fast rise time and decays on the order of 10s of nanoseconds as the dimers of xenon produced through excitation and recombination de-excite (time constants listed in table 2.2). The S2 signal arrives several μs later with the electron population spread out spatially about its centroid due to diffusion, transverse and radial [65]. The characteristic S2 signal is thus one with a slow rise and corresponding slow fall. It resembles a bell curve, as the diffused electron

population arrives, peaking at the centroid of the distribution. A 2 keV event as seen by all 122 PMT channels is showing in figure 2.9. The S1 pulse is fast and the S2 pulse is much larger with a slower rise-time. The S2 pulse is larger since a single electron creates hundred of photons as it is accelerated in the extraction region.

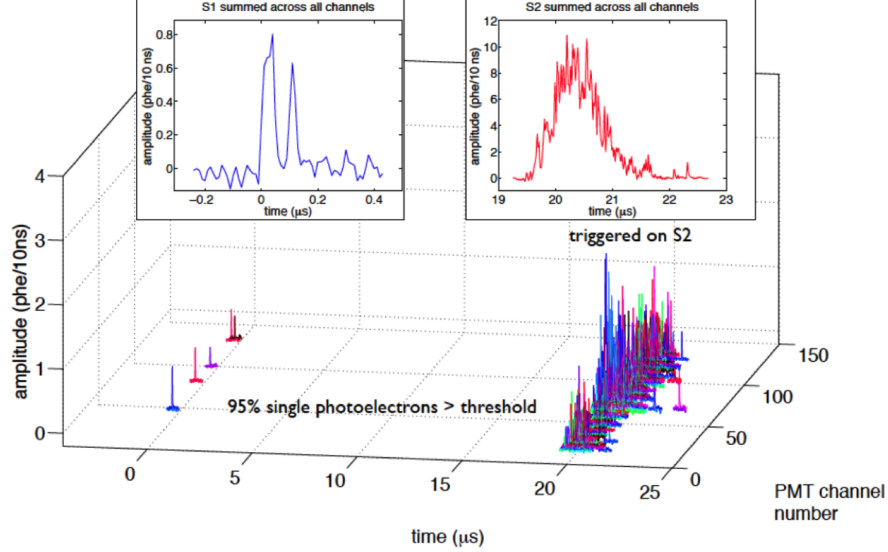


Figure 2.9: 2keV ER event as seen by each PMT channel of the LUX detector. The S1 signal summed across all channels is overlaid on the top left, and the S2 signal summed across all channels is overlaid on the top right.

To identify S1 and S2 populations we define the variable Prompt Fraction as the area covered in the first 10% of the pulse normalized to the total area. The calculation is performed on the summed waveform after a first pass which defines the pulse's start and end timestamp. The separation of population density when plotting the total Pulse Area (measured in detected photo electrons [PE]) vs. Prompt Fraction is shown in figure 2.10, for the case of a ^{83m}Kr data set (41.5 keV)

and a tritium calibration data set (1-18.5 keV). The population of single electrons, single photons and the S1 S2 pairs associated with γ , β and α interactions are well separated and are highlighted as rectangles. The upper left corner is the single photon population, their areas consist of approximately 1 PE, the definition of the PMTs response to a detected photon. The single electron population is labeled SE and peaks at roughly 20 PE with a prompt fraction of -1. For all S1 pulses the prompt fraction is found to be between 1 and 0.3 (\log_{10} of 0 and -0.5) for the entire range of Pulse Area. The pulse area is a proxy for energy deposit, spanning from 1 keV tritium events to 7 MeV alphas. The populations of S2 from ^{83m}Kr , tritium, γ , β and α are found to have Prompt Fractions more than an order of magnitude smaller than their corresponding S1.

The S1 and S2 signal corresponding to an event are identified using a prompt fraction selection that had been tuned to calibration data. Valid S1 and S2 signals that spill into the single electron and single photon region at low energies can be identified by requiring the pulses be paired. For the WIMP search we define ‘golden’ events consisting of single scatters with a single S1 paired with a subsequent S2 pulse with a timing separation not exceeding the maximum drift time inside the TPC. With the golden requirement each event has a well defined x,y coordinate and z making it possible to correct the signals for geometry and electron attenuation.

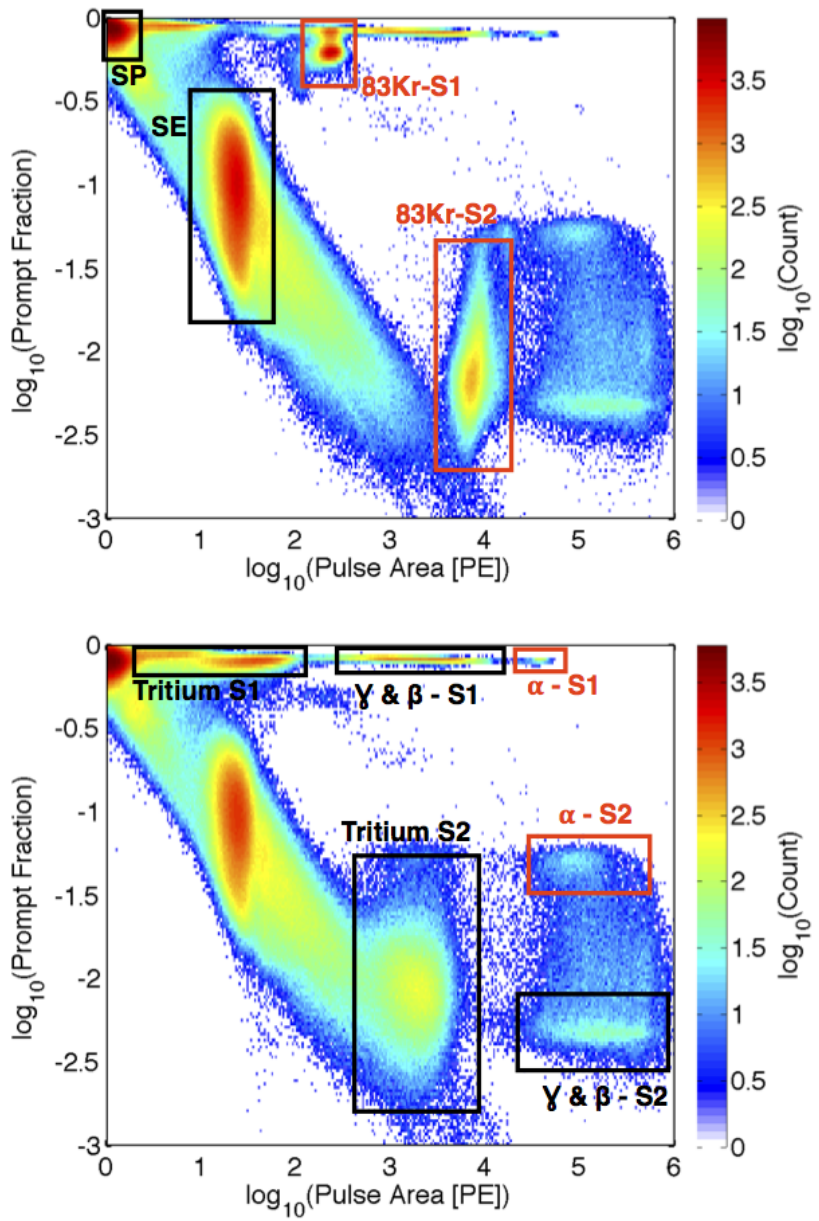


Figure 2.10: Density plot of prompt fraction vs. Pulse Area. Top: $^{83\text{m}}\text{Kr}$ data set.

Bottom: Tritium data set. Populations of single electrons, single photons and the

S1 S2 pairs associated with γ , β and α are highlighted as rectangles.

2.5 LUX Science Result (WIMP limit)

The first science run of the LUX detector consisted of 85.3 live days from April 21, 2013 to Aug 8, 2013. A total of 83,673,413 triggers were recorded with 160 remaining as golden after applying quality cuts, listed in table 2.3.

Cut	Events Remaining
all triggers	83, 673, 413
detector stability	82, 918, 902
single scatter	6, 585, 686
S1 energy (2 - 30 phe)	26, 824
S2 energy (200 - 3300 phe)	20, 989
single electron background	19, 796
fiducial volume	160

Table 2.3: Data quality cuts used for the WIMP search results presented in [38].

Detector stability cuts remove the live time in which liquid level, gas pressure or grid voltages were out of normal ranges. The single scatter cut requires a single S1 with a subsequent S2 within a time window of $324 \mu\text{s}$, the maximum time required for electrons to traverse the active region. An area cut was also placed on both the S1 and S2 in order to narrow the energy region of interest. The minimum S2 requirement of 200 PE ensures the quality of the x,y position reconstruction, with ~ 8 extracted electrons. An additional cut was placed around time windows with anomalously high single electron rates. All single scatter WIMP search events before applying the fiducial cut are shown in figure 2.11, the vast majority of events occurring at the edges of the detector. The fiducial cut reduces residual radioactivity from the detector surface and PMTs by another two orders of magnitude. The fiducial cut consists of a radial cut at radius less than 18 cm from the detector

center. The z coordinate in drift time is defined to be 0 μs at the liquid surface and 324 μs at the cathode. The fiducial cut in z required that event drift times be between 38 and 305 μs , corresponding to 6 to 46 cm below the liquid surface (drift velocity = 1.51 mm/ μs). The fiducial cut is shown as the dashed cyan line in figure 2.11.

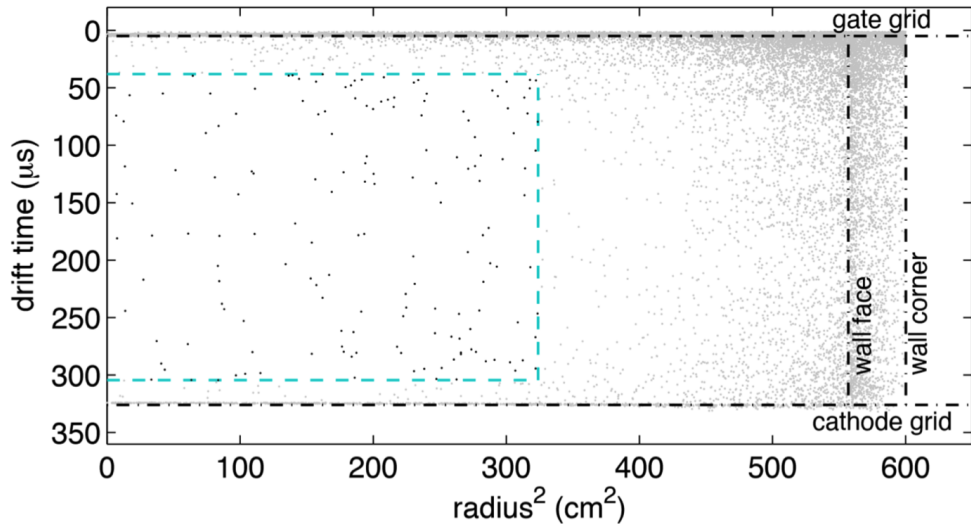


Figure 2.11: All single scatter events seen in the active region of the LUX detector over the course of the first science run passing all cuts listed in table 2.3 excluding the fiducial cut. The dashed cyan box indicates the fiducial volume.

Within the fiducial volume 160 events remain which meet our WIMP search energy requirement. The energy cut is placed in terms of S1 from 2-30 PE. As explained in chapter [Energy Calibrations] this corresponds to roughly 1.0 to 6 keV_{ee} or 3 to 25 keV_{nr}. We choose to select events based on S1 because it is directly observed, whereas true energy depends on the nature of the event (ER or NR) and must be inferred. The ER and NR discrimination band was measured using

calibration data and shown in figure 2.12. The blue and red bands represent the 10% to 90% confidence bounds of events being ER and NR type, respectively. The ER band was measured using a tritium calibration source (β^-) and the NR band was measured with neutrons from AmBe and ^{252}Cf along with NEST simulations [64]. The ER/NR discrimination at 50% NR acceptance was measured to be 99.6 ± 0.1 %. This value serves as a proxy for background events rejection, which is ultimately treated with a profile likelihood method on an event by event basis. Both the S1 and S2 signal have been corrected for spacial dependance which is discussed in further detail in Chapter . Due to cross talk or shorts, two PMTs on the top array and one on the bottom were left unbiassed. In order to avoid misreconstructing events extracted around the unbiased top PMTs only the bottom PMT array was used for the S2 signal ($S2_b$).

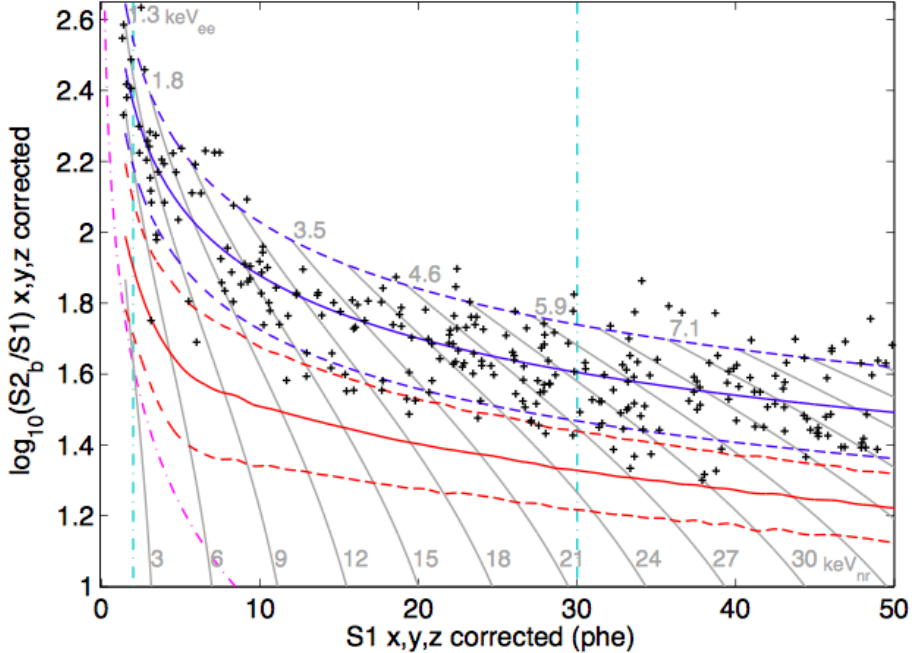


Figure 2.12: The remaining events passing the quality cuts listed in table 2.3. The charge to light ratio (S_2/S_1) is plotted vs. S_1 (proportional to energy) to show the separation of ER and NR type events. The 10-90% CF limits of the ER and NR band are plotted as the dashed blue and red curves, respectively. The band means are solid. S_2 _b stands for the S_2 signal on the bottom PMT array.

All 160 remaining events in the fiducial volume are consistent with being ER type events. The main source of BG events include residual ^{85}Kr , activated ^{127}Xe and ^{214}Pb from ^{222}Rn , described in further detail in [5]. The residual ER background rate in the WIMP region of interest as found to be 3.6 ± 0.3 mDRU (10^{73} cnts/keVee/kg/day) with an expectation of $2.6 \pm 0.2_{\text{stat}} \pm 0.4_{\text{sys}}$ mDRU.

A profile likelihood test is conducted on all WIMP search candidates remaining after the cuts listed in table 2.3. Testing the charge to light ratio (S_2 _b/ S_1) vs. energy (S_1) for likelihood of being an expected ER background. The signal model for the

test is derived from AmBe and ^{252}Cf neutron calibrations. The background rates input into the profile likelihood were independently measured and modeled with LUXSIM using NEST, described in further detail in [5] [38] [64]. The WIMP signal model was generated using an isothermal halo with a Maxwellian distribution, with a local WIMP density of 0.3 GeV/cm³ (as discussed in section 1.4). The galactic escape velocity input into the model is 544 km/s (cutting off the high end of WIMP velocity distribution), with an average WIMP velocity of 220 km/s. The earth's seasonal velocity being 245 km/s with respect to the galactic center. The result from the 2013 science run with the LUX detector is consistent with a P value of 0.35 for the background only hypothesis. The 90% upper C.L. cross section for various spin independent masses are shown in figure 2.13. The minimum cross section reported occurs at 7.6×10^{-46} cm² for a WIMP mass of 33 GeV/c² [38]. The LUX result is a factor of two improvement in WIMP cross section sensitivity over the Xenon100 limit reported in 2012 [39] and is in tension with reported WIMP signal claims from CoGent [45], CDMSLite (Silicone) [66], CRESST II [67] and DAMA/LIBRA [68].

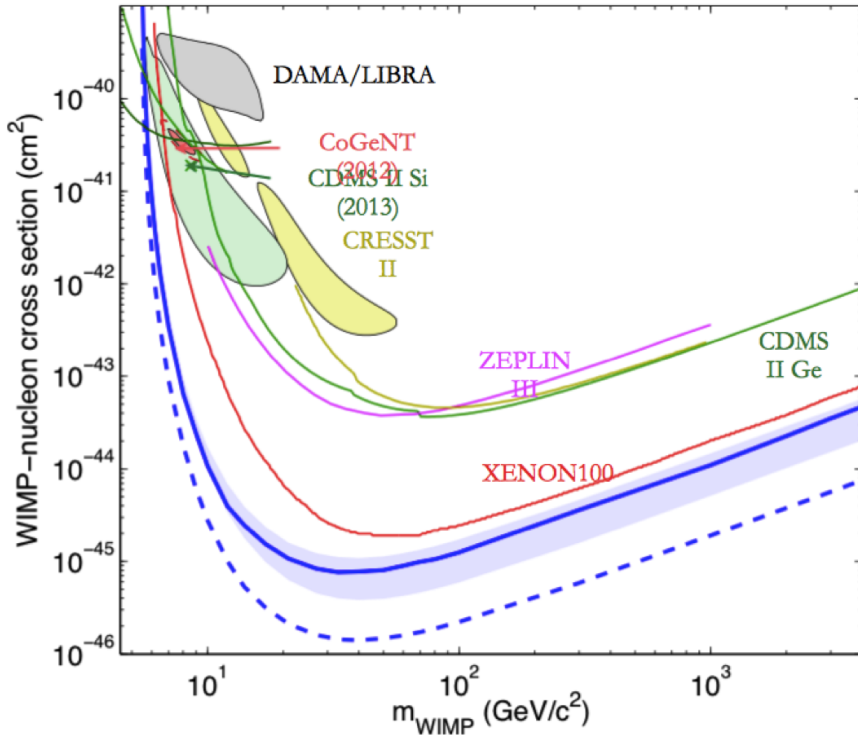


Figure 2.13: LUX detector is consistent with a P value of 0.35 of the background only hypothesis. The 90% upper C.L. cross section for various spin independent masses are shown in figure 2.13 in blue. Also shows are limits from Xenon100 (red), CDMS II (green), ZEPLIN III (magenta), and one sigma signal claimed for DAMA/LIBRA (shaded grey), CDMS II Silicone (shaded green), CRESST II (shaded yellow).

As mentioned above the ER band is measured with a novel tritium calibration source and will be discussed in further detail in Chapter [TritiumSource]. Since the initial science run we have gathered twenty times the tritium statistics to further study the ER band, with 150,000 events in the fiducial volume. We also spent several months deploying a DD neutron generated source to further study the NR band mean. The results from the improved ER and NR calibrations will be reported

in this thesis along with the implications for an improved WIMP limit. An updated profile likelihood reanalysis of the LUX WIMP search result will be submitted for publication in late Fall of 2014.

Chapter 3: Spacial Dependent Correction of the S1 and S2 Signals

In this chapter we address the spacial dependent corrections applied to the S1 and S2 signal. During the 2013 science run $^{83\text{m}}\text{Kr}$ injections were performed periodically and used to calculate the position dependent corrections that were applied to the WIMP search data. Knowing the x,y,z position of each event provides a powerful tool for reducing variations in the signals due to detector geometry. The better we can correct for position dependance of the S1 and S2 signals the smaller the observed variations will be, leading to better ER, NR discrimination and ultimately better signal to background for the WIMP search.

After the energy deposit occurs in the active region of the LUX detector the freed electrons are drifted via electric field towards the liquid surface. The S2 light is emitted as the electrons are extracted at a given x,y position from the liquid surface and accelerated by a 6 kV potential, traversing 5mm from the liquid surface to the anode. The dominant effect to correct the data for is the free electron lifetime. As charge is drifted from the event site to the extraction region (0-47 cm) electronegative impurities in the liquid latch onto them. S2s of equal sizes are exponentially attenuated with increasing depth in the detector by impurities such as O₂, H₂O, N₂ in the xenon. (7 ppb O₂ corresponds to roughly 100 μs lifetime [69]). The S2 signal

has x,y dependent variations due to non uniformities in the extraction field, tilt in the liquid level, and non uniformities in the anode-gate wire separation (potential wire grids sagging).

The S1 light propagates isotropically from the interaction site and has about a 30% variation in light collection efficiency between events near the top and bottom of the detector due to geometric effects. About 2/3 of the S1 light is collected on the bottom PMT arrays due to total internal reflection at the liquid gas interface. The closer the event to the bottom PMTs the larger the solid angle is into the bottom PMT, increasing the probability of the detecting a photon and producing a photo electron (PE). Other position-dependent effects include the photon absorption length which is negligible at the purities achieved in LUX, and teflon reflectivity which is > 90% in liquid xenon [70] [71]. The S1 position dependent correction used in the LUX analysis normalizes the photon detection probability of all events to the center of the active region, an arbitrary choice corresponding roughly to the average light response.

It should also be noted that variation in light yield and charge yield due to the non uniformity of the electric field are also folded into x,y,z deponent correction. The effect of light yield and charge yield for ^{83m}Kr due to dependance of recombination on the local electric field is on the order of 10% [64]. The field increases from about 140 to 200 V/cm from the cathode to gate in the LUX detector, the electric field model is shown in 2. Also, all S1 and S2 signals are measured as photo electron (PE) pulse areas that have been calibrated by pulsing LEDs (450 ns) located inside the TPC. Any quantum efficiency (QE) or gain variations in the 122 PMTs which

are not properly normalized by the individual gain corrections are also folded into the position dependent corrections measured from the ^{83m}Kr calibrations.

3.1 ^{83m}Kr Calibration

Throughout the science run periodic ^{83m}Kr injections were performed to calculate position dependent corrections. ^{83m}Kr is produced from the decay ^{83}Rb with a half life of 86.2 days. The ^{83}Rb source used is housed in charcoal and plumbed directly into the LUX circulation system. A decay scheme of ^{83}Rb and ^{83m}Kr is shown in figure 3.1.

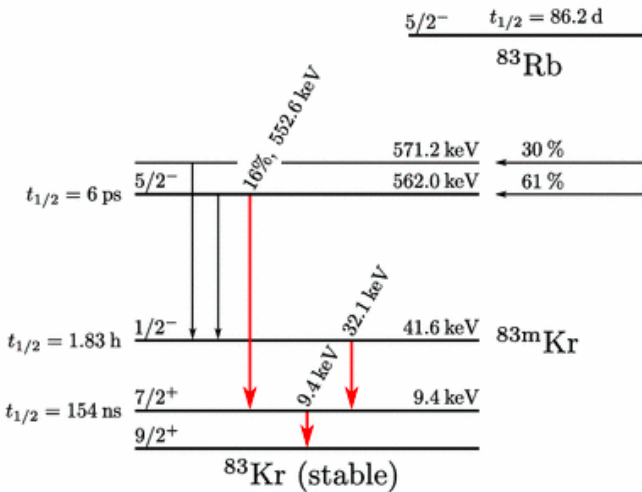
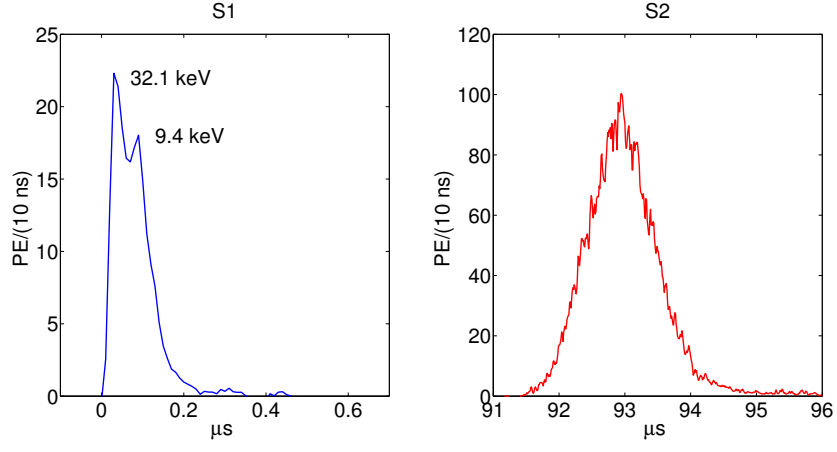


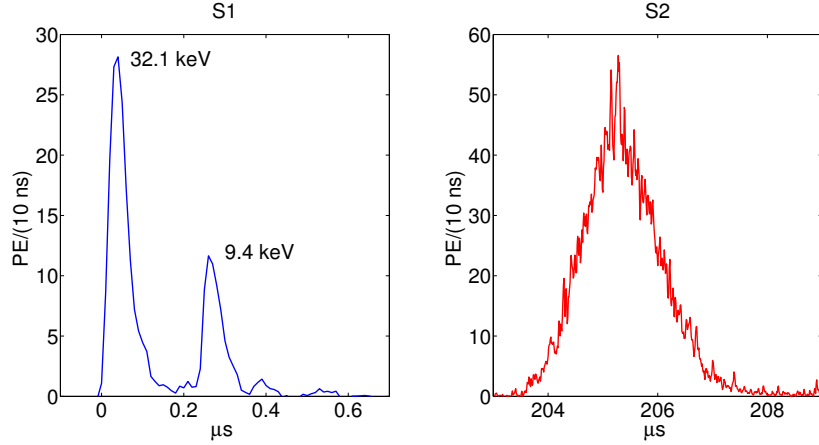
Figure 3.1: A simplified decay diagram of ^{83}Rb and ^{83m}Kr , from [7].

The daughter ^{83m}Kr is continually produced in the charcoal housing, having a half-life 1.8 hours. ^{83m}Kr decays via an electron capture first emitting a 32.1 keV x-ray followed by a 9.4 keV x-ray with a half life of 154 ns between the two [72] [9]. For the vast majority of the decays the combined S1 pulse corresponding to 41.55 keV is observed, since the minimum S1 pulse separation in the LUX reconstruction is

1000 ns. Figure 3.2 shows the waveforms (S1 and S2) for two ^{83m}Kr events with the the decay of the 32.1 and 9.4 keV x-ray split by 60 and 220 ns, both S1s shown are classified as a single S1 event. The timing separation between the S1 and S2 is used to infer the drift distance to be 14.0 and 40.0 cm below the liquid surface, respectively. The reduction of the S2 signal that originated from deeper in the detector is apparent by comparing the amplitudes of the S2, with roughly 50% charge loss. The S2 pulses are insensitive to the timing separation of the dual decay as electron diffusion smears the pulses two together as the electrons drift through the active region before extraction [65]. The PMT hit map for the events is shown in figure 3.3.

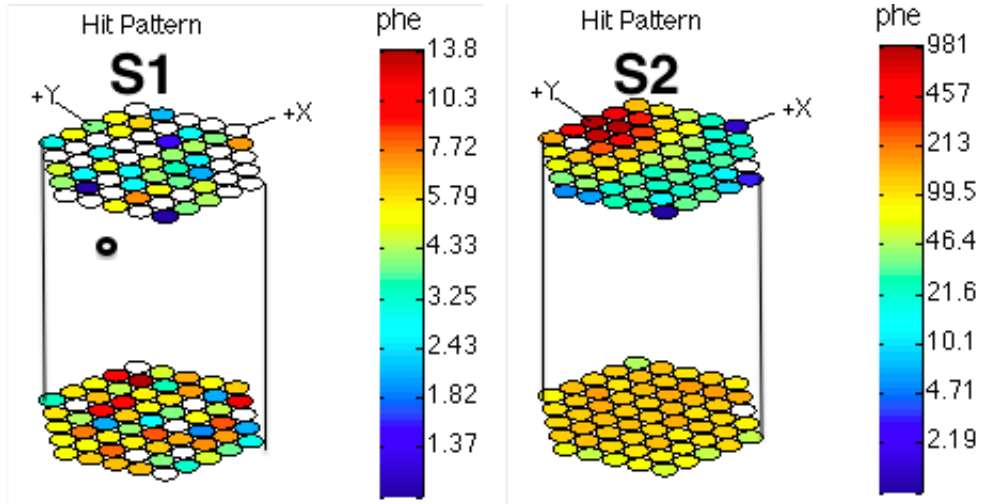


(a) $^{83\text{m}}\text{Kr}$ event with 60 ns timing separation.

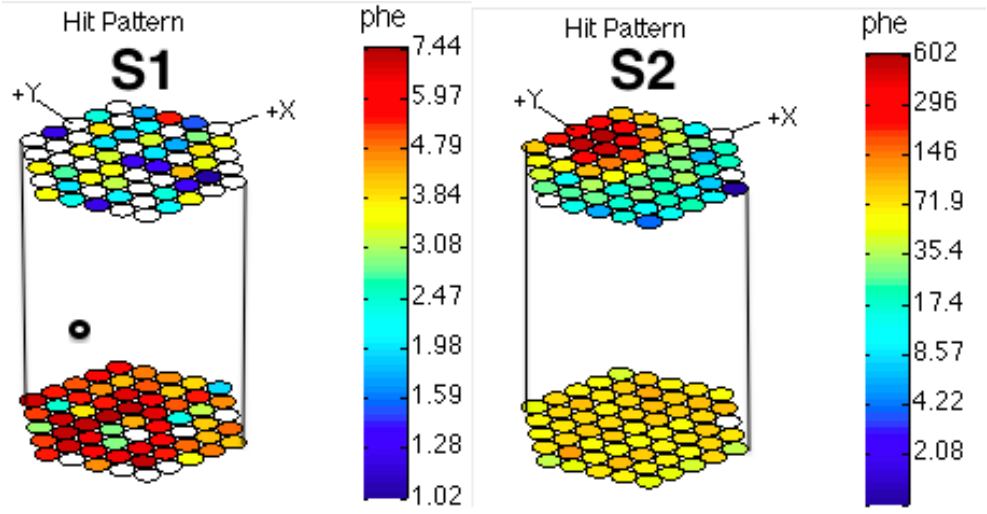


(b) $^{83\text{m}}\text{Kr}$ event with 220 ns timing separation.

Figure 3.2: The S1 and S2 of two $^{83\text{m}}\text{Kr}$ events. Top Figures (a): Show a $^{83\text{m}}\text{Kr}$ event in which the two x-rays have overlapped within 60 ns, the S2 arrives about 93 μs later. Bottom Figures (b): Show a $^{83\text{m}}\text{Kr}$ event in which the two x-rays have overlapped within 220 ns, the S2 arrives about 205 μs later. The LUX pulse finder classifies events within a 1 μs window as a single S1. The S2 pulses are insensitive to the timing separation of the dual decay as electron diffusion smears the pulses two together as the electrons drift. The PMT hit map for these events are shown below in figure 3.3.



(a) $^{83\text{m}}\text{Kr}$ event with 60 ns timing separation.



(b) $^{83\text{m}}\text{Kr}$ event with 220 ns timing separation.

Figure 3.3: The S1 and S2 of two $^{83\text{m}}\text{Kr}$ events. Top Figures (a): Show a $^{83\text{m}}\text{Kr}$ event in which the two x-rays have overlapped within 60 ns. Bottom Figures (b): Show a $^{83\text{m}}\text{Kr}$ event in which the two x-rays have overlapped within 220 ns. The black, open circle represents the location of the event. The S1 hit pattern is diffuse with more light collected on the bottom arrays due to total internal reflection at the liquid surface. The S2 is localized in the top PMT arrays in x,y at the location where the electrons are extracted, and diffuse on the bottom due to scattering. The summed waveforms for these events are shown above in figure 3.2.

3.2 ^{83m}Kr Mixing in Liquid Xenon

The ^{83m}Kr source is introduced when needed into the LUX detector by flushing the charcoal housing with xenon and diverting the flow inline with the main circulation path. The ^{83m}Kr source and delivery into the xenon detector is described in more detail in [9]. The relatively short half-life of 1.8 hours allows for several injections per week without interrupting WIMP search data taking. Once injected the source is uniformly mixed into the liquid xenon within a matter of minutes and can be used to calculate corrections for the XYZ the response of the detector. ^{83m}Kr has proved useful for calibrating liquid xenon detectors [9] [10] [13]. The solubility of krypton in liquid xenon will be discussed further in Chapter[Sampling]. Figure 3.4 shows the uniform distribution of ^{83m}Kr events in the LUX detector thirty minutes after the injection. Once uniformly mixed, the decay of ^{83m}Kr produces a well defined mono energetic peak in the detector (the S1, S2, and energy spectra are shown in section 4). Measuring the spectral peak vs. x,y,z allows for the detector's spacial dependent response to be gauged over the course of the science run.

3.3 S2 Electron Lifetime and x,y Correction

As mentioned previously, the S1 and S2 signals collected on the top and bottom PMT arrays have well defined x,y,z positions computed from the S2 hit pattern (x,y) and the signal separation in time (z). Throughout the 2013 science run the electron lifetime was measured between 500 to 1000 μs , or an attenuation length of

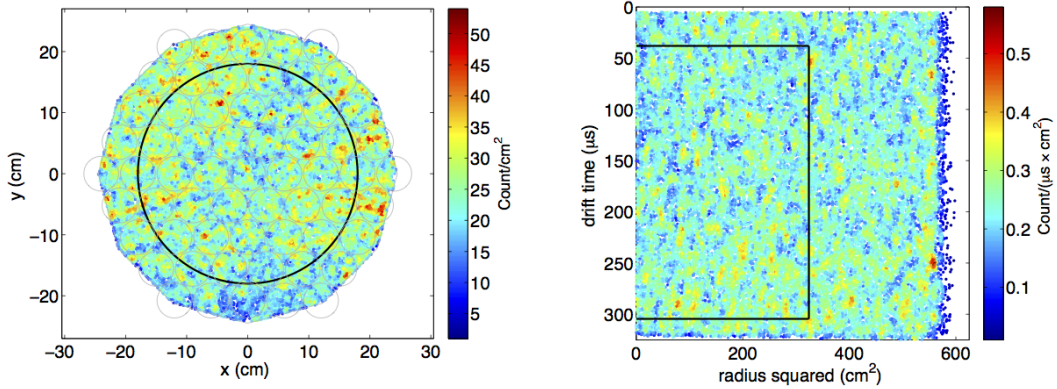


Figure 3.4: Distribution of $^{83\text{m}}\text{Kr}$ events 10 minutes after the injection. The source mixes uniformly throughout the liquid xenon illuminating all regions of the active volume. The solid black lines represent the fiducial volume used for the WIMP search.

75 to 150 cm with a drift velocity of 1.51mm/ μs . The measured electron lifetimes (or attenuation lengths) correspond to between 70% and 50% reduction in S2 signal from the cathode grid, the bottom of the active region.

The electron lifetime is calculated by binning the detector in drift time into 60 slices. In each bin a Gaussian is fit to extract the mean. Once the mean in each slice is calculated, an exponential is fit to the mean S2 response vs. z. The exponential time constant the measure of the characteristic drift time $\tau [\mu\text{s}]$, shown in figure 3.5. The characteristic attenuation length is $\lambda = \tau v_{drift}$, where v_{drift} is the electron drift velocity. For this analysis we use the S2 response of the bottom PMT array ($S2_b$) as it was used for the 2013 WIMP search analysis discussed in 2.

The z corrected $S2_b$ from each signal is calculated as follows:

$$S2_{b-z} = S2_b \cdot \exp\left(\frac{\text{drift time}[\mu\text{s}]}{\tau[\mu\text{s}]}\right) \quad (3.1)$$

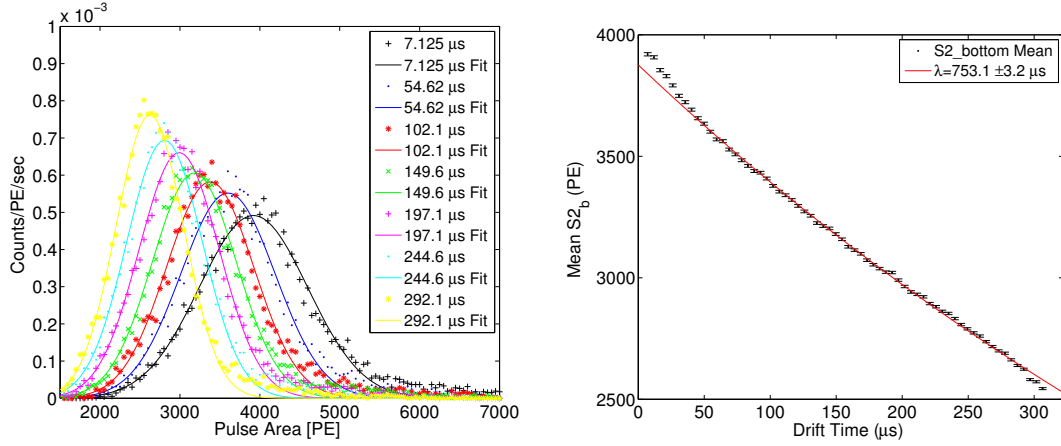


Figure 3.5: Left: Fits to the mean of S2_b of the ^{83m}Kr data in several z slices. Right, the exponential fit to the means of S2_b vs. drift time used to extract electron lifetime τ . The electron lifetime is found to be $\tau = 753.1 \pm 3.2 \mu\text{s}$. The exponential fit to the means deviates near the top and bottom of the active region since the charge yield from the ^{83m}Kr decay is sensitive to the varying electric field. The data shown was taken on May 10, 2013 (lux10_20130510_T1250) and contains 700,000 ^{83m}Kr events.

Where $S2_{b-z}$ is the z corrected S2_b signal and τ is the free electron lifetime. After correcting the dominant z dependent electron attenuation, corrected to 0 drift time, we calculate the normalization factor ($\mathcal{N}\mathcal{F}$) that will be used to correct for the x,y dependent variations in the S2 signal.

The normalization is calculated by creating a 25 x 25 grid on the x-y plane, corresponding to 2 cm x 2 cm x,y bins. For each bin the average S2_b light response is determined by fitting a Gaussian. Figure 3.6 (left) shows the measured S2_b response to 700,000 ^{83m}Kr decays normalized to the response at the center, x=y=0. This map represents the inverse of the normalization factor that we call $\mathcal{N}\mathcal{F}(x, y)$. $\mathcal{N}\mathcal{F}$ is then applied to the S2_b data by using a spline interpolation of the x,y coordinate of each event relative to the bin centers $\mathcal{N}\mathcal{F}(x, y)$. Figure 3.6 (right) shows the S2_b response after correcting the data relative to the center x=y=0 using $\mathcal{N}\mathcal{F}(x, y)$.

After applying the x,y correction the variation decreases from 10% to 1% in the inner 18 cm radius of the detector (the fiducial volume).

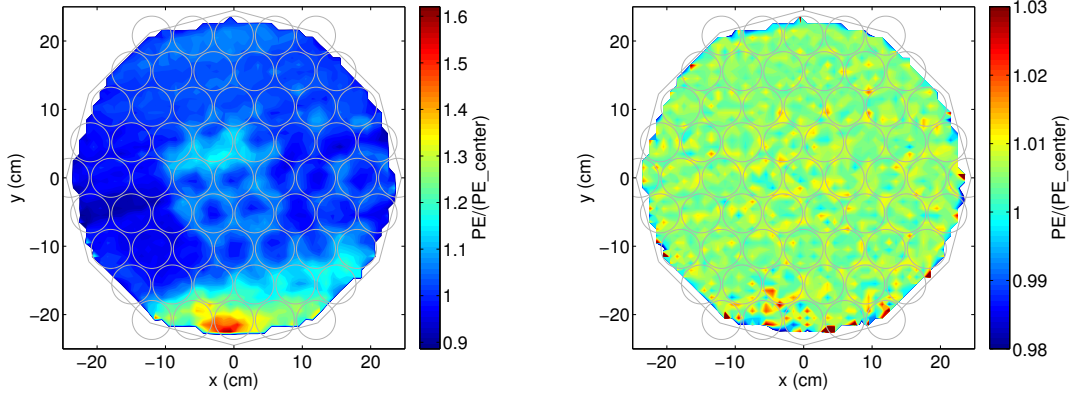


Figure 3.6: Left: Response of $S2_b$ vs. x,y normalized to the response at the center ($x=y=0$). The region of larger response around $x=0, y=-25$ is likely from an enhanced extraction field between the anode and gate wires. Right: Response of $S2_b$ vs. x,y after correcting the data using $\mathcal{N}\mathcal{F}_{S2_b}$.

After correcting for z and x,y we can define the position-dependent (x,y,z) corrected $S2_b$ signal, which we will call $S2_{bc}$ calculated as follows:

$$S2_{bc} = S2_{b-z} \cdot \mathcal{N}\mathcal{F}_{S2_b}(x, y) \quad (3.2)$$

where $S2_{bc}$ is the x,y,z corrected $S2_b$ signal and $\mathcal{N}\mathcal{F}_{S2_b}(x, y)$ is the Normalization Factor of the bottom PMT array for S2s and is a function of x,y. The interpolation of the inverse of $\mathcal{N}\mathcal{F}_{S2_b}(x, y)$ along the x,y grid is plotted in figure 3.6.

Figure 3.7 shows the improvement in the $S2_b$ signal after applying the z and x,y correction. After applying the z correction to $S2_b$ there is a fractional improvement in resolution of 18%, for the case of an 750 μ s electron lifetime. The correcting

in the x,y plane provides an additional 4.9% improvement in resolution to the S2_b signal.

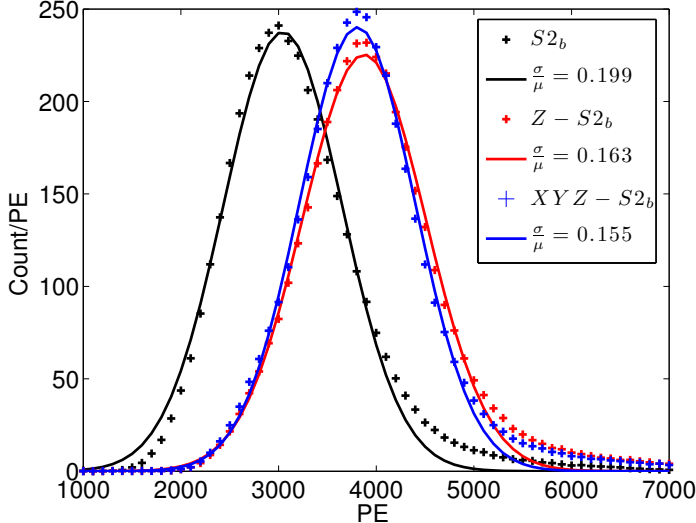


Figure 3.7: Improvement of resolution in S2_b after applying the z and x,y,z correction. Black: The uncorrected data. Red: The data with only z dependent correction, the electron lifetime correction. Blue: The data with full x,y,z dependent correction. The data shown was taken on May 10, 2013 (lux10_20130510_T1250) and contains 700,000 ^{83m}Kr events.

3.4 S1 Spacial Dependant Correction

To measure the x,y,z dependent Normalization Factor for S1 ($\mathcal{N}\mathcal{F}_{S1}$), we divide the detector into a 25 x 25 x 16 x,y,z mesh with each voxel having dimensions of 2 cm x 2 cm x 20 μ s. To achieve sufficient statistics for the correction we require at least 400,000 ^{83m}Kr events, about 40 events per voxel to define the mean. Monthly high stats calibrations are performed that yield about 1 million counts to providing precise $\mathcal{N}\mathcal{F}$ correction maps. Unlike the S2 correction, which is highly dependent on purity, the S1 has been found to be invariant to within a percent over the course

of the science run, thus the monthly calibrations with high statistics are sufficient to provide the position dependent correction.

Figure 3.10 shows the response of the detector to ^{83m}Kr normalized to the center of the detector in 16 slices of z , each with a $2\text{ cm} \times 2\text{ cm}$ x,y grid. The plotted maps and normalized to the center of the detector and represent the inverse of the normalization factor ($\mathcal{N}\mathcal{F}_{S1}$). We choose to normalize the the center of the detector as it represents the average light collection efficiency of the detector. Though the dominant correction is the z -dependance, there is also substructure in x,y to each z slice which is illustrated in figure 3.9, where we have normalized each slice to its own center. It is evident that near the top and bottom there are additional geometric effects around the radial edges, whereas in the central z slices the uniformity in x,y is much better due to the diffusion of the light scattering on the teflon.

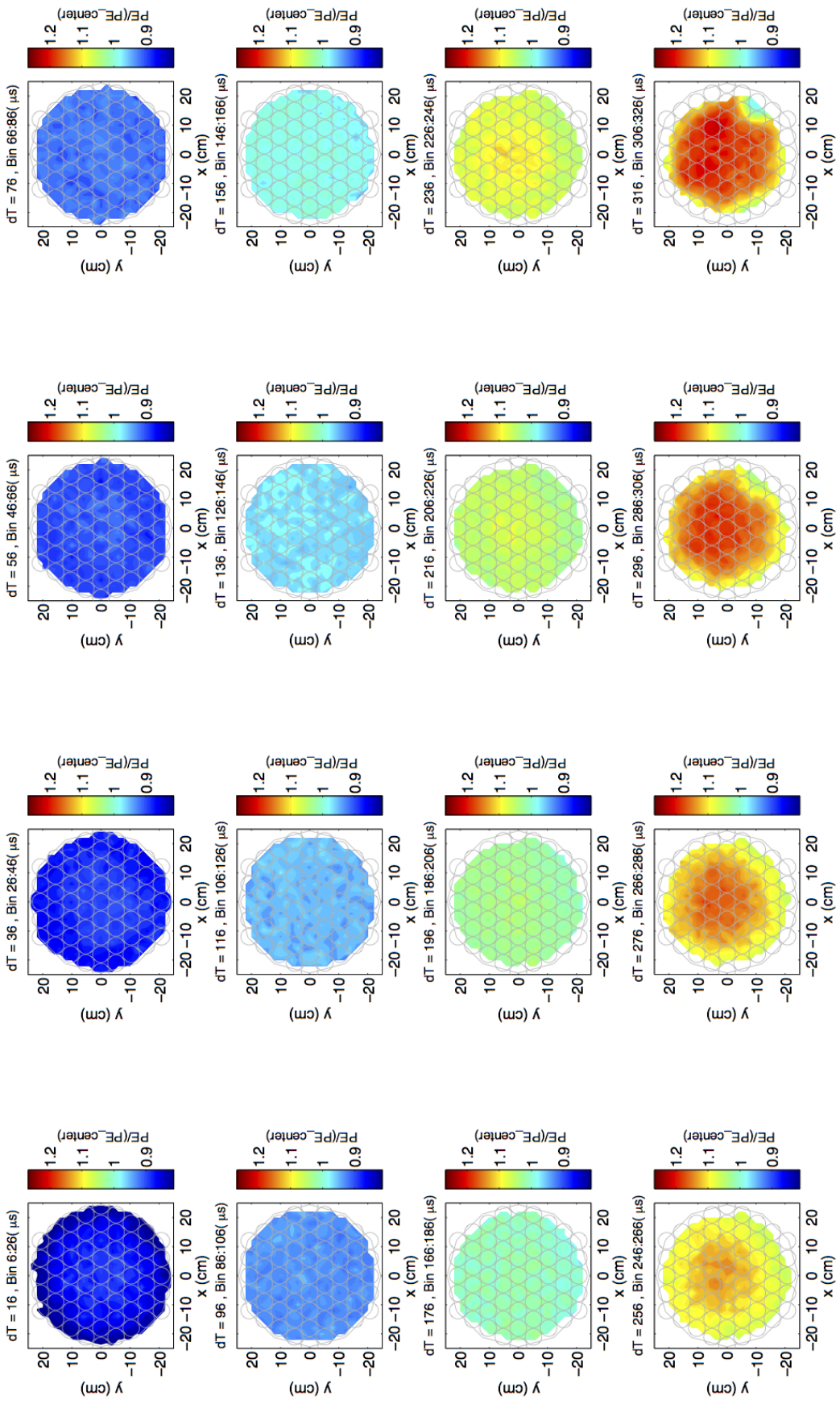


Figure 3.8: S1 x,y,z response normalized to the center of the detector. The interpolated map represents the inverse of the normalization factor $\mathcal{N}\mathcal{F}$.

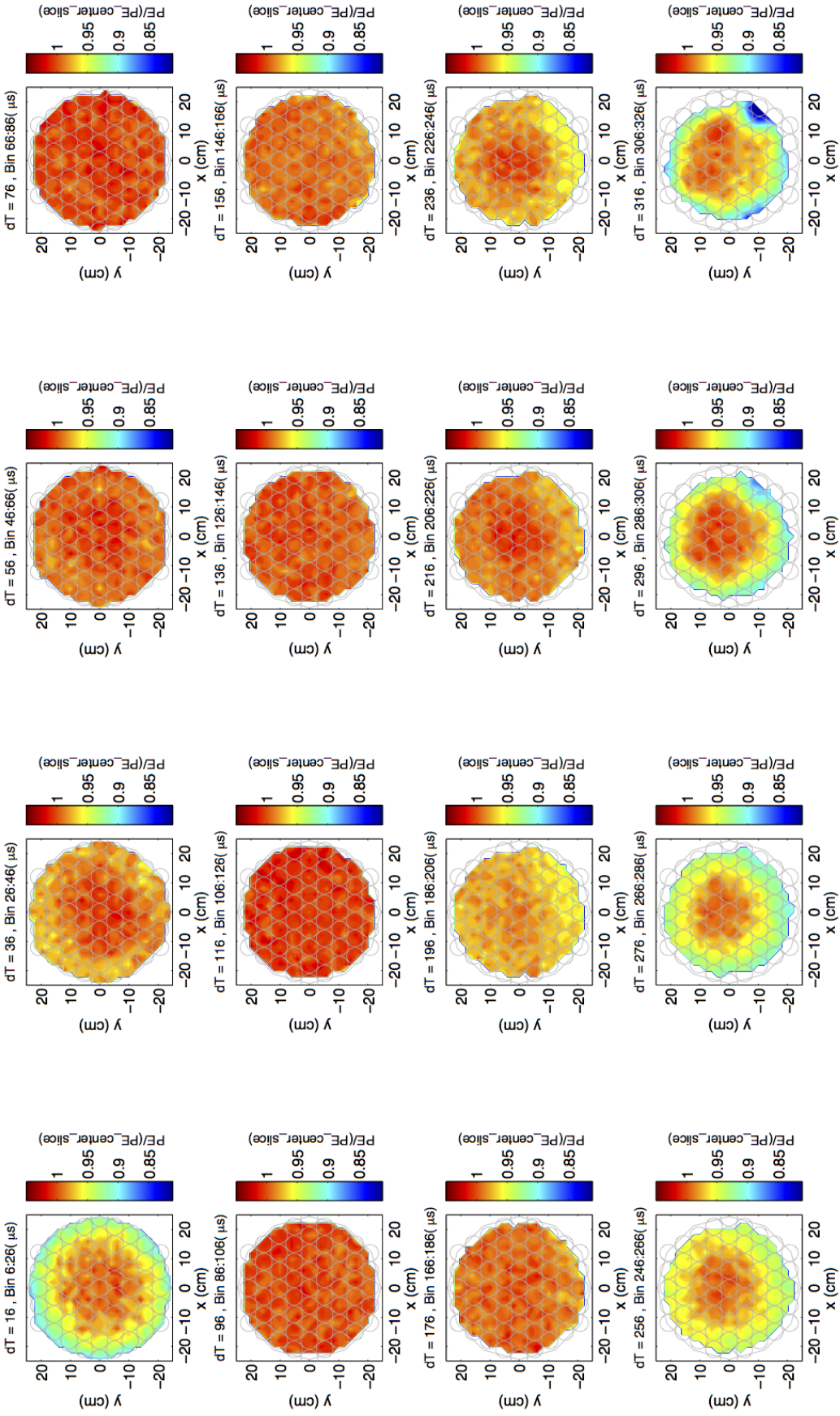


Figure 3.9: S1 x,y,z response normalized to the center of each z slice. There are greater variations near the very top and bottom 4 z slices as the solid angle for light hitting the PMT arrays increases. For the central slices the x,y response is uniform due to increased scattering off the teflon panels.

We define the position dependent (x,y,z) corrected S1 signal as $S1_c$, normalized to the center of the detector ($x=y=0$ and $z=160\mu s$) calculated as follows:

$$S1_c = S1_{(x,z,y)} = S1 \cdot \mathcal{N}\mathcal{F}_{S1}(x, y, z) \quad (3.3)$$

where $S1_c$ is the x,y,z corrected S1 signal and $\mathcal{N}\mathcal{F}_{S1}(x, y, z)$ is the Normalization Factor of the sum of all PMTs for S1s and is a function of x,y,z . The interpolation of the inverse of $\mathcal{N}\mathcal{F}_{S1}(x, y, z)$ along the x,y grid in z slices is plotted in figure 3.10. The normalization factor is applied to the S1 data by using a spline interpolation of the x,y,z coordinate of each event relative to the bin centers $\mathcal{N}\mathcal{F}_{S1}(x, z, y)$. Figure 3.10 shows the S1 response after correcting the data relative to the center of the detector. After applying the x,y,z correction the position dependent variations decrease to less than 1% in the inner radial 18 cm of the detector (the fiducial volume), with as much as 3% variations near the top and bottom edges where the interpolation fails.

Figure 3.11 shows the improvement in the S1 signal after applying the z and x,y,z correction. With z -only correction to S1 there is a fractional improvement in resolution of 31.5%. The combined correction in z and the x,y plane provides an additional 2.0% improvement in resolution over the z only correction.

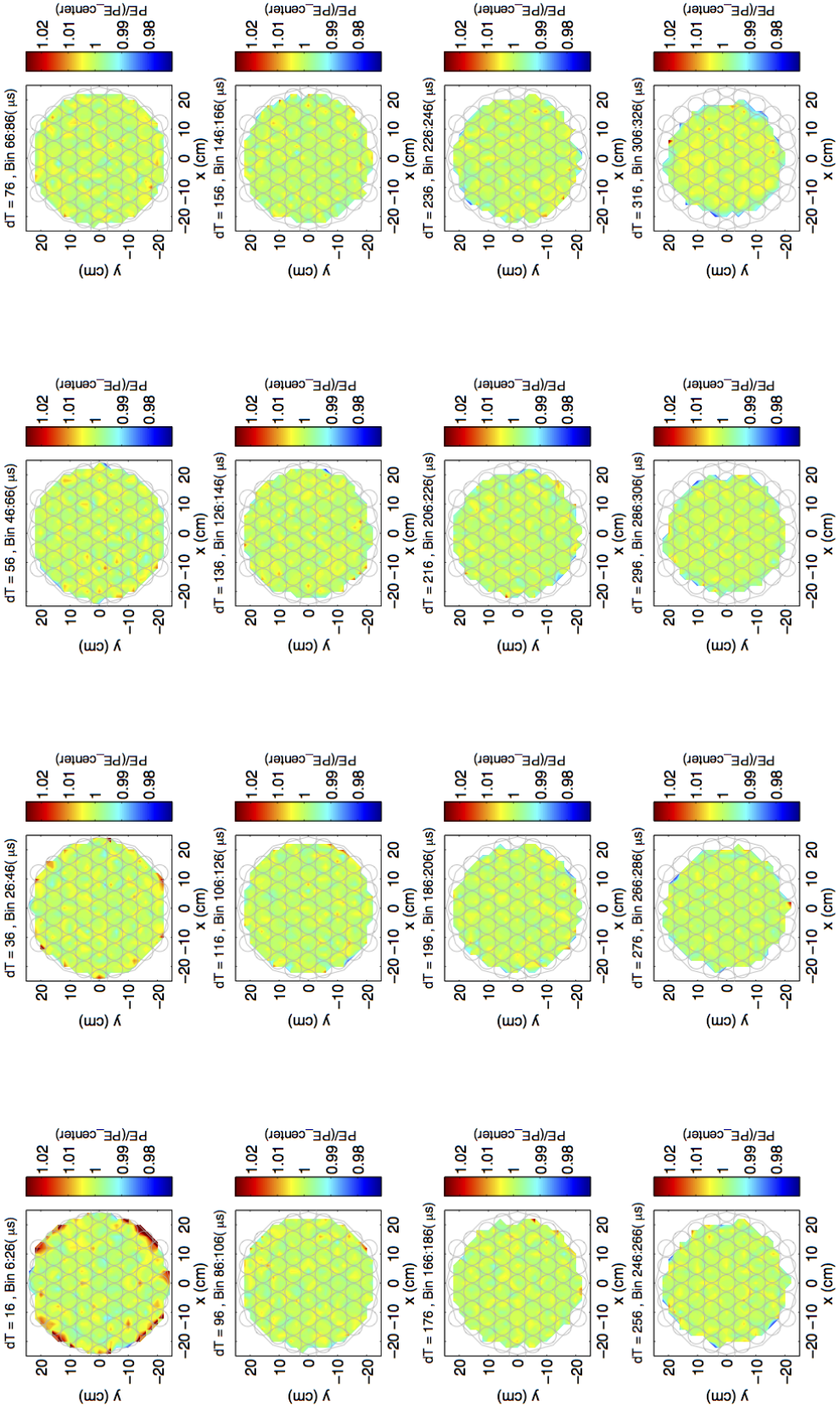


Figure 3.10: S1 x,y,z response normalized to the center of the detector after the data has been corrected and normalized to the detector center. The remaining variations in the fiducial volume ($r < 18\text{cm}$) is less than 1%. Near the top and bottom edges the deviation increases to as much as 3% due to the interpolation of the correction becoming poorly constrained.

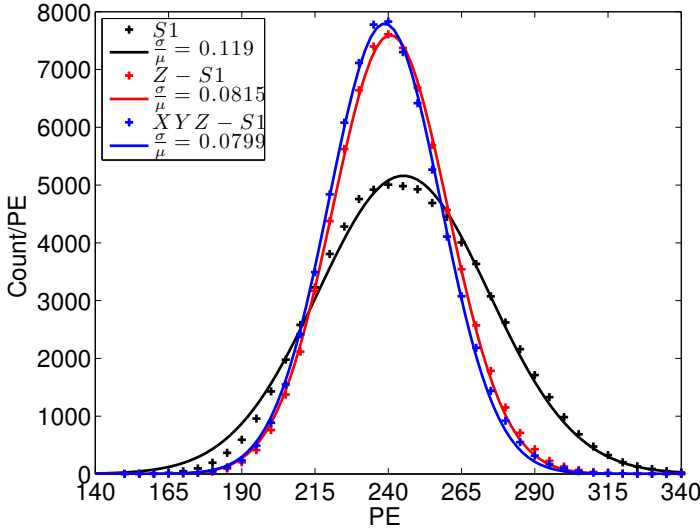


Figure 3.11: Improvement of resolution in S1 after applying the z and x,y,z correction. Black: The uncorrected data. Red: The data with only z dependent correction. Blue: The data with full x,y,z dependent correction. The data shown was taken data on May 10, 2013 (lux10_20130510_T1250) and contains 700,000 $^{83\text{m}}\text{Kr}$ events.

3.5 Application to x,y,z Corrections in Data Processing

As mentioned earlier, the purpose of the periodic $^{83\text{m}}\text{Kr}$ calibrations is to measure the position-dependent S1 and S2 corrections over the course of the 2013 science run. Before processing the WIMP search data the calibration sets were processed and a MYSQL table of electron lifetimes and corrections maps were populated for each calibration date. The electron lifetime applied to each WIMP search data set was a linear interpolation between calibration dates. For the S2 x,y correction the nearest $\mathcal{N}\mathcal{F}_{S2}(x, y)$ entry in time was used. Combined these produced the corrected $S2_c$ quantity to be used for the WIMP analysis. For the S1 x,y,z corrections, the

nearest $\mathcal{N}\mathcal{F}_{S1}(x, y, z)$ entry is used to produce the corrected $S1_c$ quantity via a spline interpolation in x, y, z . For both the $S2-x, y$ and $S1-x, y, z$ correction the time dependence is assumed to be negligible as these are geometric effects, whereas the electron lifetime varies with liquid purity each day. The electron lifetime and the stability of the $S1$ correction over the course of the 2013 science run is shown in figure 3.12 and 3.13. While the electron lifetime needs frequent monitoring, the $S1$ x, y, z response is fixed over several months of running. For the results discussed in the subsequent sections of the thesis we will only work with the x, y, z corrected $S1$ and $S2_b$ pulses ($S1_c$ and $S2_{bc}$ respectively) .

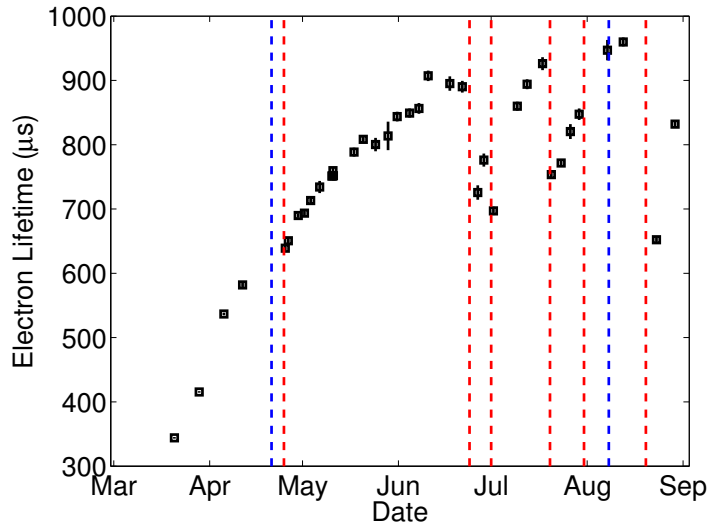


Figure 3.12: Electron lifetime measured using ^{83m}Kr calibrations during the LUX science run in 2013. The blue dashed lines show the boundaries of the WIMP search from April 21 to Aug 8, 2013. The red dashed lines indicate circulation loss events.

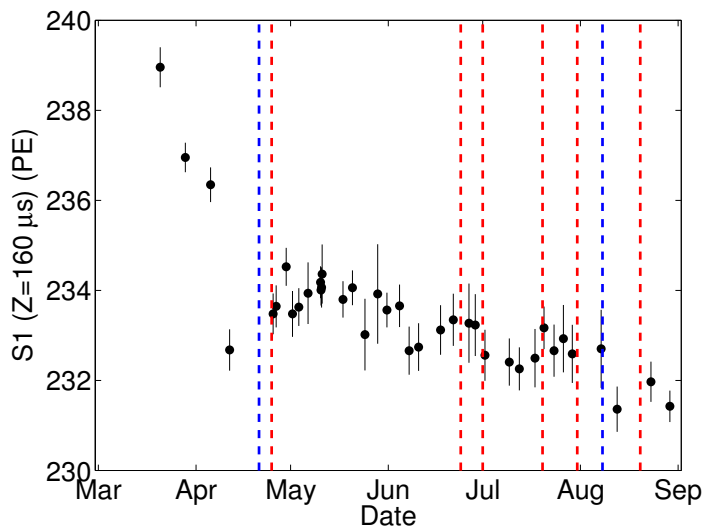


Figure 3.13: Measured response of to light from $^{83\text{m}}\text{Kr}$ calibrations at the center of the LUX detector during of the LUX science run in 2013. The blue dashed lines show the boundaries of the WIMP search from April 21 to Aug 8, 2013. The red dashed lines indicate circulation loss events.

^{83m}Kr Calibration Set	Number of ^{83m}Kr Events
lux10_YYYYMMDDThhmm	
lux10_20130320T1430	136,877
lux10_20130328T1437	444,622
lux10_20130405T1417	187,059
lux10_20130411T1524	99,724
lux10_20130425T1047	104,231
lux10_20130426T1019	92,024
lux10_20130429T1447	133,652
lux10_20130501T1508	91,465
lux10_20130503T1457	108,898
lux10_20130506T1328	45,678
lux10_20130510T1250	670,895
lux10_20130510T1607	499,743
lux10_20130510T2008	113,347
lux10_20130511T0014	44,372
lux10_20130517T1542	138,432
lux10_20130520T1504	216,709
lux10_20130524T1503	28,975
lux10_20130528T1546	11,569
lux10_20130531T1421	125,921
lux10_20130604T1421	110,219
lux10_20130607T1512	106,315
lux10_20130610T1518	116,349
lux10_20130617T1457	61,737
lux10_20130621T1533	78,707
lux10_20130626T1517	25,124
lux10_20130628T1444	44,134
lux10_20130701T1646	71,410
lux10_20130709T1009	106,230
lux10_20130712T1427	104,150
lux10_20130717T1424	66,801
lux10_20130720T1045	88,945
lux10_20130723T1452	88,626
lux10_20130726T1431	35,056
lux10_20130729T1004	59,906
lux10_20130807T1403	27,015
lux10_20130812T1546	113,560
lux10_20130823T0953	107,820
lux10_20130829T1005	479,676

Table 3.1: ^{83m}Kr sets used to calculating corrections for the 2013 LUX WIMP search [38].

Chapter 4: Calibrating the Combined Energy Scale

This section outlines the method used to calibrate the energy scale of the LUX detector for electronic recoils. The idea behind the method is to take calibration data with multiple sources and/or electric fields then combine the measured scintillation signals, primary (S1) and secondary (S2) in order to reconstruct energy. For a given energy deposit in liquid xenon an amount of quanta released is proportional to a work function W , for nuclear recoils we must also consider heat loss. The quanta created at the interaction site are the results of electron-ion pairs and excitons produced by the recoiling xenon nucleus that become photons and electrons, equation 4.1.

$$\begin{aligned} E &= W(n_i + n_{ex}) \\ E &= W(n_\gamma + n_e) \end{aligned} \tag{4.1}$$

where E is the energy of the deposition in keV, n_i , n_{ex} , n_γ and n_e are the number of ions, excitons, photons and electrons respectively. The work function (W) for xenon has been measured to be 13.7 ± 0.2 eV/quanta [8]. Excitons quickly de-excite and contribute to the primary scintillation signal (S1). Ions that recombine with their electron pairs produce scintillation light (S1), while those electrons that do not recombine are collected several μ s later in the extraction region as the larger

secondary scintillation signal S2. The interactions of NR and ER type events were discussed previously in 2.3.

There are two knobs to turn that tune the recombination fraction and probe combined energy space over a variety of S1 and S2, we can either change the energy of the source or adjust the drift field. The larger the spread in S1 and S2 the more constrained the combined energy scale will be. Measuring both light and charge allows for a vastly improved resolution compared with only using a single S1 or S2 only space, since recombination fluctuations cancel out if energy is reconstructed correctly. Using equation 4.1 and assuming that the heat loss is negligible for electronic recoils (ER) we can reconstruct energy by knowing the work function and the conversion from measured S1(light) and S2(charge) signals to the number of quanta ($n_\gamma + n_e$) liberated by the interaction. We define gain-1 (g_1) and gain-2 (g_2) as the conversion from the average number of photons and electrons propagated from the interaction site to the observed signal by the PMT arrays as a photo electron (PE), given in equation 4.2. Note for the value of S2 in this section we only use the signal on the bottom PMT array S_{2b} .

$$\begin{aligned}\langle n_\gamma \rangle &= \frac{\langle S1 \rangle}{g_1} \\ \langle n_e \rangle &= \frac{\langle S2 \rangle}{g_2}\end{aligned}\tag{4.2}$$

By using multiple mono energetic sources with known energies we can extract a best fit for the value of the gains (g_1, g_2) by making a Doke plot [73] [54]. The mono energetic lines used for the purposes of the calibration are listed in table 4.1. For each calibration point we calculate the mean light yield and charge yield and fit a

line, $S1/E$ and $S2/E$ respectively, (Equation 4.3).

$$\begin{aligned} S1/E &= \frac{n_\gamma}{(n_\gamma + n_e)} \times \frac{g1}{W} \\ S2/E &= \frac{n_e}{(n_\gamma + n_e)} \times \frac{g2}{W} \end{aligned} \quad (4.3)$$

Fitting equation 4.3 to a line yields

$$\begin{aligned} \left(\frac{S1}{E}\right) &= \left(\frac{g1}{W}\right) - \left(\frac{S2}{E}\right) \left(\frac{g1}{g2}\right) \\ y &= \frac{S1}{E}, x = \frac{S2}{E} \\ y &= m \cdot x + b \end{aligned} \quad (4.4)$$

The x and y intercepts from Equation 4.4 can be used to solve for $g1$ and $g2$.

$$\begin{aligned} g1 &= b \cdot W \\ g2 &= \frac{g1}{m} = \frac{b \cdot W}{m} \end{aligned} \quad (4.5)$$

The values of $g1, g2$ are degenerate and highly correlated such that the ratio of $g1:g2$ is always a constant, a reduction in $g1$ can be compensated by an increase in $g2$ and still yield the same number of initial quanta and visa versa. Breaking the degeneracy requires data over a wide range of $S1$ and $S2$ values near the intercept of the Doke plot. Due to the strong correlation in the fit parameters the data is fit by minimizing the likelihood and the errors in intercept and slope are determined using MCMC (Markov Chain Monte Carlo).

Source	Energy [keV]	Decay Type
Xe K shell	29.7, 34	X-ray
^{83m}Kr	41.55**	Internal Conversion
^{131}Xe	163.9	Internal Conversion
^{127}Xe	203 or 375	^{127}I daughter γ -emission
	33.8	Kb shell X-ray
	5.3	L shell X-ray
^{129m}Xe	236.1	Internal Conversion
^{214}Bi	609	γ -emission
^{137}Cs	661.6	Photo-absorption

Table 4.1: Mono energetic peaks used for g1 g2 calibration. ** ^{83m}Kr data was taken at 50 and 100 [V/cm] along with the standard field of 170 [V/cm].

4.1 Anti-Correlation Space

The first step in calibrating the energy scale is to plot the observables S1 vs. S2, by doing this the anti correlation between light and charge at a given energy become apparent, figure 4.1. For the data presented here a fiducial cut was placed at a radius of less than 18 [cm] and drift distance between 6 and 46 [cm] which greatly reduces the background event rate. To extract g1 g2 we first determine the average values of S1 and S2 at each known energy. Initially loose diagonal cuts are placed by eye on the populations, figure 4.1. Next, using a un-binned maximum likelihood fit the mean and sigma are estimated and then refit using $\pm 2\sigma$ of the initial distribution to remove tails from backgrounds. With the initial estimate for the mean S1 and S2

response to a given energy the gains g_1, g_2 are determined. The resulting value of g_1 and g_2 is found to be 0.096 ± 0.009 and 5.94 ± 1.68 respectively, the fit is shown in figure 4.2. The values of g_1 and g_2 represent a best fit to the underlying recombination theory where for each additional photon there is a corresponding reduction of one electron and visa versa. The method for extracting the uncertainties using MCMC will be discussed later in section 4.3.

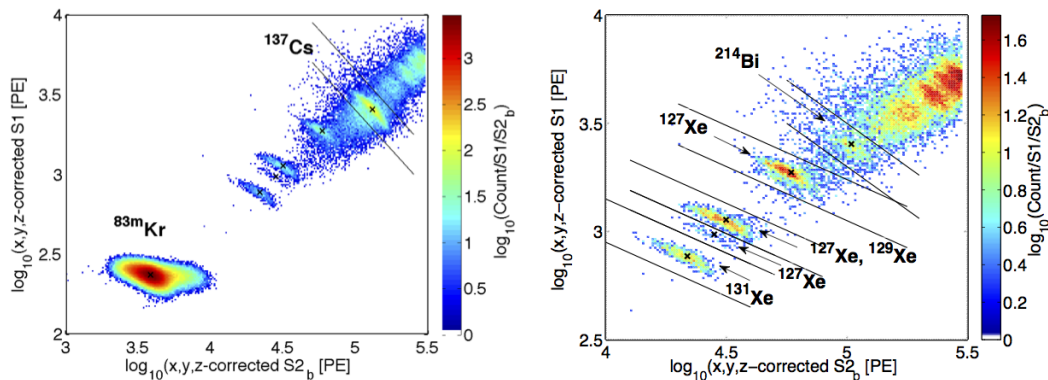


Figure 4.1: LUX data in anti correlation space (S_1 vs. S_2), the black lines indicate the initial cuts by eye used to isolate populations of constant energy. In both figures diagonals represent lines of constant energy with a slope depending on the local recombination probability. The centroids found by an unbind maximum likelihood analysis are shown as a black X, for sources shown in table 4.1.

4.2 Refitting in Combined Energy Space

From the first attempt to find g_1, g_2 in figure 4.2 there are discrepancies between the data and the fit, however this first result is only a crude estimate derived from anti correlation space. Once we have an initial estimate of gains g_1, g_2 a combined energy

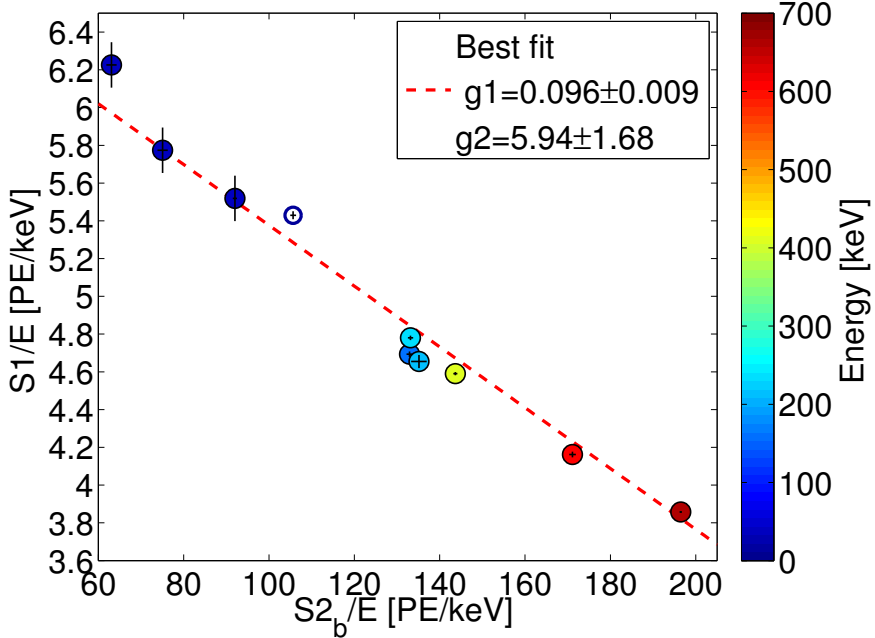


Figure 4.2: Doke plot showing the best fit for the energy calibration parameters g_1 and g_2 using S_1 and S_2 means extracted from anti-correlation space. The first three blue points, from the left, are from ^{83}Kr calibrations at 50, 100 and 170 V/cm respectively. The open circle was from the K-shell xenon X-ray and was not used for the fit as it's absolute energy and origin from the skin of the detector is uncertain.

scale can be constructed with significantly improved resolution over the initial guess, due to the fact that recombination fluctuations are canceled. With the improved resolution the data are fit around the combined energy peaks using an unbinned maximum likelihood fit to a normal distribution, and then the data refitted around 1.5σ of the initial fit. The fits used to extract the means and sigmas of the S_1 and S_2 signals at a given energy are show in figures 4.4 and 4.5. We iterate this technique twice as the convergence is rapid, in this case the initial value of g_1 and g_2 derived from anti-correlation space are already a close approximation to the true value. The

resulting value of g_1 and g_2 is found to be 0.097 ± 0.008 and 5.75 ± 1.4 respectively, the fit is shown in figure 4.3. After refitting there is a significant improvement over figure 4.2, especially the xenon activation lines in the center, which is due to better peak finding in combined energy space over anti-correlation space.

$$g_1 = 0.097 \pm 0.008 \quad (4.6)$$

$$g_2 = 5.75 \pm 1.4$$

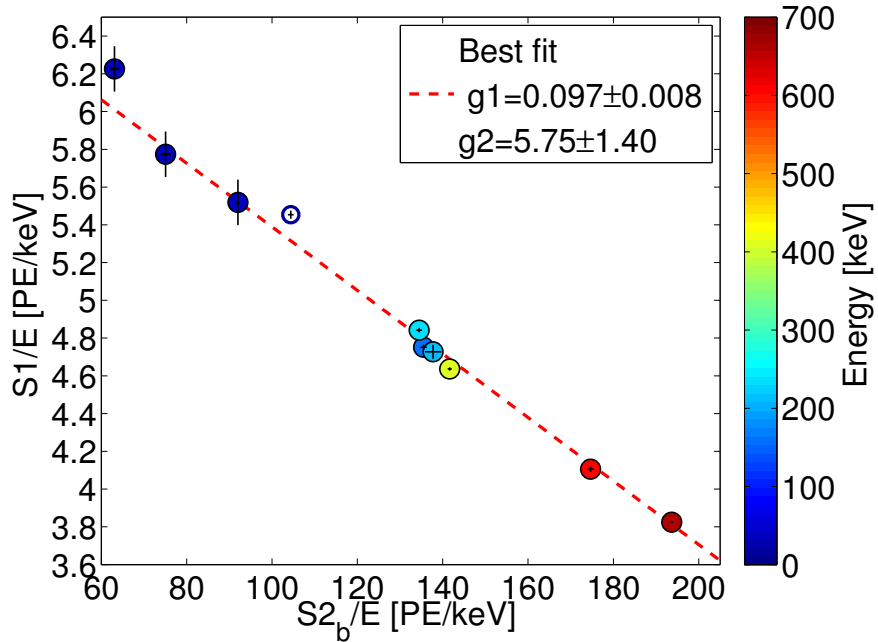


Figure 4.3: Doke plot showing the best fit for the energy calibration parameters g_1 and g_2 using S_1 and S_2 extracted from a combined energy space. The first three blue points, from the left, are from ^{83}Kr calibrations at 50, 100 and 170 V/cm respectively. The open circle was from the K-shell xenon X-ray and was not used for the fit as it's absolute energy and origin from the skin of the detector is uncertain.

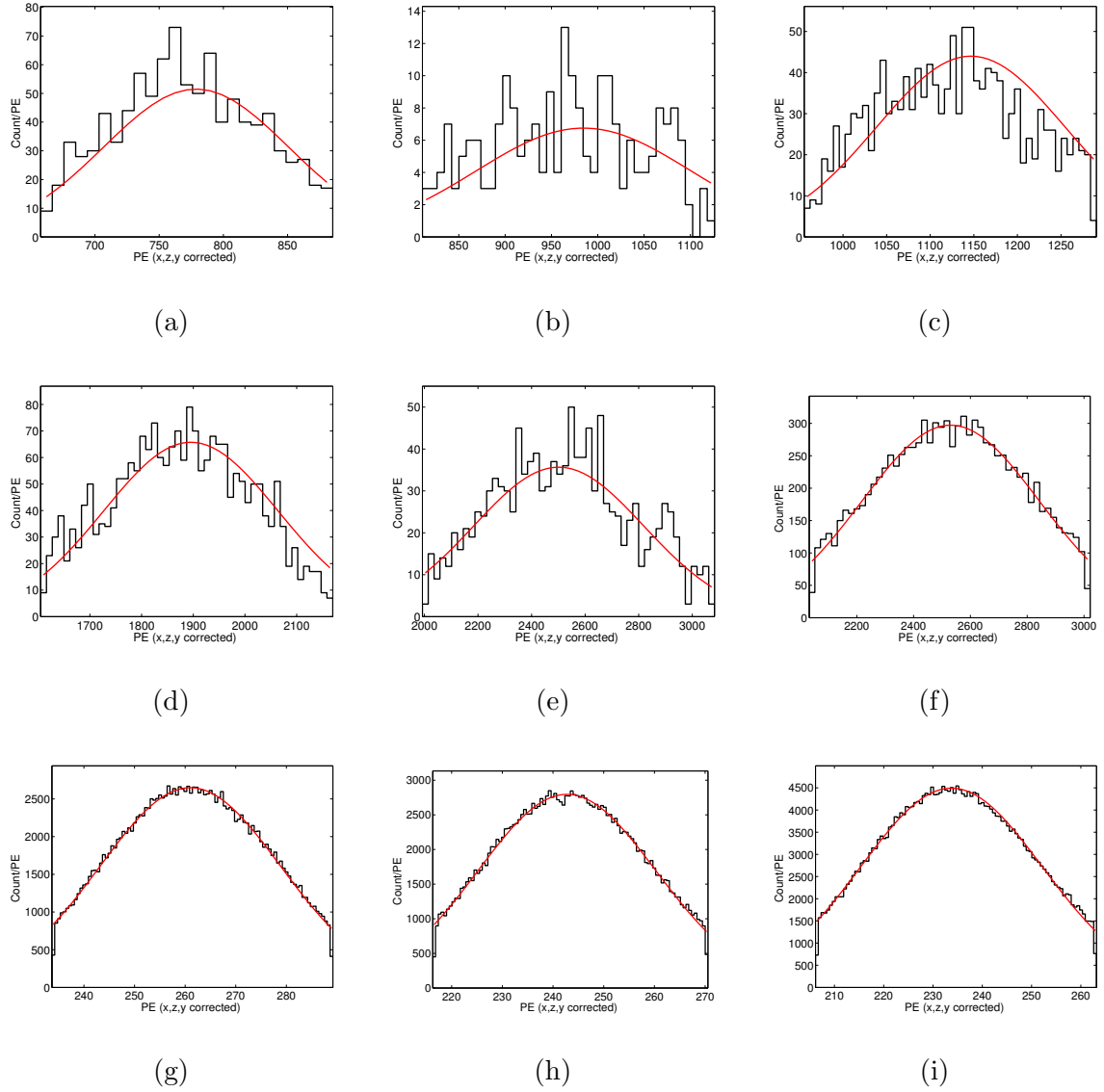


Figure 4.4: S1 fits to sources at nominal field of 170 [V/cm] unless otherwise noted.

Source and energy in keV from top left to bottom right: a) ^{131}Xe : 163, b) ^{127}Xe : 207, c) $^{127}\text{Xe} \& ^{129\text{m}}\text{Xe}$: 236.8, d) ^{127}Xe : 410, e) ^{214}Bi : 609, f) ^{137}Cs : 661.6, g) $^{83\text{m}}\text{Kr}$: 41.5 - at 50 [V/cm], h) $^{83\text{m}}\text{Kr}$ 41.5 - at 100 [V/cm], i) $^{83\text{m}}\text{Kr}$ 41.5 .

Figure 4.6 is the final Doke plot for multiple peaks the theory describes the data well using the optimal fit for g1 and g2, for each increase in number of photons there is a corresponding decrease in the number of electrons and visa versa. The

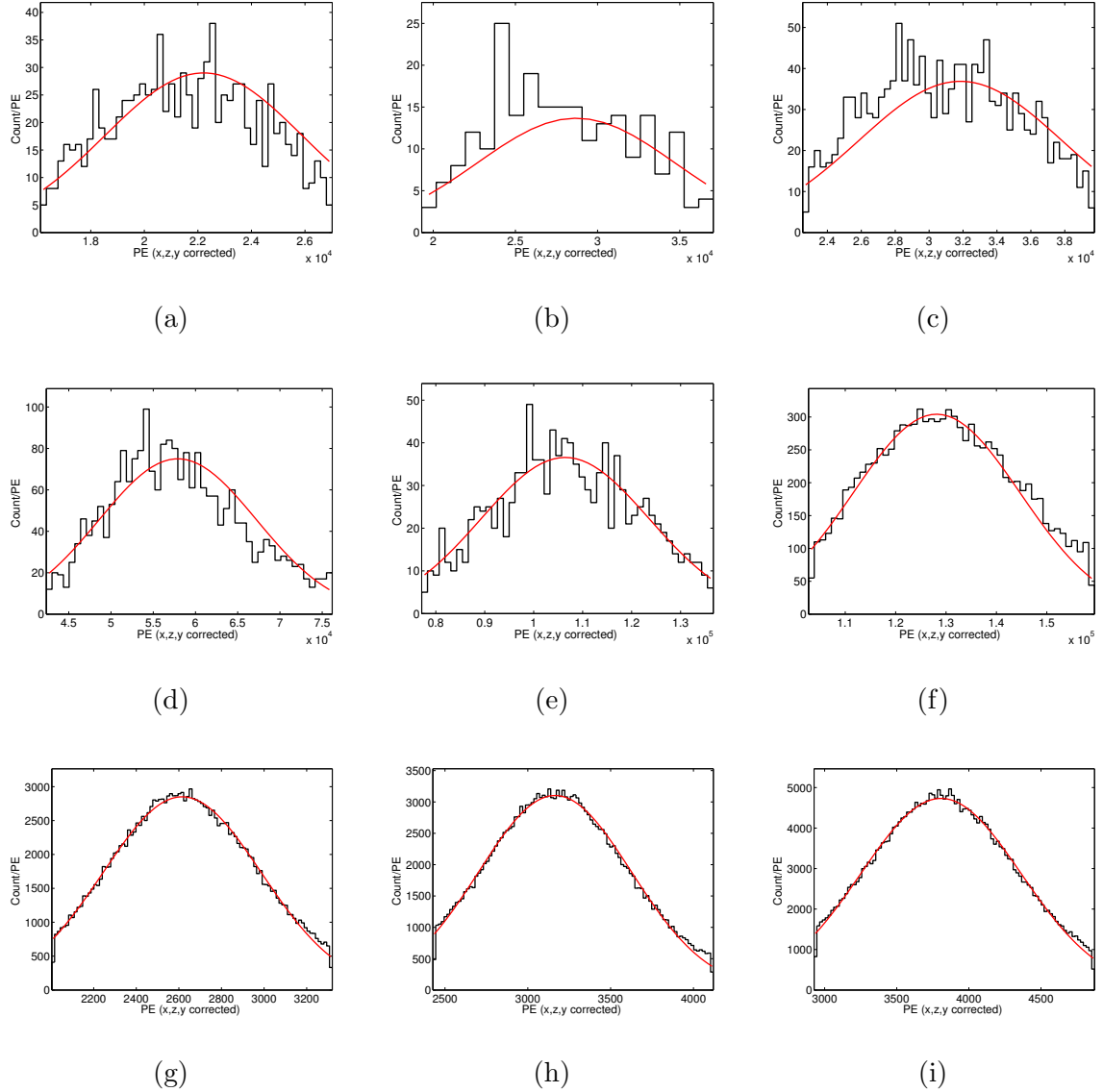


Figure 4.5: S2 fits to sources at nominal field of 170 [V/cm] unless otherwise noted.

Source and energy in keV from top left to bottom right: a) ^{131}Xe : 163, b) ^{127}Xe : 207, c) $^{127}\text{Xe} \& {^{129m}\text{Xe}}$: 236.8, d) ^{127}Xe : 410, e) ^{214}Bi : 609, f) ^{137}Cs : 661.6, g) ^{83m}Kr : 41.5 - at 50 [V/cm], h) ^{83m}Kr 41.5 - at 100 [V/cm], i) ^{83m}Kr 41.5 .

relatively large error on g2 is due to the distance of the data points from the x-intercept. As stated before the values of g1 and g2 can be locally degenerate as long as their ratio remains a constant. Thus for future studies it will be important to

probe more of the parameter space in order to place a tighter constraint on gains g1 and g2.

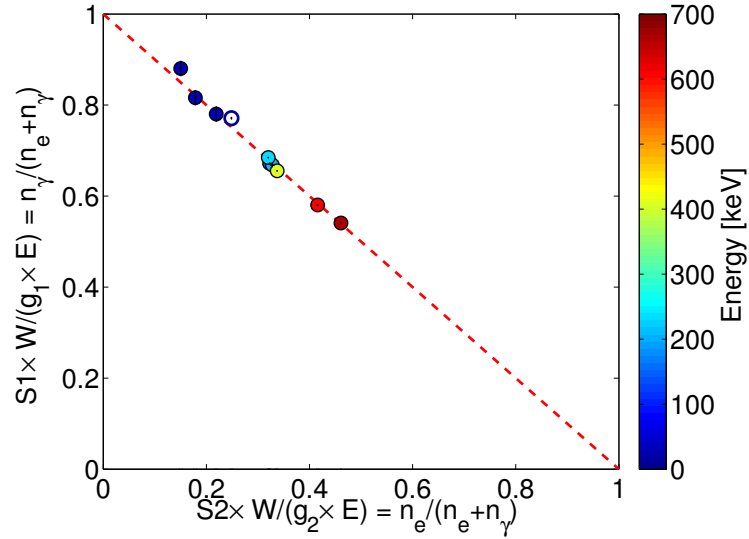


Figure 4.6: Doke plot of the data showing the light yield vs. charge yield. Only solid circles are used for the fit, the open circle is the Xe K shell X-ray from the detector edge.

4.3 Finding Errors with MCMC

The error bars reported in this section on g1 and g2 are from the error in the slope and intercept of the linear fit in the Doke plot derived using MCMC. For calculating the error in slope and intercept three random walkers were used at each data point and allowed to take 500 steps. The MCMC takes into account the covariance of the parameters, shown in figure 4.7 as a two dimensional Gaussian. There is a strong negative correlation between the slope m and intercept b which is the result of the degeneracy between gains g1 and g2 used to reconstruct energy by combining the light and charge signal. Thus, the error on g1 and g2 is such that for the positive maxima deviation in g1 we reach the negative maxima of the error on g2, and visa versa. Using standard reduced χ^2 for fitting and calculating errors in the slope and intercept would be underestimated the true error by a factor of five as it does not account for the degeneracy of the anti-correlated gains.

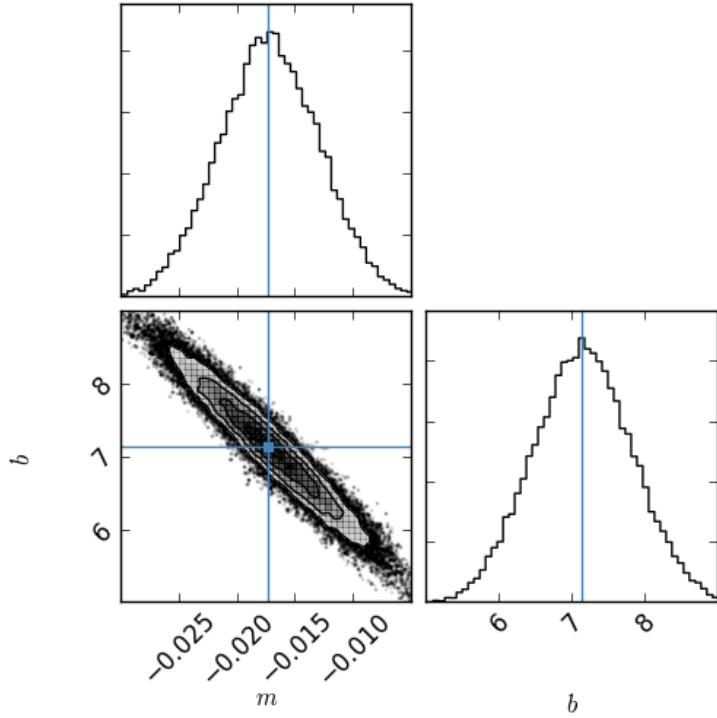


Figure 4.7: MCMC for the linear fit to the Doke plot. There is a strong negative correlation between the slope m and intercept b which results from the degeneracy between gains $g1$ and $g2$.

4.4 Combined Energy Space

With the values of $g1$ and $g2$ known the combined energy of events can be reconstructed with a significant improvement over using only the light or charge channel. In combined energy space recombination fluctuations are removed by the anti correlation of light and charge production and any residual smearing is due to intrinsic detector resolution (discussed later in section :). Figure 4.8 shows the energy histograms of the data used for the fits to gains $g1$ and $g2$ including the xenon activation lines and the ^{137}Cs calibration, along with a zoom in of the xenon K shell Xray at

34 keV. With the energy scale calibrated we can now reconstruct the energy of the events and convert the measured S1 and S2 signals to fundamental quanta using the gains g_1, g_2 allowing us to untangle instrumental and recombination fluctuations and measure light and charge yields.

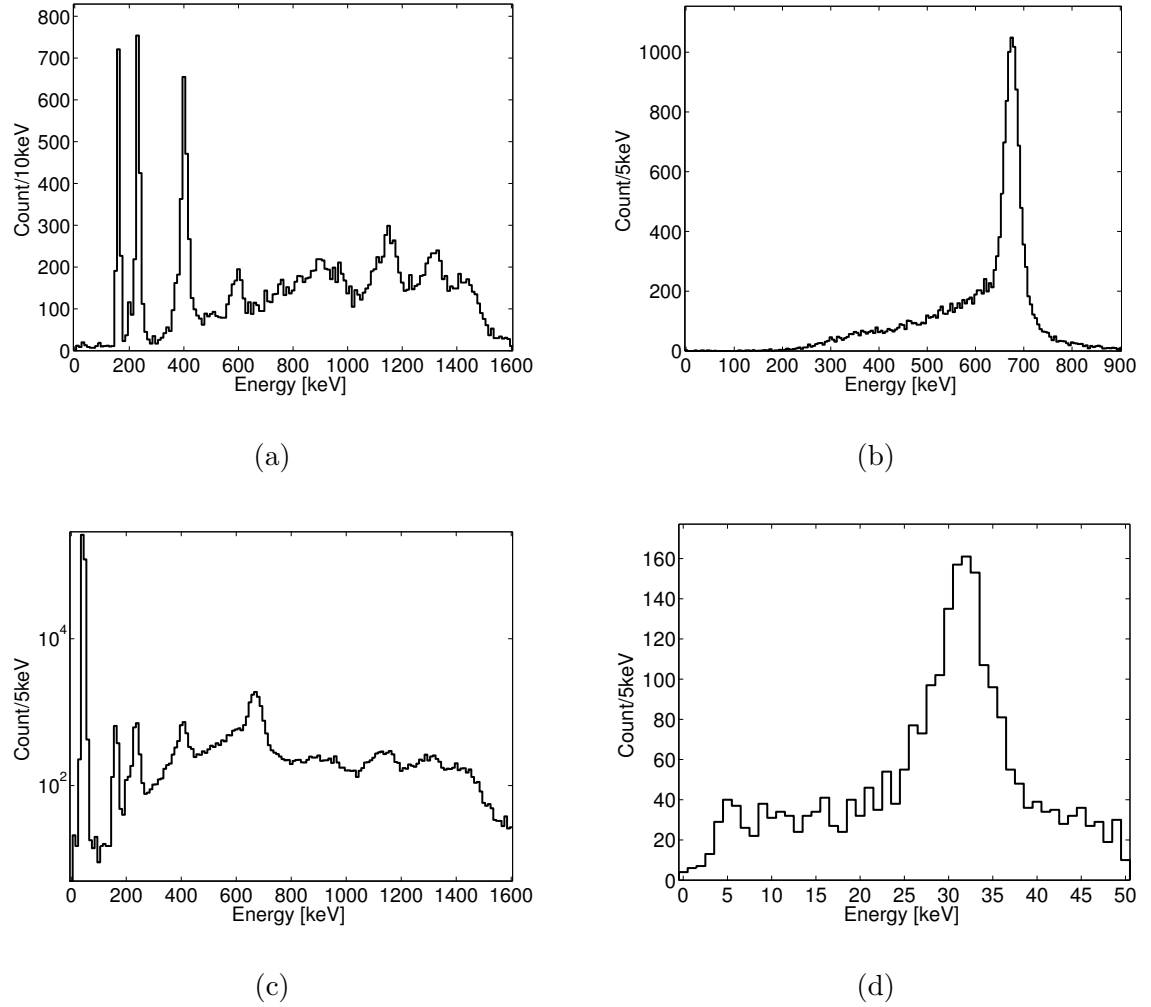


Figure 4.8: Combined energy scale. a) The xenon activation lines from early in the run. b) ^{137}Cs calibration data. c) All calibration data including the $^{83\text{m}}\text{Kr}$ calibration. d) Xenon X-ray.

4.5 Light Collection and Electron extraction

The value of g1 represents the mean efficiency for collecting photons at the center of the LUX detector, the response to S1 light is flat fielded and normalized to the detector center (section Kr calibrations). The measured value of $g1 = 0.097 \pm 0.008$ implies a 9.7% probability of a photon propagated from the center of the detector striking a PMT and being converting into a photo electron (PE) signal. The value of g2 represents the average number of PE collected for each electron that escaped recombination at the initial interaction site and then drifted, by the electric field, towards liquid-gas interface where it is extracted with some probability ϵ . The value of g2 can be thought of as the average single electron size in PE times the extraction probability ϵ .

$$g2 = \epsilon \times SE \quad (4.7)$$

where S2 is the average pulse area of a single electron. The S2 signals are corrected for depth as impurities exponentially attenuate electrons drifting through the xenon, section 3. The LUX detector is low enough in threshold to observe single electrons being extracted from the liquid. Comparing the value of g2 derived from the Doke method with the single electron size is a good sanity check on the energy scale calibration. As the electrons are extracted from the liquid they are accelerated by larger field between the gate and anode where they electro-luminesce, a single extracted electron creates tens to hundreds of photons which are collected by both PMT arrays. We can cut on the single electron population (small S2 pulses without an associated S1) and measure the single electron size along with the extraction

efficiency efficiency. The extraction efficiency is defined as the probability that an electron will be extracted from the liquid into the gas in a region, held at 3.5 kV in the liquid between the anode and the gate. For a given event the extraction of electrons is a binomial processes with a rate approaching unity for fields above 5 kV [59] [48]. Figure 4.9, shows the single electron size as measured by the bottom PMT array (used for S2 pulses in the LUX detector to avoid saturation). The population is modeled by a skew Gaussian due to the Poisson nature of measuring only a handful of photo electrons (PE) per extracted electron. The mean of the distribution is found to be 9.7 PE/e^- with a width of $\sigma_{\text{SE}} = 3.6 \text{ Phe/e}^-$. Thus, the extraction efficiency is g^2 over the single electron size and is found to be $(59.3 \pm 14)\%$, given the extraction field the value is in good agreement with previous measurements in other xenon detectors [59] [48].

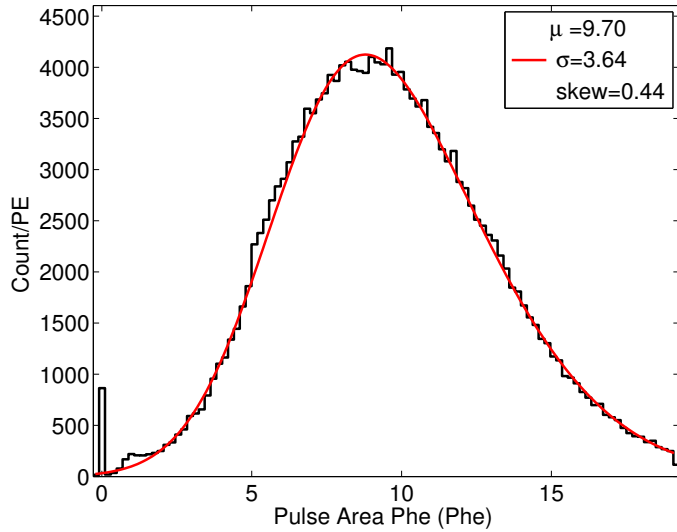


Figure 4.9: Single electron distribution as seen by the bottom PMT array fitted with a skew Gaussian model to account for the underlying Poisson statistics of observing between 9 and 10 photo electrons (PE) for each electron leaving the liquid and entering to the gas phase at a higher field causing electro-luminescence. The μ of the fit represents the true mean of the skew Gaussian distribution.

4.6 Tritium Beta Spectrum

The energy calibration in the WIMP search region can be tested by using the tritium calibration source described in Chapter]. Tritium has a Q value of 18.6 keV [74], a mean beta energy of 5.6 keV [75] and a mode of 3.4 keV [14] making it ideal for calibrating the LUX detector at the lowest energies. The tritium beta spectrum produces events at energies well below the detector threshold. Therefore, by comparing the reconstructed energy to the true tritium beta spectrum we can extract the energy threshold. We account for the detector resolution, smearing, by applying

the empirically determined resolution measured in Chapter []. Smearing the spectrum with the empirically determined detector resolution is in good agreement with that expected from the simulation package of LUXSIM.

Figure 6.4 (a,b) shows the reconstructed energy from a tritium calibration at the default field setting of 170 V/cm. The calibration contains 140,000 tritium events with an expected 2 ± 1 background events in black. In red, a simulated tritium beta spectrum from the LUXSIM package with modeled detector resolution and having gone through data processing framework. In blue and green are the theoretical tritium beta spectrum with infinite detector resolution and with the added resolution of the LUX detector, respectively. Figure 6.4 (c,d) shows the same calibration but at a lower drift field setting of 100 V/cm with only 4,500 tritium events and an expected $1\pm$ background events.

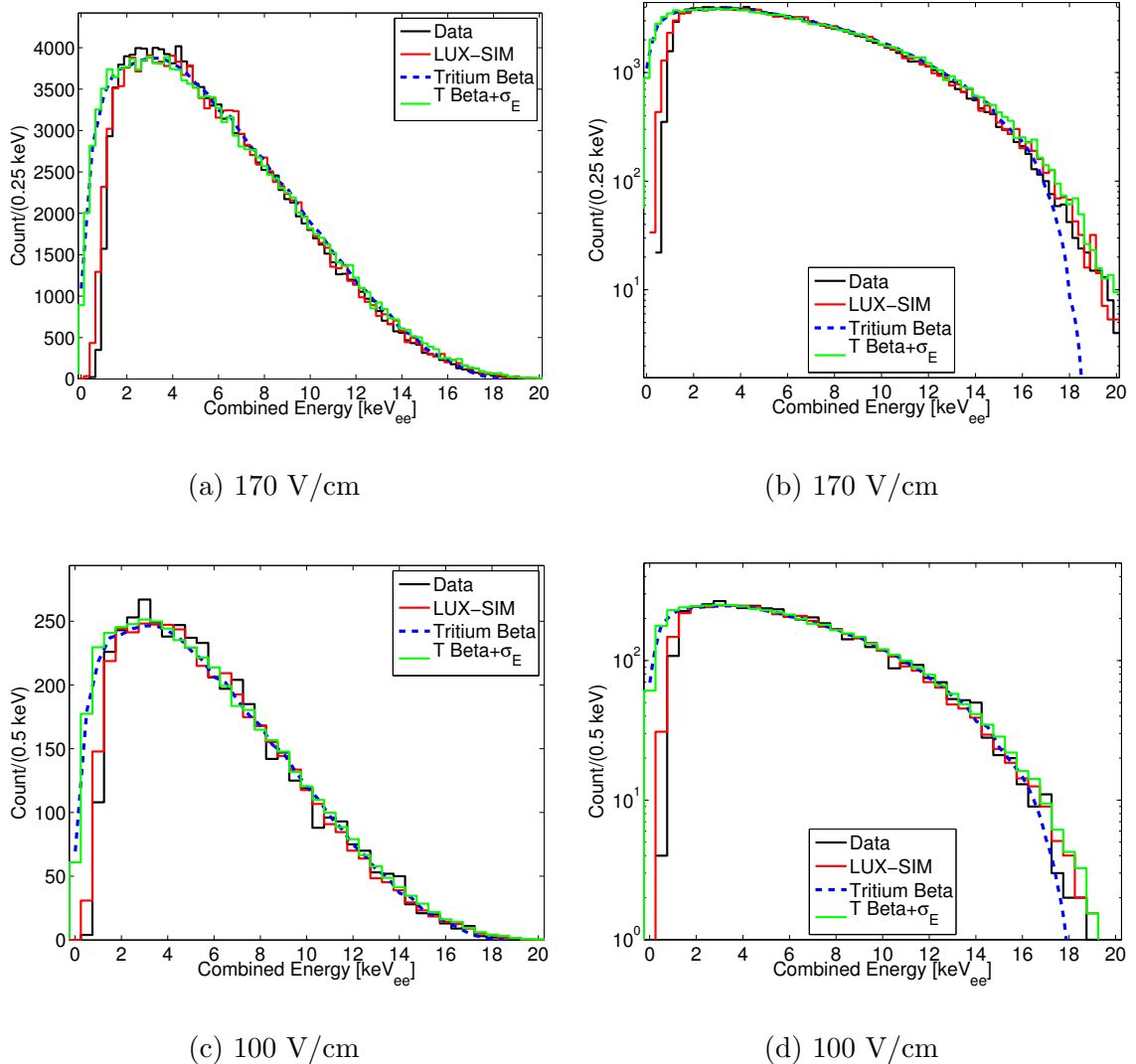


Figure 4.10: The tritium energy spectrum reconstructed from the data (black).

Along with LUX SIM (blue), and the true tritium beta spectrum (blue) and a tritium spectrum smeared with detector resolution (green).

The reconstructed energy spectrum is in good agreement with the expected tritium beta spectrum with detector resolution, using both LUXSIM and the empirically determined resolution. The detector threshold reaches 100% at about 1.5 keV making the tritium beta peak clearly visible providing crucial cross check of

the reconstructed energy around the WIMP search region of interest (1-5 keV). The 18.6 keV endpoint is another good low energy calibration point. We find that the end point of the reconstructed energy spectrum is consistent with that expected when convolving the true tritium beta spectrum with detector resolution, visible in log space. Though the energy scale for ER events was events was calibrated using mono energetic sources well above the tritium Q value the reconstructed tritium beta spectrum lines up with the expectation all the way down to the 1.5 keV threshold.

Figure 4.11 and 4.12 show the S1,S2 and Energy threshold attained by comparing the data to the expected photon, electron and energy spectrum, at 170 and 100 V/cm. The energy threshold is set by the light collection of the much smaller S1 signal. For the energy threshold we find roughly 50% efficiency at 1 keV_{ee} approaching 100% at 1.5 keV_{ee} regardless of the applied field. The S1 threshold is 50% at 2 PE and surpassed 90% above 3 PE. This translates to an S2_b threshold for golden events of 50% at 300 PE approaching 100% a 400 PE. Extracting the threshold will be discussed in further detail in Section

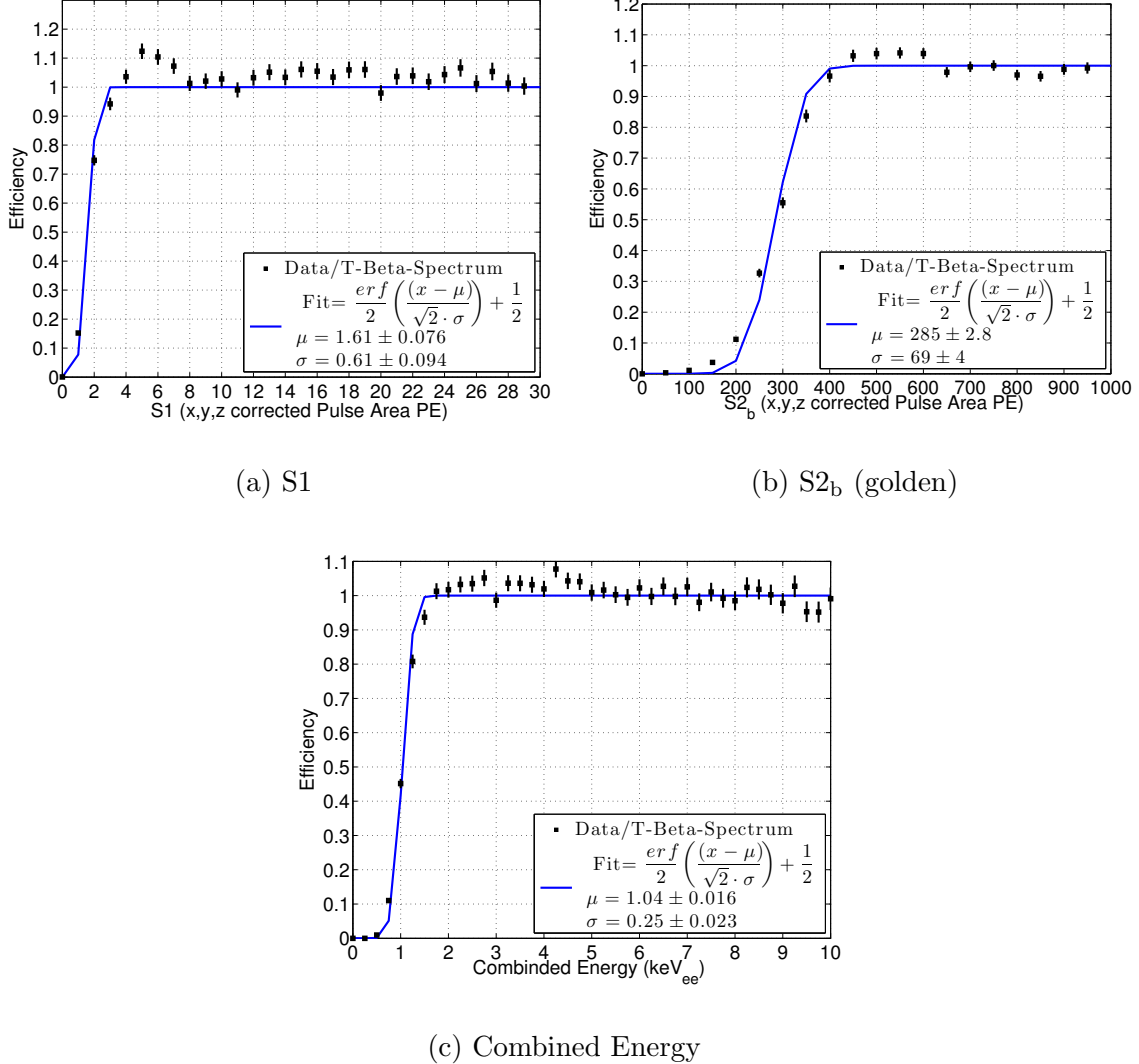


Figure 4.11: Threshold calculated from difference of simulated Tritium S1, S2 and energy spectra at 170 V/cm. a) S1 b) S2_b, c) Combined Energy .

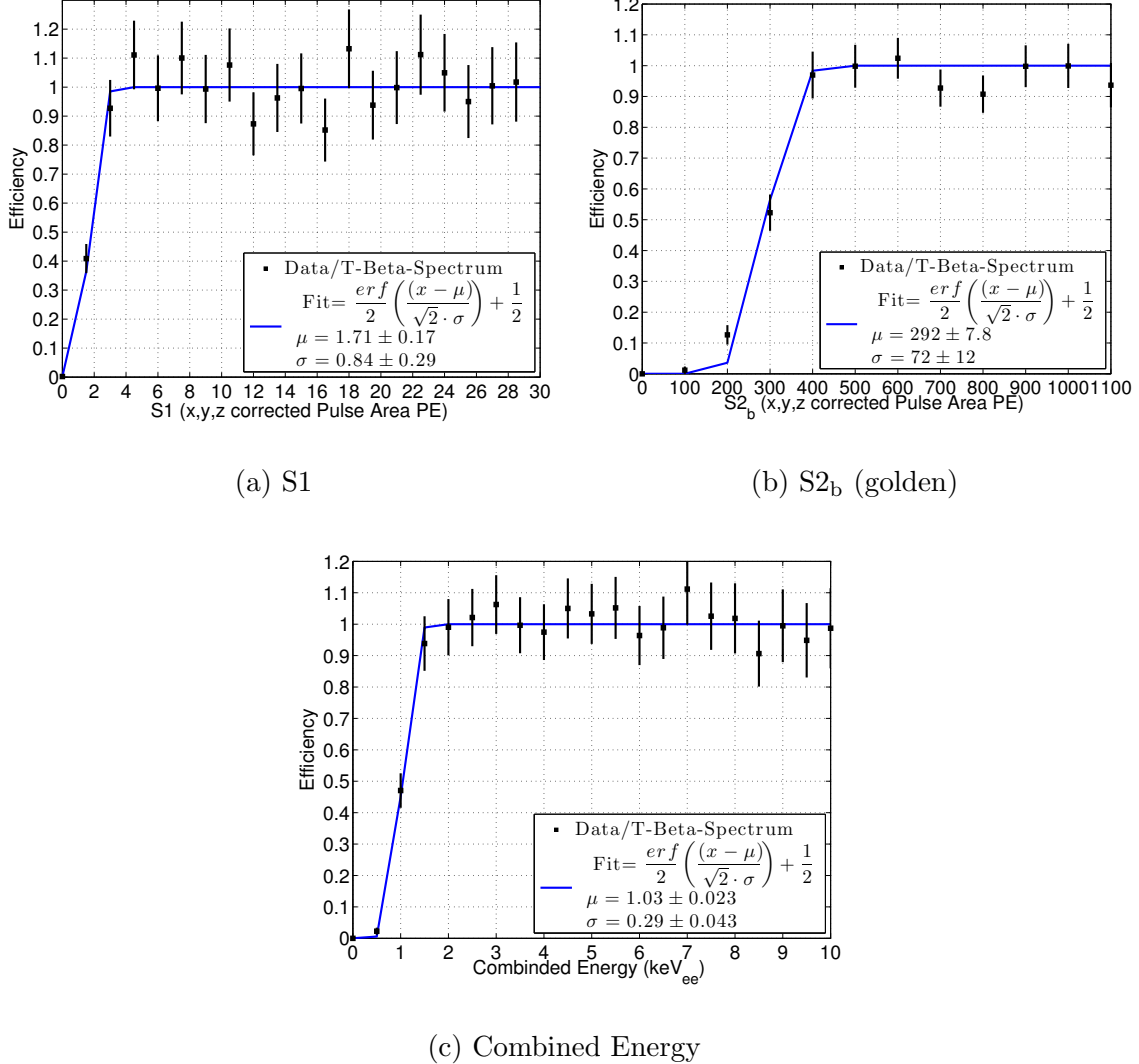


Figure 4.12: Threshold calculated from difference of simulated Tritium S1, S2 and energy spectra at 100 V/cm. a) S1 b) S2_b, c) Combined Energy .

Chapter 5: Event Level Fluctuations

In this chapter we discuss extracting recombination fluctuation down to 1 keV using the tritium calibration data. We begin by modeling the intrinsic resolution of the LUX detector, based on counting statistics. We then separate observed fluctuations in light and charge collection from recombination fluctuations using line source calibrations. Once the variances from light and charge collection are modeled the recombination fluctuations from continuous spectra can be extracted, specifically the tritium beta spectrum. We also discuss a method to correct for spectral shape of tritium and finite resolution of the LUX detector. We conclude with the results for recombination and recombination fluctuations as measured from tritium beta decay in the LUX detector along with a measure of the exciton to ion ratio alpha for ER events.

5.1 Modeling Intrinsic Detector Resolution

Intrinsic statistical fluctuations in light and charge (S1 and S2) collection in the LUX detector lead to a spread in collected quanta. To measure effects from recombination fluctuations and the Fano factor we must first decouple the detector component of resolution. We use the model described in [8] in which the measured scintillation

and ionization signals S1, S2 (measured in PE) are related to the number of photons and electrons by gains g1 and g2, equation 5.1. Specifically, the average number of photons and electrons produced for a given energy deposit are proportional to the average S1 and S2 signals at a given drift field. The gain g1 represents photon detection efficiency, the probability of a photon from an energy deposit striking a PMT convolved with the quantum efficiency of the PMTs. Gain g2 represents the average S2 signal of a single electron normalized by the average single electron size. Where S2 uses only the bottom PMT array and is corrected for lifetime.

$$\begin{aligned}\langle n_\gamma \rangle &= \frac{\langle S1 \rangle}{g_1} \\ \langle n_e \rangle &= \frac{\langle S2 \rangle}{g_2}\end{aligned}\tag{5.1}$$

The statistical fluctuations for the measured number of quanta in equation 5.1 are from the statistical processes that comprise the measured S1 and S2 signal.

$$\begin{aligned}\sigma_{n_{\gamma_{\text{stat}}}}^2 &= \frac{\sigma_{S1_{\text{stat}}}^2}{g_1^2} \\ \sigma_{n_{e_{\text{stat}}}}^2 &= \frac{\sigma_{S2_{\text{stat}}}^2}{g_2^2}\end{aligned}\tag{5.2}$$

The variance in the number of photons in equation 5.2 can be broken into two parts. First, a binomial variance due to counting a fraction, g1, of the initial photons produced. $\text{Var}_{n_\gamma} = \frac{(1-g1) \times g1 \times n_\gamma}{g1^2}$. Second, the variance in the response of the PMTs to a single photon. $\text{Var}_{n_\gamma} = \frac{g1 \times n_\gamma \times \sigma_{\text{PE}}^2}{g1^2}$. Combining the two leads to the result in equation 5.3.

$$\sigma_{n_{\gamma_{\text{stat}}}}^2 = \frac{1 - g_1 + \sigma_{\text{PE}}^2}{g_1} n_{\gamma} \quad (5.3)$$

The variance in the number of electrons in equation 5.2 is comprised of the following statistical uncertainties. First, a binomial variance due to the extraction efficiency of electrons from the liquid-gas interface. $\text{Var}_{n_e} = \frac{(1-\text{ext}) \times \text{Ext} \times n_e \times (\text{single}_E)}{g_2^2}$, Ext is the electron extraction probability and single_E is the single electron size in PE. Second, the variance in the response of the PMTs to a single electron. $\text{Var}_{n_e} = \frac{\text{Ext} \times n_e \times \sigma_{\text{SE}}^2}{g_2^2}$. Finally, the additional variance from electron attenuation is modeled as a Poisson probability of electron capture in each Z slice of the detector. The variance from each Z slice depends of the average number of electrons that will be attenuated. The probability of attenuation at each slice in drift time T is $P(T) = 1 - e^{-T/\tau}$, where τ for the data sets to be considered is 1000 μs . The drift region considered in the fiducial volume is from 38 to 304.5 μs . The average variance from events in the fiducial can be given by equation 5.4.

$$\sigma_{n_{e_{\text{att}}}}^2 = n_e \frac{\int_{T_{\min}}^{T_{\max}} (1 - e^{-T/\tau}) dT}{\int_{T_{\min}}^{T_{\max}} dT} = 0.155 \times n_e \quad (5.4)$$

Combining the variances leads to the the result for the statistical variance in the observed number of electrons equation 5.5.

$$\sigma_{n_{e_{\text{stat}}}}^2 = \frac{\text{Ext} \times \sigma_{\text{SE}}^2 + (1 - \text{Ext}) \times g_2^2}{g_2^2} n_e + \sigma_{n_{e_{\text{att}}}}^2 \quad (5.5)$$

For this analysis we use the following detector gains: 5.6.

$$g_1 = 0.097 \pm 0.008 \text{ [Phe/n}_\gamma\text{]}$$

$$g_2 = SE_b \times Ext = 5.75 \pm 1.4 \text{ [Phe/n}_e\text{]}$$

$$SE_b = 9.70 \pm 0.05 \text{ [Phe/n}_e\text{]}$$

$$\sigma SE_b = 3.64 \text{ [Phe/n}_e\text{]}$$

$$Ext = 0.593 \pm 0.144$$

$$\sigma_{PE} = 0.51 \text{ [Phe/n}_\gamma\text{]}$$

(5.6)

Combining equations 5.3-5.6 we find the intrinsic detector resolution for the average S1 and S2 signals in the LUX detector, equation 5.7. Note, the intrinsic resolution in S2 is subdominant to that of S1, since on average one electron multiplies to about ten photons detected by the bottom PMT array [ref]. Also listed in 5.8, are the instrumental fluctuations with a linear dependance on quanta measured with a global fit to mono energetic sources [next section]. The total variance in the light and charge channels is the linear combination of the statistical and instrumental variance.

$$\begin{aligned} \sigma_{n_{\gamma_{\text{stat}}}} &= 3.46\sqrt{n_\gamma} \\ \sigma_{n_{e_{\text{stat}}}} &= 0.68\sqrt{n_e} \end{aligned} \tag{5.7}$$

$$\begin{aligned}\sigma_{n_{\gamma_{\text{inst}}}} &= \frac{6.4 \pm 1.7}{100} \times n_{\gamma} \\ \sigma_{n_{e_{\text{inst}}}} &= \frac{6.6 \pm 0.9}{100} \times n_e\end{aligned}\quad (5.8)$$

$$\begin{aligned}\sigma_{n_{\gamma_{\text{Det}}}}^2 &= \sigma_{n_{\gamma_{\text{stat}}}}^2 + \sigma_{n_{\gamma_{\text{inst}}}}^2 \\ \sigma_{n_{e_{\text{Det}}}}^2 &= \sigma_{n_{e_{\text{stat}}}}^2 + \sigma_{n_{e_{\text{inst}}}}^2\end{aligned}\quad (5.9)$$

5.2 Measuring Recombination Fluctuations with Mono-Energetic Sources

To model recombination we start with the assumption that for a given energy deposit in liquid xenon the number of quanta produced is equal to the number of excitons and the number of ions. The number of ions cerated contains a spread given by a Fano factor F . The value of F for liquid xenon is small, has a theoretical value of 0.05 [61].

$$\begin{aligned}\frac{E}{W} &= n_q = n_i + n_{ex} \\ \frac{E}{W} &= n_{\gamma} + n_e\end{aligned}\quad (5.10)$$

Where E is energy in [keV], W is the work function in [keV/quanta], n_q is the number of quanta, n_i is the number of ions and n_{ex} is the number of excitons. The theoretical value of the number of excitons produced to ions is $\frac{n_{ex}}{n_i} = \alpha = 0.20$ [73] and is not expected to change vs. energy [53] [54] [8]. For the subsequent equations in this section we will simplify equations 5.10 to that in 5.11.

$$\alpha = 0.20$$

$$n_i = \frac{E}{W} \frac{1}{(1 + \alpha)} = \frac{n_\gamma + n_e}{(1 + \alpha)} \quad (5.11)$$

$$\sigma_{n_i}^2 = F \times n_i$$

Equation 5.11 gives us a simple model for the number of ions and excitons produced for a given interaction, the only spread in quanta thus far is due to a Fano factor governing the spread in initial quanta produced. We now convert ions and excitons to scintillation and ionization signals that are measured in the LUX detector, S1 and S2 respectively. The number of photons observed for a given energy deposit arise from the excitons that de-excite and from ions which recombine with freed electrons. The number of electrons corresponding to a given energy deposit will be equal to the number of ions that did not recombine with a freed electron.

$$n_\gamma = n_{ex} + n_i \times r = n_i \times (r + \alpha)$$

$$n_e = n_i \times (1 - r) \quad (5.12)$$

$$r = \frac{\frac{n_\gamma}{n_e} - \alpha}{\frac{n_\gamma}{n_e} + 1}$$

Where r represents the electron-ion recombination probability. A key measurable quantity is the size of recombination probability fluctuation σ_r . Since we measure n_γ and n_e as S1 and S2 signals and not ions and excitons, an additional variance arises from the ion-electron recombination fluctuations. These recombination fluctuations are dependent on the dE/dx of each individual electron produced making them much larger than the spread from the Fano factor. We now combine

the uncertainties from the Fano factor, recombination and the statistical uncertainty from detector resolution (σ_{Det}) and solve for the observed quantities given in 5.13:

$$\begin{aligned}\sigma_{n_\gamma}^2 &= \sigma_{n_{\text{ex}}}^2 + \sigma_{n_i}^2 r^2 + \sigma_r^2 n_i^2 + \sigma_{n_{\gamma_{\text{Det}}}}^2 = \sigma_{n_{\text{ex}}}^2 + n_i F(r^2) + \sigma_r^2 n_i^2 + \sigma_{n_{\gamma_{\text{Det}}}}^2 \\ \sigma_{n_e}^2 &= \sigma_{n_i}^2 (1 - r)^2 + \sigma_r^2 n_i^2 + \sigma_{n_{e_{\text{Det}}}}^2 = n_i F(1 - r)^2 + \sigma_r^2 n_i^2 + \sigma_{n_{e_{\text{Det}}}}^2\end{aligned}\quad (5.13)$$

For convenience we will work with $n_i = (n_\gamma + n_e)/(1 + \alpha)$, this convention is chosen because both the Fano factor and recombination fluctuations act on number of ions and also because the number of ions are linearly related to the initial energy deposit. Using a mono energetic source and combined energy(equation 5.10) we can measure $\sigma_{n_\gamma}^2$ and σ_e^2 and σ_E^2 . Dropping the contribution form the Fano factor and the the number of excitons it can be shown that the value recombination fluctuations σR can be determined by rearranging equation 5.13, keeping in ming that σE contains no recombination fluctuations. Where σR is in units of quanta, $\sigma_R = n_i \sigma_r$.

$$\sigma_R^2 = \frac{1}{2} \left(\sigma_{n_\gamma}^2 + \sigma_{n_e}^2 - \frac{\sigma_E^2}{W^2} \right) \quad (5.14)$$

Where the spread in observed quanta $\sigma_{n_\gamma}^2$ and $\sigma_{n_e}^2$ result from a linear combination of the variance from detector resolution and recombination fluctuations.

$$\begin{aligned}\sigma_{n_\gamma}^2 &= \sigma_{n_{\gamma_{\text{Det}}}}^2 + \sigma R^2 \\ \sigma_{n_e}^2 &= \sigma_{n_{e_{\text{Det}}}}^2 + \sigma R^2\end{aligned}\quad (5.15)$$

We do not directly observe the fluctuation in number of photons and electrons, instead we measure the fluctuations in the corresponding S1 and S2. The fluctuation

in the S1 and S2 signal when divided by the gains g1 g2 represent on average the fluctuation in photons or electrons due to detector resolutions (statistical and instrumental variance) combined with recombination fluctuations. 5.15.

$$\begin{aligned}\sigma_{n_{\gamma\text{Det}}}^2 &= \frac{\sigma_{S1}^2}{g_1^2} - \sigma R^2 \\ \sigma_{n_e\text{Det}}^2 &= \frac{\sigma_{S2}^2}{g_2^2} - \sigma R^2\end{aligned}\quad (5.16)$$

Combining equations 5.14 and 5.16 leads to the results in equation 5.17, which is a formula to directly measure recombination fluctuations using a mono energetic source.

$$\sigma_R^2 = \frac{1}{2} \left(\frac{\sigma_{S1}^2}{g_1^2} + \frac{\sigma_{S2}^2}{g_2^2} - \frac{\sigma_E^2}{W^2} \right) \quad (5.17)$$

Equations 5.17 and 5.16 gives us a method to measure recombination fluctuations along with fluctuations in n_γ and n_e due to intrinsic detector resolution, (will be discussed in the next section). It is important to note that $\sigma_{n_\gamma}^2$, $\sigma_{n_e}^2$ and σ_E^2 are observable quantities when using a mono energetic source. The variance in combined energy does not contain variance from recombination fluctuations as those fluctuation occur along lines of constant energy. Note, we have dropped the contribution from the Fano factor and the spread is excitons as they are much smaller than recombination fluctuations or the variances from measuring light and charge intrinsic to the detector. The observed variance in the light and charge channels (S1, S2) is the result of two compounded random processes. After the initial charge deposit the number of charge and light quanta undergo recombination fluctuations.

Subsequently, as the light or charge is collected in the detector an additional variance from detector resolution occurs. The result is the sum of two random processes thus the variance are added.

Using equation 5.17 and 5.16 along with the measurements of g1 g2, we construct a combined energy and deconvolve the recombination fluctuations from variances in the light and charge channel of the detector. The result is shown in figure 5.1, the black white and red lines represent σ_R , $\sigma_{n_{\gamma_{\text{Det}}}}$, $\sigma_{n_{e_{\text{Det}}}}$, respectively for sources listed in Table 4.1. A variance with a linear and root term is fit to the data and used to extract instrumental fluctuations and constrain the statistical fluctuations. The linear term corresponds to instrumental fluctuations and the root term corresponds to statistical fluctuations. Instrumental fluctuations go like the signal size and may potentially be due to ripples in the liquid surface caused by xenon bubbles or other systematics that are unaccounted for. The root term should result purely from counting photo electrons, described earlier. We find:

$$\begin{aligned}\sigma_{n_{\gamma_{\text{Det}}}}^2 &= \sigma_{n_{\gamma_{\text{Stat}}}}^2 + \sigma_{n_{\gamma_{\text{Inst}}}}^2 = (0 \pm 10 \cdot \sqrt{n_\gamma})^2 + ((6.4 \pm 1.8)/100 \cdot n_\gamma)^2 \\ \sigma_{n_{e_{\text{Det}}}}^2 &= \sigma_{n_{e_{\text{Stat}}}}^2 + \sigma_{n_{e_{\text{Inst}}}}^2 = (1 \pm 4 \cdot \sqrt{n_e})^2 + ((6.6 \pm 0.6)/100 \cdot n_e)^2 \\ \sigma_R^2 &= ((5.5 \pm 0.5)/100 \cdot n_q)^2\end{aligned}\quad (5.18)$$

5.3 Measuring Recombination Fluctuations in Desecrate Energy Bins

The pervious subsection demonstrated the power of using a mono energetic source measure recombination fluctuations, equation 5.14. In this section we present a

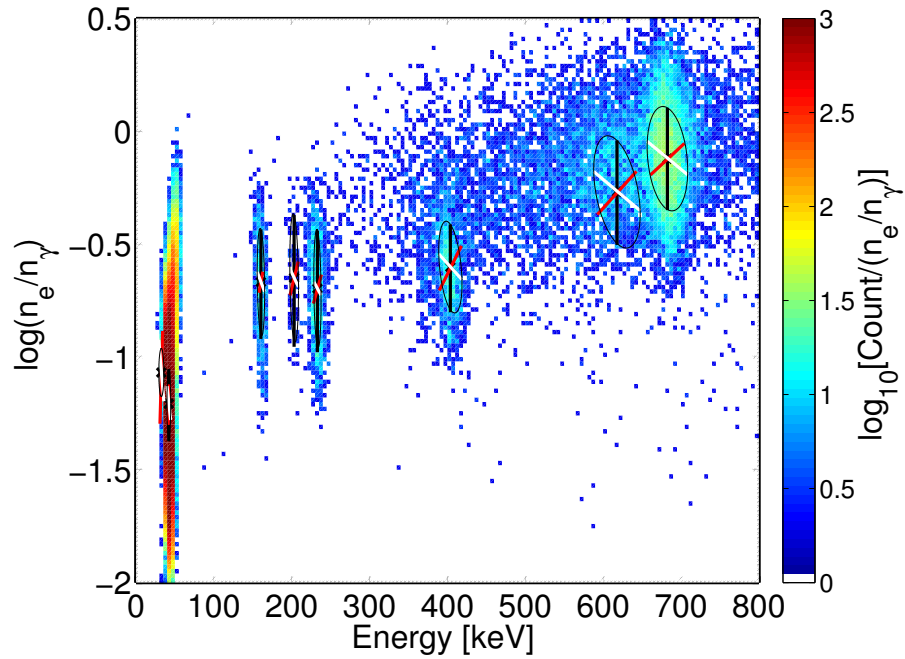


Figure 5.1: Populations of calibration sources in discrimination space $\log\left(\frac{n_e}{n_\gamma}\right)$ vs. combined energy [keV_{ee}]. The ovals represent the combination of σR , $\sigma n_{\gamma\text{Det}}$, $\sigma n_{e\text{Det}}$ in black, white, red respectively.

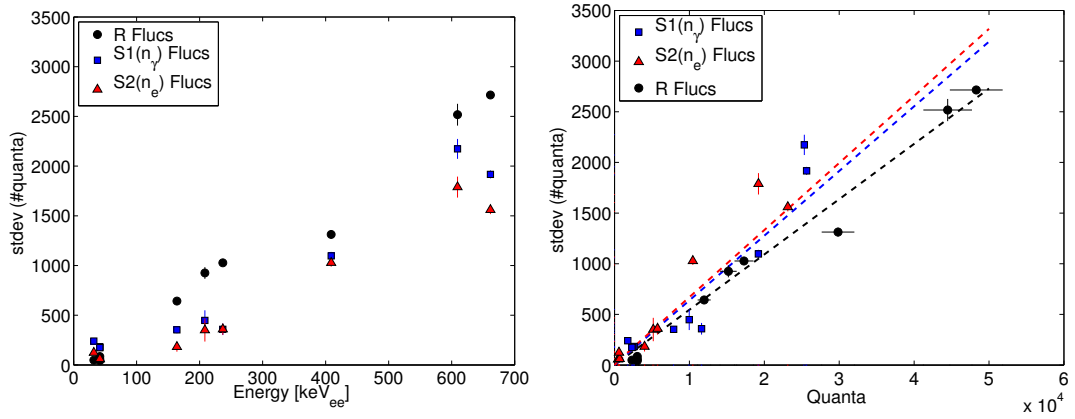


Figure 5.2: Measured values of σR , $\sigma n_{\gamma\text{Det}}$, $\sigma n_{e\text{Det}}$ vs. Energy on the left and vs. Quanta on the right. Measured using sources listed in Table 4.1.

method to decouple statistical variance from recombination fluctuations when confined to an energy bin of width Δ_E . The consideration of descrete binning is crucial when dealing with a continual energy spectrum. Take the tritium beta spectrum as an example, we lose the ability to independently measure $\sigma_{n_\gamma}^2$, $\sigma_{n_e}^2$, σ_E^2 and are only left with a smear of n_γ , n_e , E . However, there are two key pieces of information still left at our disposal. First, the combined energy can be reconstructed from global fits to g_1 and g_2 , and even corrected for spectral shape and detector resolution (discussed later in section [link]). Second, we can calculate values of statistical variance for the light and charge channels as a function of energy, described in 5.7, 5.8. It will be shown in this section that having a priori knowledge of g_1 and g_2 and the functional for of the statistical variance from detector resolution will be sufficient to measure recombination fluctuations for a continual energy spectrum binned in energy with width Δ_E .

We begin the treatment of binning with the the case of having a finite bin width around the central combined energy of a mono energetic source. First, we quantify the change in the statistical components of equation 5.13 when slicing out a bin in combined energy space. The slice in combined energy is illustrated for a toy model at quanta corresponding to that of the combined 41.6 keV ^{83}Kr decay in Figure 5.3. All contribution from recombination fluctuations are included when slicing out a section of combined energy, illustrated in Figure 5.3. However, the slice contains only a reduced statistical component from both the light and charge signals, and in the limit that ΔE goes to zero the statistical component of light and charge converge to a value defined as χ_{stat} (where χ is the measured σ in a bin of

combined energy). To solve for the value of χ_{stat} we first calculate the slope induced by statistical variance in the number of photons vs. quanta and the complementary slope of electrons vs. quanta, defined as M and $1-M$ respectively. The value of M depends on the magnitude of the statistical variances and is given in equation 5.19. The sum of the two slopes must equal one as the sum of photons and electors make up combined energy.

$$M = \tan(\theta_{n_{\gamma\text{Det}}}) = \frac{\sigma_{n_{\gamma\text{Det}}}^2}{\sigma_{n_{\gamma\text{Det}}}^2 + \sigma_{n_{e\text{Det}}}^2} \quad (5.19)$$

$$1 - M = \tan(\theta_{n_{e\text{Det}}}) = \frac{\sigma_{n_{e\text{Det}}}^2}{\sigma_{n_{\gamma\text{Det}}}^2 + \sigma_{n_{e\text{Det}}}^2}$$

With the slope between combined energy and $\sigma_{n_{\gamma\text{Det}}}$ and between energy and $\sigma_{n_{e\text{Det}}}$ defined in equation 5.19 the value of the shared statistical uncertainty in combined energy space can be determined. We first treat the case of $\Delta E = 0$ in equation 5.20 which is also valid when the centroid of light yield and change yield has been subtracted (discussed later).

$$\chi_{\text{Det}}^2 = M^2 \sigma_{n_{e\text{Det}}}^2 + (1 - M)^2 \sigma_{n_{\gamma\text{Det}}}^2 \quad (5.20)$$

The variable χ is used to represent the observed σ when dealing in bins of combined energy. Let's briefly consider the implication of equation 5.20. For the case of $\sigma_{n_{e\text{Det}}}^2 = \sigma_{n_{\gamma\text{Det}}}^2$, $M=0.5$, resulting in $\sigma_{n_{e\text{Det}}}^2 = \sigma_{n_{\gamma\text{Det}}}^2 = \chi_{\text{Det}}^2$. This case can be thought of as sweeping out equal variance from the statistical population which would for a circle as illustrated in Figure 5.3. For the case of $\sigma_{n_{e\text{Det}}}^2 \neq \sigma_{n_{\gamma\text{Det}}}^2$ the observed statistical variance in a slice of combined energy will become less than the

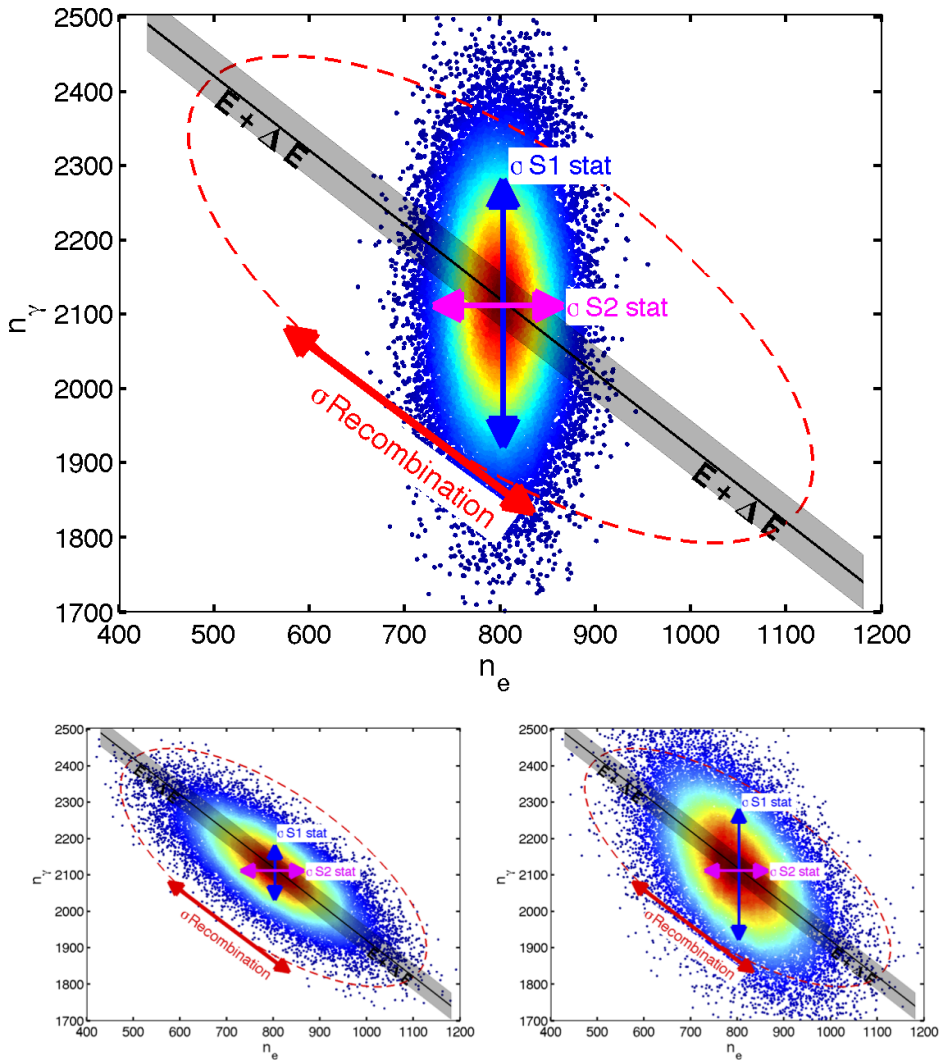


Figure 5.3: Top: Illustration of statistical variance, recombination fluctuations are set to 0. The spread in number of photons moves vertically and the spread in number of electrons moves horizontally. In black, a line of constant energy along the mean of combined energy with a width ΔE . Bottom left: Dominated by recombination fluctuations which move 45° to statistical variances. Bottom Right: Typical values for recombination and S1, S2 Stat for Kr^{83} .

variance of the best channel. Specifically for the LUX detector the implication of equation 5.20 is that the statistical variance measured in a slice of combined energy will collapse to less than that of the S2 statistical uncertainty, as bin width Δ_E goes to zero.

To complete the treatment of binned energy in this section we now add the final piece to the observed statistical variance, the contribution from the bin width Δ_E . The residual variance arises from rotating the population of 2D gaussian about the bin center, the rotation having a slope of M or (1-M) as given in equation 5.19. Note, the residual term from the slope can also be removed by centroid subtraction of the photons and electrons vs. energy as discussed later in section 5.3.4, in that case we are only left with χ^2_{Det} shared between the two channels.

$$\begin{aligned}\chi^2_{n_{\gamma_{\text{Det}}}} &= \chi^2_{\text{Det}} + \frac{(MW\Delta_E)^2}{12} \\ \chi^2_{n_{e_{\text{Det}}}} &= \chi^2_{\text{Det}} + \frac{((1-M)W\Delta_E)^2}{12}\end{aligned}\quad (5.21)$$

Were χ^2 is defined in 5.20, M is given in equation 5.19, W is the work function in [quanta/keV], Δ_E is a bin of energy [keV], the normalization of 12 arrises from the second moment of a rotated line about its center. The total observed variance, χ^2 , in the number of photons and electrons considering a bin of combined energy can now be determined transforming equation 5.13 to 5.22.

$$\begin{aligned}\chi_{n_\gamma}^2 &= \sigma_{n_{ex}}^2 + n_i F(r)^2 + \sigma_r^2 n_i^2 + \chi_{n_{\gamma_{Det}}}^2 \\ \chi_{n_e}^2 &= n_i F(1-r)^2 + \sigma_r^2 n_i^2 + \chi_{n_{e_{Det}}}^2\end{aligned}\quad (5.22)$$

In equation 5.22 we have defined the observed standard deviation in units of quanta χ for n_γ, n_e when working with bins of combined energy. In the limit that $F, \sigma_{n_{ex}}^2$ and Δ_E go to zero the observed variance in number of photons and electrons (χ_{n_γ} and χ_{n_e}) are related to the size of recombination fluctuations in a given combined energy bin, equation 5.23. Where σ_R is in units of quanta, $\sigma_R = n_i \sigma_r$.

$$\begin{aligned}\sigma_{R_\gamma}^2 &= \chi_{n_\gamma}^2 - \chi_{n_{\gamma_{Det}}}^2 \\ \sigma_{R_e}^2 &= \chi_{n_e}^2 - \chi_{n_{e_{Det}}}^2\end{aligned}\quad (5.23)$$

We have arrived at the conclusion of this section, armed with equation 5.23 we now have two methods for determining the size of recombination fluctuations, σ_R^2 where the subscript γ or e is used to represent the channel of quanta used for the calculation. Either the observed variance in the light and charge channel can be used to measure the size of recombination fluctuation in a bin of energy. Any asymmetry between the two methods has implications which are discussed in the following subsection.

5.3.1 Measuring the Fano Factor in Bins of Energy

There are three terms in equation 5.22 that give rise to an asymmetry between the observed variance $\sigma_{R_\gamma}^2$ and $\sigma_{R_e}^2$. The small difference in variance from the slope

can be solved for exactly leaving just the Fano factor F and $\sigma_{n_{ex}}^2$. By taking the difference of variance in the two channels component of recombination variance drops out leaving only the Fano factor and the variance in number of excitons, given in equation 5.22.

$$\sigma_{R_\gamma}^2 - \sigma_{R_e}^2 = \sigma_{n_{ex}}^2 + n_i F(2r - 1) \quad (5.24)$$

F is the Fano factor, equation 5.11, $\sigma_{n_{ex}}^2$ is the variance of the number of excitons produced and r is the recombination fraction, equation 5.12. Consider the case such that variance in the number of excitons $\sigma_{n_{ex}}^2$ is much less than the contribution from the Fano factor. In such a regime we can solve for the Fano factor, potentially energy dependent, from equations 5.24.

$$F(E) = \frac{\sigma_{R_\gamma}^2 - \sigma_{R_e}^2}{n_i(2r - 1)} \begin{cases} r \neq \frac{1}{2} \end{cases} \quad (5.25)$$

There is an underlying subtlety to equation 5.25. Remarkably, in the limit that Δ_E goes to zero the Fano factor can be extracted with minimal knowledge of intrinsic detector statistical variance. Further, when the statistical variance of S1 and S2 are identical the value of M (equation ??) will be 0.5. In that special case no knowledge of the statistical variance is needed to measure the Fano factor.

When $r = \frac{1}{2}$ the coefficient in front of the Fano factor becomes zero in equation 5.24. At this value an equal contribution from the Fano factor goes into the variance χ^2 of photons and electrons, allowing for the smaller value of σ_{ex}^2 to be extracted.

$$\sigma_{n_{ex}}^2 = \sigma_{R_\gamma}^2 - \sigma_{R_e}^2 \left\{ r = \frac{1}{2} || \sigma_{n_{ex}}^2 >> n_i F(2r - 1) \right. \quad (5.26)$$

Equation 5.26 is also valid in the case that $\sigma_{n_{ex}}^2$ is much larger than the contribution from the Fano factor. This happens to be true when dealing with the time dependent light yield of ^{83m}Kr , this topic will be explored in the next section.

5.3.2 Application to ^{83}Kr

Using the high stats Kr83 calibration data we can validate the method for working in a bin of energy since the exact solution for recombination and detector fluctuations can be measured, as outlined in section 5.2 and 5.3. Once the fluctuations from detector resolution are measured in the light and charge channel (S1 and S2 signals), the asymmetry between the two channels can be used to calculate the Fano factor (equation 5.22). The asymmetry in fluctuations in the light and charge channel arises from the Fano factor acting on ion production which is later amplified through the recombination fraction, as long as the recombination fraction does not equal 0.5. For the case of the ^{83m}Kr calibration the recombination fraction was 0.772 resulting in recombination fluctuations of 3 to 4 more quanta in the light channel as compared to the charge channel, see table 5.3. Though the additional recombination fluctuation is small having ample statistics the Fano factor can be constrained. The errors in the measurement were derived from simulated Kr data sets of 400,000 events with the Fano factor turned off, using 100 trials. First, recombination fluctuations were turned off and only fluctuations from detector resolution as calculated in section 5.2

were used, see Table 5.1. It was found that the error of the difference in recombination fluctuation from the light and charge channel ($\sigma_{R_\gamma}^2$ and $\sigma_{R_e}^2$) along with the error in ion production and recombination fraction were enough to constrain the Fano factor to 0.001-0.003. Next, the value of recombination was set slightly higher than the actual value of 82 to 100 quanta and the trials were repeated, see table 5.2. With the addition of recombination fluctuations to detector resolution fluctuations the error on measuring the Fano factor grew to 0.002-0.009, with smaller bin sizes (ΔE around the center leading to the smallest error as seen from equation 5.21.

ΔE [keV]	Count	$\sigma(\sigma_{R_\gamma}^2)$	$\sigma(\sigma_{R_e}^2)$	$\sigma(\sigma_{R_\gamma}^2 - \sigma_{R_e}^2)$	σF
0.025	1528	77.8	77.9	1.3	0.0008
0.05	3063	54.4	54.6	1.8	0.0012
0.1	6128	36.4	36.6	2.6	0.0016
0.2	12242	23.7	23.8	3.7	0.0023
0.25	15290	22.9	22.9	4.0	0.0026
0.5	30528	17.5	17.5	5.2	0.0033

Table 5.1: Values for the standard deviation of the observed value of σ_R^2 from n_γ and n_e along with the standard deviation of the difference, for a simulated ^{83m}Kr decay with recombination set to zero. Note, since the two methods for determining σ_R^2 are correlated the standard deviation of the measured difference is small leading to an improved error when calculating the Fano factor or $\sigma_{n_{ex}}^2$.

The results of the high stats calibration data are shown in table 5.3, containing

Δ_E [keV]	Count	$\sigma(\sigma_{R_\gamma}^2)$	$\sigma(\sigma_{R_e}^2)$	$\sigma(\sigma_{R_\gamma}^2 - \sigma_{R_e}^2)$	σF
0.025	1523	498	498	3.2	0.0020
0.05	3056	347	347	4.1	0.0026
0.1	6118	237	237	5.3	0.0033
0.2	12225	171	171	8.6	0.0054
0.25	15285	149	148	9.5	0.0060
0.5	30514	101	99.4	14.3	0.0090

Table 5.2: Values for the standard deviation of the observed value of σ_R^2 from n_γ and n_e along with the standard deviation of the difference, for a simulated ^{83m}Kr decay with recombination set to 100 quanta. Note, since the two methods for determining σ_R^2 are correlated the standard deviation of the measured difference is small leading to an improved error when calculating the Fano factor or $\sigma_{n_{\text{ex}}}^2$.

400k events in the fiducial volume of the detector. Using equation 5.23 we find good agreement between the method described in equation 5.14 and the recombination fluctuation calculated from the charge channel (σ_{R_γ} and σ_{R_e}). The accuracy helps us build confidence that the statistical components of the detector are modeled well enough to measure recombination fluctuation to within 3%. Further, the ability to see the asymmetry in recombination fluctuations between the light and charge channel demonstrates the power of using binned combined energy (section 5.3). Any observed difference between the two channels can only be from either the Fano factor or spread in exiton production, but we assume the fluctuations in exiton

production are much less than fluctuations in ion production. The Fano factor is derived from equations 5.25 and the uncertainty was determined from simulations. The total fluctuation as number of quanta is listed in the rightmost column. The Fano factor manifests itself as an asymmetry between fluctuations in the light and charge channel as given in equation 5.22, the recombination fraction was found to be $r = 0.772$ and the average number of ions produced per decay was $n_i = 2900$. Having demonstrated the method for a mono energetic calibration source the next step will be to apply the method on the continuous beta spectrum of the tritium data.

5.3.3 Application to Simulated Tritium Data (any continuous spectrum)

Adapting the equation of the previous section to continuous energy spectra requires that the centroid of a continue spectrum be subtracted off so that the variance from the light yield or charge yield vs. energy is removed. After applying the Smearing Model of Section 4 we apply the method described in this section to extract recombination fluctuations form the tritium data.

In this subsection we test method outlined in section 5.3 for dealing in bins of combined energy specifically applied to the tritium beta spectrum, but the method outlined can be used for any continue spectrum. To first order the treatment of the continuous spectrum is identical to that outlined for the mono energetic source as outlined previously in subsection 5.3. Figure 5.4 illustrates a tritium beta spectrum

σ_R 5.14 (Quanta)	Δ_E (keV)	Count	$\sigma_{R_\gamma} = \sqrt{\chi_{n_\gamma}^2 - \chi_{n_{\gamma\text{Det}}}^2}$ (Quanta)	$\sigma_{R_e} = \sqrt{\chi_{n_e}^2 - \chi_{n_{e\text{Det}}}^2}$ (Quanta)	$F = \frac{\sigma_{R_\gamma}^2 - \sigma_{R_e}^2}{n_i(2r-1)}$ (Quanta)	$\sqrt{Fn_i}$ (Quanta)
82.4 ± 4.0	0.025	1518	87.2 ± 2.9	87.1 ± 2.9	0.010 ± 0.002	5.8 ± 0.5
	0.05	3124	85.0 ± 2.0	84.9 ± 2.0	0.005 ± 0.003	3.8 ± 1.1
	0.1	6269	87.8 ± 1.3	87.6 ± 1.3	0.023 ± 0.003	8.1 ± 0.5
	0.2	12508	90.0 ± 1.0	89.7 ± 1.0	0.021 ± 0.005	7.8 ± 0.9
	0.25	15557	88.5 ± 0.8	88.3 ± 0.8	0.013 ± 0.006	6.1 ± 1.3
	0.5	30826	87.0 ± 0.6	86.7 ± 0.6	0.027 ± 0.009	8.8 ± 2.2

Table 5.3: Values for the standard deviation of the observed value of σ_R^2 from n_γ and n_e along with the standard deviation of the difference, for a $^{83\text{m}}\text{Kr}$ data set with 400k events in the fiducial volume. The Fano factor is derived from equations 5.25 and the uncertainty was determined from simulations. The total fluctuation as number of quanta is listed in the rightmost column. The Fano factor manifests itself as an asymmetry between fluctuations in the light and charge channel as given in equation 5.22, with a recombination fraction of 0.772 and $n_i = 2900$.

convolved with detector resolution similar to that measured for the LUX detector, the figure is analogous to Figure 5.3. As the bin size around a value of combined energy is squeezed to zero the statistical variance in the number of photons and electrons converge, the value is given by equation 5.21. Whereas, regardless of bin size recombination fluctuations remain since they move along lines of constant energy. In order to adapt the methodology developed for a mono energetic source to a continuous energy spectra requires that the centroid of the light and charge yield

be subtracted off. The slope in the light and charge channels from the fundamental yield induce a further variance on top of χ_{Det} from the population in an energy bin being tilted as demonstrated in figure 5.5. For the purposes of this study, we find it sufficient to fit a quadratic form to the centroid of the entire population and subtract off the local slope from the measured variance. An analogous methods for centriod subtraction to extract recombination fluctuations are described in detail in [Patrick's Thesis].

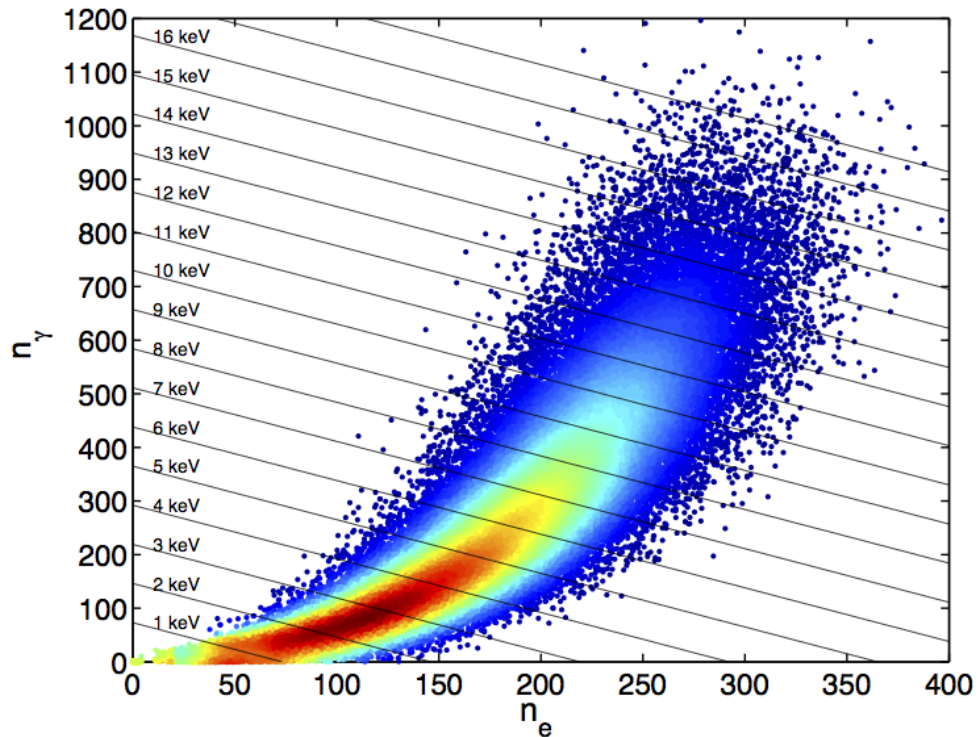


Figure 5.4: Illustration of statistical variance for the tritium beta spectrum, recombination fluctuations are set to 0. This plot is analogous to Figure 5.3 which illustrates the case for the mono energetic ^{83m}Kr decay. Recombination fluctuation move along lines of constant energy, S1 statistical fluctuation move vertically and S2 statistical fluctuations move horizontally.

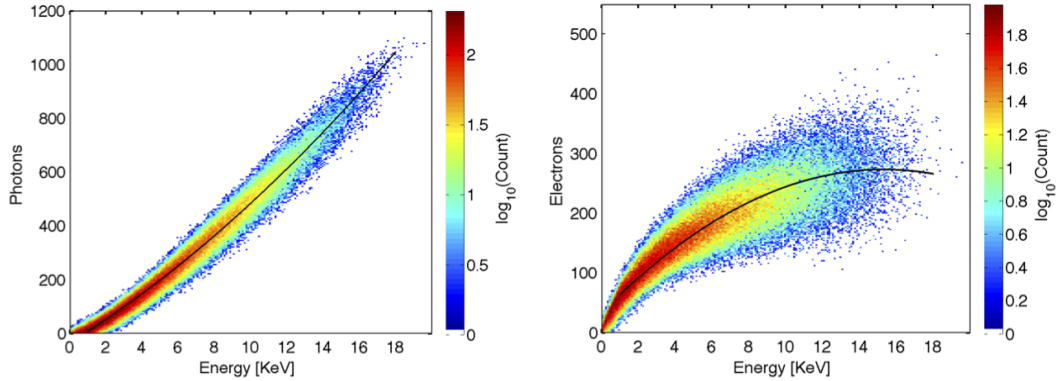


Figure 5.5: Light yield (left) and Charge yield (right) of a simulated tritium spectrum, with the fit to the centroid show in black. The variance in number of photon and electrons per energy bin is used to extract recombination fluctuations.

5.3.4 Centriod Subtraction

For the case of a continuous source we expand upon the result from section 5.3 where the additional variance from detector resolution was calculated per energy bin as

$\chi_{n_{\gamma_{\text{Det}}}}^2$ and $\chi_{n_{e_{\text{Det}}}}^2$. When dealing with a continuous source we must subtract off the centroid of the number of photons and electron vs. energy to remove additional variance induced by the slope. What results is a common variance from detector resolution shared by both the charge and light channel in each bin of energy, defined as $\chi_{\text{Det}}^2 = \chi_{n_{\gamma_{\text{Det}}}}^2 = \chi_{n_{e_{\text{Det}}}}^2$, equation 5.27. The value of χ_{Det}^2 is derived in 5.28 for a small variation in n_e around combined energy, and is identical to that found for the case of the mono energetic source in equation 5.20. This is analogous to saying that the centroid subtraction is removing the additional variance from the slope of light field and charge yield. The local slope of n_e with respect to quanta ($n_\gamma + n_e$)

is $(1-M)$, given in 5.19. To demonstrate the effectiveness of the method we use the measured detector resolution along with a test recombination fluctuation and simulate a tritium spectrum. The result of extracting recombination is shown in figure 5.6 for various energy bin widths. As long as the recombination is greater than χ_{Det} , which is being added in quadrature, the value of recombination can be determined to good precision using the method. The small deviation around the first and last bins is due to the spectral shape, a correction for spectral shape will be discussed in the next section and will improve the measurement of σ_R . The analytic solution for extracting recombination given in equation 5.27 is sufficient to first order, we ignore second order corrections in this analysis. After correcting observables for the tritium beta spectral shape we will be ready to use the tools of this section to decouple detector resolution and measure recombination fluctuations from the tritium data

$$\begin{aligned}\sigma_{R_\gamma}^2 &= \chi_{n_\gamma}^2 - \chi_{\text{Det}}^2 \\ \sigma_{R_e}^2 &= \chi_{n_e}^2 - \chi_{\text{Det}}^2\end{aligned}\tag{5.27}$$

$$\begin{aligned}
\delta[\Delta n_e] &= \delta[n_e] - \delta \left[\langle n_e \rangle_{n_e + n_\gamma} \right] \\
&= \frac{\cancel{dn_e}}{\cancel{dn_e}} \overset{1}{\delta[n_e]} + \frac{\cancel{dn_e}}{\cancel{dn_\gamma}} \overset{0}{\delta[n_\gamma]} - \delta \left[\langle n_e \rangle_{n_e + n_\gamma} \right] \\
&= \delta[n_e] - \frac{d \langle n_e \rangle}{d(n_e + n_\gamma)} \frac{d(n_e + n_\gamma)}{dn_e} \delta[n_e] - \frac{d \langle n_e \rangle}{d(n_e + n_\gamma)} \frac{d(n_e + n_\gamma)}{dn_\gamma} \delta[n_\gamma] \\
\delta[\Delta n_e] &= \delta[n_e] - (\delta[n_\gamma] + \delta[n_e]) \frac{d \langle n_e + n_\gamma \rangle}{d(n_e + n_\gamma)}
\end{aligned}$$

$$\delta[\Delta n_e] = (M)\delta[n_e] - (1-M)\delta[n_\gamma]$$

$$\chi^2_{Det} = Var(\Delta n_e) = (M)^2 \delta^2[n_e] + (1-M)^2 \delta^2[n_\gamma] - 2M(1-M) \underbrace{\delta[n_e] \delta[n_\gamma]}_0$$

(5.28)

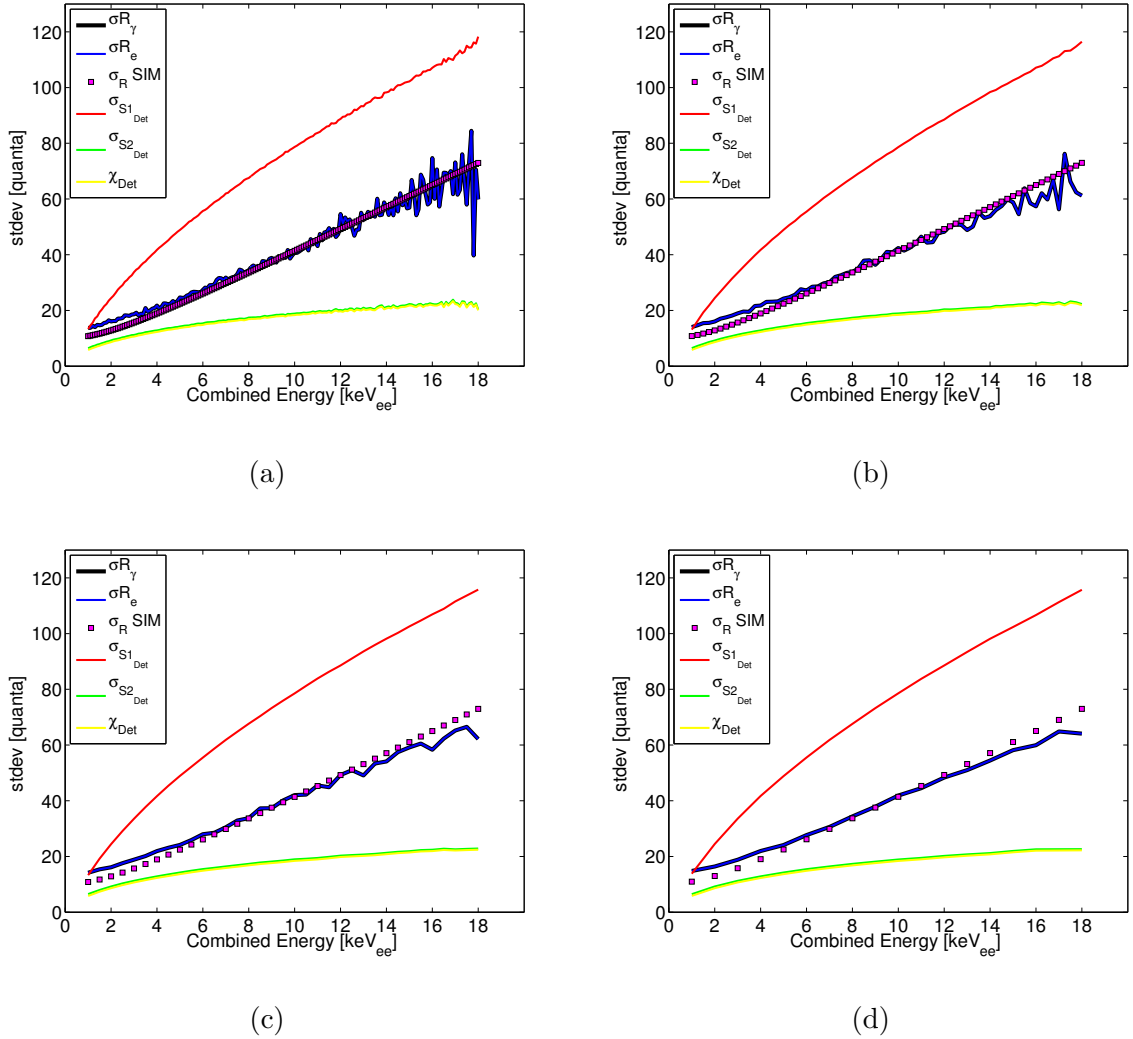


Figure 5.6: Simulated tritium spectrum with the detector resolution of the LUX detector, $\sigma_{S1_{\text{Det}}}$ and $\sigma_{S2_{\text{Det}}}$, and an arbitrary recombination fluctuation σR (magenta). After centroid subtraction we apply the methodology described in the previous section to extract σR (black and blue) through the light and charge channel using our knowledge of detector resolution per each energy bin χ_{Det} (green), $S1_{\text{Det}}$ (red) and $S2_{\text{Det}}$ (yellow). The plots show cases for various bin widths in [KeV]: a) $\Delta E = 0.1$ b) $\Delta E = 0.25$ c) $\Delta E = 0.5$ d) $\Delta E = 1$.

5.4 Extracting Recombination Fluctuations from Tritium Calibration Data

In this section we apply the methods outlined in this chapter and use them to extract the recombination fluctuations vs. energy from the tritium data. The first step in this process was calibrate the energy scale solving for g1 and g2 as outlined in 4. Second, the S1 and S2 signals of the tritium calibration data were corrected for spectral shape as outlined previously in section 6.1 and discussed in more detail in 6. Finally, having modeled and measured the statistical and instrumented variances for light collection of the LUX detector 5.9 5.7 5.8 the component of detector resolution in each energy bin can be calculated χ_{Det}^2 5.20, refeq:Angle, eq:Centroid. For the remained of the thesis we will work in centroid subtracted space as detailed in equation eq:Centroid, the results are identical to working in non centroid subtracted space using a bin width correction of equation 5.23, which is the equivalent of making a linear approximation to the local slope.

Since the tritium beta spectrum is continuous the calibration data is divided into energy bins. In each energy bin the mean of S1 and S2_b is measured and converted to the mean number of photons and electrons using g1 and g2. Once that is known the variance from detector resolution in each bin can be determined, defined as χ_{Det}^2 5.28, 5.20. We then measure the variance of both the fluctuations in the photon and electron channels using Gaussian fits to the distributions in each energy bin, defined as χ^2 . The recombination variance and variance from detector

resolution are two independent processes making the observed variance in each bin χ^2 a sum of χ_{Det}^2 and σ_R^2 . We measure the variance of both the light and channel χ_γ^2 and χ_e^2 and solve for $\sigma_{R_\gamma}^2$ and $\sigma_{R_e}^2$ where the subscripts γ and e denote the photon and electron channel respectively. Using this we find

$$\sigma_R^2 = \sigma_{R_\gamma}^2 = \sigma_{R_e}^2 = \chi^2 - \chi_{\text{Det}}^2 \quad (5.29)$$

the same result as outlined in 5.27. The recombination fluctuation σ_R can be extracted from the tritium calibration data. The result of the tritium calibration is shown in figure 5.8 for both the 170 V/cm and 100 V/cm data. The 170 V/cm data had 140,000 tritium beta decays in the fiducial volume and the 100 V/cm data contained 4,500 events.

The figures on the left in 5.8 (a: 170 V/cm, c: 100 V/cm) show the extracted recombination fluctuation σ_R from the light (black) and charge (red) channel denoted with subscript γ and e respectively, note they are identical. Also shown are the fluctuations in light collection χ_{Det}^2 (blue), charge collection $\chi_{e_{\text{Det}}}^2$ (cyan), and their manifestation as detector resolution in a combined energy bin as χ_{Det} (magenta). The detector resolution is actually slightly better than the resolution of the best channel, for the case of LUX is the charge collection. The remaining fluctuations in the light and charge channel after subtracting off the detector resolution in quadrature are shown in black and red, respectively. In regions where the measured recombinations are larger than the fluctuations caused by detector resolution any error in quanta counting from uncertainty on $g1$ and $g2$ is negligible as the signals add in quadrature. At the higher energy bins the uncertainty grows as the result

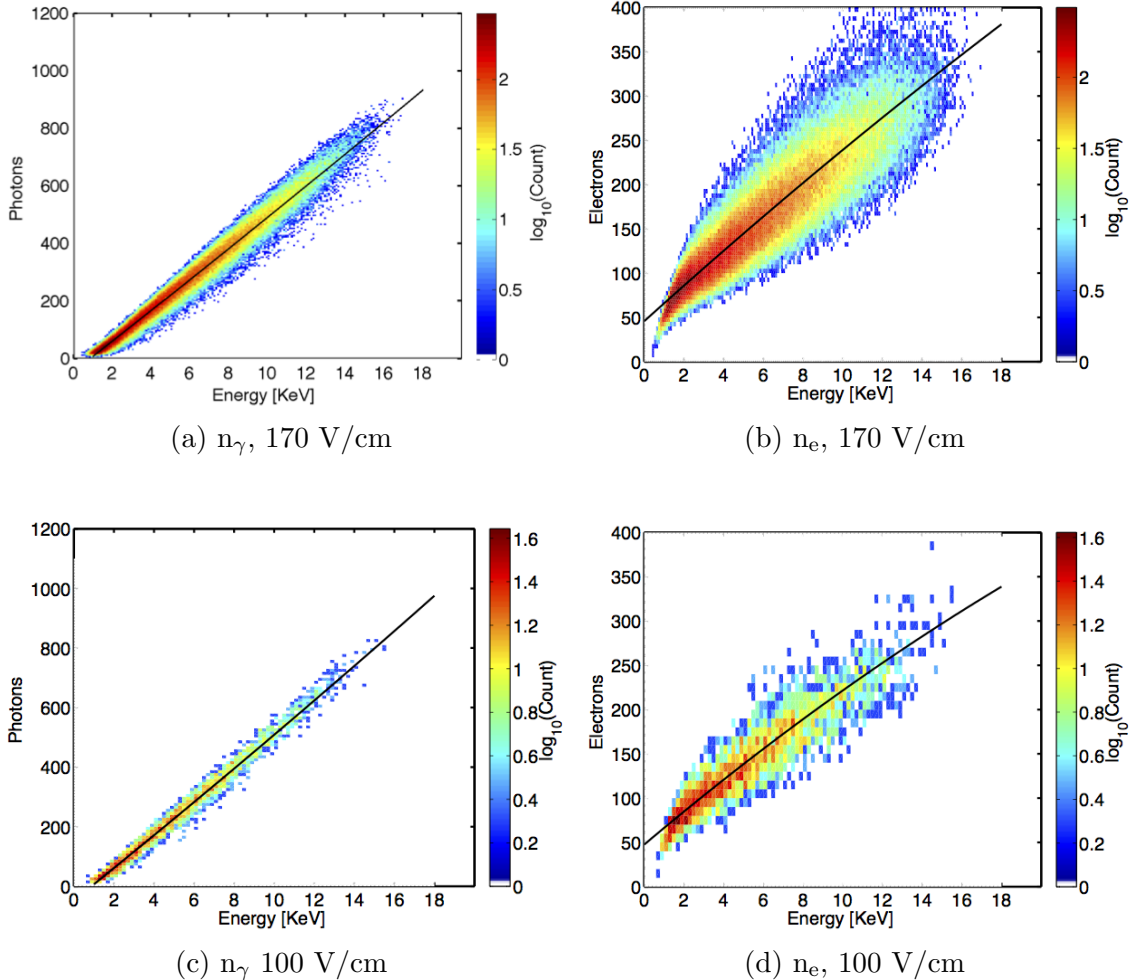


Figure 5.7: a: Density plot of number of photons vs. energy in keV using the tritium calibration data at 170 V/cm. b: Number of electrons vs. energy in keV using the tritium calibration data at 170 V/cm. c: Number of photons vs. energy in keV using the tritium calibration data at 100 V/cm. d: Number of electrons vs. energy in keV using the tritium calibration data at 100 V/cm. The data has been corrected for spectral shape. The black line indicates the quadratic fit to the centroid of the population.

becomes statistics limited.

The figures on the left in 5.8 (a: 170 V/cm, c: 100 V/cm) show the extracted recombination fluctuation σ_R from the light (black) and charge (red) channel denoted with subscript γ and e respectively, note they are identical. Also shown are the fluctuations in light collection $\chi^2_{\gamma_{\text{Det}}}$ (blue), charge collection $\chi^2_{e_{\text{Det}}}$ (cyan), and

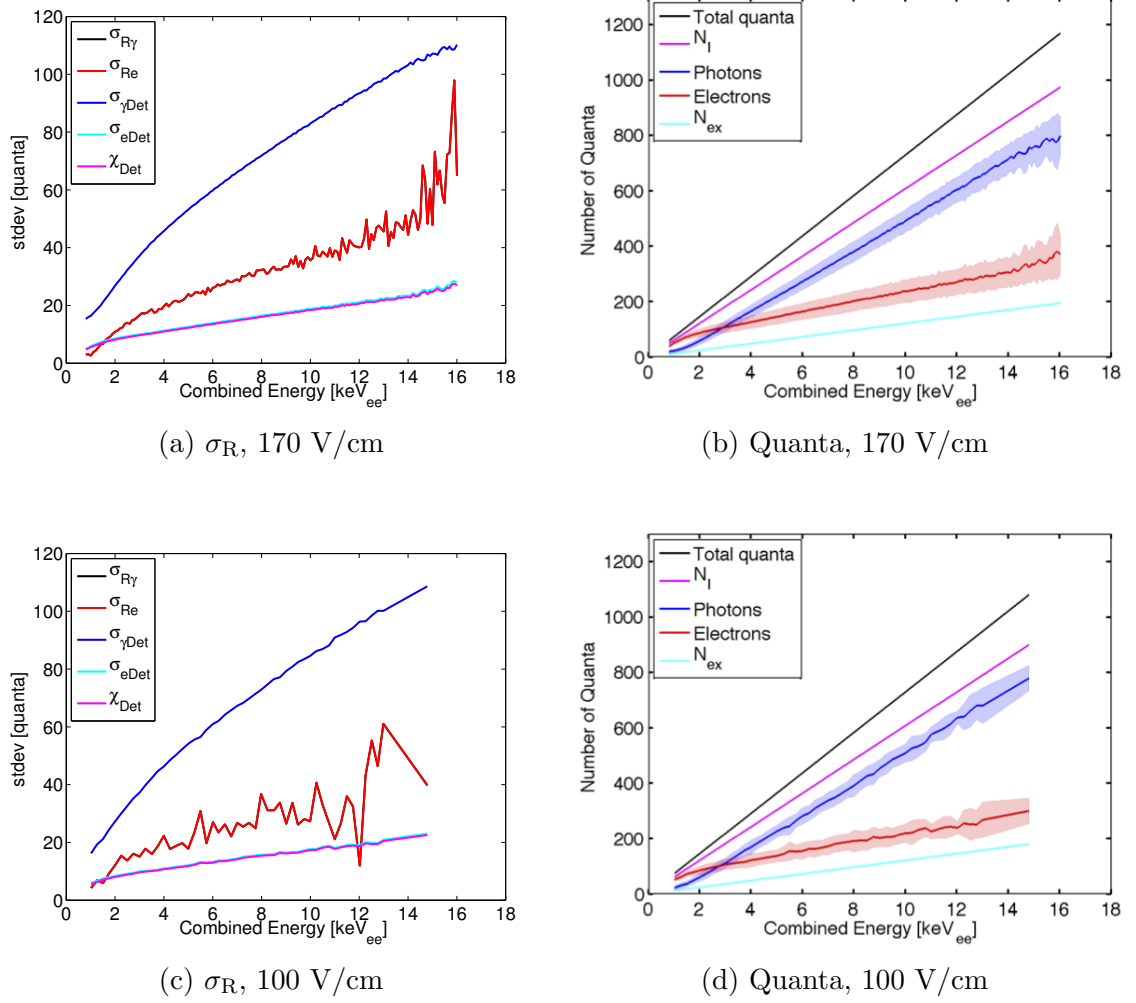


Figure 5.8: The figures on the left in 5.8 (a: 170 V/cm, c: 100 V/cm) show the extracted recombination fluctuation σ_R from the light (black) and charge (red) channel denoted with subscript γ and e respectively, note they are identical. Also shown are the fluctuations in light collection $\chi^2_{\gamma\text{Det}}$ (blue), charge collection $\chi^2_{e\text{Det}}$ (cyan), and their manifestation as detector resolution in a combined energy bin as χ_{Det} (magenta). The figures on the right in 5.8 (b: 170 V/cm, d: 100 V/cm) show the mean and one sigma standard deviation of the measured number of photons (blue) and electrons (red). Also shown is the total quanta (in black) which is the sum of photons and electrons and the expected number of ions (magenta) and excitons (cyan) using $\alpha = 0.20$.

their manifestation as detector resolution in a combined energy bin as χ_{Det} (magenta). The figures on the right in 5.8 (b: 170 V/cm, d: 100 V/cm) show the total quanta (black) which is the sum of the photons (blue) and electrons (red) and the

expected number of ions (magenta) and excitons (cyan), using $\alpha = 0.20$. Since the detector resolution χ_{Det} is solved for in terms of photons and electrons the means of the of number of photons and electrons in each energy bin must be measured first.

5.4.1 Extracting Recombination fraction From Tritium Data

Having measured the mean number of photons and electrons in each bin the value of recombination probability r can be determined using equation 5.12. Figure 5.9 shows the measurement of recombination probability r for the 170 V/cm and 100 V/cm tritium calibration data. The shaded region represents the one sigma of the recombination probability which can be thought of in terms of the recombination fluctuation $\sigma_r = \sigma_R/n_{\text{ions}}$. Note, the bands converge below 4 keV_{ee} meaning that the light yields and charge yields also converge (discussed in ch 6), this leads to the energy thresholds at 1.5 keV being identical for at the two fields as seen in 4. Further, the ER and NR discrimination in this region overlap as will be discussed in the next subsection. All this translates into no observed improvement in either energy threshold or background rejection from 1 to 4 keV_{ee} between using a 100 and 170 V/cm field.

5.4.2 Modeling the ER Band

The main purpose of this section, and the tritium calibrations, are to be able to make predictions about WIMP sensitivity at various electric fields and in the WIMP search energies of interest, 1-5 keV_{ee}. We now have the ability to reconstruct the electronic

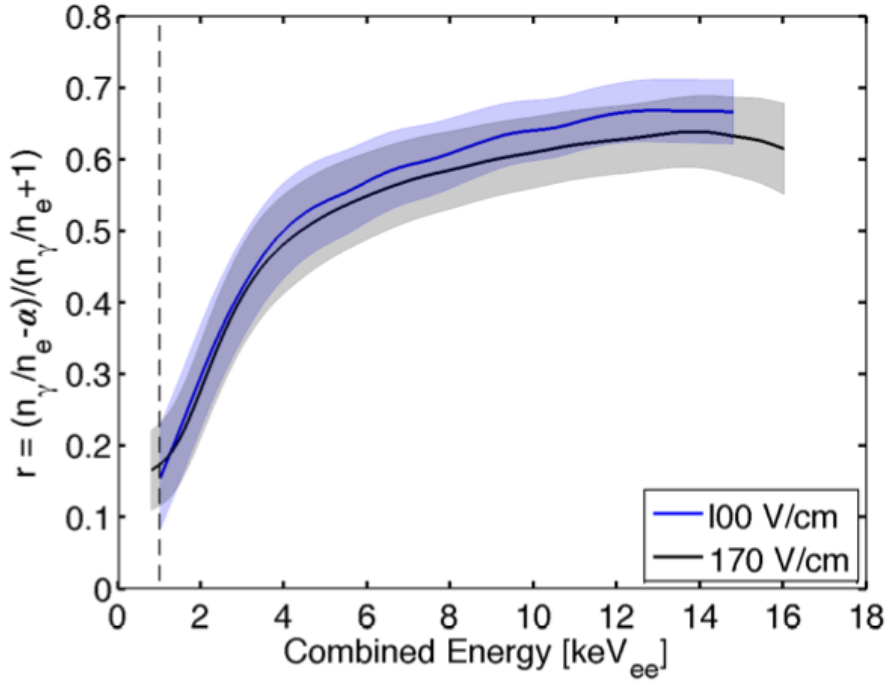


Figure 5.9: Recombination Fraction at 170 V/cm (black) and 100 V/cm (blue). The shaded regions represent the one sigma of the observed fluctuations in recombination fractions σ_r . The dashed line at 1.0 keV_{ee} represents the 50% detection threshold.

recoil band as it would appear with infinite detector resolution, with the ability to expand the band width by adding the measured detector resolution. Knowing the mean and width of the electronic recoil band and the mean of the NR band (described later) we can make predictions for ER and NR type discrimination which is a proxy for background event rejection.

The mean of the ER band in discrimination space can be written as

$$\log_{10}(S2_b/S1) = \log_{10} \left(\frac{(1-r)N_i}{(r+\alpha)N_i} \right) + \log_{10} \left(\frac{g2}{g1} \right) \quad (5.30)$$

where the observed charge and light signals S2_b and S1 have been converted to recombination probability r, number of ions N_i and the exciton to ion ratio α using

equations 5.1 and 5.12.

The variance of the band can be written as,

$$\text{Var}_{\log_{10}(S2_b/S1)} = \frac{1}{(\log(10))^2} \times \sigma_R^2 \left(\frac{-(\alpha + 1)}{(1 - r)(r + \alpha)N_i} \right)^2 \quad (5.31)$$

Which has been written in terms of the number of ions N_i , the recombination fraction r , and the measured recombination fluctuation σ_R , defined to be $\sigma_r \times N_i$. The result of the ER band's mean population and its corresponding 1 sigma fluctuation are shown in figure 5.10 for the case of 100 V/cm (blue) and 170 V/cm (black). This result shows the ER band with recombination fluctuations only. One can add light and charge collection fluctuations in quadrature to complete the modeling specific to any detector. Above 4 keV_{ee} the band separate as the higher drift field increased the charge extraction leading to better discrimination.

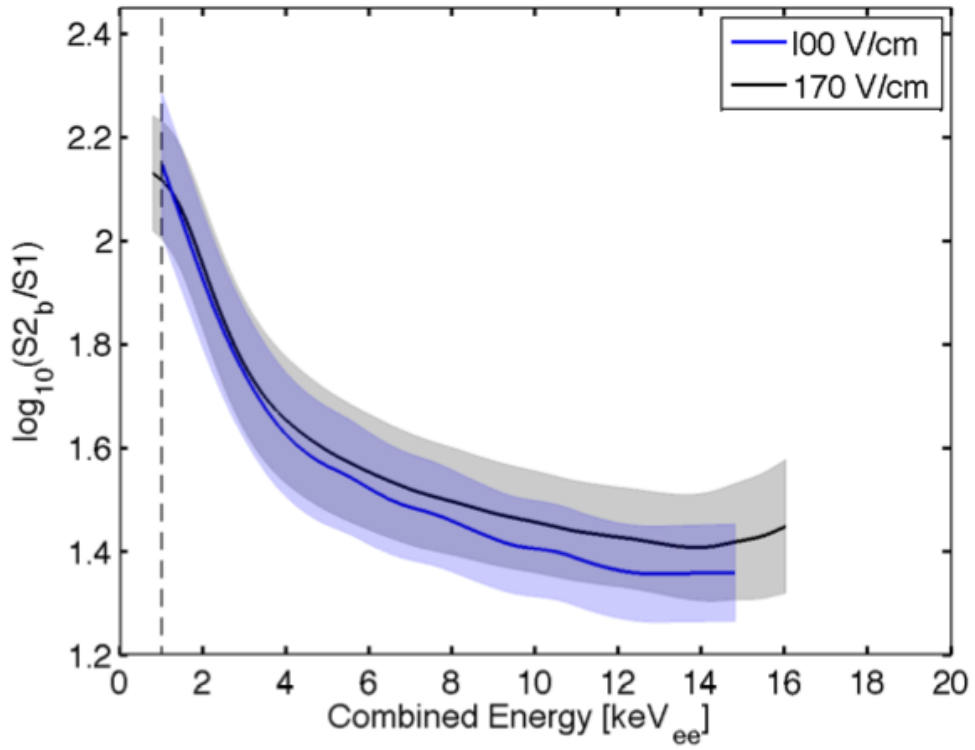


Figure 5.10: The result of the ER band's mean population and its corresponding 1 sigma fluctuation for the case of 100 V/cm (blue) and 170 V/cm (black). We find an overlap below 4 keV_{ee} where the additional strength of the drift field is either improving threshold of discrimination. Above 4 keV_{ee} the bands separate as the higher drift field increased the charge extraction leading to better discrimination.

5.4.3 Measuring Alpha From the Tritium Data

Having measured r and σ_r from the tritium calibration data the constancy of the exciton to ion ratio α can be checked by requiring that as the number of ions tends to one the recombination fluctuations tend to that of a binomial process. This is justified as a single ion-electron pair will either recombine or not with some

recombination probability r having a binomial variance written as,

$$\text{BinoVar} = (1 - r)rN_i \quad (5.32)$$

where r is the recombination probability and N_i is the number of ions which can be thought of as the number of trials for the binomial process. In figure 5.11 the y axis shows the ratio of the measured standard deviation of recombination to the standard deviation of a purely binomial process. The figure on the right has the expected binomial standard deviation on the x axis. The best alpha is one in which the observed standard deviation converges with that of a binomial process as the binomial variance tends to 1. The figure on the left has the number of ions available for recombination on the x axis. As the number of ions approaches one the standard deviation of recombination should become that of a binomial process. A single ion will either recombine or not with probability r . The extrapolation is made by fitting the lowest energy bins above 90% threshold 1.3 to 3 keV. Going below the value of one on the y axis implies that recombining electron-ion pairs have a variance better than binomial, which is unphysical if it is a random process. We find that the best intercept converging to a purely binomial process is with $\alpha = 0.20$ consistent with the measurement in [73] and not 0.06 as used in [8].

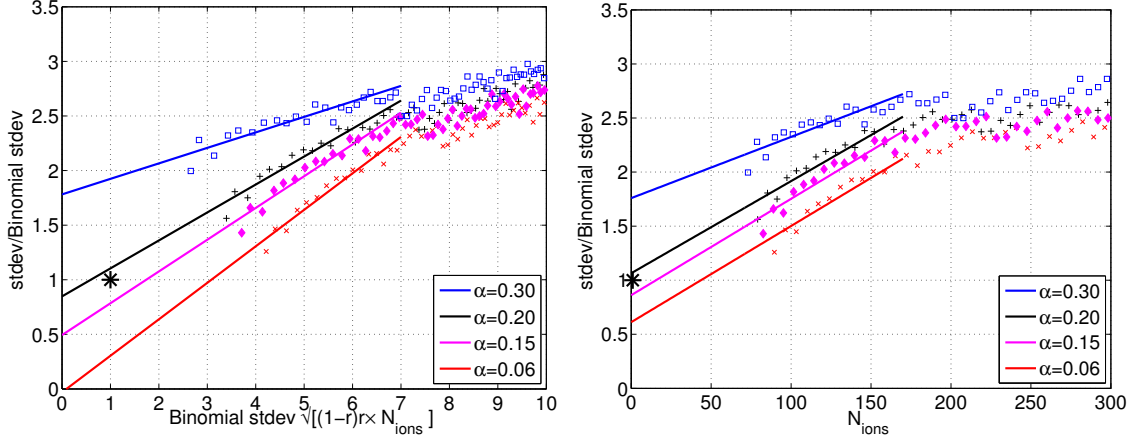


Figure 5.11: Determining the best α using the tritium calibration data, with $\alpha = 0.3$ (blue), 0.2(black), 0.15(magenta) and 0.06(red). Left: The y axis is the ratio of the measured standard deviation of recombination to that of a binomial processes and is plotted vs. the expected binomial standard deviation on the x axis. The best α is one for which the observed standard deviation converges with that of a binomial process as the binomial variance tends to 1. Right, the same y axis as on the left but plotted vs. the number of ions available for recombination. As the number of ions approaches one the standard deviation of recombination should become that of a binomial process. A single ion will either recombine or not with probability r . The best intercept converging to a purely binomial process (black star) is with $\alpha = 0.20$. Falling below the value of one on the y axis implies that recombining electron-ion pairs have a variance better than binomial, which is unphysical if it is a random process. Note, the fits use only data above 90% threshold at 1.3 keV, starting from the third data point from the left. The higher end cut off at 3 keV corresponds to the end of the fitted lines.

5.5 Extracting Recombination Fluctuations from ^{137}Cs Calibration

To expand the picture of recombination fluctuation to higher energies the same method used for the tritium calibration was applied to the Compton edge of a ^{137}Cs external calibration source. The ^{137}Cs source provides ER calibration data from the backscatter peak around 150 keV to the photo peak at 662 keV. Figure 5.12 on the left shows the measured mean number of photons, electron in each energy bin along with their one sigma fluctuation (shaded). The number of excitons and ions are also

show assuming an $\alpha = 0.20$. Once the mean number of photons and electrons are measured the recombination probability is determined and plotted on the right in figure 5.12. The inflection around 662 keV is due to the sharp rise and fall of the photo peak skewing the measurement of number of photons and electrons.

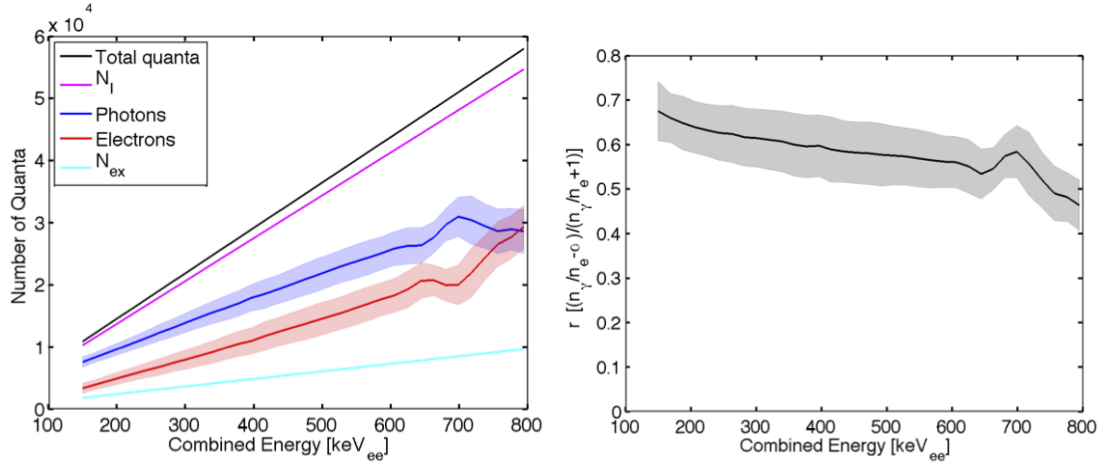


Figure 5.12: Left: The mean and one sigma standard deviation of the measured number of photons (blue) and electrons (red). Also shown is the total quanta (in black) which is the sum of photons and electrons and the expected number of ions (magenta) and excitons (cyan) using $\alpha = 0.20$. Right: The recombination probability r (solid black) and the one sigma fluctuation σ_r (shaded).

5.6 Recombination Fluctuations, The Bigger Picture

We have now measured the recombination probability and fluctuation over a wide range of energies and at two fields for tritium (100 and 170 V/cm). The calibrations range from the 1.0 keV 50% threshold with tritium to about 700 keV with the ^{137}Cs calibration, and include the line sources used for the energy calibration in 4 and table 4.1. Also shown is a ^{57}Co calibration at a variety of electric fields ranging from 60 to 5000 V/cm from [8]. Figure 5.13 on the left shows the observed recombination fluctuation σ_R measurements vs. the standard deviation expected from a purely binomial process (equation 5.32). At our field of 100 and 170 V/cm we find good agreement with a simple power law fit which can be thought of as the fluctuation receiving an amplification over the underlying binomial process.

Figure 5.13 on the right shows the measured recombination fluctuation σ_R vs. the number of ions available for recombination N_i . The x axis is chosen to be number of ions as recombination fluctuations only act on ions and not excitons, the conversion to energy on the x axis is simply $E = W \times n_i(1 + \alpha)$. It is found that the measured recombination fluctuation can be well described by a generic power law fit.

There is no physical justification for the power law fit in figure 5.13 to the apparent binomial variance amplification. This is a fatal flaw in our recombination model. The observed variance is off by roughly a factor of N_{ions} , surpassing 1000 in the cesium data. The recombination model we are using assumes that every electron ions pair is a separate entity that either recombines or not, thus the variance should

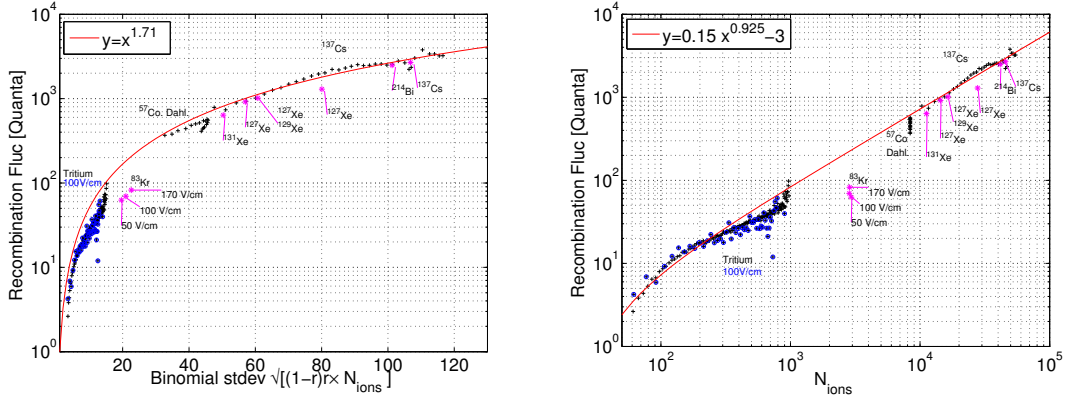


Figure 5.13: Recombination fluctuations measurements are labeled on the plot and include data from tritium at 170 V/cm, tritium at 100 V/cm, ¹³⁷Cs calibration, the line sources used for the energy scale calibration listed in table 4.1 and a ⁵⁷Co calibration at a variety of electric fields ranging from 60 to 5000 V/cm from [8]. Left: the observed recombination fluctuation σ_R measurements vs. the standard deviation expected from a purely binomial process, equation 5.32. The red curves represent power law fits to the data.

be binomial. There is another issue with the recombination model. The decline of recombination probability as the energy (or N_i) tends to zero is unphysical yet is observed in the data, shown in figure 5.9. The probability of the electron ion-pair to recombine should be insensitive to the number of electron-ion pairs created by the energy deposit. We take this as a first clue to solving the problem and outline the consequences of allowing for electron-ion pair mixing with some encounter probability in the next two sub-sections. Culminating with a model which will simultaneously reproduce the observed recombination fraction, explain its decline at low energy, and yield the correct recombination fluctuations.

5.6.1 Encounter Recombination Probability

The apparent amplification of the observed ER fluctuations over that of a binomial process is troubling. What causes the ER events to be so erratic over their nuclear recoil counterparts which can be well described by binomial fluctuation [8]. The key difference that lends a clue to solving the puzzle is that for a given energy nuclear recoils will produce significantly less electron-ion pairs. It has been observed for ER events that as the number of ions goes to one the recombination fluctuations do indeed become more binomial like, shown in figure 5.11. Before we move on, it should be noted that the method outlined in this section will succeed in explaining recombination fluctuation but will fail to reproduce the recombination fraction probability. This subsection is meant as a discussion on encounter recombination probability leading to the model in the subsection to follow that will bridge measuring recombination probability and its variance.

In order to tackle the issue of recombination fluctuations we introduce encounter recombination probably r_ϵ . The term r_ϵ will couple freed electrons to ions other than its own. There are well motivated arguments to be made to include a r_ϵ term. First, in liquid xenon the decay of the calibration source ^{83m}Kr has been observed to receive an enhancement of several percent in the light yield of the second 9.4 keV following the first decay of 32.1 keV [72]. This can be attributed to the second decay occurring surrounded by a ball of charge from the first decay resulting in an enhanced encounter recombination probability and increased light yield. The two ^{83m}Kr decays are separated by a half life to 154 ns [11]. The shorter the

timing separation between the two decays the greater the light yield enhancement, with light yield enhancement observed past 1000 ns [9], [10] [LUX data shows enhancement out to 2000 ns could add this plot to thesis...]. This lends evidence that freed electrons can be attracted to ions while diffusing from the interaction site on the time scales of hundreds of nano seconds. Further, the idea of encounter probability was worked out by Mozumder noting the need for encounter recombination probabilities of 0.01 in order to explain the ion production rate in liquid xenon [76].

In this subsection we set out to model the variations resulting from the recombination porbability containing a component from encounter recombination probability. Once the model for variance is worked out we can fit to the tritium and ^{137}Cs calibration data in order to extract the encounter recombination probability.

First we start with expression for the variance of a binomial process with some recombination probability r .

$$\text{Var}_r = (1 - r)rN_i \quad (5.33)$$

where N_i is the number of ions, and can be thought of as the number of trials. Next we split the total observed recombination probability into two components.

$$r = r_s + r_e \quad (5.34)$$

where r_s is the self recombination probability and r_e is the encounter recombination probability. The expectation is that $r_e \ll r_s$, [76]. The variance resulting from the two terms can be considered as independent processes occurring subsequently thus,

the total variance of the process is the sum of the individual variances for each ion. In our modeling every free electron has an average encounter probability r_ϵ with each ion. The variance of N_i ions is given in equation 5.33 and is illustrated in figure 5.14 for the case of one ion. At this point we pause to point out the fatal fall in this theory. As the number of ion-electron pairs grow all ions will recombine as each ion is unable to avoid recombination from the bombardment of N_i electrons. The observed recombination probability for this process becomes $r = r_s + N_i \cdot r_\epsilon$. With that note, we proceed to learn more about encounter recombination probability.

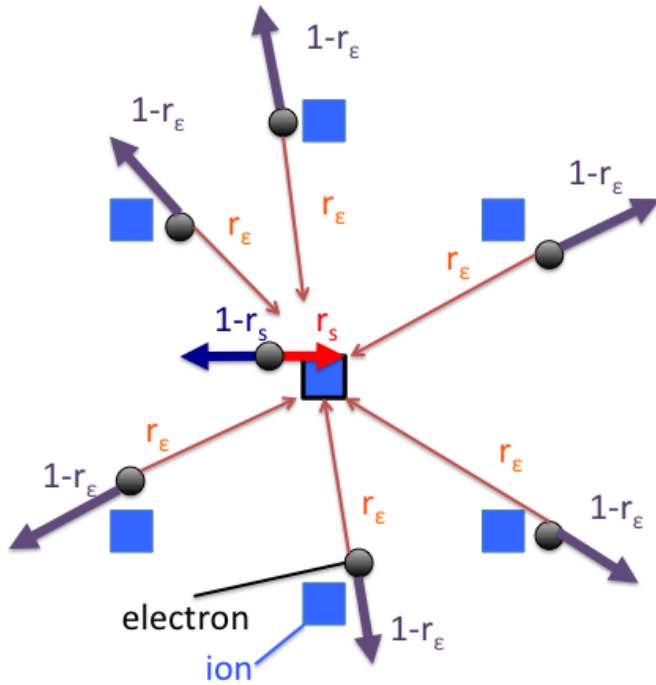


Figure 5.14: Illustration of recombination for the case of a single ion, blue box highlighted in black at the center. The total recombination probability for one ion is the combination of the dominant self recombination probability (r_s) plus the sum of the encounter recombination probabilities (r_ϵ) from the remaining $N-1$ electrons. This process is repeated for N number of ion-electron pairs leading to a binomial variance given in equation 5.35.

$$\text{Var}_{(r_s+r_e)} = \sum_{N_i} r_s(1-r_s) + \sum_{N_i} r_e(1-r_e)(N_i - 1) \quad (5.35)$$

the first term of equation 5.35 is the binomial variance of a single electron-ion pair with some probability r_s to recombine. The second term is the binomial variance of the average encounter probability r_e with all other electrons excluding its own escaped electron, a total of $(N_i - 1)$. Both terms are summed over all possible ions, accounting for all N_i ions with $N_i - 1$ electrons available to be encountered. Due to the relatively slow mobility of ions vs electrons, the ions are treated as fixed with the freed electrons having some probability of encounter an ion. This is a simplistic model that treats the encounter probability as an overall average for all electron-ion pair combinations. Assuming N_i is large equation 5.35 can be simplified to

$$\text{Var}_{(r_s+r_e)} = r_s(1-r_s)N_i + r_e(1-r_e)N_i^2 \quad (5.36)$$

The result of splitting the recombination probability into self and encounter recombination is subtle, yet has huge implications. Comparing equation 5.33 to 5.35 we find that the binomial variance of the process with encounter recombination probability will grow like N_i^2 as opposed to the binomial variance of a self recombination process that grows like N_i . To better understand the amplification of the binomial fluctuation observed in the data, figure 5.13, we define an amplification term as the ratio of the binomial variance with encounter recombination probability to that of a binomial process with self recombination probability r .

$$\mathcal{A} = \frac{\text{Var}_{(r_s+r_\epsilon)}}{\text{Var}_r} \quad (5.37)$$

$\text{Var}_{(r_s+r_\epsilon)}$ and Var_r are given in equations 5.36 and 5.33, respectively.

We will treat two cases. First, we will assume that $r_\epsilon \ll r_s$ and $r_s \simeq r$. Second, we will hold the ratio of r_ϵ/r to be a constant. The second case is motivated by the idea that electric field and energy dependance that governs self recombination probability also applies to encounter recombination probability.

The amplification of the binomial variance from equation 5.37 is

$$\mathcal{A} = \frac{N_i}{N_i} \left(\frac{r_s(1-r_s) + r_\epsilon(1-r_\epsilon)N_i}{r(1-r)} \right) \quad (5.38)$$

assuming that $r_\epsilon \ll r_s$ and $r_s \simeq r$ equation 5.38 can be simplified to,

$$\mathcal{A} = \left(1 + \frac{r_\epsilon(1-r_\epsilon)N_i}{r(1-r)} \right) \quad (5.39)$$

Using equation 5.39 the value of encounter recombination probability r_ϵ can be extracted from the tritium and ^{137}Cs data using N_i , r , and \mathcal{A} . Where the value of binomial amplification \mathcal{A} is the extracted from the data defined as the recombination fluctuation σR over σR -binomial, shown in figure 5.13. The result of extracting encounter recombination probability r_ϵ is shown in figure 5.15. The overall average of r_ϵ from the calibration data is $r_\epsilon = 0.0042$ varying from 0.002 to 0.007, in good agreement with Mozumder [76].

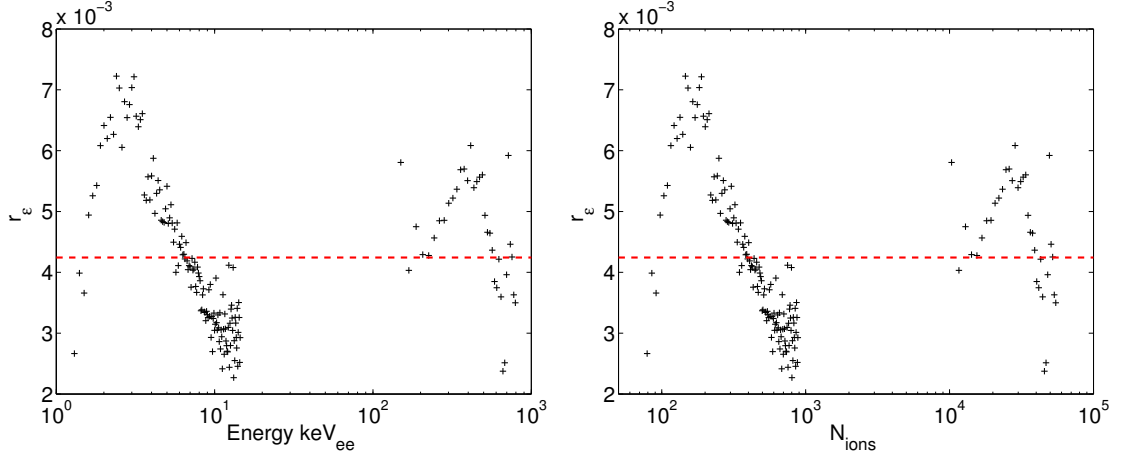


Figure 5.15: Encounter recombination probability r_e extracted from the tritium and ^{137}Cs calibration data at 170 V/cm, derived from equation 5.39. Left plotted vs. energy in keV. Right: plotted vs. the number of ions. The solid red line represents the overall average of r_e from the calibration data is $r_e = 0.0042$.

Taking the value of r_e as a constant of 0.0042 we find that the observed ER recombination fluctuations are infact consistent with binomial fluctuation at our field of 170 and 100 V/cm, shown later in figure 5.17. This is a step in the right direction for understanding recombination fluctuations. Our data is limited to only two electric fields at 100 and 170 V/cm making it difficult to model field dependance. To expand the model we include data from Dahl, using a ^{57}Co source with fields ranging from 60 to 5000 V/cm [8]. We then extract r_e , shown as the black points in figure 5.16.

The data from Dahl, shown in 5.16, provides good motivation to proceed with our second assumption, modeling the ratio of r_e/r to be a constant. There appears to be correlation between the recombination probability and the encounter recombination probability. This correlation is sensible, considering that as the electric field is increased the freed electrons can escape the ions more readily. Thus, both

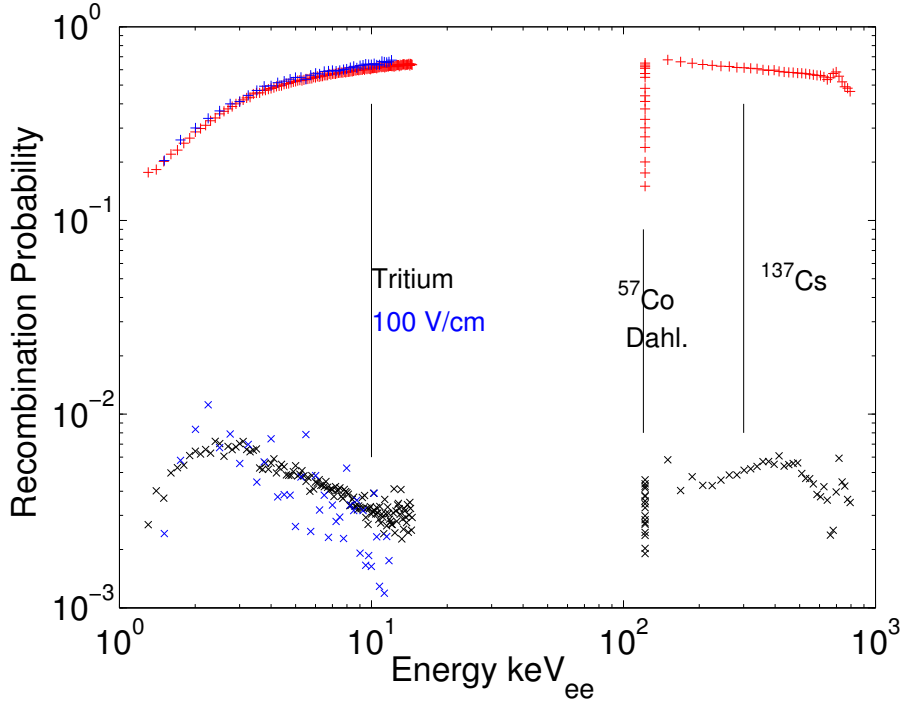


Figure 5.16: The red crosses indicate the total recombination probability r for the calibration sources labeled on the plot. The black x-s indicate the encounter recombination probability r_ϵ . The blue points indicate the tritium data at 100 V/cm. The data includes tritium at 170 V/cm (black), tritium at 100 V/cm (blue), ^{137}Cs and data from Dahl for ^{57}Co ranging from 60 to 5000 V/cm [8].

the self and encounter recombination decline as a function of applied electron field. However, the assumption that r_ϵ and r are always correlated is to be taken with a grain of salt, and is not supported by the tritium data. Between 2.5 and 10 keV the recombination probability r and r_ϵ become anti-correlated. With that caveat mentioned, we proceed with the second case.

$$r_\epsilon = r_{\epsilon_0} + \mathcal{C}r \quad (5.40)$$

where \mathcal{C} is a constant linking the observed recombination probability r to r_ϵ . The best fit for both cases is show in figure 5.17. Case one, is with a global average of $r_\epsilon = 0.0042$, extracted from the tritium and ^{137}Cs data. Case two, is using $r_\epsilon =$

$0.0011 + 0.006r$. The fit for case one is within 30% when excluding the data from Dahl, and the fit for the second case deviates less than 30% from all of the data.

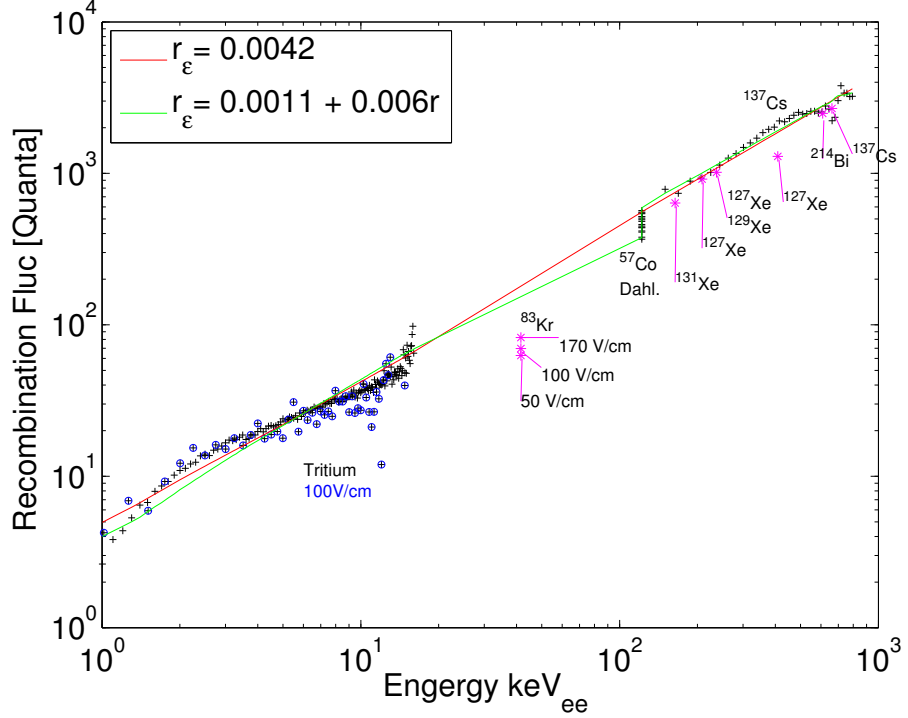


Figure 5.17: Fit to the observed ER recombinations modeled with binomial fluctuations where the recombination probability includes an encounter recombination component. Case one (red) is with a constant $r_\epsilon = 0.0042$, extracted from the tritium and ^{137}Cs data. Case two (green) is using $r_\epsilon = 0.0011 + 0.006r$. Case two is in significantly better agreement with the field dependent data from Dahl, as it accounts for field effects [8]. The fit for case two (green) deviates less than 30% from the data.

The simplistic model outlined in this subsection demonstrates that recombination fluctuation of electronic recoil can indeed be the result of binomial statistics. Remarkably, a sub 1% component of recombination probability r from encounter probability leads to an apparent binomial amplification factor of 1 to 1000, shown in the right plot in figure 5.13. The tiny value of r_ϵ makes a significant impact when considering the combinatorics of the recombination process. This is good progress, we have found a simplistic way to gain an additional factor of N_i for recombination

fluctuations vs. energy, instead of applying a power law fit to binomial amplification with no physical basis. However, we still need to clean up the problem of total ion-electron pair recombination resulting from such a model. We have found the correct variance but have failed to produce the correct recombination probability. The fix the the issue is described in the next subsection.

5.6.2 Clusters of Encounter Recombination

In the previous subsection a model was introduced which could predict the observed recombination fluctuations of ER events. However, the model failed to produce the correct recombination probability. We found that as the energy (or N_i) rises the recombination probability tends to 1, and beyond as $r = r_s + N_i \cdot r_\epsilon$. The zeroth order correction to this problem is to remove the self recombination term r_s and treat self recombination as just another encounter recombination probability, $r_s = r_\epsilon$. Next, we will not allow the full N_i electrons to interact with each ion as this is unphysical. Instead, only a small number of the total ions N_ϵ are allowed to have encounters for each energy deposit, illustrated in 5.14. The value of N_ϵ is set by the requirement to reproduce the correct recombination probability. The observed recombination probability r is then written as,

$$r = r_s + (N_\epsilon - 1)r_\epsilon = N_\epsilon r_\epsilon \quad (5.41)$$

where r is the observed recombination probability at a given energy, r_s is the self recombination probability taken to be equal to the encounter recombination prob-

ability r_ϵ , and N_ϵ is the average number of electron encounters for each ion. Note that the value of N_ϵ used is an average and can also vary event to event depending on the ER track geometry. The equation for recombination probability in 5.41 inadvertently solves the other issue of the original recombination model. By taking self recombination r_s to be equal to r_ϵ the observed recombination probability r naturally vanishes as the energy (N_i) tends to zero, as observed in the data shown in figure 5.9. The binomial variance of such a process is,

$$\text{Var}_{N_\epsilon r_\epsilon} = (1 - N_\epsilon r_\epsilon)N_\epsilon r_\epsilon N_i \quad (5.42)$$

where $\text{Var}_{N_\epsilon r_\epsilon}$ is the recombination variance in number of quanta squared for a given interaction with N_i ions, encounter recombination probability r_ϵ with an average of N_ϵ encounters. The variance derived in equation 5.42 grows like N_i and suffers the same problem as our original model. The variance needs to grow like N_i^2 to explain the observed recombination fluctuations in the data, as seen in the previous subsection.

The solution is surprisingly straight forward considering the two requirements. First, in order to maintain the correct recombination probability r the value of encounter interactions N_ϵ must be fixed. Second, to get the additional factor of N_i in variance the process of size N_ϵ must be repeated, with the repetition scaling like N_i . Remember, we are only allowing a small number, N_ϵ , of the total ions available ions to have encounters. Consider the picture in figure 5.14 but for N_ϵ encounters repeated N_i/N_ϵ times in N_C clusters, such a process is illustrated in figure 5.18. The

number of clusters N_C for a given in equation 5.43.

$$N_C = N_i/N_e \quad (5.43)$$

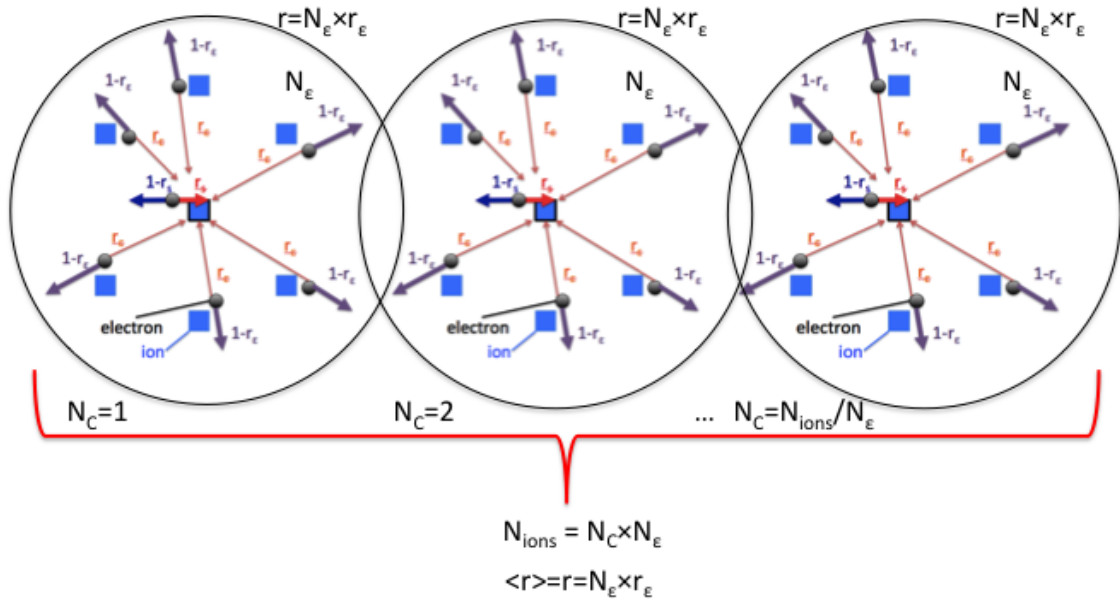


Figure 5.18: Illustration of recombination for the case of a single ion occurring in N_C clusters with number of encounters N_e . The total recombination probability for all clusters is equal to the average of each individual cluster. In each cluster the recombination probability is equal to the number of interaction N_e times the encounter recombination probability r_e . The process is repeated for N_C clusters, resulting in an additional factor N_i in the observed variance while maintaining the correct average recombination probability r .

The value N_e can be considered as the number of encounters per cluster, or generalized to the number of ions per cluster. The electron-ion pairs have N_e encounters in each cluster with an average recombination probability r . The total recombination probability of the system of clusters remains equal to $r = N_e r_e$ without blowing up to unity. Since the process is repeated for N_C clusters the variance from equation 5.42 becomes

$$\text{Var}_{N_\epsilon r_\epsilon} = \sum_{N_C} (1 - N_\epsilon r_\epsilon) N_\epsilon r_\epsilon N_i \quad (5.44)$$

where $\text{Var}_{N_\epsilon r_\epsilon}$ is the recombination variance of equation 5.42 for N_C clusters. Plugging in the value of N_C from equation 5.43 we find

$$\text{Var}_{N_\epsilon r_\epsilon} = (1 - N_\epsilon r_\epsilon) N_\epsilon r_\epsilon N_i (N_i/N_\epsilon) \quad (5.45)$$

where the multiplication by N_C is written as N_i/N_ϵ . Further simplifying equation 5.45 and recalling that $r = N_\epsilon r_\epsilon$,

$$\begin{aligned} \text{Var}_{N_\epsilon r_\epsilon} &= (1 - N_\epsilon r_\epsilon) r_\epsilon N_i^2 \\ \text{Var}_{N_\epsilon r_\epsilon} &= (1 - r) r N_i^2 \\ \text{Var}_{N_\epsilon r_\epsilon} &= (1 - r) r \frac{N_i^2}{N_\epsilon} \end{aligned} \quad (5.46)$$

Taking the result for variance given in equation 5.46 we calculate the apparent amplification factor \mathcal{A} over that of a binomial process, our original recombination theory.

$$\begin{aligned} \mathcal{A} &= \frac{\text{Var}_{N_\epsilon r_\epsilon}}{\text{Var}_r} = \frac{(1 - r)r N_i^2 / N_\epsilon}{(1 - r)r N_i} \\ \mathcal{A} &= \frac{N_i}{N_\epsilon} = N_C \end{aligned} \quad (5.47)$$

the amplification factor in equation 5.47 remarkably simple. The amplification over that of a binomial process reduces to the number of clusters N_C . Note, the value of N_ϵ is the ratio of r/r_ϵ . This is the key to the cluster recombination model. We have picked up an additional factor N_i in the variance while maintaining the

correct average recombination probability r . Using equation 5.47 we can extract the encounter probability r_e , the cluster size N_e and the number of clusters N_C from our calibration data.

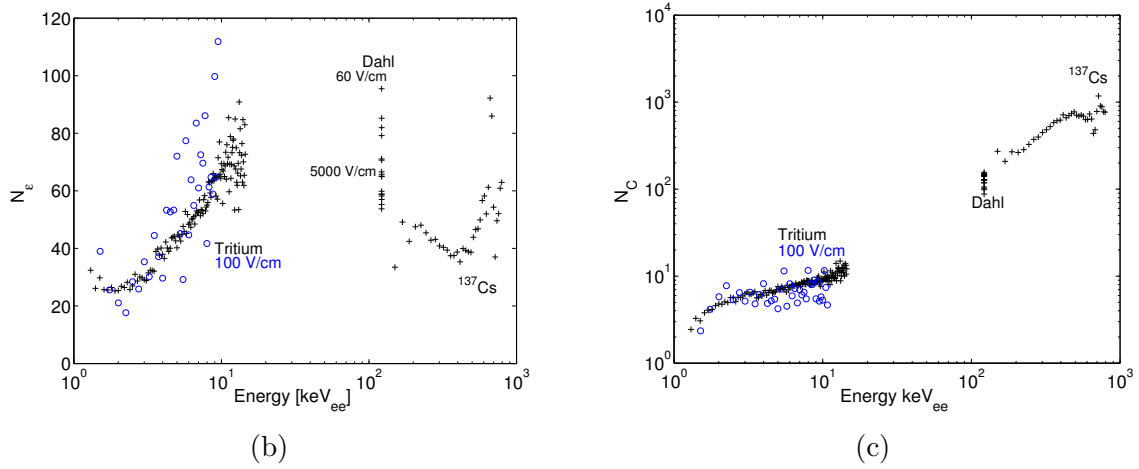
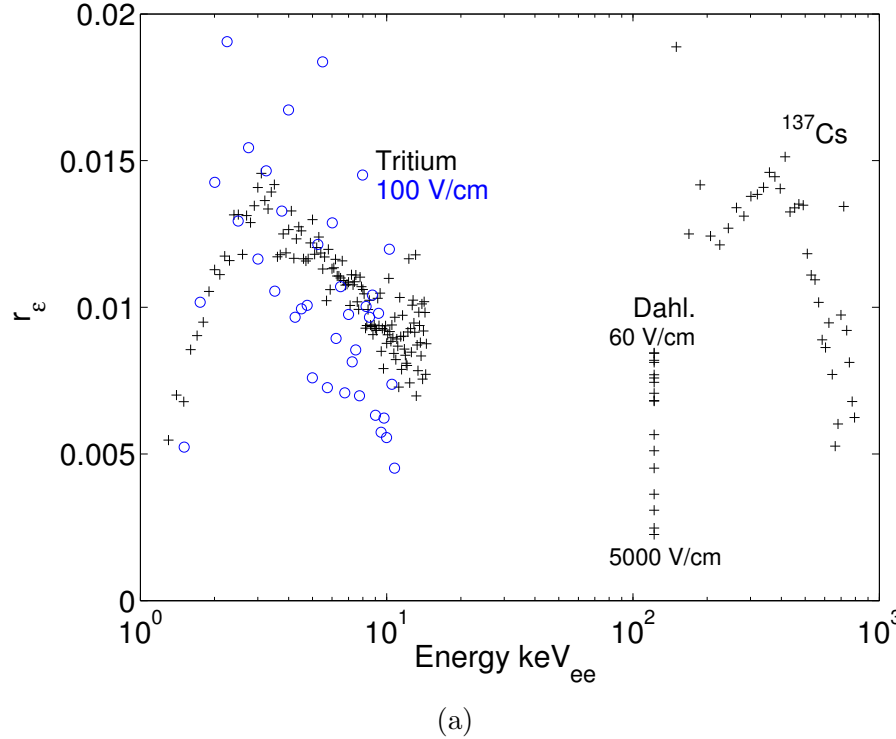


Figure 5.19: The data shown are labeled on the plot and include calibration data of tritium data at 170 V/cm, tritium at 100 V/cm (blue), ^{137}Cs at 170 V/cm, and data over a range of fields using ^{57}Co from Dahl. [8]. a) The encounter recombination probability r_e plotted vs. energy. b) The number of encounters per cluster N_e vs. energy. c) The number of clusters N_C vs. energy.

The average value of r_ϵ over a wide range of energies is found to be 0.01, shown in figure 5.19. The value of r_ϵ determined by using the cluster-encounter model is consistent with that noted by Mozumder in 1995 to explain ion fluctuations in liquid xenon [76]. The value of $r_\epsilon = 0.01$ corresponds to an average value of encounters $N_\epsilon = 50$, which can be thought of as the cluster size. Figure 5.19 (c) also shows the number of clusters vs. energy, which grows linearly with N_i . Note, the number of clusters is the factor by which the binomial fluctuations of the initial self-recombination model are amplified at a given energy.

The number of interaction per cluster N_ϵ , or cluster size, sets the encounter probability r_ϵ in this model. The value of N_ϵ appears to level off around 25 as energy tends to zero and varies between 25 to 100 over a wide range of energies and electric fields. Both r_ϵ and N_ϵ appear to have dependencies on electric field and energy. Which is not surprising as both the track geometry and interaction probability depend on electric field and energy. The data from Dahl over the range of 60 to 5000 V/cm especially illuminates the dependancies vs. field. We proceed with a simplified model and take the value of N_ϵ as a constant. The average value of $N_\epsilon = 50$ is used to calculate the expected variance at each energy using equation 5.47, the result is shown in figure 5.20.

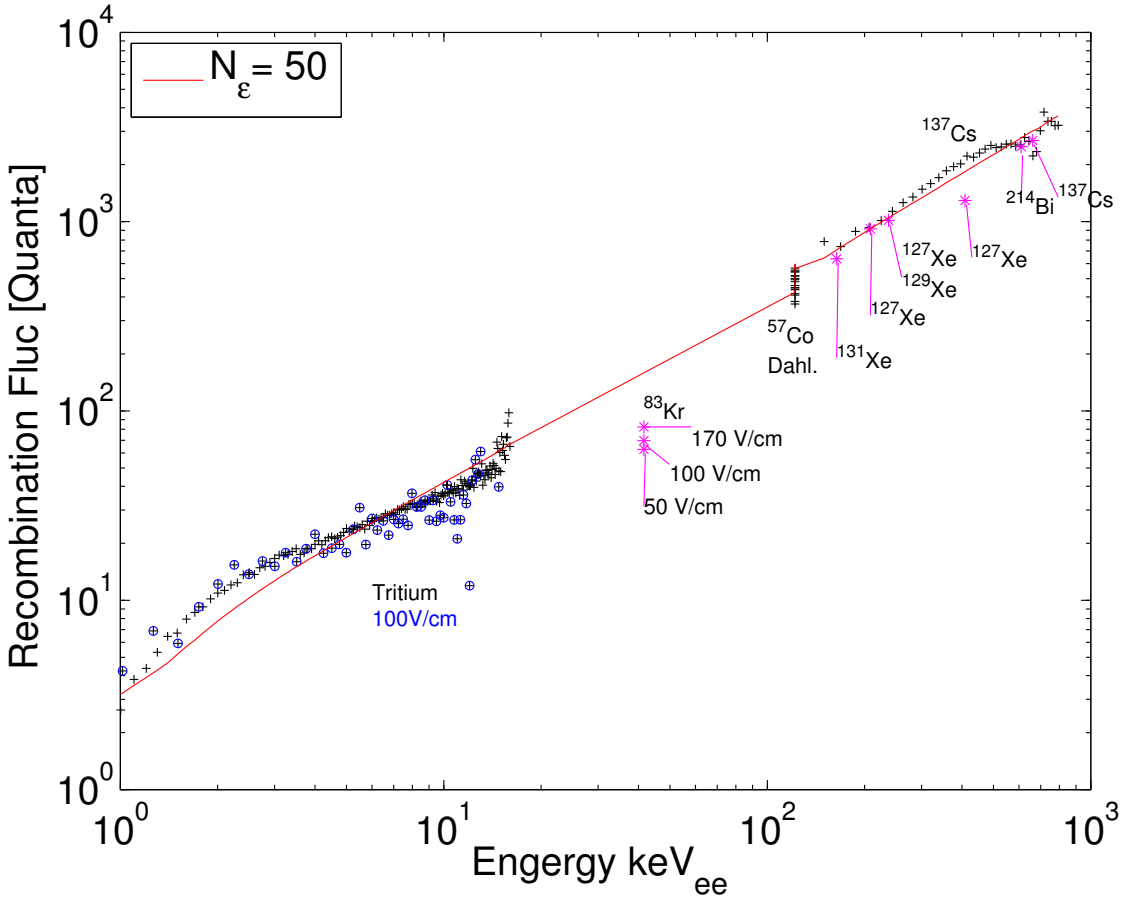


Figure 5.20: The measured recombination fluctuations from calibration data vs. energy. The red line indicates the expected recombination fluctuation of the clustering model given in equation 5.46, assuming a cluster size of $N_\epsilon = 50$. $N_\epsilon = 50$ corresponds to an average encounter recombination probability of $r_\epsilon = 0.01$. The deviation of the fit from the data is less than 30%. The ^{83m}Kr data point is the result of two decays and is expected to fall below the curve by 40% considering the sum of the individual variances.

Figure 5.20 shows the measured recombination fluctuations vs. energy along with that expected for the clustering model given in equation 5.46, for $N_\epsilon = 50$, corresponding to an average encounter recombination probability of $r_\epsilon = 0.01$. The deviation of the fit and the data is less than 30%, including Dahl's data taken at electric fields ranging from 60 to 5000 V/cm.

With the clustered encounter model we can now account for the recombination

fluctuations and understand why recombination tends to zero as energy tends to zero. Having explained these two phenomena, the clustered-encounter model is a significant improvement over the initial recombination model. The flaw of the initial recombination model was to assume that the recombination process only consists of ion-electron pair self recombination. This assumption is what lead to the observed variance being off by a factor of N_i and the inability to explain the dependance of recombination fraction as energy tends to zero. The picture of ER band mean and width is now complete, only requiring recombination fraction r as an input. The recombination fraction is dependent on the energy of the interaction and electric field, modeled by Thomas & Imel [77] and NEST [63], [64].

5.7 Conclusion

There have been numerous steps in this section culminating in expanding our knowledge by extracting as much information as possible from the calibration sources. We have measured that the best exciton to ion ratio α measured to be 0.20 in the WIMP search energies, which is consistent with the measurement from [73]. The value of alpha was constrained by extrapolating the recombination fluctuations from the tritium data from 3 to 1.2 keV and requiring that for a single ion-electron pair the fluctuation be purely binomial, shown in figure 5.11.

The recombination model presented in this section can be used to predict the ER band for any xenon detector, as shown in figure 5.10. The most critical results are those specific to our WIMP search, 10-100 GeV WIMPs, which are focused in the range of 1 to 5 keV_{ee} and well covered by the tritium calibration data. Having extracted the values of r and σ_r for ER events the generic mean and band widths can be determined. Thus, the ER band shape can be determined for any xenon detector with the application of the additional variance from the specific detector resolution. The knowledge of this band shape can be used to make predictions about the background rejection power of a given experiment.

It is surprising to find that changing the drift field from 100 V/cm to 170 V/cm had only an epsilon impact on the mean of ER band below 4 keV_{ee}, figure 5.10. Further, there was no impact on the energy threshold since the light and charge yields merge at the threshold of 1 keV. A more dramatic field dependance was expected from [8] and [64]. However, the low energy region never been probed

to such high precision as with the tritium calibration using the LUX detector. To expand upon the modeling at low energies it will be useful for the next science run using the LUX detector to take tritium calibration data at a verity of fields. This will allow us to predict exactly how much additional NR and ER discrimination can be achieved by increasing the field.

Chapter 6: Ionization and Scintillation Yield from Tritium Calibration

In this section we measure the scintillation yield and ionization yield from the tritium calibration data. Using the measurement of gains g_1 and g_2 in chapter 4, the average number of photons, electrons and the corresponding combined energy can be determined. With that information the light yield (n_γ/keV) and charge yield (n_e/keV) are extracted from tritium data down to 1 keV_{ee}. Before the yields can be measured, the effect of finite detector resolution convolved with the tritium spectral shape must be accounted for. Detector resolution was characterized in chapter 5 and will be used to model the smeared tritium spectra as observed by the LUX detector. Once the spectral shape has been corrected we report the values of light yield and charge yield measured at 170 and 100 V/cm. The results are compared to two recent measurements for light yield in the keV range using Compton scatters. This provides a crucial cross check that the ER band calibration using the tritium beta source is valid for use with the more generic backgrounds found in WIMP search data consisting of Compton scatter from high energy gammas. At low energies the light yields and charge yields from betas and gammas are expected to be identical [63] [64].

6.1 Correcting for Spectral Shape for Finite Resolution

The distribution of tritium events convolved with the detector's finite resolution for S1 (scintillation) and S2 (ionization) causes the observed mean of the spectra to shift from the actual mean. The shift is non-trivial and depends on the spectral shape and the functional form of the resolution over a range of energies. A large negative derivative of the spectral shape will tend to pull the observed mean to lower values, and a large positive slope will pull the observed mean to higher values. Figure 6.1 and equations 6.2 and 6.4 demonstrate a simple model to solve for the relation between observed mean and actual mean. Consider, for example, a linearly declining distribution. Starting with infinite detector resolution we set up bins of width Δx . To account for finite energy resolution we distribute the counts in each rectangular bin into Gaussians centered at μ_i , with a spread of σ_i , and normalized to the area of the bin $N_i \times \Delta x$ with amplitude c_i . Each rectangular bin(i) can be written as a Gaussian $G(i)$:

$$c_i = \frac{N_i \times \Delta x}{\sigma_i \sqrt{2\pi}}$$

$$G_i(x) = c_i \times \exp\left(\frac{-(x - \mu_i)^2}{2\sigma_i^2}\right)$$
(6.1)

where N_i is the count in the i^{th} bin, Δx is the bin width, μ_i is the bin center and σ_i is the resolution at the i^{th} bin. Figure 6.1 show the application of equation 6.1 to a

linear energy distribution with a \sqrt{E} dependent σ . The observed distribution is the sum of the Gaussians, shown in red.

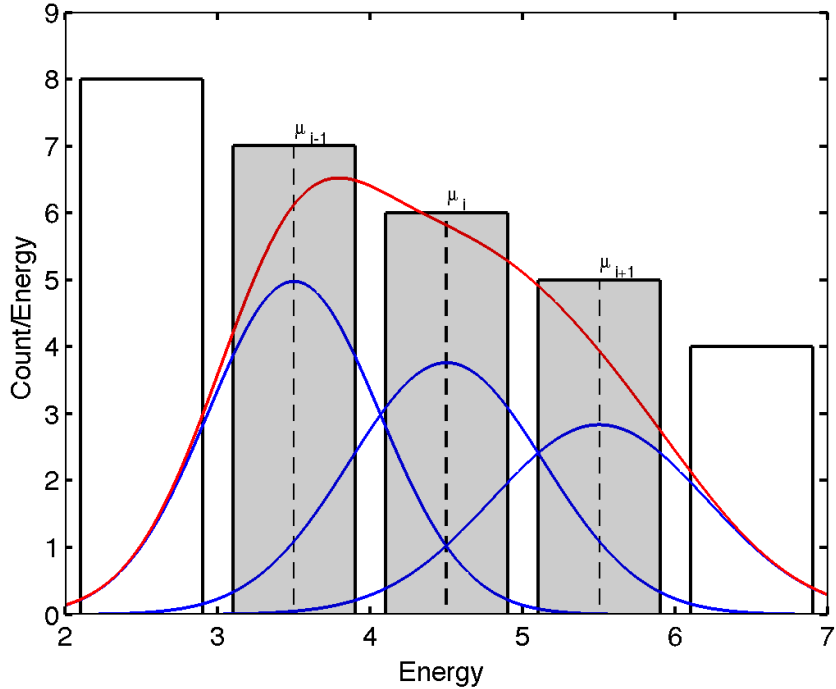


Figure 6.1: Smearing of a linear spectrum using equation 6.1 for an arbitrary energy scale E . The counts in each shaded bin are redistributed into normalized Gaussians (blue) with the resolution σ_E growing like \sqrt{E} . The spectrum smeared with detector resolution is the sum of Gaussians shown in red.

6.1.1 Calculating the Observed Energy

After modeling the finite resolution with Gaussians the mean observed at each bin can be calculated from the overlap of all bins weighted by the corresponding means. We can write the observed mean in the i^{th} bin, ν_i , in terms of the bin centers μ and

overlapping areas of all bins using the normalizations c_i from equation 6.1:

$$\nu_i = \frac{\sum_{j=1}^n \mu_j \int_{\mu_i - \frac{\Delta x}{2}}^{\mu_i + \frac{\Delta x}{2}} G_j(x) dx}{\sum_{j=1}^n \int_{\mu_i - \frac{\Delta x}{2}}^{\mu_i + \frac{\Delta x}{2}} G_j(x) dx} \quad (6.2)$$

Equation 6.2 can be solved in terms of error function and complimentary error function. First we will generalize a formula to solve for the overlapping area from the j^{th} bin into the i^{th} bin.

$$A_{i,j} = \int_{\mu_i - \frac{\Delta x}{2}}^{\mu_i + \frac{\Delta x}{2}} G_j(x) dx = \begin{cases} c_i \operatorname{erf}\left(\frac{\Delta x}{\sigma_i \sqrt{2}}\right), & j = i \\ \frac{c_j}{2} \operatorname{erfc}\left(\frac{|\mu_j - \mu_i| - \frac{\Delta x}{2}}{\sigma_j \sqrt{2}}\right) - \frac{c_i}{2} \operatorname{erfc}\left(\frac{|\mu_j - \mu_i| + \frac{\Delta x}{2}}{\sigma_j \sqrt{2}}\right), & j \neq i \end{cases} \quad (6.3)$$

The error function and complementary error function are defined in equation 6.4 and the coefficient c_i is defined in equation 6.1.

$$\begin{aligned} \operatorname{erf}(x) &= \frac{2}{\sqrt{\pi}} \times \int_0^x \exp(-t^2) \\ \operatorname{erfc}(x) &= \frac{2}{\sqrt{\pi}} \times \int_x^\infty \exp(-t^2) = 1 - \operatorname{erf}(x) \end{aligned} \quad (6.4)$$

As μ approaches zero the Gaussian distribution of equation 6.1 begins to spill over into negative values, which in some cases may be unphysical. For instance, the Gaussian assumption leads to negative photons. We can chose to ignore this area or make the distribution more Poisson-like by bouncing the Gaussian back at $\mu = 0$.

The formula for accounting for the area of the reflected Gaussian is described in 6.5. Ultimately this assumption has little impact on the S1 and S2 analysis because the threshold cut off well before the zero interface is reached, but it does make the distributions more Poisson like near the zeroth bins. Equation 6.5 is the same as 6.3 with the bin center μ_i mapped to $-\mu_i$.

$$B_{i,j} = \frac{c_j}{2} \operatorname{erfc} \left(\frac{|\mu_j + \mu_i| - \frac{\Delta x}{2}}{\sigma_j \sqrt{2}} \right) - \frac{c_j}{2} \operatorname{erfc} \left(\frac{|\mu_j + \mu_i| + \frac{\Delta x}{2}}{\sigma_j \sqrt{2}} \right) \quad (6.5)$$

Finally, we solve for the observed mean in the i^{th} bin by summing all the Gaussian overlaps $A_{i,j} + B_{i,j}$ (equations 6.3,6.5), weighting the overlapping area from each bin by the corresponding bin center μ_j . The result is shown in equation 6.6 and is equivalent to equation 6.2 when the area from the reflected Gaussian is not considered, $B_{i,j}=0$.

$$\nu_i = \frac{\sum_{j=1}^n \mu_j \cdot (A_{i,j} + B_{i,j})}{\sum_{j=1}^n (A_{i,j} + B_{i,j})} \quad (6.6)$$

6.1.2 Smearing a Toy Spectrum

To demonstrate the application of equation 6.6 we use it to smear a toy linearly decaying spectrum. By modifying the dependence of σ_i on μ_i we can better understand the effects of the spectral shape and the functional form of the resolution.

Figure 6.2 shows the effect of the finite resolution on a linearly decaying spectral shape. Using a constant resolution σ the observed mean, when accounting for finite resolution, shifts down due to the spectral shape. In the case with $\sigma_i \sim \sqrt{\mu_i}$

the observed mean at first shifts higher as the increasing width at higher value bin centers, even with lower counts, out weighs the lower bin centers with higher counts and narrower widths. In both cases as the bin centers approach zero the observed mean shifts higher due to an imposed threshold at zero, where Poisson statistics take over and the Gaussian characterization leads to a loss of events below zero. Thus, for the sake of the toy model in figure 6.2 we only characterize the relation between the real mean and the observed mean from the second bin center. It is also worth mentioning that for the case of having a varying resolution in figure 6.2 the shift in spectral shape seems minor, yet there is a significant 20% deviation in the observed mean of the last bin.

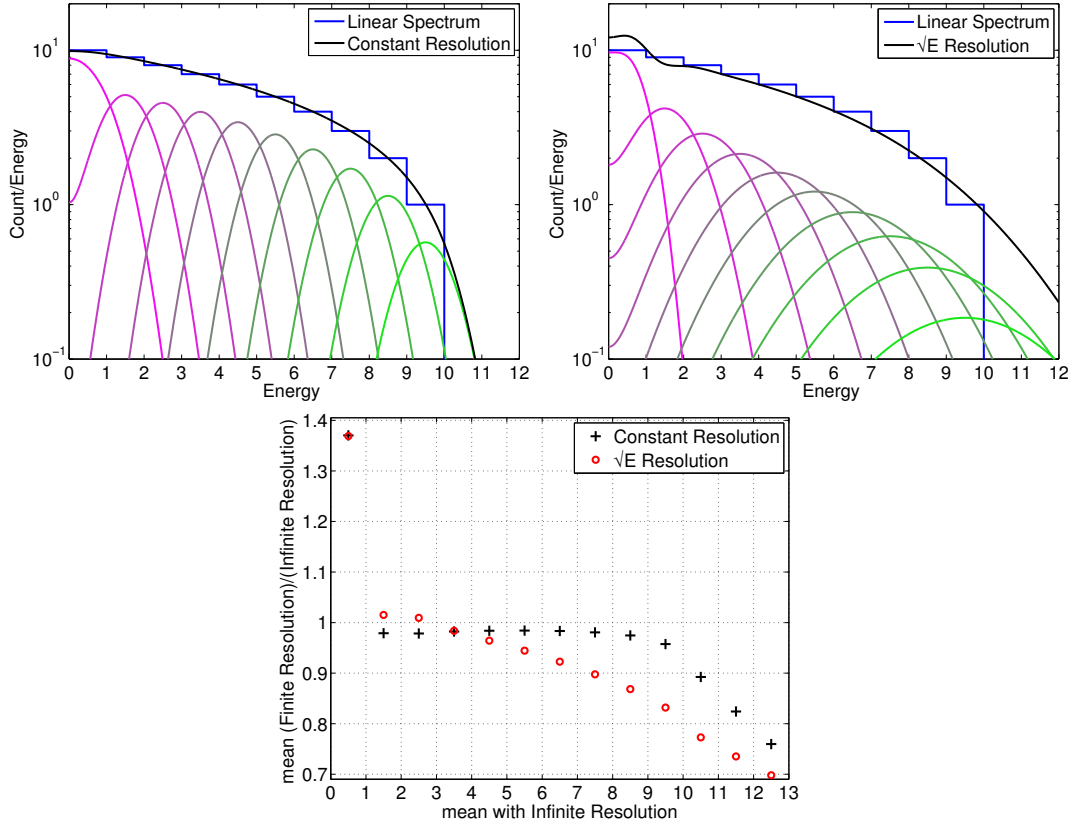


Figure 6.2: Top Left: A linearly decaying spectrum, in blue. The black curve represents the sum of the Gaussians assuming a constant resolution. Top Right: A linearly decaying spectrum, in blue. The black curve represents the sum of the Gaussians with a $\sigma = \sqrt{E}$ dependent resolution. Bottom: The observed mean, with finite resolution, compared to the real mean with infinite resolution. The black points are for the case with linear resolution and the red points represent the case with $\sigma = \sqrt{E}$ dependent resolution.

6.2 Light Yield, Charge Yield and Comparison to NEST Modeling

The first attempt to remove the effect of the tritium spectral shape and finite detector resolution is to use the NEST model from [64]. NEST stands for Nobel Element

Simulation Technique. NEST fits data from previous xenon and argon detectors to recombination models, producing predictions for light yield n_γ/keV and charge yield (n_e/keV) at a verity of electric fields, energy deposits, and particle types. We take the light yield (LY) and charge yields (QY) from NEST and convolve it with the known tritium energy spectrum to produce the S1 and S2 spectra. The S1 and S2 spectra are then smeared with detector resolution and recombination fluctuations, determined in chapter 5. It is found that the S1 and S2 spectra from the data deviate from the NEST model making it difficult to reverse-engineer the effect of smearing. However, taking the NEST model to be correct within 20%, the spectral shape correction is calculated and found to be small. We proceed to extract LY, QY and recombination fluctuation (σ_R) from the tritium data without any correction producing a model that is more accurate than NEST. It should be noted that the NEST model which has not been confirmed at our electric field and energy.

6.2.1 Tritium S1 and S2 vs. NEST

The spectral shape correction for the mean of the observed S1 and S2 signal from tritium beta decay can be found using equation 6.6. We start with NEST to get the expected S1 and S2 tritium spectrum. The variance of S1 and S2 arise from recombination fluctuations and detector resolution (statistical and instrumental fluctuations), given in equation 5.7 and 5.8. We use equations 6.7 and 6.8 to smear the photon and electron yields, essentially putting in detector resolution by hand. Then, by applying equations 6.1-6.6 the S1 and S2 bin centers after smearing can

be mapped back to the true bin centers before smearing.

$$\begin{aligned}\sigma_{S1_R}^2 &= g_1^2(\sigma_R^2) \\ \sigma_{S1_{\text{Det}}}^2 &= g_1^2(\sigma_{n_{\gamma_{\text{stat}}}}^2 + \sigma_{n_{\gamma_{\text{inst}}}}^2) \\ \sigma_{S1}^2 &= \sigma_{S1_R}^2 + \sigma_{S1_{\text{Det}}}^2\end{aligned}\tag{6.7}$$

$$\begin{aligned}\sigma_{S2_R}^2 &= g_2^2(\sigma_R^2) \\ \sigma_{S2_{\text{Det}}}^2 &= g_2^2(\sigma_{n_{e_{\text{stat}}}}^2 + \sigma_{n_{e_{\text{inst}}}}^2) \\ \sigma_{S2}^2 &= \sigma_{S2_R}^2 + \sigma_{S2_{\text{Det}}}^2\end{aligned}\tag{6.8}$$

where g_1 and g_2 are the gains to convert S1 and S2 to number of photons and electrons, respectively. The values $\sigma_{S1_R}^2$ and $\sigma_{S2_R}^2$ are the variances in S1 and S2 given only recombination fluctuations, this is what a detector with infinite resolution would observe. Detector resolution is comprised of the statistical and instrumental fluctuations in light and charge collection written as $\sigma_{S1_{\text{Det}}}^2$ and $\sigma_{S2_{\text{Det}}}^2$, this would be the resolution given no recombination fluctuations. The total variance in S1 and S2 observed by a detector with finite resolution is the sum of recombination fluctuations and detector resolution $\sigma^2 = \sigma_R^2 + \sigma_{\text{Det}}^2$ (where the subscripts S1 and S2 have been removed). The use of Gaussian sigma down to low S1 is an acceptable approximation since the underlying distribution actually consists of the number of photons, $n_\gamma = \frac{S1}{g1}$. With $g1=0.097$ there are still 30 photons near the S1 threshold of 3 PE. The S2 threshold for golden events is around 400 PE, $n_e = \frac{S2}{g2}$. With $g2=5.75$ there are still 70 electrons near the lower end of the tritium spectrum.

Figure 6.3 (a,c) shows the application of smearing from equation 6.7 and 6.8

to the expected S1 and S2 tritium spectrum, respectively, overlaid with the data. The mapping of the observed S1 and S2 mean values to the real S1 and S2 mean values is shown in 6.3 (b,d). The mapping from observed mean to real mean is the result of starting with infinite resolution containing recombination fluctuations only (σ_R) and applying the model as outlined in 6.1 with detector resolution (σ_{Det} of equations 6.7 and 6.8).

We find that that peak location of the S2 spectra from NEST deviates from the data by up to 20%. These discrepancies maybe arising from the error in g_1 and g_2 which could systematically shift light yield and charge yield by the appropriate amount. However, modifying g_1 and g_2 only induces a horizontal shift left or right, and the data indicates the need to modify the derivative of LY and QY from NEST.

Since the means of the model do not line up with the data the calculated corrections in figure 6.3 can't be applied. In order to account for detector resolution as outlined in section 6.1 we must have a reasonably accurate initial guess of the spectrum with infinite resolution. In this case we do not. However, even though the means from NEST light and charge yields are off we find that the effect of recombination fluctuations and detector resolution is relatively small. The correction for the S1 ranges from +30% to -20% and the S2 correction from +2% to -10%. We takes these as small enough to proceed with extracting light yield, charge yield and recombination without any correction in order to construct a more accurate model than our initial NEST prediction. Having outlined a method for mapping the observed S1 and S2 means to their real values we will now gauge the effect of finite resolution on the observed total energy.

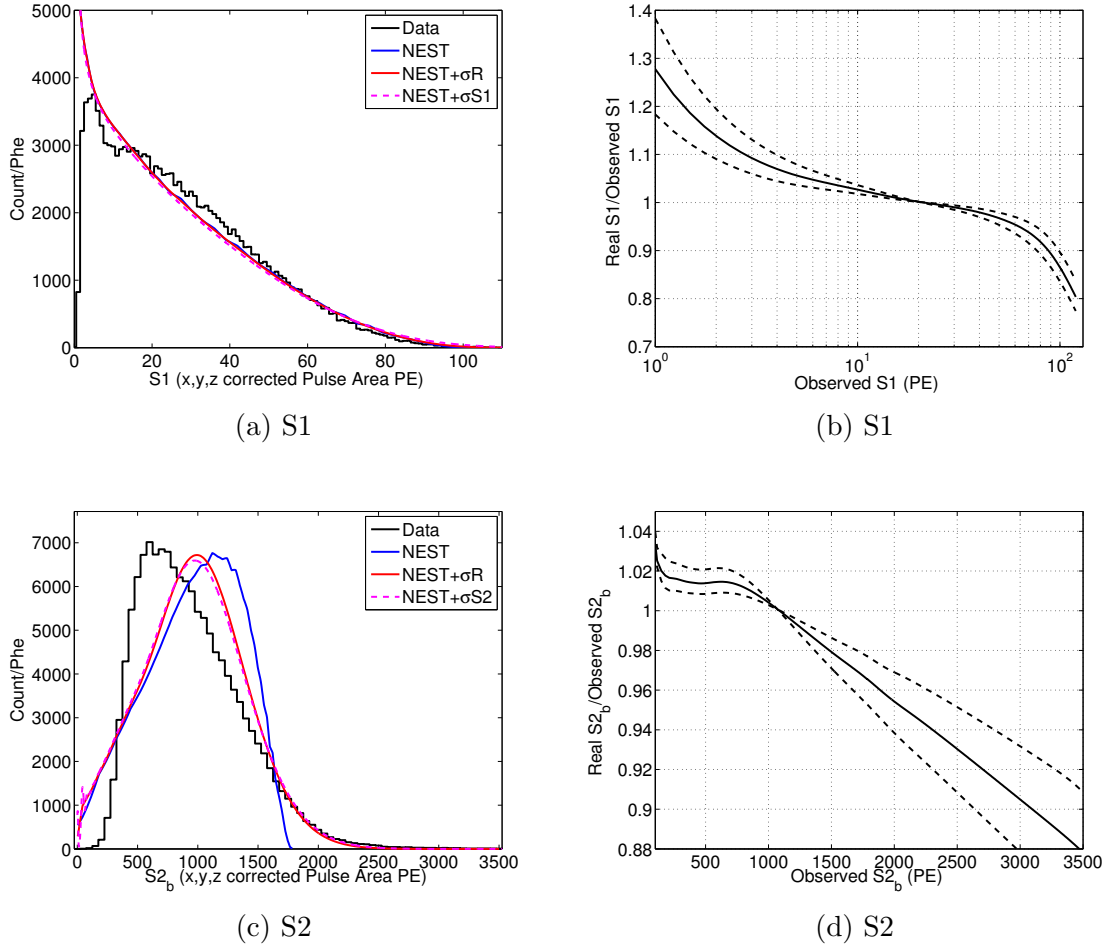


Figure 6.3: a): In Black S1 tritium S1 spectrum extracted from the data. In blue, The NEST light yield curve. In red, the NEST light yield curve with recombination fluctuations. Dashed magenta is NEST light yield with smearing from equations 6.7. b): The ratio of the real S1 mean to the S1 observed mean vs. the observed mean after smearing. Note, the S1 threshold at about 3 PE in S1. c): In Black S2 tritium spectrum extracted from the data. In blue, The NEST light yield curve. In red, the NEST light yield curve with recombination fluctuations. Dashed magenta is NEST light yield with smearing from equations 6.8. d): The ratio of the real S2 mean to the S2 observed mean vs. the observed mean after smearing.

6.2.2 Tritium Energy Spectrum

Unlike the S1 and S2 spectra which are dependent on light and charge yield, the tritium energy spectrum is well known [14]. The tritium spectrum is perhaps the most studied beta spectra, so there is no need to rely on modeling. Also, recombination

fluctuations cancel out in combined energy space leaving only detector resolution to be applied for smearing, given equation 6.11. The accuracy of the smearing model described in equations 6.1-6.6 can be tested by comparing it against the energy observed after a full simulation, which accounts for detector geometry and having been processed by the full offline framework. Using equation 5.25, 5.1 and 6.9 we solve for the the variance of E (σ_E^2),

$$E = W(n_\gamma + n_{e^-}) \quad (6.9)$$

$$\sigma_E^2 = W^2(\sigma_{n_\gamma}^2 + \sigma_{n_{e^-}}^2) \quad (6.10)$$

$$\sigma_E^2 = W^2(a_\gamma^2 n_\gamma + a_e^2 n_{e^-}) \quad (6.11)$$

W is the work function $0.0137 \pm 0.002 \frac{\text{keV}}{N_{\text{quanta}}}$, n_γ and n_e and number of photons and electrons respectively. The constants a_γ and a_e represent the coefficients of the \sqrt{n} term for the statistical uncertainty given in equation 5.7. There is also an instrumental component which is proportional to n_γ and n_e . However, the instrumental term is subdominant at the low tritium energies with coefficients given in equation 5.8.

Starting with the tritium energy spectrum with infinite resolution we apply the empirically determined resolution in equation 6.11. Figure 6.4 shows the comparisons of the true tritium spectrum, the spectrum with smearing from equation 6.11, the expectation from LUXSIM and the data. The smearing from the model described in equations 6.1-6.6 is found to be almost identical to the output of LUXSIM.

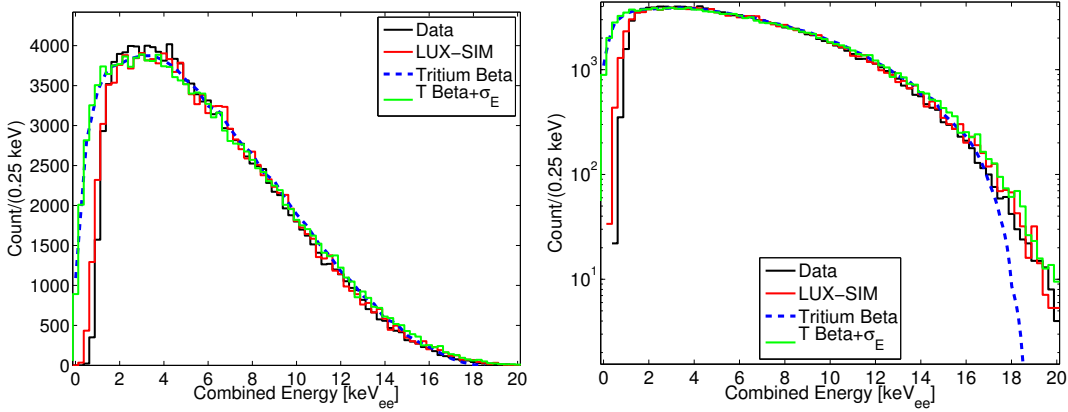


Figure 6.4: The tritium energy spectrum reconstructed from the data (black). Along with LUX SIM (red), the true tritium beta spectrum (dashed blue) and a tritium spectrum smeared with detector resolution of equation 6.11 (green).

Comparing the true tritium spectrum, the data, LUXSIM and the spectrum with 6.11, we find that for the cases with finite resolution the endpoint flare out above 16 keV. With the endpoint reaching out past 20 keV instead of terminating at 18.6 keV. This effect is precisely what the modeling in section 6.1 attempts to undo. Clearly events observed at 20 keV must have fluctuated up from bins below the tritium endpoint at 18.6 keV [74]. Most importantly, besides the additional fluctuation around the endpoint the difference in spectral shape after accounting for finite resolution is hardly noticeable.

The mapping for observed energy to true energy is calculated for both LUXSIM and the simpler smearing model of equation 6.11. From the LUXSIM data the initial Monte Carlo values of each event are compared to the final reconstructed energies. Each energy deposit is simulated with photon and electron propagation along with light collection in the LUX detector. Figure 6.5 shows the results for mapping

observed energy to real energy using both smearing methods.

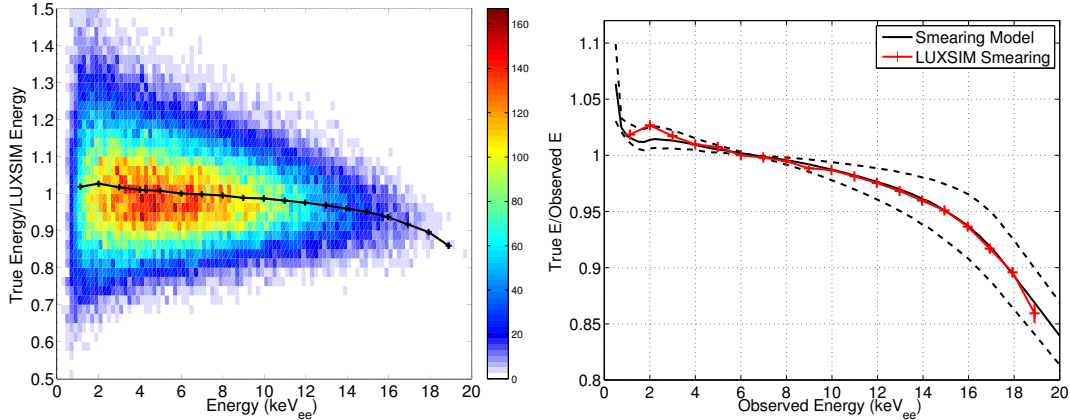


Figure 6.5: Left, mapping from real Monte Carlo energy to observed energy plotted vs the observed energy after applying a finite resolution using LUXSIM. Right, comparing the correction determined from the Monte Carlo (Red) to the detector smearing model (black) given in equation 6.11. The dashed lines represent the uncertainty in the measured values. The agreement is within errors from 1 to 18 keV_{ee}. The Energy threshold is 50% at 1.0 keV_{ee}.

The shift in the observed mean from the true mean for both LUXSIM and the model of equation 6.11 are in good agreement down to the threshold of 1.5 keV, the agreement with simulation is always within 1%. Below 2 keV the model predicts the ratio of true energy to observed energy to rise as there are greater number of events at higher energy spilling over to lower energy. The simulation however does not show this behavior leading to a 5% discrepancy in the 1 keV bin. Comparing the modeled detector resolution to the more complex LUXSIM simulations provides a proof of principle of the model.

The effect of detector resolution on skewing the true energy to observed energy

is found to be minor, blowing up only at the tail end of the tritium spectrum. Over 95% of the tritium event occur between 1 and 15 keV were the correction is less than 5%. With this information we proceed with extracting light and charge yields without concern about incorrectly assigning the energy bin.

6.2.3 Results for Light Yield, Charge Yield and Recombination

As shown in figure 6.3 the S1 and S2 spectral shape is not a good match with the light yield model from NEST, thus applying a correction to the observed means using NEST is not prudent. Fortunately, both for the S1 and S2 the spectral shape correction is less than 10% in the region where the vast majority of the tritium events are populated. Further, the reconstructed energy is also valid to within 5%. Knowing this we can move forward with extracting a more accurate light yield and recombination fluctuations.

By the same method outlined in section 5.4, the number of photons, electrons and recombination fluctuation is extracted from the tritium data. This is the result of the raw data uncorrected for the spectral shape. The result is shown in figure 6.6.

Having measured number of photons, electrons in each energy bin we compare the tritium data to NEST yields, shown in figure 6.7. The disagreement between the data and the NEST yields was expected since before the S1 and S2 tritium spectrum did not line up, shown in figure 6.3 . Though the means do not match the measured light yield is within 1 sigma considering the large systematic uncertainty in gains

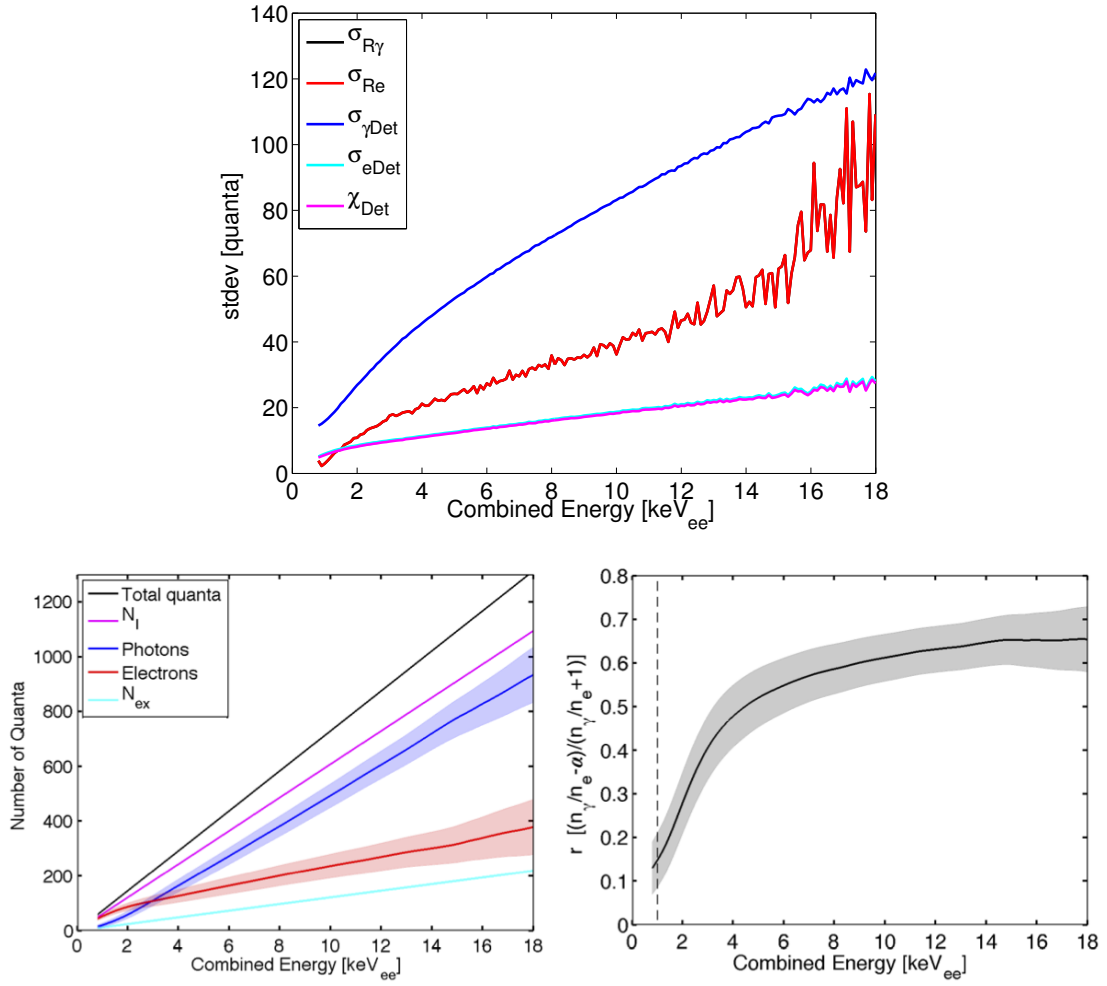


Figure 6.6: Top: Extracted recombination fluctuation from the tritium data from fluctuations in photons and electrons (Black and Red respectively). Bottom right: mean number of quanta in photons, electrons, ions, excitons vs. energy keV for the tritium calibrations. Bottom left: Recombination fraction and the one sigma (shaded) vs. energy keV.

g1 and g2. The figure also shows the one sigma prediction of the yields from NEST [64] shaded in blue where the model is interpolated and magenta where the model is extrapolated.

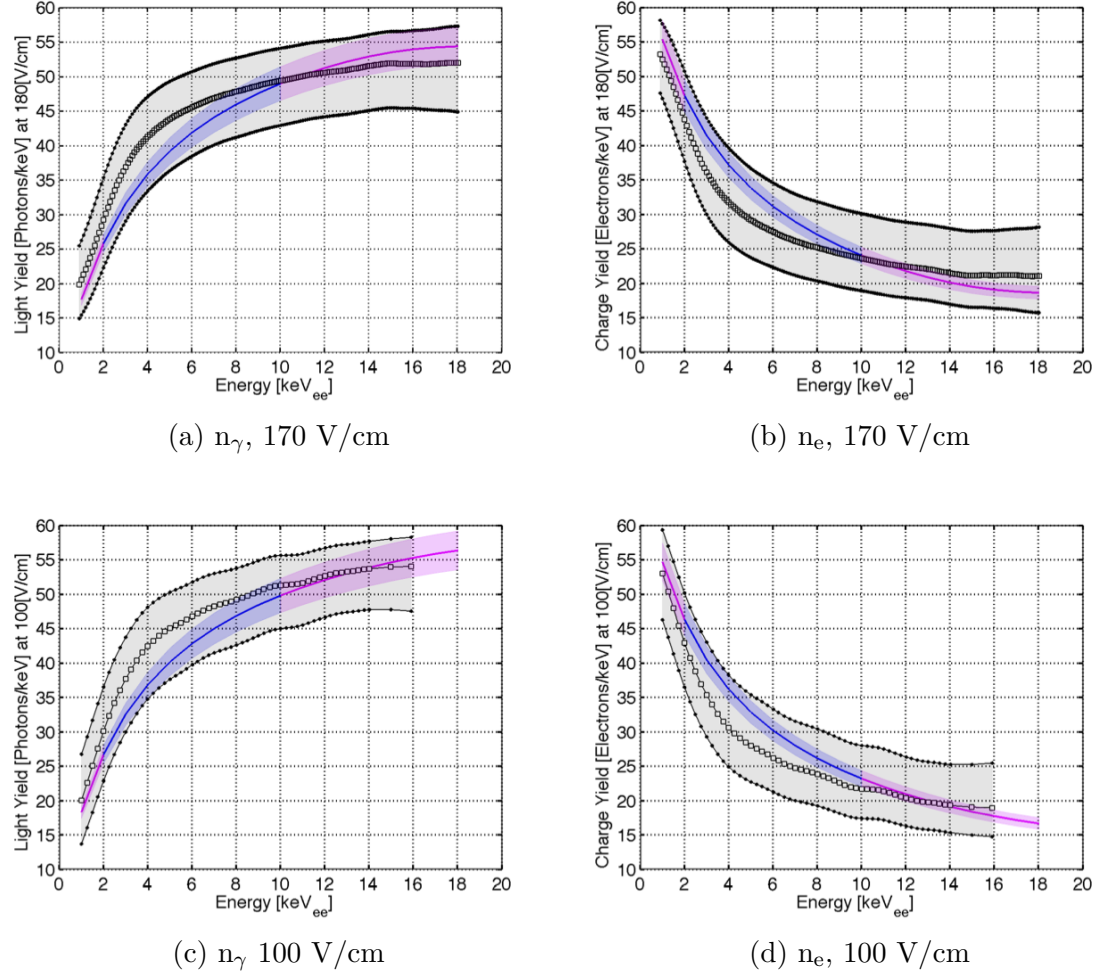


Figure 6.7: Light yield and charge yield from tritium data without spectral shape correction at 170 V/cm in black. The shaded region represents the one sigma systematic uncertainty on g1 and g2. The NEST yield prediction and its corresponding 1 sigma is shaded in blue. NEST interpolation is shown in magenta to energies where the model is not vetted. Note that the statistical errors are about the size of the data points and the dominant uncertainty illustrated by the shaded region is 100% correlated bin-to-bin. A one sigma shift up in light yield corresponds to a one sigma shift down in charge yield and visa versa.

The yields and recombination fluctuations measured from the tritium data

can be used to construct an improved model over the initial NEST prediction. As mentioned previously, the effect of detector resolution can be ignored in the region where the vast majority of the tritium events occur. Having built a new model for yields we now proceed to patch up the 20-30% shifts which occur at the edges of the S1 and S2 tritium spectra.

6.3 Measuring Light Yield, Charge Yield and Recombination, Corrected for Spectral Shape

Using the light yield and charge yield measurements extracted from the uncorrected tritium data we improve the light yield and charge yield model over the initial NEST-based model. In this section we will take the information gathered in the previous section to calculate the spectral shape correction for the tritium S1 and S2. With the improved model for LY and QY we can determine the efficiency for detecting S1s, S2s and the energy threshold. Finally, after applying the correction we can extract the true light yield and charge yield information from the tritium data.

6.3.1 Tritium S1 and S2 Correction

We now proceed to calculate the spectral shape correction using the method outlined in section 6.2.1 with NEST yields replaced by those measured from the uncorrected tritium data. Figure 6.8 (a,c) shows the application of smearing from equation 6.7 and 6.8 applied to the light and charge yield extracted from the uncorrected tritium

data. The mapping of the observed S1 and S2 to the real S1 and S2 is also shown in the figure 6.8 (b,d). The correction is determined by using the extracted yields, applying the gains g_1 and g_2 , and convolving it with a true tritium beta spectrum along with the measured recombination fluctuations, equation 6.7 and 6.8. Given infinite detector resolution this is the spectrum the LUX detector would observe for S1 and S2, labeled on the figure as $LY-T + \sigma_R$ and $QY-T + \sigma_R$ respectively. After applying detector resolution from equation 5.9 to the plotted $LY-T + \sigma_R$ and $QY-T + \sigma_R$ spectrum we calculate the mapping from the real S1 and S2 means to the observed means using the model outlined in 6.1. The final spectrum with recombination fluctuations and detector resolution is labeled as $LY-T + \sigma_R + \sigma_{S1}$ and $QY-T + \sigma_R + \sigma_{S2}$.

As expected, we find good agreement between the smeared tritium S1 and S2 spectra with the data. The spectral shape correction found for both S1 and S2 is consistent with those found by using NEST previously, shown in figure 6.8. This gives us confidence that we can apply the mapping of true mean to observed to the data.

The meaning of the spectral shape corrections for S1 and S2 shown in figure 6.8 (b) and (d) can be understood as a mixture of spectral shape and varying resolution. As the measured value of S1 drops to 1 PE (20% detection efficiency) we find the correction factor rises to a factor of 1.3. Even though the count rate is growing in lower S1 bins the narrowing S1 resolution cancels out the spill over from lower S1s as compared to the overlap from larger S1s with a lower count. This effect causes an observed S1 mean of 1 PE to actually be comprised of events with a mean of 1.3

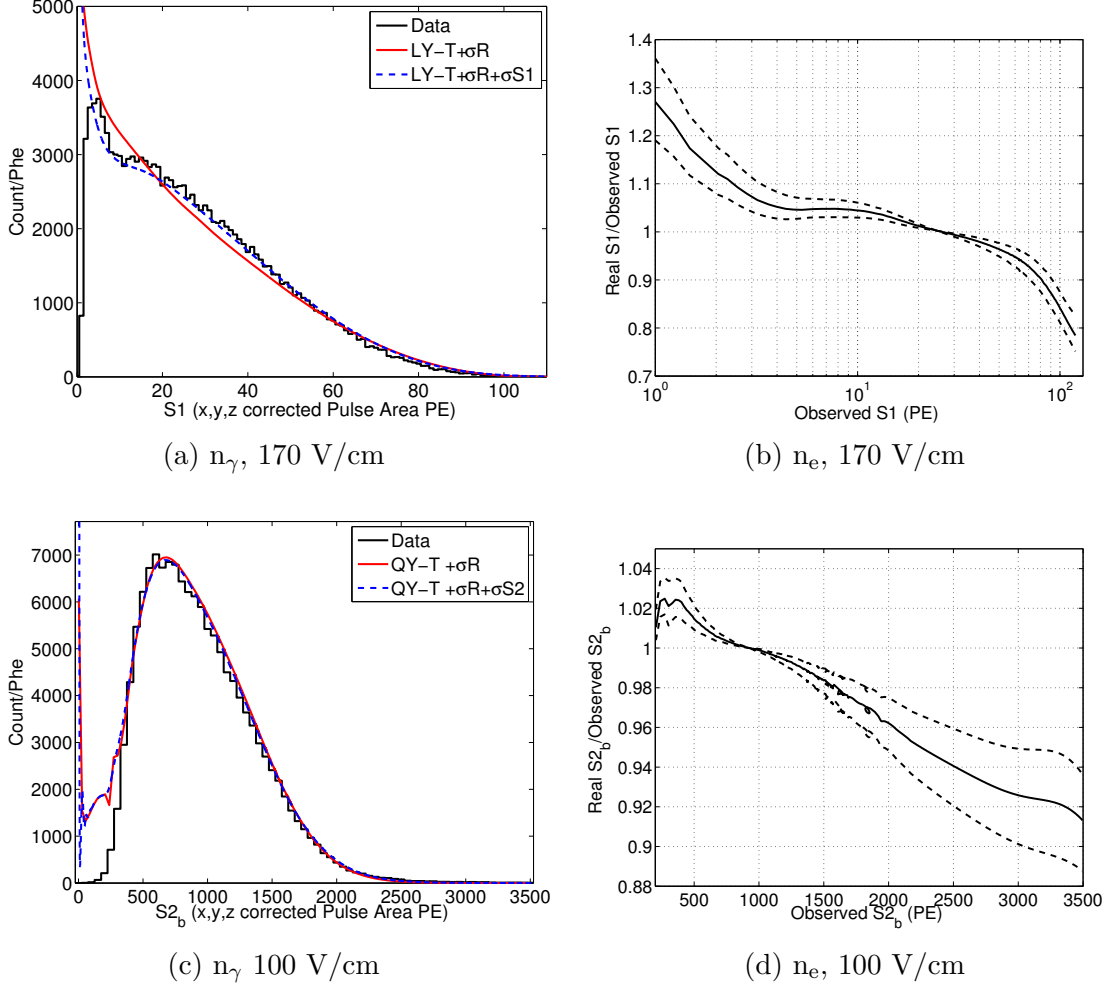


Figure 6.8: a): In Black S1 tritium S1 spectrum extracted from the data. In red, the S1 spectrum based upon the LY and QY measured from the tritium data after applying recombination fluctuations. In dashed blue, the expected S1 spectrum after applying finite detector resolutions of equation 6.7. b): The ratio of the real mean to the observed mean vs. the observed mean after smearing the tritium photon spectrum with detector resolution. Note the S1 threshold at about 3 PE in S1. c): In black, tritium S2 spectrum from the data. In red, the S2 spectrum based upon the LY and QY measured from the tritium data after applying recombination fluctuations. In dashed blue, the expected S2 spectrum after applying finite detector resolutions of equation 6.8. d): The ratio of the real mean to the observed mean vs. the observed mean after smearing the tritium electron spectrum from NEST with detector resolution. Note the S2 threshold at about 400 PE in S2.

PE. On the other end the correction is straight forward. As the beta spectrum is dropping sharply to reach 0 at the Q value of 18.6 keV [74] events from the more populated lower energy bins spill over into higher energy regions. This effect causes

the observed mean at the endpoint of 18.6 keV to actually be comprised of events with an average energy of 15 keV. Note, that the energy spectrum with detector resolution extends to 21-22 keV due to upward statistical fluctuations in S1 and S2. The S2 spectrum exhibits the same behavior at the high end above the peak of the spectrum around 1000 PE. As the S2 approaches threshold of 400 PE there is a < 3% correction to the mean to account for the spill over of the more populated regions to the right. This is different than case of S1 at low PE as the S2 resolution is about a factor of three better at the threshold.

6.4 Ionization and Scintillation Yield After Correction

The light and charge yield which can now be extracted from the tritium data are unique properties of liquid xenon given for ER interaction at low energies. Figure 6.9 shows the data used to calculate the means after having corrected for the S1 and S2 spectral shape. Two tritium calibration data sets are shown, one with high statistics at 170 V/cm containing 140,000 events and the second at 100 V/cm with a modest 2,500 events. (Both numbers correspond to events in the fiducial volume).

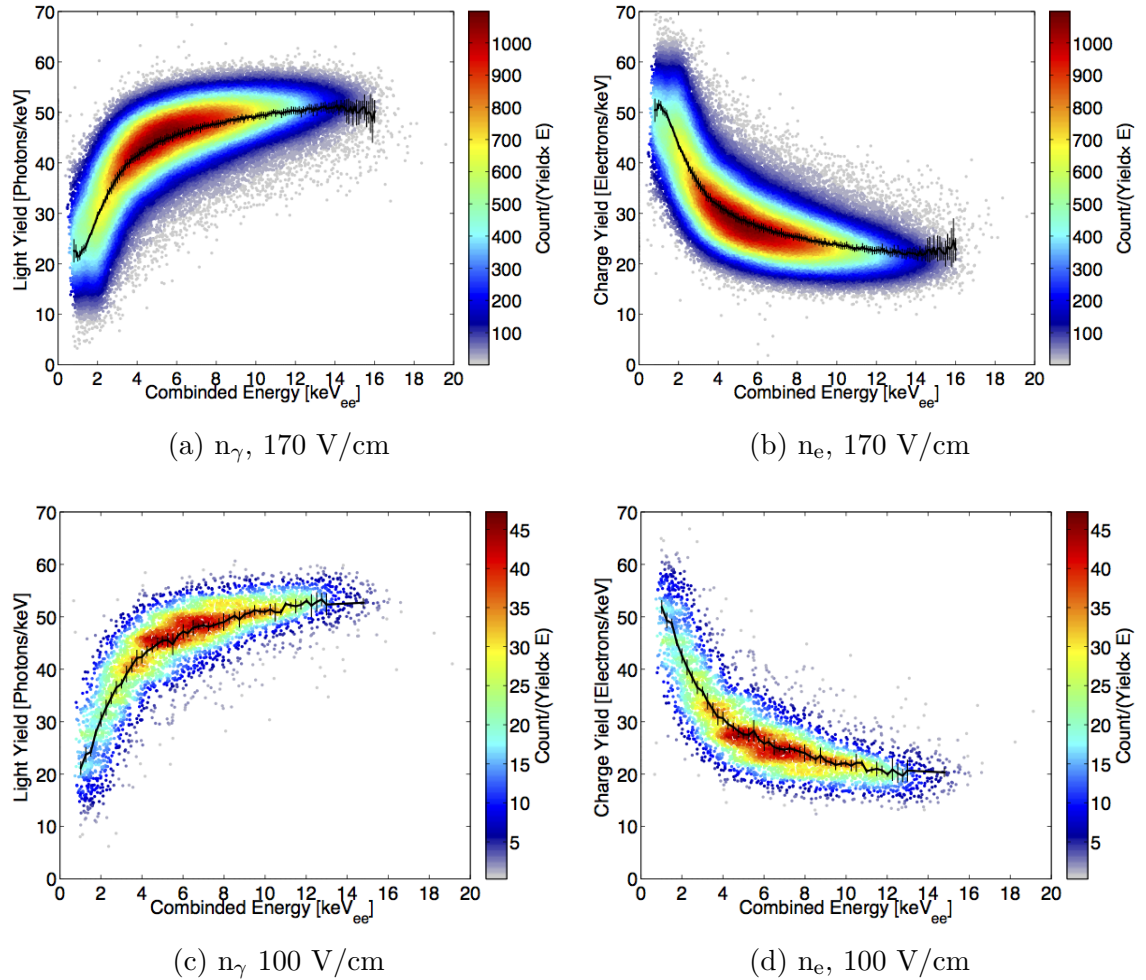
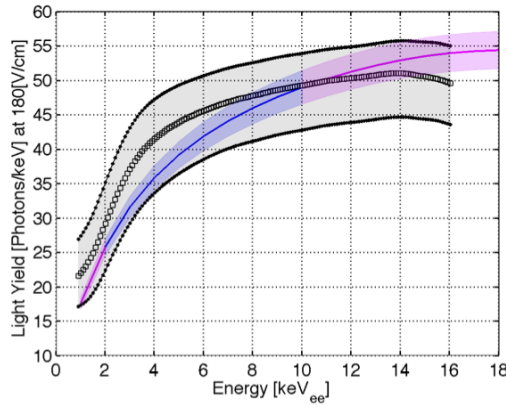


Figure 6.9: Means of the light yield and charge yield from tritium data corrected for spectral shape along with the 1 sigma statistical errors.

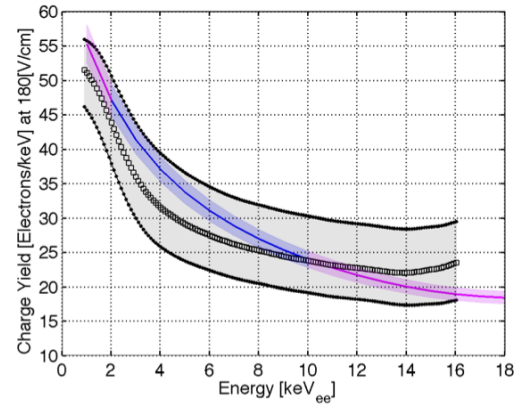
The means used for LY and QY are the population means in each slice of energy for our best value of g1 and g2. The errors shown are the statistical errors along with a small systematic component from the difference of the population mean from the Gaussian mean. The systematic offset from the constraint of g1 and g2 are treated in figure 6.10. With the potential for tighter constraints on the value of gains g1 and g2, the remaining uncertainty in the measurement of LY and QY would be less than 3% below 10 keV. The tritium calibration source has the potential to be used to determine the light and charge yield in liquid xenon to less than 3% including at the detector threshold. This calibration source hold great promise considering that few yield measurements exist below 5 keV.

Figure 6.10 shows the mean yields with the one sigma bands from the uncertainty in gains g1 and g2. The errors are anti-correlated, thus a shift up in light yields corresponds to a shift down in charge yield preserving the energy. The figure also shows the one sigma prediction of the yields from NEST [64] shaded in blue where the model is interpolated and magenta where the model is extrapolated.

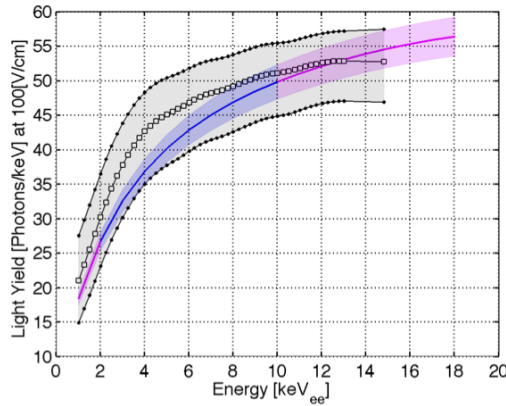
The overlap between the data and the NEST model is within one sigma considering errors in g1 and g2. However, as the errors in g1 and g2 are systematic and 100% correlated bin-to-bin they can only shift the curves up or down. Even under such a shift, the shape of the tritium data would not agree perfectly with the NEST prediction. As the statistical uncertainty alone constrains the means to better than 3% below 10 keV for the 170 V/cm data set.



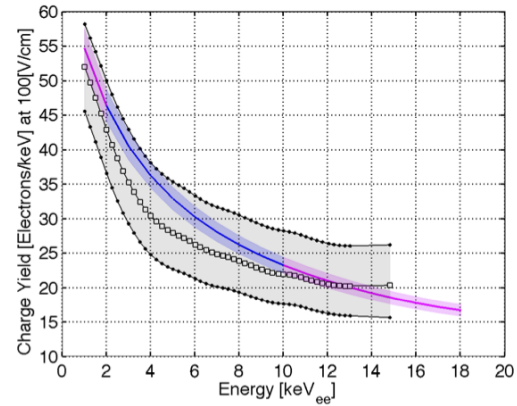
(a) n_γ , 170 V/cm



(b) n_e , 170 V/cm



(c) n_γ 100 V/cm



(d) n_e , 100 V/cm

Figure 6.10: Light yield and charge yield from tritium data corrected for spectral shape along with the 1 sigma systematic constraint on $g1$ and $g2$. The blue and magenta curve are NEST extrapolation and interpolation, respectively.

The comparison of measured light and charge yield before and after the tritium spectral shape correction is shown in figure 6.11 . The band in red is the result from using the raw data and combined energy, the band shown in blue is after the correction. The yields before and after the correction overlap with the exception of the last 15-18 keV bins which are pulled back as the events reconstructed at those energies on average were the result of events with 20% less energy, having upward fluctuated. In the middle regions however the spectral shape correction of the energy, the photon (S1) and electron (S2) spectrum are canceled. Recalling that yield is defined as n_γ/E , and n_e/E , with $E = W(n_\gamma + n_e)$. Thus, on average the upward or downward fluctuations in collected photons and electron are canceled by the corresponding fluctuations in reconstructed energy E.

One question remaining to be answered is if the yields and ER band defined by tritium beta decays are consistent with the more generic Compton Scatter backgrounds, which are expected to be found in the WIMP search data. It is expected that betas and gammas are indistinguishable below 10 keV [63] [64]. In the following section we will compare the light yield results from the tritium data with recent Compton scattering measurements that have probed light yield in xenon down to 1.5 keV.

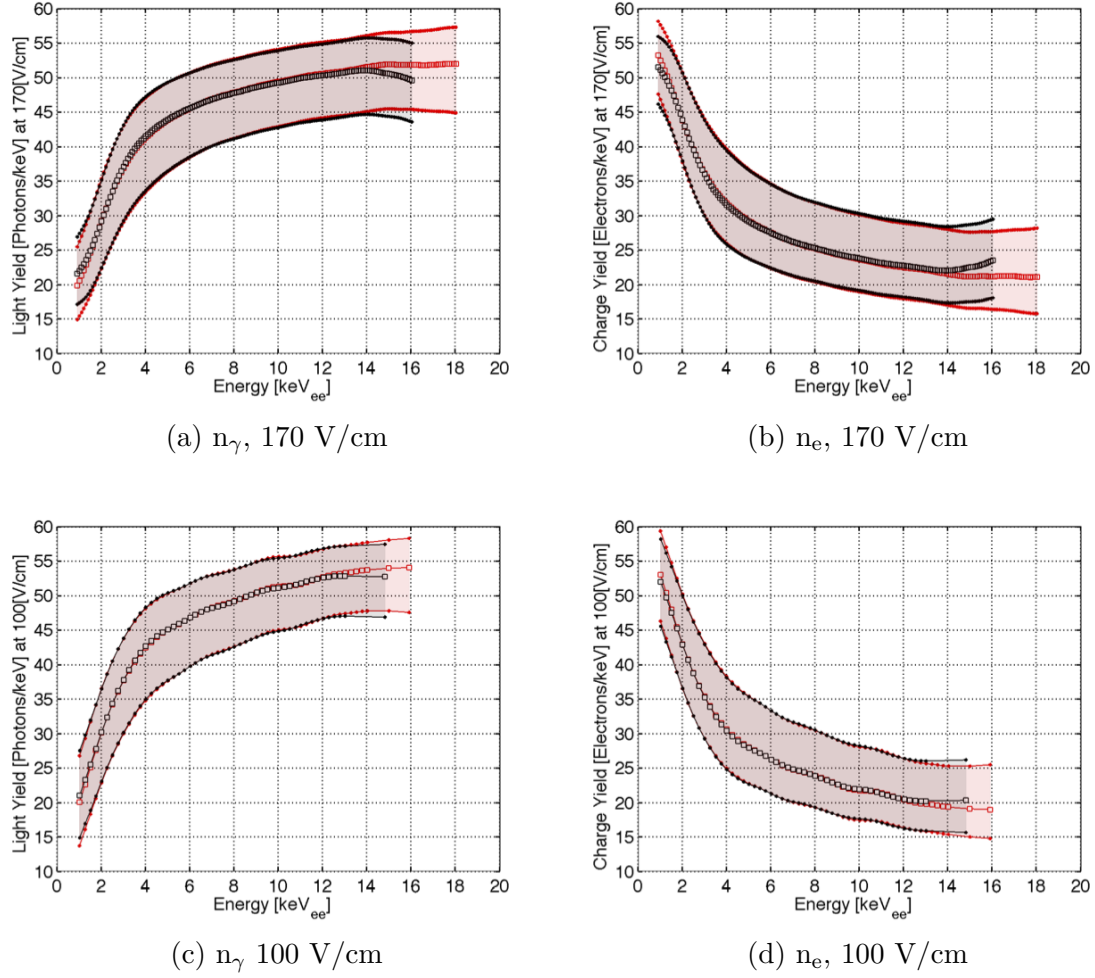


Figure 6.11: In black, the light yield and charge yield from tritium data corrected for spectral shape. In red, the light yield and charge yield from tritium data uncorrected for spectral. The shaded region represent the one sigma systematic error from the constraint on g_1 and g_2 shaded.

6.5 Comparison of Light Yield Measured With Tritium to Other Measurements With Compton Scatters

In this section we compare the LY measured with tritium in LUX to that measured with Compton scatters by other researchers. When comparing measurements from different xenon detectors it is prudent to report the result relative to that of a standard calibration source. The light yields reported for low energy Compton scatter measurements from [10] [13] are normalized to the first 32.1 keV decay of ^{83m}Kr . Before comparing the light yields results from the tritium calibration we first need to measure the light yield in LUX at zero field from ^{83m}Kr .

6.5.1 The Standard Candle: Light Yield from ^{83m}Kr

The ^{83m}Kr source was discussed in greater in chapter 3. The decay of ^{83m}Kr consists primarily of the emission of two internal conversion electrons at 32.1 keV and 9.4 keV, with a half life of 154 ns between the two [9] [11] [12]. The combined signal (41.6 keV) is found by the LUX pulse finder in the majority of cases. However, the combined signal is not useful as a standard calibration. The second 9.4 keV decay receives an enhancement in light yield due to increased recombination probability from the presence of ions and electrons from the initial 32.1 keV decay. It has been observed that the light yield enhancement depends upon the decay time separation, out to 1000 ns [9] and [10]. In the LUX detector we have also observe the enhancement of the light yield of the second 9.4 keV out to 2000 ns shown in

figure 6.12. Our ability to split pulses with 100% efficiency starts at 1200 ns.

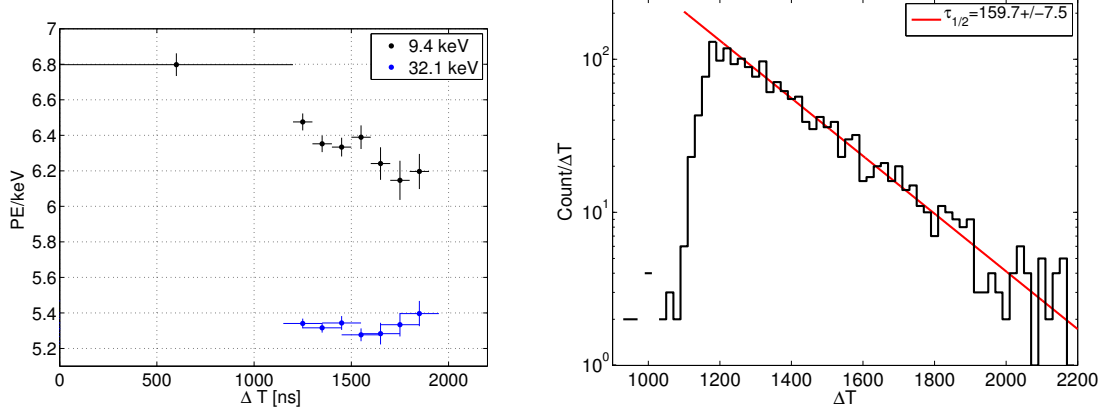


Figure 6.12: Left: The light yields of the 9.4 and 32.1 keV decay of $^{83\text{m}}\text{Kr}$ plotted vs. timing separation, for events separated by more than 1200 ns. The point at 600 ns is calculated assuming the 32.1 keV yield remains flat to 200 ns as observed in [9] and [10]. Right: the histogram of $^{83\text{m}}\text{Kr}$ events vs timing separation finding a best fit to the half life of 159.7 ± 7.5 consistent with the measured value of 154 ns [11] [12].

Fortunately, the first 32.1 keV appears to have no time dependance as it decays under normal circumstances in the xenon, without the presence of additional free ions or electron [10], [13]. Using a $^{83\text{m}}\text{Kr}$ data set at zero field the yield of the 32.1 keV decay was determined. Since the S2 (charge) signal is unavailable at zero drift field we rely on the top-bottom asymmetry of the PMTs to define the Z coordinate of the event, $\frac{\text{top-bottom}}{\text{top+bottom}}$. We must know at least the Z coordinate in order to apply the position dependent corrections outlined in chapter 3. The XY correction is subdominant to the Z-dependent correction for the S1 signal and can be ignored. Each event, given a top-bottom asymmetry, is mapped to a detector depth

Z allowing for the Z -dependent correction to be applied. The correction normalizes the pulse area PE to the detector center (241.6 mm below the gate grid). The result for the zero field data set is shown in figure 6.13 and is reported in table 6.1.

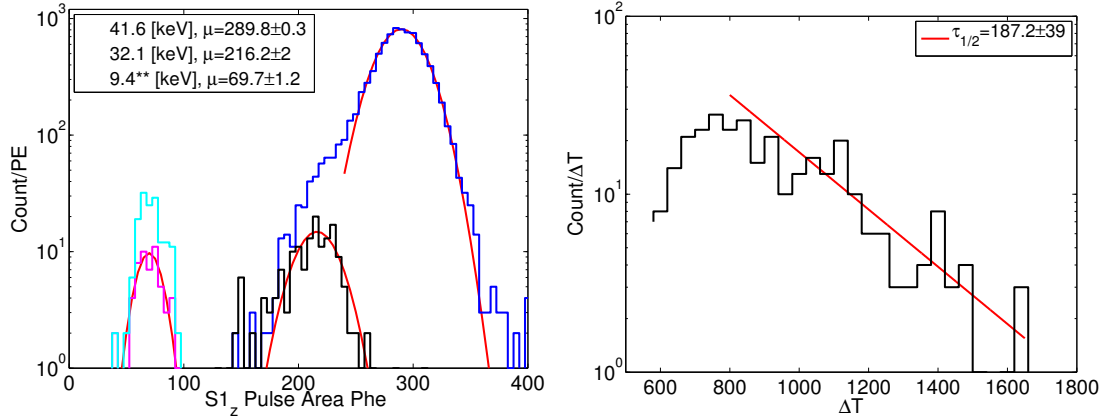


Figure 6.13: Left: S1 ^{83m}Kr peaks at zero field. Right: shows the histogram of the separated 32.1 and 9.4 keV decays plotted above vs. time. The half life fit to the population is in good agreement with the measured half-life of 154 ns [11] [12].

Table 6.1 shows the measured scintillation of the 32.1 keV internal conversion electron from ^{83m}Kr using the LUX detector at various fields. The table also includes the NEST predictions [64]. Electron mobility and charge separation at the interaction site increases with drift field leading to less recombination, causing scintillation yield to be quenched. The field effect is more dramatic at higher energies than in the low energy regions probed by the tritium data.

6.5.2 Comparing Tritium Scintillation Yield with Compton Scatters

We report the measured light yield of tritium relative to the 32.1 keV decay of ^{83m}Kr at zero field, defined as \mathcal{R}_e . The comparison is done as a proof of principle

Field V/cm	S1 PE	Photons $\langle n_\gamma \rangle$	Yield $\langle n_\gamma \rangle / \text{keV}$	NEST $\langle n_\gamma \rangle / \text{keV}$
0	216.2 ± 5.0	2228.9 ± 50.5	69.4 ± 1.6	64.2 ± 3.2
50	195.0 ± 0.7	2010.3 ± 7.2	62.6 ± 0.2	59.8 ± 3.0
100	178.4 ± 0.7	1839.2 ± 7.2	57.3 ± 0.2	55.8 ± 2.8
170	171.4 ± 0.9	1767.0 ± 9.2	55.0 ± 0.3	51.9 ± 2.6

Table 6.1: Field dependance of the light yield form the 32.1 keV decay of $^{83\text{m}}\text{Kr}$ along with the NEST [64] predictions.

that the light yield from betas and gammas overlap at low energies, at least within the rather large systematic uncertainties. Further, this is a cross check that the residual $< 10 \times 10^{-12} \text{ g/g}$ concentration of methane injected for the tritiated-methane calibration had negligible impact on the light yield, as expected from previous measurements with methane[78]. The result for \mathcal{R}_e is shown in figure 6.14, with the one sigma regions plotted as bands for the tritium data.

We find good agreement between the centroids of the tritium data at 100 and 170 V/cm with the zero field and 450 V/cm Compton scattering measurements from [13] and [10]. The finding are consistent with the expectation that tritium light yield data at 100 and 170 V/cm lie between the zero field light yield measurements the light yield at 450 V/cm. The error bars from the Compton scattering measurement are rather large due to the uncertainty in scattering angle and the need for Monte Carlo to reconstruct the energy deposit in the liquid xenon. In those measurements, the combined energy of the deposit in the liquid xenon is uncertain as both experiments were done in light-only collection mode [13] [10] (even for the 450 V/cm measurement). The errors on the tritium results are systematic and dominated by the constraint of g1 and g2 and are comparable with the errors on the Compton

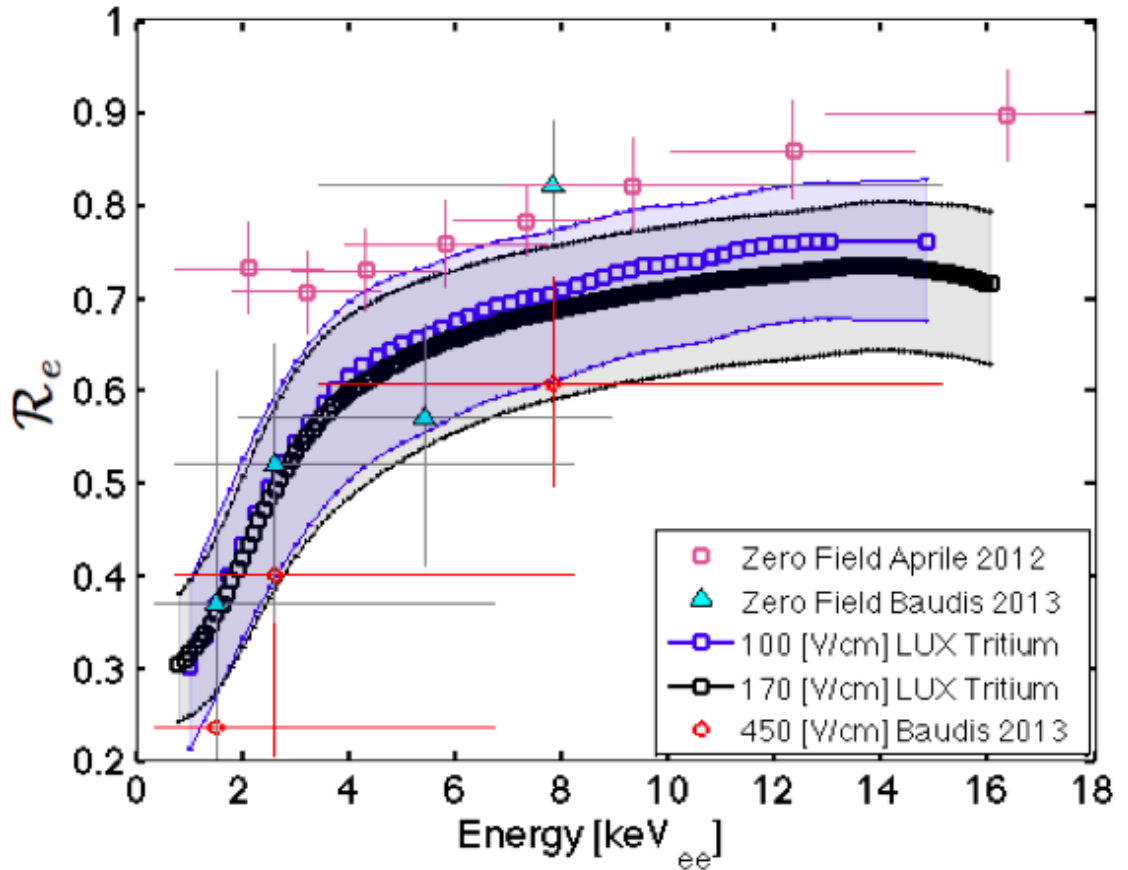


Figure 6.14: LY relative to the light yield of the 32.1 keV decay of $^{83\text{m}}\text{Kr}$ at zero field.

The black and blue bands represent the results from tritium at 170 and 100 V/cm respectively. The shaded region represents the systematic error due to the one sigma constraints on g1 and g2. Magenta points are Compton scattering measurements from [13]. The grey and red represent zero field and 450 V/cm Compton Scattering measurements from [10].

scattering measurements.

If the constraint on g1 and g2 in LUX is improved by future calibrations, then the errors on the tritium data will shrink significantly to below 3% making the tritium calibration a powerful tool for calibrating both light yields and charge

yields all the way to the energy threshold. The tritium light and charge yields reported here extend down to 1 keVee corresponding to the 50% threshold of LUX. The measurements also confirm, within systematic errors, that the ER band as calibrated by the tritium data is applicable to the more generic Compton scatter backgrounds in the WIMP search region of 1 to 5 keV_{ee}. Compton scatters comprises about 2/3 of the expected background in LUX with the remaining 1/3 being from the beta decay of ⁸⁵Kr [5].

6.6 Summery

In this section we have extracted the light and charge yields using the tritium calibration source in energies ranging from 1 to 16 keV_{ee}, shown in figures 6.9 and 6.10. The light and charge yields measured are a fundamental property electronic recoils in liquid xenon, in this work the liquid density was 2.888 g/cm³. We find agreement, within the systematic errors, between the light yields measured with the tritiated-methane source with Compton scattering measurements down to 1.5 keV_{ee}, figure 6.14. The result supports the model that low energy betas leave identical tracks to low energy Compton scatters in liquid xenon [63] [64]. Having measured the yields, the S1 and S2 signals can be modeled for any background source only requiring the energy spectrum as an input. The ratio of charge (S2) to light (S1) characterizes a xenon detector's ability to reject background events from WIMP candidates at a particular energy. We have also found that the light and charge yields measured at 170 and 100 V/cm merge below 5 keV_{ee}, indicating that below this energy recom-

bination is insensitive to field. The results for ER and NR discrimination using the tritium calibration source will be discussed in the next chapter.

Chapter 7: Tritiated-Methane Calibration Source and the ER Band

In this final chapter we overview the development, implementation and the main results of the tritiated-methane calibration source. The source was developed to be a method of calibrating the electronic recoil (ER) band in current and future large scale xenon detectors (+100 kg). As opposed to external ER calibration sources, the tritiated-methane is internal and mixes with the bulk xenon. Internal sources have a great advantage over external sources as they trivially overcome the formidable stopping power of liquid xenon, illuminating the fiducial volume of the detector. The tritiated-methane calibration source was ultimately used to characterize background ER events from potential NR signals of WIMP. Once the ER band is defined the background rejection of WIMP candidates at a particular energy is treated with a profile likelihood analysis, described in [38].

7.1 The need for an Internal Calibration Source

Over the past two decades liquid noble TPCs used for dark-matter experiments have been growing in size to net more kg-days of exposure for WIMP searches. With the additional mass, noble detectors benefit from the self shielding properties of the dense liquid inside the inner fiducial volume of the detector, as the outer

volume is used as an active veto [48]. With current generation liquid xenon detectors containing +100 kg, the detectors are vitally insensitive to external gamma radiation in the WIMP search region of interest of 1-10 keV_{ee} [5] [39] [40] [41]. Being insensitive to external radioactivity is great for improving the signal to background ratio for WIMP searches. Unfortunately, it is also equally as great for shielding against external calibration sources. With plans for even larger xenon detectors already moving forward [79] [80], we must develop a new method for introducing controlled radioactivity for calibration purposes.

The fiducial volume of the LUX detector is surrounded by more than than 6 cm of liquid xenon providing excellent shielding from both external backgrounds and calibration sources [5]. For example, a 100 keV gamma has a mean free path of about 2 mm in liquid xenon and would require thirty mean free paths to penetrate into the fiducial volume. A higher energy source such as ¹³⁷Cs (662 keV) has a longer mean free path of 4 cm however, the probability of a low energy deposit from forward scattering in the fiducial followed by an escape is greatly suppressed. We would expect less than one ER event per day between 1-10 keV_{ee} in the fiducial region if calibrating with an external ¹³⁷Cs or Th source, [5]. Further, calibrating with high energy sources or high rate sources brings along systematic uncertainties from high energy deposits near the detector edge and high rates would overwhelm the DAQ.

7.2 Tritiated-Methane as a Calibration Source

In order to overcome the issues with external calibrations, the source used to calibrate the ER band must satisfy three requirements. First, it should illuminate the WIMP search band with single scatter events (1-10 keV_{ee}). Second, it must be able to mix with the xenon and be delivered as an internal source. Third, it should either have a short half-life or be easily separated from xenon by commercially available bettering technology. ^{83m}Kr has been developed and used as an internal source with liquid xenon detectors [9] [10]. However, in LUX ^{83m}Kr only produces a mono energetic peak at 42.1 keV_{ee} being too high in energy to calibrate the WIMP search region. In order to populate the ER band with single scatter events between 1- 10 keV a beta emitter should be injected. Tritium is an ideal candidate, satisfying all but the removal requirement. Tritium has a Q value of 18.6 keV [74], a mean beta energy of 5.6 keV [75] and a mode of 3 keV [14], see figure 7.1.

Tritium has a half life is 12.3 years [81]. Thus, it is not practical to wait for the tritium activity to decay away. The tritium must be removed after the calibration is complete in order to continue a low background WIMP search run. Hydrogen, being chemically identical to tritium, can be removed from the bulk xenon by standard gettering technology [82]. However, the removal is complicated by tritium's high diffusion rate into plastics and other detector materials [83]. A botched tritium injection would mean the end of a dark matter experiment.

To mitigate the effect of tritium diffusion into plastics we use a tritiated-methane source instead of bare tritium. Tritiated-methane consists of a tritium

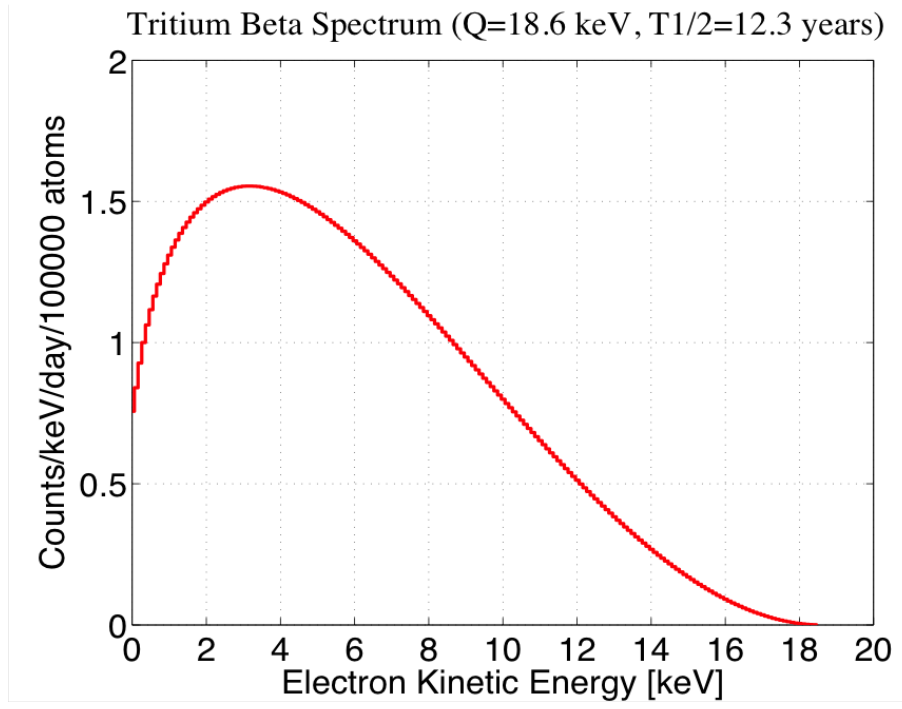


Figure 7.1: True tritium beta spectrum from [14].

atom and three hydrogen atoms bound to a carbon molecule, and is chemically identical to methane. Using tritiated-methane reduces the diffusion of tritium into detector internals by an order of magnitude [83]. The weak molecular bond, < 1 eV, to the methane molecule does not impact the nuclear physics of the tritium beta decay. Also, methane is known to be soluble in liquid xenon and is sometimes used to quench scintillation light when injecting relatively large amounts into the liquid [84], [78], [85]. Finally, We have studied the removal of methane by the commonly used SAES heated zirconium getter and found that significant amounts of methane can be removed from xenon at flow rates commonly employed in large scale liquid xenon experiments [86],[87].

7.3 Removal of CH₄ from LUX

The injection and removal of tritiated-methane into a liquid xenon vessel containing plastics was first conducted in an experimental setup at UMD. Even with conservative estimates for diffusion rates into plastics, we could not be certain about the behavior of tritiated-methane in the much larger LUX detector. Prior to injecting the tritiated-methane into LUX a much larger natural methane injection was performed in order to characterize diffusion, being chemically identical tritiated-methane. A xenon gas analysis system, developed at UMD, allowed for in situ purity analysis from several ports plumbed directly into the LUX xenon circulation loop. The analysis system has ppt (part-per-trillion) sensitivity to CH₄ and better than ppt sensitivity to Kr. The compact system allows for hourly sampling and is used for detection of several key impurities (N₂, O₂, He, Ar, Kr, CH₄, H₂). The design is compact, the analysis can be done on site, and is significantly less expensive than the more complex techniques used by [88] and [89]. The purity analysis technique is described in [87], [86], [90], [49], and will be described for the LUX system in a future publication.

Figure 7.2 shows the results from the xenon gas analysis system for a 50 ppb (g/g) methane injection into the bulk xenon. After the first hour, the 50 ppb of methane mixes into the liquid and appears as 300 ppb in the gas returning from the bulk liquid. The enhancement in the gas phase is due to the solubility of methane dissolved in liquid xenon and is characterized by the Henry's constant .

Having in situ sampling provided crucial diagnostics for methane removal and

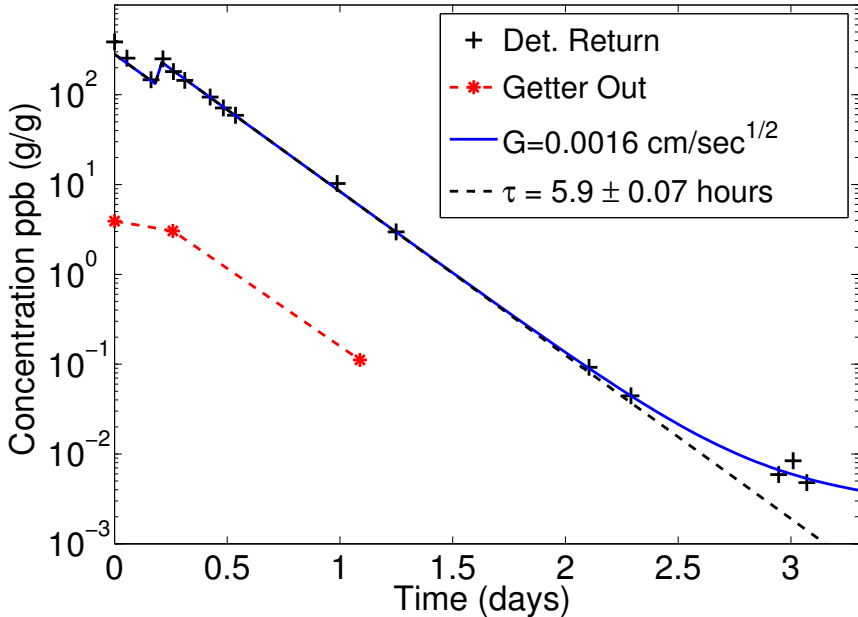


Figure 7.2: Removal of natural methane observed by the integrated xenon sampling system prior to the tritiated-methane injections. The red points indicate measurements at the getter outlet, we find a 97% one pass removal efficiency at a flow rate of 25 SLPM. The blue curve shows the improved upper limit on the effect of outgassing from the plastics. The black dashed lines shows the exponential fit to the natural methane removal from the xenon with a time constant of 5.9 ± 0.07 hours. 5×10^{-3} ppb (g/g) is the limit of detection for methane.

diffusion into plastic components in the LUX detector. We measured the one pass purification efficiency for methane to be 97% by the SAES PS4-MT15-R-1 MonoTorr getter ([82]) at a flow rate of 27 SLPM. The getter's health for hydrocarbon removal is important to check prior to an injection, as an aged zirconium getter will lose its ability to remove CH_4 before failing for N_2 and O_2 [86]. Crucially, we confirmed that natural methane could be removed by more than five orders of magnitude without residual back diffusion. The plateau seen in the end of figure 7.2 is caused by the 5 ppt limit for methane detection rather than diffusion from plastic components which absorb the impurity when it is initially injected. Taking the background as the limit

for back diffusion we infer a diffusion constant of less than $1.6 \times 10^{-3} \text{ cm/sec}^{1/2}$.

The results from the natural methane injection gave us the confidence to proceed knowing that the goal of reducing the tritium rate to less than 5% of background could be met in the LUX detector. The purification time constant for natural methane removal was measured to be 5.9 ± 0.07 hours as seen in figure 7.2. The removal time constant is 1/6 of that expected based on xenon circulation rates alone, and is exactly the ratio of methane concentration in the gas to the methane concentration in the liquid. The enhanced purification time constant is reasonable as the methane is purified from the gas phase where it is more abundant, with the equilibrium concentration in the gas above the liquid set by the solubility.

7.4 Light Yield Quenching from CH₄ in LUX

It is well known that at high concentrations, of several percent, methane will quench scintillation in liquid xenon [84], [78], [85] [91]. The quenching of scintillation in liquid argon has been observed with methane concentrations as low as 10 ppb (parts-per-billion) [92]. When performing a tritiated-methane calibration for the LUX detector, containing 350 kg of xenon, the amount of natural methane injected is <10 ppt (parts-per-trillion). This is far to low to cause any shift in the observed light yield and impact the ER band measurement. To prove the case, a natural methane injection of 100 ppm was performed along with periodic ^{83m}Kr calibrations that were used to track the light yield of the line source normalized at the center of the detector. Figure 7.3 shows the result of ^{83m}Kr calibration along with the

methane concentration in the gas measured by the analysis system.

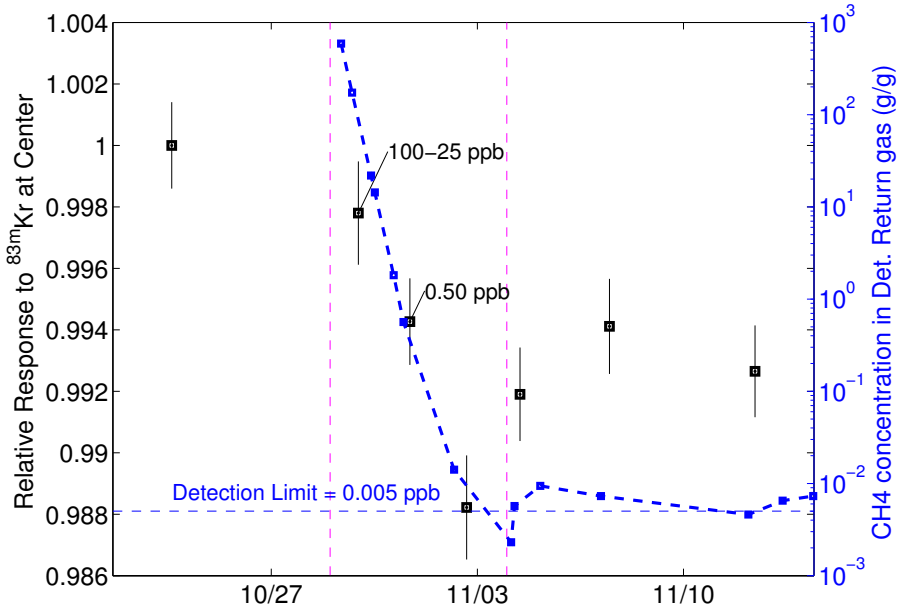


Figure 7.3: In black, the response to scintillation from $^{83\text{m}}\text{Kr}$ at the center of the detector normalized to the first data point before the natural methane (CH_4) injection. The dashed magenta lines represent the time window from the beginning of the natural methane injection to the time the background of 5 ppt is reached. The blue points represent that methane concentration in the gas returning from the bulk liquid of the detector. The concentration in the liquid xenon is roughly 1/6 of the concentration measured in the gas phase due to solubility.

In figure 7.3, there are two $^{83\text{m}}\text{Kr}$ data sets that had methane concentrations above background levels. The first measurement is made with greater than 25 ppb in the gas corresponding to greater than 4 ppb in the liquid. The second contained greater than 50 ppt in the gas corresponding to greater than 83 ppt in the liquid. The shifts in yield are purely systematic, as the two light yield measurements containing methane fall between the measured yields of the first (prior to and injection) and last (well below 5ppt) data points. We constrain light yield quenching induced by 4 ppb (g/g) of methane in liquid xenon to < 1%. Note, that a typical tritiated-methane calibration contains roughly three orders of magnitude less methane than

4 ppb (g/g).

7.4.1 Tritiated Methane injection into the LUX detector

Following the natural methane test, the tritiated-methane injection was conducted at the end of the first underground science run, on Aug 8th 2013. An absolute activity of 20 mBq of tritiated-methane was injected at the purifier's outlet while circulating. A removal time constant of 6.0 ± 0.5 hours was measured in the liquid volume, figure 7.4, and is consistent with the natural methane removal measured in the gas by the sampling system 7.2. After a day of circulating through the getter the tritium decay rate had fallen below detectable levels confirming the effective removal of the tritiated-methane with the getter. A second, larger injection of 800 mBq was performed a week later yielding a similar removal time constant of 6.4 ± 0.1 . The second injection produced 20,000 beta decays in the LUX detector before being completely removed, 7000 of which were in the fiducial volume and could be used to calibrate the ER band in the WIMP search region of 1-50 PE (about 1-8 keVee). The injections were performed while circulating and with the getter actively purifying in order to maintain detector purity and stability. Prior to LUX detector upgrades in December 2013, a total of 10 Bq of tritiated-methane was injected into the LUX detector and successfully removed providing over 140,000 beta decays within the fiducial volume.

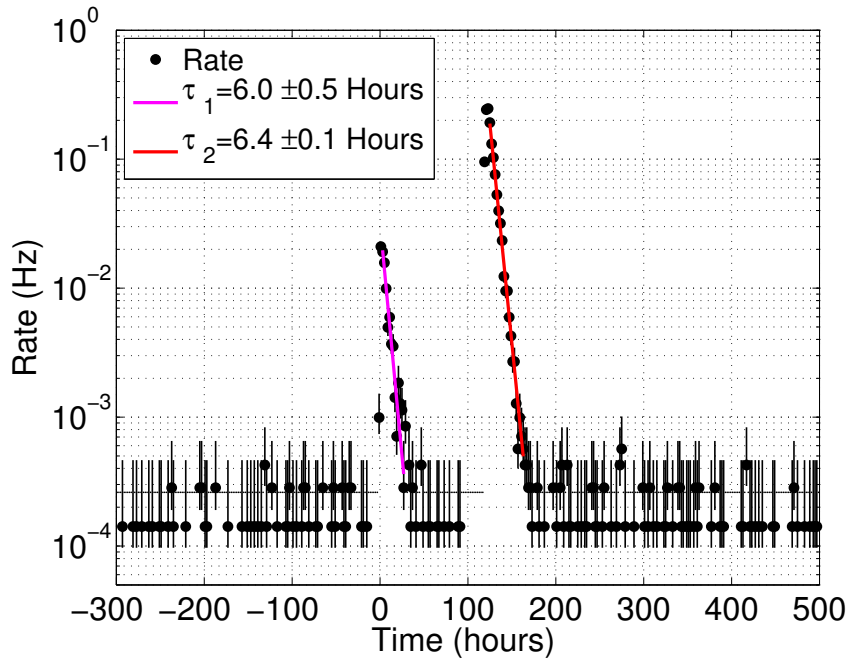


Figure 7.4: The rate of single scatter events with S1 below 100 PE in the fiducial volume. 100 PE in S1 is about 18.6 keV_{ee}, the endpoint to the tritium beta spectrum. The magenta and red curves are fits to the first and second tritium injection's removal rate. Note, the removal of tritiated-methane is consistent with the natural methane removal rate measured independently.

7.4.2 Mixing of Tritiated Methane in Liquid Xenon

Tritium events appear uniformly distributed in the liquid volume several minutes after injecting the tritiated-methane inline with the xenon gas circulation path.

Figure 7.5 shows the R² vs. Z distribution of tritium events thirty minutes after an injection. The events shown cover the region from the gate to the cathode and radially outward to the edge of the detector.

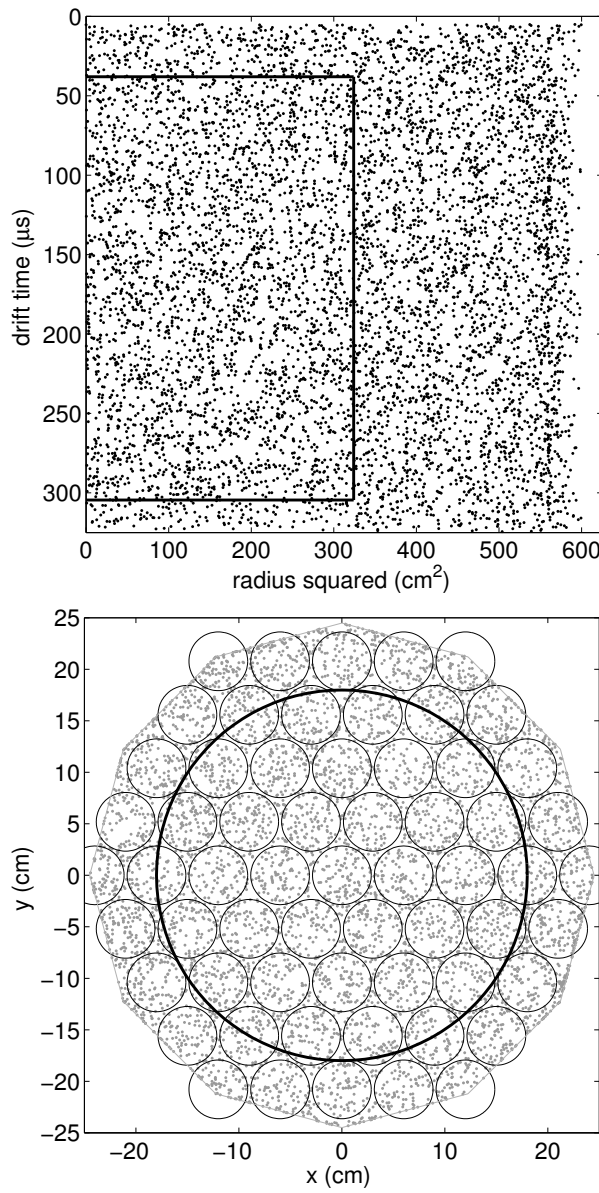


Figure 7.5: The distribution of tritium events vs. detector radius squared. The solid black line represents the fiducial volume. Right: The distribution of tritium events vs. XY in the region between the gate and the cathode. The solid black line represents the fiducial volume and the black circles represent the locations of PMTs (photo multiplier tubes).

7.4.3 Definition of Electronic Recoil Band. ER and NR Discrimination

The electronic recoil band in the fiducial volume of the LUX detector was calibrated to unprecedented accuracy using the tritium source. The calibration data was acquired in a 40 hour time window in which less than four out of the 140,000 events in the fiducial are expected to be non tritium [5]. Nearly every data point (99.997%) that will be presented in the subsequent figures is the result of a tritium beta decay in the fiducial volume of the LUX detector. Figure 7.6 shows the tritium calibration data with fits to the mean of the ER band along with the 10-90% confidence bounds ($\pm 1.28\sigma$), at a drift field of 170 V/cm. Also shown in red is the nuclear recoil (NR) mean measured using a mono energetic DD neutron generator calibration, described in [future publication].

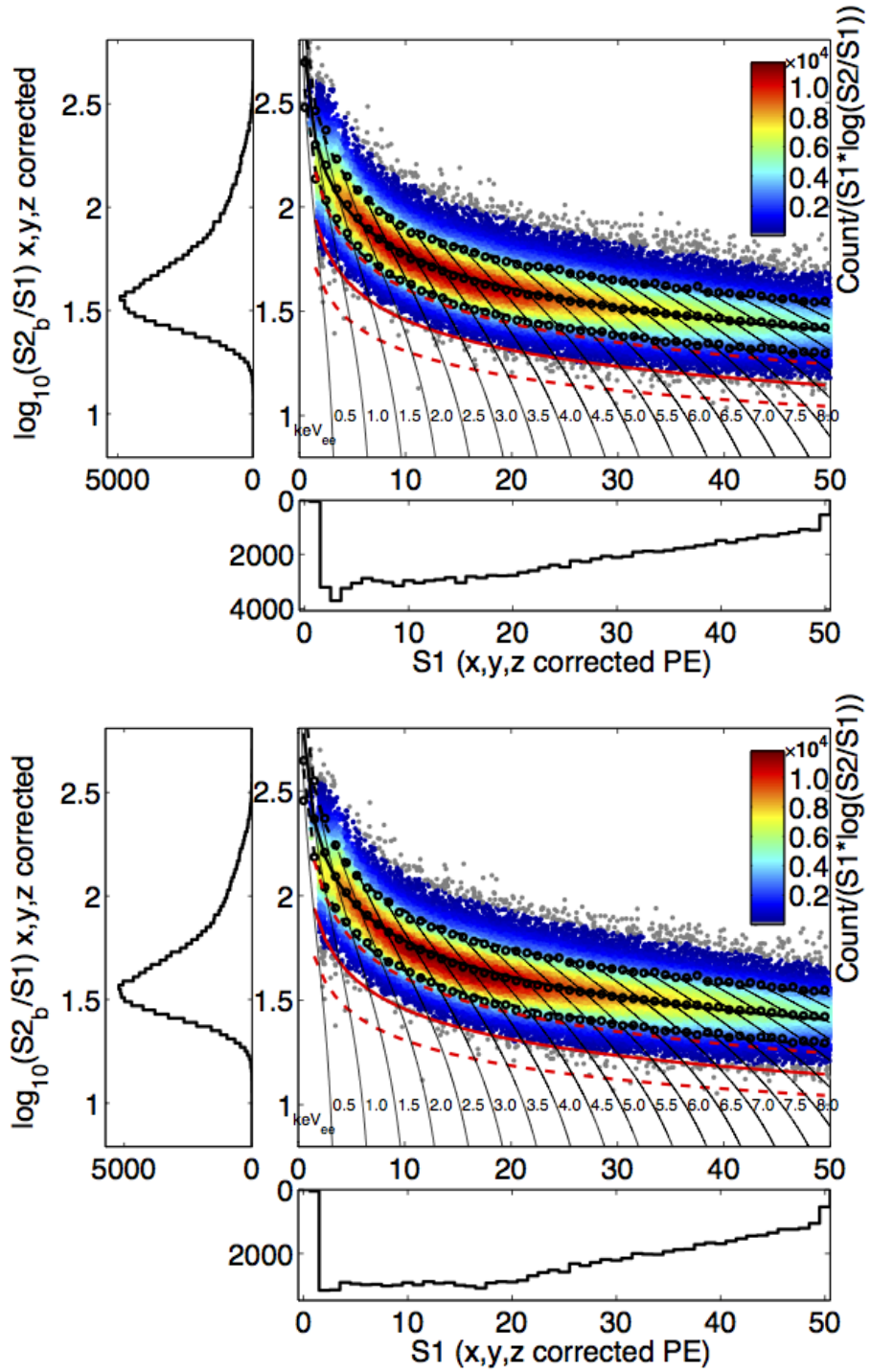


Figure 7.6: Charge to light ratio $\log_{10}(S2_b/S1)$ plotted vs. $S1$, the energy contours are also shown. Top, the tritium data uncorrected for spectral shape. Bottom, with the spectral shape correction discussed in chapter 6. The calibration consists of over 112,000 tritium beta decays between 1 and 50 PE in $S1$ ($1 - 10 \text{ keV}_{\text{ee}}$), in the fiducial volume of the detector. The black circles represent the ER band mean and 10% to 90% bounds, $\pm 1.28\sigma$. The red solid line is the NR band mean determined using a DD neutron generator calibration. The dashed red lines indicate the 10% to 90% bounds of the NR band.

The ER band defined by the tritium data shown in figure 7.6 has been corrected for spectral shape discussed in chapter 6. The spectral shape correction recovers the true ER band for a flat energy spectrum, left uncorrected the ER band would peak up slightly faster in the lowest S1 bins, below 5 PE. The discrimination between ER and NR events at 50% NR acceptance can be determined by counting the number of tritium events that fall below the mean of the NR band. Note, below 15 PE in S1 the NR acceptance actually becomes greater than 50% due to the asymmetric shape of the NR band at low energies, which works in our favor [63] [64]. The values of the leakage fraction at 50% NR acceptance per each 1 PE bin in S1 are shown in 7.7. Discrimination and leakage fraction is listed listed at several acceptance fractions in table 7.1.

NR %	Leakage Fraction $\times 10^{-3}$	Discrimination %	Leakage Fraction* $\times 10^{-3}$	Discrimination* %
90	52 ± 0.70	94.8 ± 0.07	49 ± 0.60	95.1 ± 0.06
80	18.8 ± 0.40	98.1 ± 0.04	17.4 ± 0.40	98.3 ± 0.04
70	8.6 ± 0.30	99.1 ± 0.03	7.6 ± 0.30	99.2 ± 0.03
60	4.2 ± 0.20	99.58 ± 0.02	3.7 ± 0.20	99.63 ± 0.02
50	2.1 ± 0.14	99.79 ± 0.014	1.8 ± 0.13	99.82 ± 0.013
40	0.97 ± 0.09	99.90 ± 0.009	0.87 ± 0.09	99.91 ± 0.009
30	0.49 ± 0.07	99.95 ± 0.007	0.44 ± 0.06	99.96 ± 0.006
20	0.23 ± 0.05	99.977 ± 0.005	0.22 ± 0.04	99.978 ± 0.004
10	0.08 ± 0.03	99.992 ± 0.003	0.08 ± 0.03	99.992 ± 0.003

Table 7.1: Leakage fraction at various NR acceptance % over the range of 1-50 PE in S1, using tritium data at 170 V/cm. For the case without spectral shape correction, and with spectral shape correction to the left (columns marked with *). Note, these are conservative estimates assuming Gaussian behavior about the NR mean. Below 15 PE in S1 the NR band actually becomes bottom heavy, which works in our favor [63] [64].

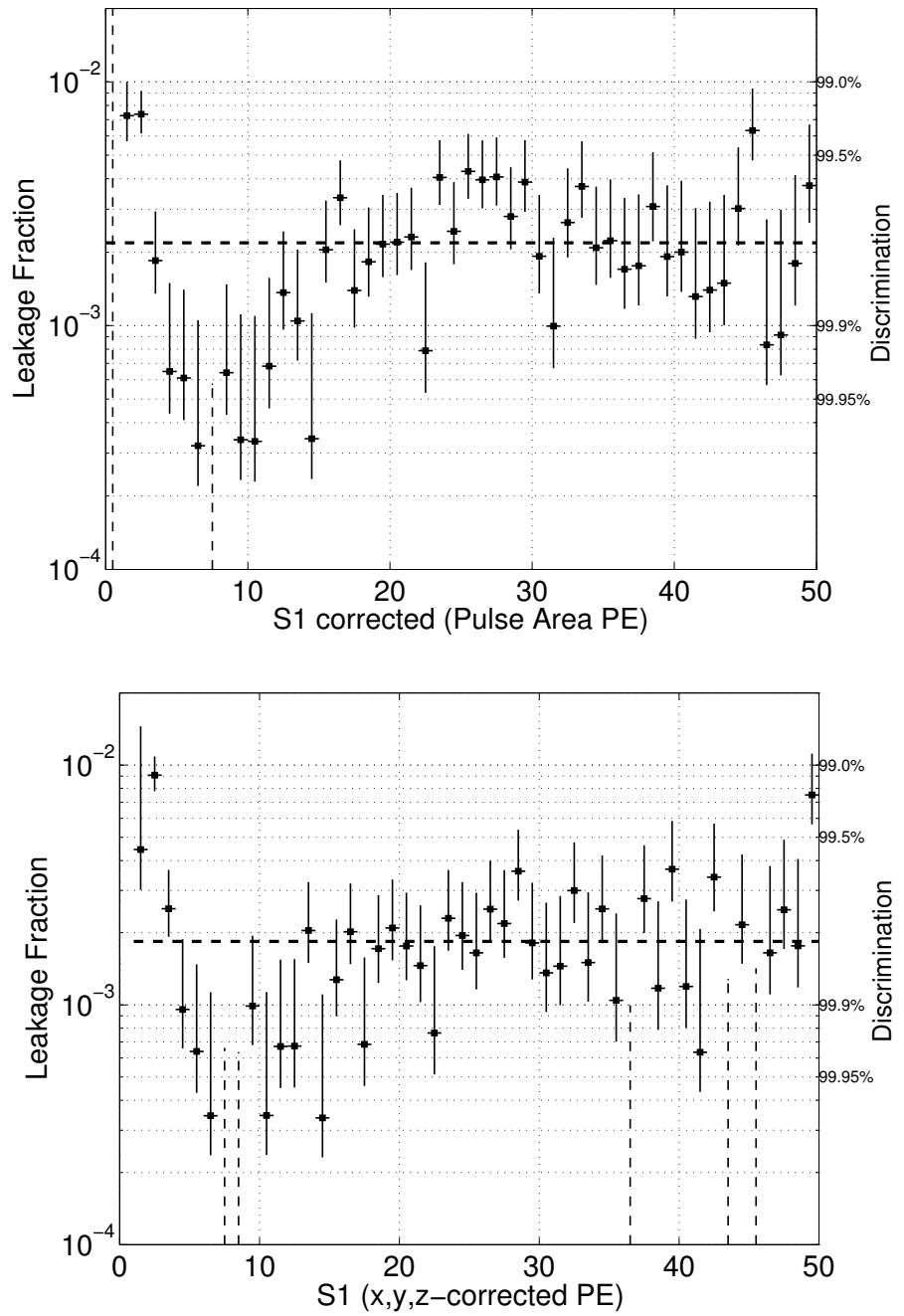


Figure 7.7: Discrimination vs. S1 using over 112,000 tritium beta decays between 1 and 50 PE in S1 ($1-10\text{ keV}_{ee}$), using tritium data at 170 V/cm . Top, the tritium data uncorrected for spectral shape. Bottom, with the spectral shape correction discussed in chapter 6. The dashed horizontal lines indicate the mean leakage fraction from 1 to 50 PE.

7.5 ER Band Gaussianity

With the high statistics tritium data set we could test the Gaussianity of the ER band in the WIMP search region. The charge to light ratio used to discriminate ER and NR events (plotted as $\log(S_2/S_1)$) and has been assumed to have Gaussian behavior in past experiments. The largest tritium calibration yielded 112,000 tritium beta decays with only four expected to be non tritium events [5] in LUX detector's fiducial region. Figure 7.8 shows the same ER band of figure 7.6 but with the centroid subtracted off, and is plotted for cases of without and with the spectral shape correction. We find that below 3 sigma of the ER mean the data begins to deviate from Gaussian behavior, potentially due to instrumental fluctuations. For example, the probability of finding an ER event below the NR mean at 4 sigma below the ER mean is nearly 10 times higher than the probability that would be assigned by a Gaussian PDF. If not treated properly by data driven calibrations, this could be falsely interpreted as a WIMP event by a profile likelihood analysis.

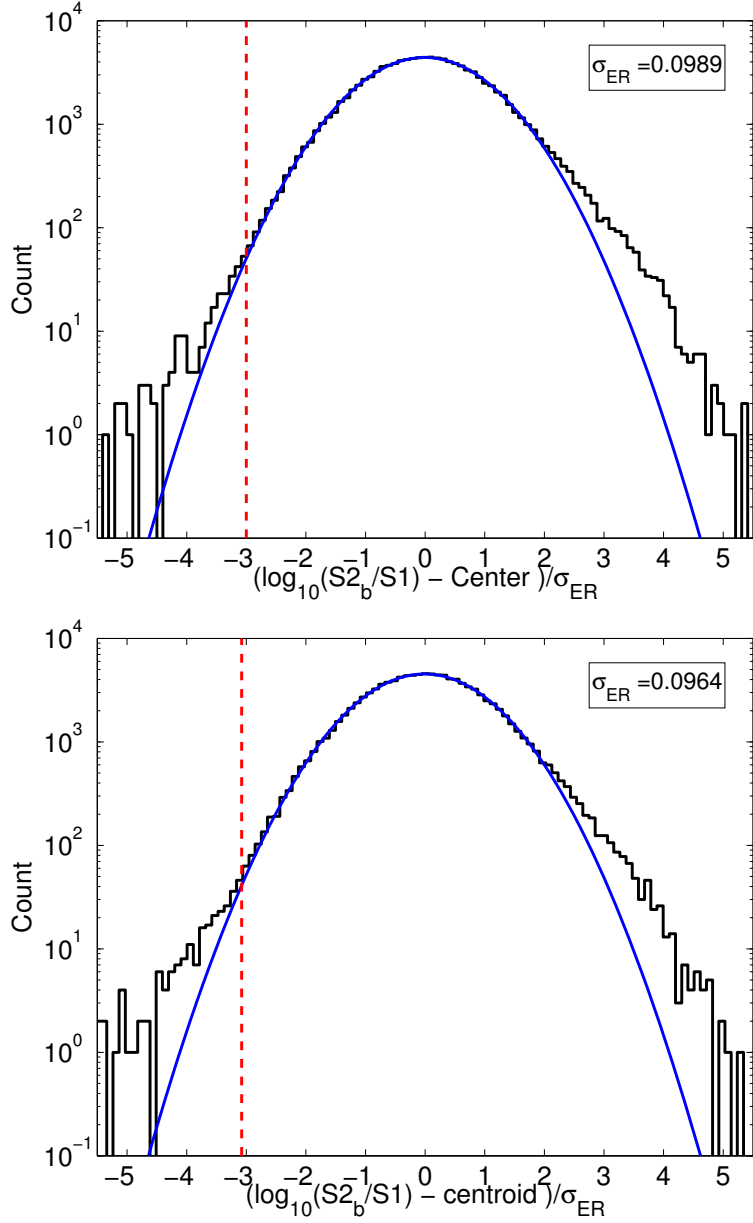


Figure 7.8: ER band Gaussianity from 0-50 PE with the centroid of the ER band subtracted off, using tritium data at 170 V/cm. Top, the tritium data uncorrected for spectral shape. Bottom, with the spectral shape correction discussed in chapter 6. The dashed vertical red line indicates the mean of the NR band from 1 to 50 PE.

7.6 S1 Threshold For Golden Events, Using Tritium

The tritiated-methane calibration source provides beta decays with energies well below the energy threshold of the detector 1.5keV_{ee}. The energy threshold was

measured by comparing to the combined energy to the true tritium spectrum in chapter 4. The S1 detection efficiency, or the efficiency for detecting golden events, can be determined in the same manner by taking the ratio of the S1 spectrum observed to expected S1 spectrum. The observed S1 spectrum overlaid with the expected S1 spectrum is shown in figure 6.8 a). The result for detection efficiency of S1 measured using tritium data at 170 and 100 V/cm is shown in figure 7.9, along with the efficiency measured using LED calibrations. The efficiency for detecting S1 signals at 2 PE is found to be 75%, rising to >95% at 3 PE.

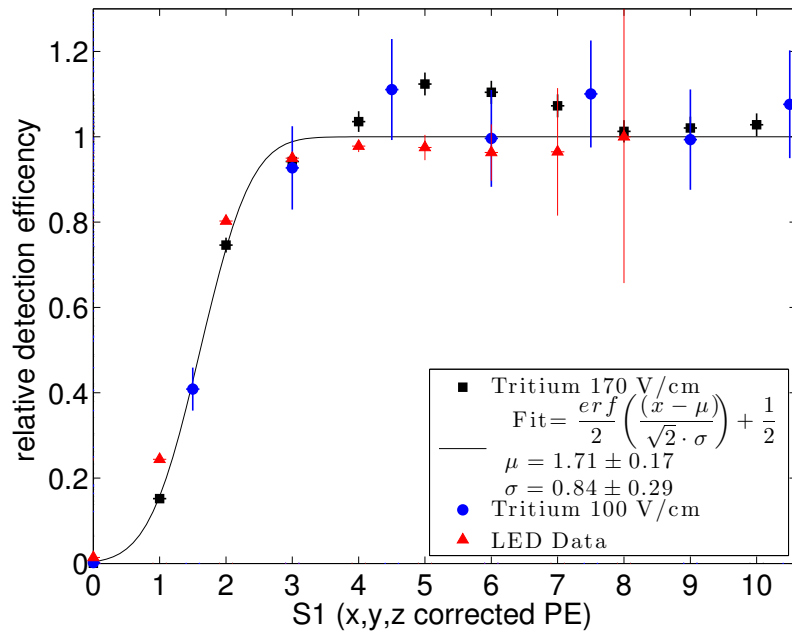


Figure 7.9: The S1 detection efficiency measured from tritium data at 170 V/cm (black square) and 100 V/cm (blue circle) is plotted along with the best fit to an error function to the higher statistics 170 V/cm data. The red triangles are detection efficiency determined from LED pulsing.

7.7 Conclusion

In this chapter we have described the development and implementation of a tritiated-methane calibration source. The primary application of the tritiated-methane calibration is to characterize the ER band in the WIMP search regions of 1-50 PE (1-10 keV_{ee}). This is of great importance, as it gauges the detectors ability to reject background (ER) events from potential WIMP signals (NR). Having both high statistics and high data purity from the tritium calibration, the future LUX profile likelihood analysis will not have to rely on the assumption that the ER band can be characterized by a Gaussian PDF. All previous xenon dark-matter searches using liquid xenon have assumed ER band Gaussianity in the WIMP search region, all having been calibration statistics limited. We find that the use of a Guassian PDF, for the LUX detector, fails below 3 sigma of the ER mean which is just below the NR mean, shown in figure 7.8. The deviation maybe arising from instrumental fluctuations or is perhaps a fundamental property of electronic recoils.

Using the calibration data collected, a purely data driven PDF can be constructed to characterize the distribution of ER events in each S1 bin, greatly improving the accuracy of the next WIMP limit. Much more fundamental xenon physics could be probed with the tritium calibration source, discussed in chapters 4, 5,6. The tritium calibration was used to test the energy scale calibration over the range from 1 to 18 KeV_{ee}, and to measure the light yield, charge yield and recombination fluctuation, and the detection thresholds down to 1 keV_{ee}. The data taken with the LUX detector has allowed for improvements to the NEST model down to 1 keV_{ee}

and at our fields of 100 and 170 V/cm.

Bibliography

- [1] M. Weber and W. de Boer. Determination of the local dark matter density in our Galaxy. *AAP*, 509:A25, jan 2010. doi:10.1051/0004-6361/200913381.
- [2] Anse Slosar, et al. Measurement of Baryon Acoustic Oscillations in the Lyman-alpha Forest Fluctuations in BOSS Data Release 9. *JCAP*, 1304:026, 2013. doi:10.1088/1475-7516/2013/04/026.
- [3] J.D. Lewin and P.F. Smith. Review of mathematics, numerical factors, and corrections for dark matter experiments based on elastic nuclear recoil. *Astropart.Phys.*, 6:87–112, 1996. doi:10.1016/S0927-6505(96)00047-3.
- [4] Richard H. Helm. Inelastic and elastic scattering of 187-mev electrons from selected even-even nuclei. *Phys. Rev.*, 104:1466–1475, Dec 1956. doi:10.1103/PhysRev.104.1466.
- [5] D. S. Akerib, et al. Radiogenic and muon-induced backgrounds in the LUX dark matter detector. *Astroparticle Physics*, 62:33–46, March 2015. doi:10.1016/j.astropartphys.2014.07.009.
- [6] Scott Hertel. private communication, 2014.
- [7] M. Arenz and R. Vianden. 83mkr, a potentially powerful pac probe. *Hyperfine Interactions*, 222(1-3):73–76, 2013. ISSN 0304-3843. doi:10.1007/s10751-012-0723-3.
- [8] C. E. Dahl. *Ph.D. Thesis*. Ph.D. thesis, Princeton University, 2009.
- [9] L.W. Kastens, S. Bedikian, S.B. Cahn, A. Manzur, and D.N. McKinsey. A 83Krm Source for Use in Low-background Liquid Xenon Time Projection Chambers. *JINST*, 5:P05006, 2010. doi:10.1088/1748-0221/5/05/P05006.
- [10] L. Baudis, et al. Response of liquid xenon to compton electrons down to 1.5 kev. *Phys. Rev. D*, 87:115015, Jun 2013. doi:10.1103/PhysRevD.87.115015.

- [11] I. Ahmad, et al. Half-lives of isomeric states in fe57 and kr83. *Phys. Rev. C*, 52:2240–2241, Oct 1995. doi:10.1103/PhysRevC.52.2240.
- [12] S. L. Ruby, Y. Hazoni, and M. Pasternak. Lifetimes of the low-energy m1 transitions in la137 and kr83. *Phys. Rev.*, 129:826–828, Jan 1963. doi:10.1103/PhysRev.129.826.
- [13] E. Aprile, et al. Measurement of the scintillation yield of low-energy electrons in liquid xenon. *Phys. Rev. D*, 86:112004, Dec 2012. doi:10.1103/PhysRevD.86.112004.
- [14] P Venkataramaiah, K Gopala, A Basavaraju, S S Suryanarayana, and H Sanjeeviah. A simple relation for the fermi function. *Journal of Physics G: Nuclear Physics*, 11(3):359, 1985.
- [15] J. H. Oort. The force exerted by the stellar system in the direction perpendicular to the galactic plane and some related problems. *BAIN*, 6:249, August 1932.
- [16] F. Zwicky. On the Masses of Nebulae and of Clusters of Nebulae. *API*, 86:217, October 1937. doi:10.1086/143864.
- [17] K. G. Begeman, A. H. Broeils, and R. H. Sanders. Extended rotation curves of spiral galaxies: dark haloes and modified dynamics. *Monthly Notices of the Royal Astronomical Society*, 249(3):523–537, 1991. doi:10.1093/mnras/249.3.523.
- [18] Robert H. Brandenberger. Formation of structure in the universe. 1995.
- [19] Ryan Cooke, Max Pettini, Regina A. Jorgenson, Michael T. Murphy, and Charles C. Steidel. Precision measures of the primordial abundance of deuterium. 2013.
- [20] P.A.R. Ade et al. Planck 2013 results. XVI. Cosmological parameters. *Astron. Astrophys.*, 2014. doi:10.1051/0004-6361/201321591.
- [21] D. J. Fixsen. The Temperature of the Cosmic Microwave Background. *APJ*, 707:916–920, December 2009. doi:10.1088/0004-637X/707/2/916.
- [22] P.A.R. Ade et al. Planck 2013 results. I. Overview of products and scientific results. 2013. doi:10.1051/0004-6361/201321529.
- [23] Daniel J. Eisenstein, Hee-jong Seo, and 1 White, Martin J. On the Robustness of the Acoustic Scale in the Low-Redshift Clustering of Matter. *Astrophys.J.*, 664:660–674, 2007. doi:10.1086/518755.
- [24] W. J. Percival, et al. Baryon acoustic oscillations in the Sloan Digital Sky Survey Data Release 7 galaxy sample. *mnras*, 401:2148–2168, February 2010. doi:10.1111/j.1365-2966.2009.15812.x.

- [25] Maxim Markevitch. Chandra observation of the most interesting cluster in the universe. 2005.
- [26] Douglas Clowe, et al. A direct empirical proof of the existence of dark matter. *Astrophys.J.*, 648:L109–L113, 2006. doi:10.1086/508162.
- [27] Peter J. Kernan and Lawrence M. Krauss. Refined big bang nucleosynthesis constraints on Omega (baryon) and N (neutrino). *Phys.Rev.Lett.*, 72:3309–3312, 1994. doi:10.1103/PhysRevLett.72.3309.
- [28] Q.R. Ahmad et al. Direct evidence for neutrino flavor transformation from neutral current interactions in the Sudbury Neutrino Observatory. *Phys.Rev.Lett.*, 89:011301, 2002. doi:10.1103/PhysRevLett.89.011301.
- [29] George R. Blumenthal, S.M. Faber, Joel R. Primack, and Martin J. Rees. Formation of Galaxies and Large Scale Structure with Cold Dark Matter. *Nature*, 311:517–525, 1984. doi:10.1038/311517a0.
- [30] Masahiro Kawasaki and Kazunori Nakayama. Axions: Theory and Cosmological Role. *Ann.Rev.Nucl.Part.Sci.*, 63:69–95, 2013. doi:10.1146/annurev-nucl-102212-170536.
- [31] C.A. Baker, et al. An Improved experimental limit on the electric dipole moment of the neutron. *Phys.Rev.Lett.*, 97:131801, 2006. doi:10.1103/PhysRevLett.97.131801.
- [32] R. D. Peccei and Helen R. Quinn. CP. *Phys. Rev. Lett.*, 38:1440–1443, Jun 1977. doi:10.1103/PhysRevLett.38.1440.
- [33] R. D. Peccei and Helen R. Quinn. Constraints imposed by CP conservation in the presence of pseudoparticles. *Phys. Rev. D*, 16:1791–1797, Sep 1977. doi:10.1103/PhysRevD.16.1791.
- [34] E. Arik et al. Probing eV-scale axions with CAST. *JCAP*, 0902:008, 2009. doi:10.1088/1475-7516/2009/02/008.
- [35] S. J. Asztalos, et al. SQUID-Based Microwave Cavity Search for Dark-Matter Axions. *Physical Review Letters*, 104(4):041301, January 2010. doi:10.1103/PhysRevLett.104.041301.
- [36] Gerard Jungman, Marc Kamionkowski, and Kim Griest. Supersymmetric dark matter. *Phys.Rept.*, 267:195–373, 1996. doi:10.1016/0370-1573(95)00058-5.
- [37] Andriy Kurylov and Marc Kamionkowski. Generalized analysis of weakly interacting massive particle searches. *Phys.Rev.*, D69:063503, 2004. doi:10.1103/PhysRevD.69.063503.
- [38] S. Akerib, D. et al. First results from the lux dark matter experiment at the sanford underground research facility. *Phys. Rev. Lett.*, 112:091303, Mar 2014. doi:10.1103/PhysRevLett.112.091303.

- [39] E. Aprile, et al. Dark Matter Results from 225 Live Days of XENON100 Data. *Physical Review Letters*, 109(18):181301, November 2012. doi:10.1103/PhysRevLett.109.181301.
- [40] Mengjiao Xiao et al. First dark matter search results from the PandaX-I experiment. 2014.
- [41] K. Abe, et al. Light WIMP search in XMASS. *Physics Letters B*, 719:78–82, February 2013. doi:10.1016/j.physletb.2013.01.001.
- [42] A. Wright. The DarkSide Program at LNGS. In S. Giani and et al., editors, *Astroparticle, Particle, Space Physics and Detectors For Physics Applications - Proceedings of the 13th ICATPP Conference. Edited by Giani Simone et al. Published by World Scientific Publishing Co. Pte. Ltd., 2012. ISBN #9789814405072, pp. 414-420, pages 414–420*. August 2012. doi: 10.1142/9789814405072_0061.
- [43] A. Hime. The MiniCLEAN Dark Matter Experiment. *ArXiv e-prints*, October 2011.
- [44] CDMS II Collaboration, et al. Dark Matter Search Results from the CDMS II Experiment. *Science*, 327:1619–, March 2010. doi:10.1126/science.1186112.
- [45] C. E. Aalseth, et al. CoGeNT: A search for low-mass dark matter using p-type point contact germanium detectors. *prd*, 88(1):012002, July 2013. doi: 10.1103/PhysRevD.88.012002.
- [46] S. Archambault et al. Constraints on Low-Mass WIMP Interactions on ^{19}F from PICASSO. *Phys.Lett.*, B711:153–161, 2012. doi:10.1016/j.physletb.2012.03.078.
- [47] E. Behnke, et al. First dark matter search results from a 4-kg CF_3I bubble chamber operated in a deep underground site. *prd*, 86(5):052001, September 2012. doi:10.1103/PhysRevD.86.052001.
- [48] E. Aprile and T. Doke. Liquid xenon detectors for particle physics and astrophysics. *Rev. Mod. Phys.*, 82:2053–2097, Jul 2010. doi:10.1103/RevModPhys.82.2053.
- [49] Attila Dobi, et al. Detection of krypton in xenon for dark matter applications. *Nucl.Instrum.Meth.*, A665:1–6, 2011. doi:10.1016/j.nima.2011.11.043.
- [50] A.I. Bolozdynya, P.P. Brusov, T. Shutt, C.E. Dahl, and J. Kwong. A chromatographic system for removal of radioactive ^{85}Kr from xenon. *Nuclear Instruments and Methods in Physics Research Section A: Accelerators, Spectrometers, Detectors and Associated Equipment*, 579(1):50 – 53, 2007. ISSN 0168-9002. doi: DOI:10.1016/j.nima.2007.04.011. Proceedings of the 11th Symposium on Radiation Measurements and Applications.

- [51] K. Abe, et al. Distillation of liquid xenon to remove krypton. *Astroparticle Physics*, 31(4):290 – 296, 2009. ISSN 0927-6505. doi:DOI:10.1016/j.astropartphys.2009.02.006.
- [52] John R de Laeter, et al. Atomic weights of the elements. review 2000 (iupac technical report). *Pure and Applied Chemistry*, 75(6):683–800, 2003.
- [53] M. Miyajima, et al. Average energy expended per ion pair in liquid argon. *Phys. Rev. A*, 9:1438–1443, Mar 1974. doi:10.1103/PhysRevA.9.1438.
- [54] T. Takahashi, et al. Average energy expended per ion pair in liquid xenon. *Phys. Rev. A*, 12:1771–1775, Nov 1975. doi:10.1103/PhysRevA.12.1771.
- [55] T. Doke and K. Masuda. Present status of liquid rare gas scintillation detectors and their new application to gamma-ray calorimeters. *Nucl.Instrum.Meth.*, A420:62–80, 1999. doi:10.1016/S0168-9002(98)00933-4.
- [56] S Kubota, M Hishida, and J Raun. Evidence for a triplet state of the self-trapped exciton states in liquid argon, krypton and xenon. *Journal of Physics C: Solid State Physics*, 11(12):2645, 1978.
- [57] Akira Hitachi, et al. Effect of ionization density on the time dependence of luminescence from liquid argon and xenon. *Phys.Rev.*, B27:5279–5285, 1983. doi:10.1103/PhysRevB.27.5279.
- [58] Jeremy Mock, et al. Modeling Pulse Characteristics in Xenon with NEST. *JINST*, 9:T04002, 2014. doi:10.1088/1748-0221/9/04/T04002.
- [59] J. V. Dawson, et al. A study of the scintillation induced by alpha particles and gamma rays in liquid xenon in an electric field. *Nuclear Instruments and Methods in Physics Research A*, 545:690–698, June 2005. doi:10.1016/j.nima.2005.01.343.
- [60] David P. Lide, editor. *CRC Handbook of Chemistry and Physics*. CRC PRESS, 81 edition, 2000.
- [61] T. Doke, A. Hitachi, S. Kubota, A. Nakamoto, and T. Takahashi. Estimation of Fano factors in liquid argon, krypton, xenon and xenon-doped liquid argon. *Nucl.Instrum.Meth.*, 134:353–357, 1976. doi:10.1016/0029-554X(76)90292-5.
- [62] Jens Lindhard, V Nielsen, M Scharff, and PV Thomsen. *Integral equations governing radiation effects*. Munksgaard i komm., 1963.
- [63] M. Szydagis, et al. NEST: A Comprehensive Model for Scintillation Yield in Liquid Xenon. *ArXiv e-prints*, June 2011.
- [64] Matthew Szydagis, Adalyn Fyhrie, Daniel Thorngren, and Mani Tripathi. Enhancement of NEST Capabilities for Simulating Low-Energy Recoils in Liquid Xenon. *JINST*, 8:C10003, 2013. doi:10.1088/1748-0221/8/10/C10003.

- [65] W. . Chen, et al. Measurement of the transverse diffusion coefficient of charge in liquid xenon. *ArXiv e-prints*, September 2011.
- [66] R. Agnese et al. Search for Low-Mass Weakly Interacting Massive Particles Using Voltage-Assisted Calorimetric Ionization Detection in the SuperCDMS Experiment. *Phys.Rev.Lett.*, 112(4):041302, 2014. doi:10.1103/PhysRevLett.112.041302.
- [67] G. Angloher, et al. Results from 730 kgdays of the cresst-ii dark matter search. *The European Physical Journal C*, 72(4):1971, 2012. ISSN 1434-6044. doi:10.1140/epjc/s10052-012-1971-8.
- [68] R. Bernabei, et al. Final model independent result of DAMA/LIBRA-phase1. *European Physical Journal C*, 73:2648, December 2013. doi:10.1140/epjc/s10052-013-2648-7.
- [69] A. Dobi, et al. A xenon gas purity monitor for EXO. *Nuclear Instruments and Methods in Physics Research A*, 659:215–228, December 2011. doi:10.1016/j.nima.2011.09.017.
- [70] C. Silva, et al. A model of the reflection distribution in the vacuum ultra violet region. *Nuclear Instruments and Methods in Physics Research A*, 619:59–62, July 2010. doi:10.1016/j.nima.2009.10.086.
- [71] C. Silva, et al. Reflectance of polytetrafluoroethylene for xenon scintillation light. *Journal of Applied Physics*, 107(6):064902, March 2010. doi:10.1063/1.3318681.
- [72] V. Eckardt, et al. Calibration of the STAR forward time projection chamber with krypton-83m. 2001.
- [73] Tadayoshi Doke, et al. Absolute scintillation yields in liquid argon and xenon for various particles. *Japanese Journal of Applied Physics*, 41(3R):1538, 2002.
- [74] Sz. Nagy, T. Fritioff, M. Bjorkhage, I. Bergström, and R. Schuch. On the q -value of the tritium β -decay. *EPL (Europhysics Letters)*, 74(3):404, 2006.
- [75] D. P. Gregory and D. A. Landsman. Average decay energy of tritium. *Phys. Rev.*, 109:2091–2091, Mar 1958. doi:10.1103/PhysRev.109.2091.
- [76] A. Mozumder. Free-ion yield and electron-ion recombination rate in liquid xenon. *Chemical Physics Letters*, 245(45):359 – 363, 1995. ISSN 0009-2614. doi:[http://dx.doi.org/10.1016/0009-2614\(95\)01024-4](http://dx.doi.org/10.1016/0009-2614(95)01024-4).
- [77] J. Thomas and D. A. Imel. Recombination of electron-ion pairs in liquid argon and liquid xenon. *Phys. Rev. A*, 36:614–616, Jul 1987. doi:10.1103/PhysRevA.36.614.

- [78] K. N. Pushkin, et al. Scintillation light, ionization yield and scintillation decay times in high pressure xenon and xenon methane. *Nuclear Science, IEEE Transactions on*, 54(3):744–750, June 2007. ISSN 0018-9499. doi: 10.1109/TNS.2007.894815.
- [79] D. C. Malling, et al. After LUX: The LZ Program. *ArXiv e-prints*, October 2011.
- [80] E. Aprile and XENON1T collaboration. The XENON1T Dark Matter Search Experiment. *ArXiv e-prints*, June 2012.
- [81] L. L. Lucas and M. P. Unterweger. Comprehensive review and critical evaluation of the half-life of tritium. *Journal of Research of NIST*, 105(4):541 – 551, 2000. ISSN 0883-2889. doi:<http://dx.doi.org/10.6028/jres.105.043>.
- [82] *PS4-MT3/15-R/N SPECIFICATIONS.*
- [83] Hitoshi Miyake, Masao Matsuyama, Kan Ashida, and Kuniaki Watanabe. Permeation, diffusion, and solution of hydrogen isotopes, methane, and inert gases in/through tetrafluoroethylene and polyethylene. *Journal of Vacuum Science Technology A: Vacuum, Surfaces, and Films*, 1(3):1447–1451, Jul 1983. ISSN 0734-2101. doi:10.1116/1.572038.
- [84] A Bondar, et al. Two-phase argon and xenon avalanche detectors based on gas electron multipliers. *Nuclear Instruments and Methods in Physics Research Section A: Accelerators, Spectrometers, Detectors and Associated Equipment*, 556(1):273–280, 2006.
- [85] Eido Shibamura, et al. Drift velocities of electrons, saturation characteristics of ionization and w-values for conversion electrons in liquid argon, liquid argon-gas mixtures and liquid xenon. *Nuclear Instruments and Methods*, 131(2):249 – 258, 1975. ISSN 0029-554X. doi:[http://dx.doi.org/10.1016/0029-554X\(75\)90327-4](http://dx.doi.org/10.1016/0029-554X(75)90327-4).
- [86] A. Dobi, et al. Study of a zirconium getter for purification of xenon gas. *Nuclear Instruments and Methods in Physics Research Section A: Accelerators, Spectrometers, Detectors and Associated Equipment*, 620(23):594 – 598, 2010. ISSN 0168-9002. doi:<http://dx.doi.org/10.1016/j.nima.2010.03.151>.
- [87] D.S. Leonard, et al. A simple high-sensitivity technique for purity analysis of xenon gas. *Nuclear Instruments and Methods in Physics Research Section A: Accelerators, Spectrometers, Detectors and Associated Equipment*, 621(1-3):678 – 684, 2010. ISSN 0168-9002. doi:DOI:10.1016/j.nima.2010.04.152.
- [88] E. Aprile, T. Yoon, A. Loose, L. W. Goetzke, and T. Zelevinsky. An atom trap trace analysis system for measuring krypton contamination in xenon dark matter detectors. *Review of Scientific Instruments*, 84(9):093105, September 2013. doi:10.1063/1.4821879.

- [89] Sebastian Lindemann and Hardy Simgen. Krypton assay in xenon at the ppq level using a gas chromatographic system and mass spectrometer. *Eur.Phys.J.*, C74:2746, 2014. doi:10.1140/epjc/s10052-014-2746-1.
- [90] A. Dobi, et al. Xenon purity analysis for EXO-200 via mass spectrometry. *Nucl.Instrum.Meth.*, A675:40–46, 2012. doi:10.1016/j.nima.2012.01.066.
- [91] J. Escada, et al. A Monte Carlo study of the fluctuations in Xe electroluminescence yield: pure Xe vs Xe doped with CH₄ or CF₄ and planar vs cylindrical geometries. *Journal of Instrumentation*, 6:8006, August 2011. doi:10.1088/1748-0221/6/08/P08006.
- [92] B.J.P. Jones, et al. The Effects of Dissolved Methane upon Liquid Argon Scintillation Light. *JINST*, 8:P12015, 2013. doi:10.1088/1748-0221/8/12/P12015.